Unsteady Nearshore Currents on Longshore Varying Topographies

Francisco Sancho and Ib A. Svendsen

RESEARCH REPORT NO. CACR-97-10
December, 1997

Center for Applied Coastal Research
Ocean Engineering Laboratory
University of Delaware
Newark, DE 19716
U.S.A.

ACKNOWLEDGMENTS

Funding for this study was provided by the Office of Naval Research, Coastal Sciences (contract N00014-95-C-0075). Support was also provided by the "Ciência" and "PRAXIS XXI" programmes, of the "Junta Nacional de Investigação Científica e Technológica" (JNICT), under contract numbers BD/1761/91-1G and BD/3656/94. The contribution from the "Laboratório Nacional de Engenharia Civil" in Portugal was carried out via the G3 Coastal Morphodynamics Programme (contract MAS2-CT92-0027).

The authors are thankful to Joan Oltman-Shay, Bill Birkemeier, and Ed Thornton for providing the field data for the comparisons in this work.

TABLE OF CONTENTS

LIST OF FIGURES

6.43 Cross-shore distribution at the primary cross-shore array of the terms in the time-averaged momentum equations for the 19/10/90:1221 simulation. Terms in the x–momentum balance: $gh\frac{\partial \bar{\zeta}}{\partial x}$ (+), $\frac{1}{\rho}\frac{\partial S_{xx}}{\partial x}$ (——), $\frac{1}{\rho}\frac{\partial S_{yx}}{\partial y}$ (○), $\overline{\frac{\partial}{\partial x}\left(\frac{\bar{Q}_x^2}{h}\right)}$ (×), $\overline{\frac{\partial}{\partial y}\left(\frac{\bar{Q}_x\bar{Q}_y}{h}\right)}$ (∗), – turb. mixing (– ·), $\frac{\tau_x^B}{\rho}$ (– –), – dispersive mixing (–•–), $\frac{\tau_x^S}{\rho}$ (. . .). Terms in the y–momentum balance: $gh\frac{\partial \bar{\zeta}}{\partial y}$ (+), $\frac{1}{\rho}\frac{\partial S_{yy}}{\partial y}$ (——), $\frac{1}{\rho}\frac{\partial S_{xy}}{\partial x}$ (○), $\overline{\frac{\partial}{\partial y}\left(\frac{\bar{Q}_y^2}{h}\right)}$ (×), $\overline{\frac{\partial}{\partial x}\left(\frac{\bar{Q}_x\bar{Q}_y}{h}\right)}$ (∗), – turb. mixing (– ·), $\frac{\tau_y^B}{\rho}$ (– –), – dispersive mixing (–•–), $\frac{\tau_y^S}{\rho}$ (. . .). 294

LIST OF TABLES

ABSTRACT

In this thesis we examine the effect of longshore varying topographies on the nearshore currents. The governing equations are derived from the conservation of mass and momentum principles, integrated over the depth and the short-wave and turbulent motions. The turbulent Reynolds stresses are modeled using the eddy viscosity concept, which provides a simple closure to determine analytical profiles for the vertical variation of the horizontal currents. A second closure in the model equations is provided by a nonlinear formulation for the wave-current bottom shear stress. The coupled wave-current problem is separated by considering only the effects of the short waves on the currents. The short-wave quantities are given by an external "wave-driver" model, and thus the wave-induced forcing is assumed known. The coupling between the depth-varying and the depth-integrated equations forms the Quasi-3D model system considered here. The model equations are solved numerically using a high-order finite difference scheme.

We compare the solution of the present numerical model with that of a simplified, semi-analytical model derived by Putrevu *et al.* (1995) for two beach configurations. This comparison provides an analysis of the limitations of the simplified model, which turns out to be grossly inaccurate for a barred beach with a small rip-channel. The reasons for the discrepancies are analyzed and found to be due to several factors, the most important being that the largest forces (i.e., terms) in the longshore direction are an order of magnitude smaller than the largest cross-shore forces, and this is not properly recognized in the model of Putrevu *et al.* (1995).

We also examine the development and propagation of shear instabilities over a longshore uniform plane beach. Our results are compared with those of previous authors (Özkan-Haller and Kirby, 1995) and we further study the phase spectra of the cross-shore and longshore velocity fluctuations (associated with the shear wave motion) calculated at the same location. Shear waves over a barred beach with a small rip-channel are predicted as well for two different incident wave conditions. In the absence of dispersive mixing, the shear instabilities are very energetic, though, this mixing is reduced with the inclusion of the dispersive mixing (depth-varying currents) in the model equations. In general, it appears that a balance exists between the dispersive and the shear wave mixing, which are also dependent on the eddy viscosity formulation. We predict the formation of rip-currents for a barred beach under wave conditions with a strong longshore variability of the wave field in the neighborhood of the rip-channel. The results show that the largest driving force for the longshore currents in that region is the longshore gradient of the mean surface elevation. Both unsteady rip-currents and shear waves are predicted simultaneously, which suggests that both phenomena share a common instability mechanism.

Finally, we apply the present model to simulate the conditions observed at three dates during the DELILAH 1990 field experiment, corresponding to different wave and tidal conditions. The comparisons between the model predictions and the data suggests that we failed to predict the large longshore current measured over the trough region for the 10th of October. The possible existence of a larger scale longshore pressure gradient during DELILAH is discussed, and found to be a possible driving mechanism to justify the discrepancy. A second mechanism that can explain this disagreement is the too simplistic representation of the wave forcing provided by the wave-driver used herein. For the other dates we find a closer agreement between the model and data results, which gives confidence to the use of the present model, though several improvements are suggested.

Chapter 1

INTRODUCTION

1.1 Nearshore currents

The term "nearshore currents" was introduced in the literature by Shepard and Inman (1950) to define the currents directly associated with the action of the wind generated waves in and near the breaker zone. Nearshore circulation is dominated by wave-induced forces, associated with shallow water wave breaking. However, due to the range of time and length scales that affect the nearshore region, other forcing mechanisms for the nearshore circulation should not be neglected (e.g., wind and tide). These motions usually affect a larger area than the surf zone region and thus the currents in that region are distinguished by those authors as "coastal currents".

In the nearshore region the flow pattern is dominated by wind-generated waves that evolve from deep water to the shoreline under the processes of refraction, diffraction, shoaling and breaking. Closer to the shore, as the waves propagate into shallower water, wave breaking starts dominating the transformation processes and turbulence is produced, convected, diffused and dissipated after breaking occurs. The momentum carried by these waves is released as they break, providing a driving force for the nearshore currents.

The wave and current motions create lifting forces in the sediments from the sea-bed, which can be picked up and transported for considerable distances. Hence, the fluid motion is responsible for the sediment transport and bed variations. Although the sediment motion can affect the fluid motion (especially in the region closer to the bed), this influence can be considered small enough such that we account for it only by means of the bottom drag on the flow above it.

Shepard and Inman (1950), furthermore, considered the nearshore circulation as a combination of the following sub-systems:

1. Shoreward mass flux of water carried by the wind generated waves;
2. Longshore currents as those which flow along the coast, and are caused by the obliquely incident waves and longshore mean surface elevation gradient;
3. Seaward returning currents, which are subdivided into rip-currents and uniform seaward return flow (nowadays recognized as undertow).

In the following subsections we will provide a detailed description of these flows and the interaction between them as they are not independent.

1.1.1 Short-wave motion and nearshore current generation mechanisms

Wave breaking can be considered as the process of transformation from an essentially irrotational wave motion into rotational and turbulent flows (Battjes, 1988). The shallow water steepening has been identified as the primary cause of breaking for waves on a beach. On natural sloping beaches the most common wave breakers are spilling and plunging breakers. As the waves reach a limiting steepness, a portion of the water front becomes vertical and then overturns, projects forward,

and forms a jet of water. The turbulence generated by wave breaking destroys the organized nature of the motion, which then results in a motion characterized by the propagation of a bore into shallower water (Peregrine, 1983). A surface roller in the front of the bore acts as the main generation mechanism of turbulence, but behind this region turbulence continues to spread (Peregrine and Svendsen, 1978).

Roller (or vortex) formation does not cause an immediate decrease of the total kinetic energy, but it induces a loss of the energy associated with the wave motion. A decrease in wave energy is accompanied by a more or less proportional decrease in total convective momentum flux. Because total momentum is conserved, a positive mean horizontal pressure gradient is induced, resulting in a setup of the mean water level.

Short waves carry mass towards the shore due to the open orbital trajectories of the particle motions above the surface trough level. After wave breaking, the surface bore that forms also transports water with it shorewards. This shoreward mass flux of water is returned offshore by the undertow and, when present, by rip-currents.

Wave breaking is not only responsible for small-scale turbulence, but also creates other motions of different types and scales, such as low-frequency waves and steady flows. Low-frequency waves can propagate along the shore, trapped by refraction, as well as across the shore, radiating energy between the nearshore and offshore regions. The first type are recognized as edge waves, while in the second case they are generally known as "leaky" waves. The importance of both types of waves is evidenced by the fact that natural beaches often exhibit morphological features such as bars and beach cusps with length scales considerably in excess of those of the wind waves. In fact, this length scales often show to be of the same order as the observed long-wave length scale.

Three classes of steady flows can be considered, which were already mentioned above: longshore currents, rip currents and undertow. Longshore currents are originated mainly by the transfer of longshore momentum when waves break onto the beach. A longshore gradient in the mean surface elevation can cause strong longshore currents as well, and also rip-currents. The latter are known to carve rip-channels in the sand bed, which in turn reinforce the convergence of the water towards them and lowers the setup that it would exist otherwise. An early account of rip-currents and rip-channels morphodynamics is given by Shepard *et al.* (1941). Dalrymple (1978) classified rip-currents into two categories, the first being related to forcing by wave-wave or wave-current interactions, and the second being related to a longshore non-uniform bottom topography. A simple linear model given by that author illustrates the formation of rip-currents on a barred beach with rip-channels, forced by a local longshore pressure gradient. The water flowing seawards along the rip-current originates from the shoreward mass transported over the bar by the short waves.

The undertow is the offshore flow beneath the trough level, opposite to the shoreward mass flux above the trough, carried along the wave motion. Several studies address this two-dimensional (in a vertical plane) flow, where a good literature review can be found in Svendsen (1984a) and Dally and Dean (1986). This flow is forced by the cross-shore pressure gradient, which in turn is mainly caused by a decrease (in the breaking region) of the cross-shore component of the wave radiation stress. The description of the undertow flow is not a closed problem yet, mainly due to the unknown characteristics of the flow in the breaking and surf zones, and the interaction between the mean flow and the short-wave motion (Nielsen and You, 1996). The correct estimation of the wave mass transport is another issue that deserves further research (Osiecki and Dally, 1996; Garcez Faria *et al.*, 1996a).

1.1.2 Unstable motions

Rip-currents are just a feature of general horizontal circulation cells which can be caused by a variety of factors, all involving some alongshore nonuniformity in the geometry and/or the incident waves. A stability analysis was performed by Hino (1974) for a system of normally incident waves on an initially plane beach, with allowance for changes in morphology as a result of sediment transport caused by the flow field. Results showed that the system was unstable against longshore perturbations: both the flow field and the bottom topography allowed for longshore periodic solutions in a slow time-scale, such that the flow field was considered quasi-stationary. Their instability mechanism predicted the formation of cusps and oblique crescentic sand bars. Similar studies have recently been presented by Christensen *et al.* (1994) and Falqués *et al.* (1996).

A similar type of instability mechanism was identified by Bowen and Holman (1989) for the longshore currents, as a result of a shear in the cross-shore distribution of the longshore currents, leading to the so-called shear waves or vorticity waves. Their solution allowed for a hydrodynamic instability mechanism on a shorter time-scale than that of Hino (1974), such that the bottom was considered fixed and the unstable wave modes are of the order of 100–1000 s. This mechanism has similar properties to that of the Rayleigh instability of inviscid parallel flows. Evidence of these motions have been observed both in field (Oltman-Shay *et al.*, 1989) and laboratory (Reniers *et al.*, 1997) conditions.

There are also indications that rip-currents can be hydrodynamically unstable, in a similar fashion to that of the shear waves motion. In fact, rip-currents are analogous to plane jets, and these are known to be unstable (Drazin and Reid, 1982). Field observations of fluctuations of the rip-currents have been reported by

Shepard and Inman (1950) and Sonu (1972). Recent experimental results in laboratory facilities (Haller *et al.*, 1997) also suggest that flow instabilities can be present in rip-currents.

1.1.3 Horizontal and vertical distribution: Quasi-3D concept

It is convenient to distinguish between two major classes of models to describe the motion in the nearshore region: (i) the time-dependent models that resolve the instantaneous state of the motion, and (ii) the wave-averaged models where the short-wave (wind induced) motion is separated from the mean motion. Only the second method will be discussed in this work.

Among the wave-averaged models, several approaches have been used for the last three-decades. A common approach has been by means of a two-dimensional horizontal (2DH) flow model. This type of models is based on the turbulence-averaged, depth-integrated, time-averaged (over the short-wave period) Navier-Stokes equations and describe the mean current and surface elevation for a coastal area. Another modeling concept, known as cross-shore circulation or two-dimensional vertical (2DV) model, describes the mean motion on a vertical plane normal to the shoreline – the undertow flow.

Both of the above formulations are simplifications of the fully three-dimensional (3D) problem. A class of models describing a simplified 3D situation, known as quasi-3D models, has been developed for shallow water flows in estuaries and coastal waters (Davies, 1987; De Vriend and Stive, 1987; Svendsen and Lorenz, 1989; Jin *et al.*, 1991, among others). This concept makes use of the existing techniques both for the 2DH and the 2DV current models. Complete 3D models have recently seen some advances (Pechon and Teisson, 1994; Mayerle *et al.*, 1994), although they

require considerably more computer time and memory than the quasi-3D models. Thus, they are still in an early state of development.

The formulation of the quasi-3D models combines the depth-uniform horizontal current with the vertically non-uniform flow. One of the first models utilizing this concept is given by De Vriend and Stive (1987). These authors divided the time-averaged horizontal current into two parts: a primary flow, defined as the flow in the direction of the depth-averaged velocity and driven by the depth-invariant part of the forces (e.g. the pressure gradient); and a secondary flow, which is driven by the vertical non-uniformity of the wave-induced forces and primary flow accelerations, and the surface wind shear stress (when present). The secondary flow model (driven mostly by the wave motion) is based on the 3-layer concept, assuming different regimes in the bottom boundary layer, middle layer and upper layer, but solving only for the velocity in the central layer whereas the other layers interact by means of shear stresses.

A slightly different quasi-3D model was presented by Sanchez-Arcilla *et al.* (1990). The current velocity was split into a depth-invariant part and a vertical variation with zero mean flow integrated over the central layer. However, these authors kept in their derivation some of the terms that gave rise to the interaction between the depth-averaged and depth-varying flows. The model also uses the 3-layer concept and solutions were presented for a coupled solution of the middle and bottom layers by Sanchez-Arcilla *et al.* (1992).

Similar to the previous model, Svendsen and Lorenz (1989) split the vertically varying longshore and cross-shore currents with the assumption of (very) weak dependence. However, unlike the previous authors, they did not need to integrate the flow equations only up to the wave-trough level, but instead, over the whole water column. Using a simple bottom shear stress boundary condition they studied the

motion only for the middle-layer. Their results showed that the total vertical current profile has a spiral shape, resulting from the combination of the (depth-varying) undertow with the (depth-varying) longshore currents.

Svendsen and Putrevu (1990) formulated a steady-state quasi-3D circulation model using analytical solutions for the vertical variation of the currents in combination with a numerical solution of the depth-integrated 2DH equations. Later, Putrevu and Svendsen (1992a) and Svendsen and Putrevu (1994) showed that the coupling between the cross-shore current (undertow) and the longshore current is rather important and it induces a mixing mechanism similar to the turbulence effect, but of much stronger magnitude. The steady-state model of Svendsen and Putrevu (1990) with the current-current and wave-current interaction terms was extended by Van Dongeren *et al.* (1994) to a time-dependent model, able to study non-stationary phenomena. The extension of that model to a non-cylindrical coast is given in Putrevu and Svendsen (1997) and Van Dongeren and Svendsen (1997b), allowing the study of general nearshore phenomena such as surf-beat, edge waves, longshore currents, shear waves and rip-currents. Furthermore, the vertical variation of these flows can be analyzed as well. In the present work we continue the development of the model presented by the previous authors, named SHORECIRC, with emphasis on the model closures.

In summary, over the last ten years we have seen the development of several quasi-3D models. These are, in principle, able to describe the flow in general beach topographies varying both in the cross-shore and longshore directions. Nevertheless, most applications of these models have been so far for longshore uniform situations (e.g., De Vriend and Stive, 1987; Rodriguez *et al.*, 1994; Garcez Faria *et al.*, 1995; Van Dongeren and Svendsen, 1997b; Rakha and Kamphuis, 1997). Applications to longshore non-uniform beaches introduce longitudinal gradients in the model

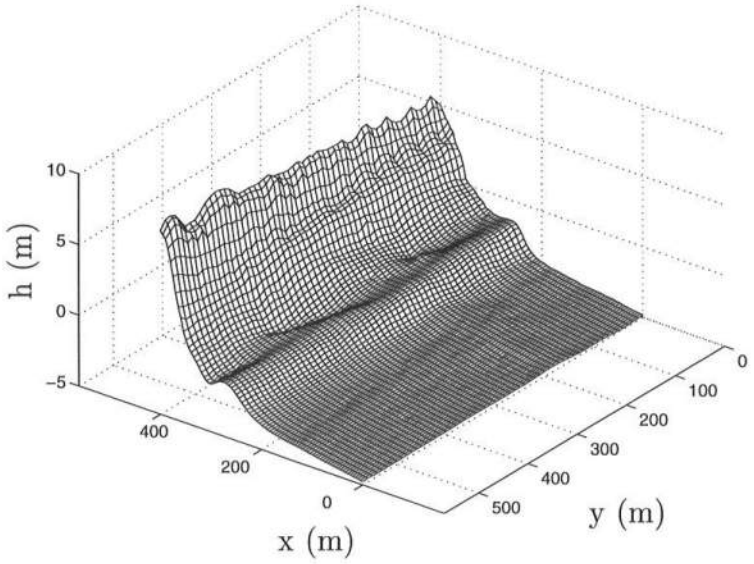

Figure 1.1: Observed bathymetry on October, 10, 1990, during the DELILAH field experiment at the Field Research Facility in Duck, NC.

equations and allow for the modeling of far more complex phenomena involving 3D interaction between the short-wave averaged velocities. An example of such situation is given by Sancho *et al.* (1996) for the simulation of a particular flow condition at the Field Research Facility in Duck, North Carolina, observed during the DELILAH experiment. The modeled bathymetry was strongly three-dimensional, exhibiting oblique sand bars superposed over a longshore bar (Figure 1.1). The preliminary results of those authors showed the ability of the present quasi-3D model to simulate non-steady nearshore currents over a longshore non-uniform bottom.

Lastly, it will be shown in the derivation of the present quasi-3D model (SHORECIRC) that few terms are neglected. Thus, compared to fully 3D models, the SHORECIRC model contains the same mechanisms and interactions that account for the vertical variation of the flow. The simplifications of the model equations are only to a degree equivalent to that of simplifications also needed in a 3D

model, such as (for example) the description of the short-wave related quantities.

1.2 Motivation and Objectives

From the studies mentioned above and others it is accepted that the processes governing the nearshore currents are very complex and cover a vast spectrum of frequencies. The dynamics of the vertical and horizontal nearshore circulation are governed primarily by the breaking incident waves. High-frequency (turbulence) and low-frequency motions usually play a secondary role. However, infragravity wave motions, in particular, can play an important role as the currents can no longer be considered quasi-steady. The interaction between wind-generated waves and the currents is of importance too, specially at inlets where waves can meet strong tidal currents. Wave groups generate surf-beat which can be observed as time-varying currents. Inhomegeneities in the bottom topography can affect significantly affect not only the short-wave motion but the nearshore currents as well. On natural beaches, the bed is not fixed and the time-scale at which the topography can vary is, sometimes, of the same time-scale at which the incident wave field changes and, therefore, the nearshore current field.

It is therefore the objective of the present work to contribute to the understanding of the nearshore currents. We analyze in particular steady and non-steady flows originated by a quasi-stationary incident wave field. Several simplifying canonical beach configurations are considered, where we carry numerical simulations by means of the quasi-3D numerical model SHORECIRC. The development of this model is part of the work presented in this dissertation and also given by Van Dongeren and Svendsen (1997b). We pursue our objectives by interpreting the model results and analyzing the magnitude and importance of the various terms in the model equations. In one example we expand the analysis given by Sancho *et al.*

(1995) to a slightly different beach topography. In particular, we simulate and examine the development of steady and non-steady rip-currents over a longshore non-uniform barred beach. For waves coming obliquely at the same beach, shear waves can be simulated depending on the choice of critical physical parameters.

To help on the verification and calibration of the model, and the physical parameters it contains, we present an extensive comparison of the model results against field data. Hence, the model is applied to simulate the flow characteristics observed at times during the DELILAH experiment (for a summary of this data set see Birkemeier *et al.*, 1997). Furthermore, one of the objectives of this comparison is to guide future research in the areas where it needs most. Hence, we can identify mechanisms that require a better knowledge in order to properly simulate them.

1.3 Methodology

This work describes the nearshore circulation induced by the action of breaking waves over several beach geometries. The bottom is assumed fixed, but this condition is not absolutely necessary as a sediment transport model could be coupled to the present circulation model. We, therefore, intrinsically assume that there are no topography variations during the simulated time. Regarding the model comparison with data this requirement is not always met, as sometimes the beach was active even during periods of few hours. Thus, care should be taken with respect to the interpretation of the results.

The coupled wave-current problem is separated by considering only the effects of waves on currents, where the short-wave quantities are given by a wave-driver model. This procedure results from the assumption that the time scale of the wave transformation is much shorter than that related to the currents variation, and

that the short waves are stationary. The wave-driver model should include the most relevant physical processes that act as the waves propagate shorewards. In the field, randomness of the short waves is an important property that should be accounted for by the wave model. Refraction, shoaling and breaking induced by variable depths are also of primary importance. Current refraction and breaking can be significant when waves propagate onto strong currents such as rip-currents. Several of these phenomena have, however, been simplified into our simulations. For most calculations we neglect the action of current-refraction on the short waves. We find in a field application example that current-refraction due to longshore currents is minimal, and thus it is neglected for practical reasons. For waves propagating against rip-currents, current-refraction is important though in the present study it is neglected as well to center our interest on other processes. We further focus our attention in the currents induced by a periodic wave field.

Due to the unavailability of reliable nonlinear 2DH wave models at the present time, linear wave theory is used herein to describe the kinematics of the waves both inside and outside the surf zone. The use of nonlinear theories could provide an improved description of the flow prior to the breaking point, though for breaking and broken waves no valid wave theory is available. The wave height and direction on a general beach are estimated using the model REF/DIF1 (Kirby and Dalrymple, 1994). This model is based on a parabolic approximation of the mild-slope equation including weak-nonlinearity (Stokes third order amplitude dispersion) in the wave speed (Kirby and Dalrymple, 1983). It is, nevertheless, a linear wave model and can account for current and depth-induced refraction, wave diffraction, shoaling, breaking and bottom-induced energy dissipation. Wave reflection from structures or the bottom is neglected, and therefore we limit the model applications to mildly-varying beaches where reflection is minimal. The results from this model are used to calculate the short-wave radiation stresses and wave-induced mass flux.

The quasi-3D model SHORECIRC is formed by two components dependent on each other:

1. A numerical module which solves the short-wave averaged equations of motion for the depth-averaged values of the (time-dependent) currents ($\vec{\bar{V}}$) and mean surface elevation ($\bar{\zeta}$).

2. A second component that evaluates the analytical solutions to the vertical distribution of the horizontal velocities in the time varying currents.

The model SHORECIRC makes use of the short-wave averaged quantities determined by REF/DIF1. Several submodels (or closures) are included in SHORECIRC, such as an eddy viscosity parameterization, and the bottom shear stress formulation. A detailed description of these submodels is provided later.

The model equations of module (1) are solved numerically by a finite difference scheme. The horizontal domain of integration is discretized by a rectangular grid with open boundaries everywhere except at the shoreline, which constitutes the landward boundary. At the seaward boundary a generating-absorbing condition is used (Van Dongeren *et al.*, 1994; Van Dongeren and Svendsen, 1997a). At the shore-normal lateral boundaries, a periodicity condition is implemented, which limits the present applications to longshore periodic domains. In applications where the lateral flow would be known, the current velocity could be specified along the lateral boundaries, defining a well-posed problem. However, without the knowledge of currents flowing into (or out of) the model domain, the use of periodic lateral boundaries is likely to be a good approximation provided the regions outside the model domain do not exhibit hydrodynamic or morphological features too different from the ones within the model region.

1.4 Outline of the present work

This dissertation is outlined as follows. In Chapter 2 we derive the governing equations of the short-wave averaged nearshore current model. The 2DH model interacts with the vertically-varying currents by means of integral terms that provide a dispersive mixing. These terms are derived under certain assumptions, which we discuss in detail. We finalize Chapter 2 giving the closure sub-models to completely define our nearshore current model.

The solution method to our model equations is given in Chapter 3. Finite differences are utilized to seek a numerical solution for these equations. The properties of the numerical method are analyzed and discussed in detail as well.

In Chapter 4 we deal with the presentation and discussion of a simplified model for longshore currents that accounts for the influence of the longshore pressure gradient caused by the presence of a weakly longshore non-uniform bathymetry (this model was originally given by Putrevu *et al.*, 1995). A detailed comparison of that model with a solution of the complete SHORECIRC model shows the range of applicability and deficiencies of the simplified semi-analytical solution.

Several model applications are shown in Chapter 5 in order to illustrate various mechanisms that can exist in nearshore flows. We start with the study of shear waves over a plane beach, and compare our results with those of Allen *et al.* (1996) and Özkan-Haller and Kirby (1997) for the same case. This comparison provides an illustration of the dynamics of the shear waves, and also confirms the accuracy of our numerical method. Furthermore, several experiments are given to examine the sensitivity of the numerical model to the spatial and temporal discretizations. The effect of the inclusion of the vertically-varying currents in the model equations over a barred beach is analyzed in section 5.2. The interaction terms provided by the

vertically-varying currents cause a dispersive mixing, and are seen to affect significantly the development of shear instabilities of the longshore currents. In section 5.3 we show the formation of rip-currents over the same barred beach as in the previous example, due to a modification of the incident wave field. The seaward moving mass flux carried by the rip-currents is provided by longshore currents converging towards the rip-channel. The importance of the longshore pressure gradient as a driving force for these large longshore currents is also examined. We finalize Chapter 5 with a brief example on the effect of the bottom shear stress, which illustrates the need for a correct estimation of this quantity.

Having gained in Chapter 5 some insight on the model performance and the physical phenomena we are modeling, in Chapter 6 we proceed with the simulation of field conditions. We chose to model the situation observed at times during the DELILAH 1990 nearshore field experiment at Duck, NC, where previous modeling efforts have failed to predict the measured large longshore currents in the trough region of a barred beach. The model results are compared with the field data, and a discussion is provided on the importance and effect of the mechanisms that affect the results. Using the default free parameters of the model (the bottom friction and eddy viscosity coefficients), the results compare fairly well with the data. Unlike the measured currents our model results indicate a maximum of the longshore current over the bar-crest, though. Several reasons are pointed out for that discrepancy.

The summary and conclusions are provided in Chapter 7. We finish that chapter by stating suggestions for future research in the areas we found it is needed most. The model assumptions are re-examined, and further work is suggested to prove their validity under certain applications. Especially, we find there is need for further field and laboratory experiments, such that the model assumptions and parameterizations could be assessed and improved.

Chapter 2

EQUATIONS OF MOTION IN THE NEARSHORE REGION

In this chapter we will briefly rederive the dynamical conservation equations for mass and momentum of a wave motion superimposed on a current field. We follow the steps outlined in Svendsen and Putrevu (1996) and given in detail by Putrevu and Svendsen (1991) for a depth-varying current, whose derivation is similar to that presented by Phillips (1977) (pp. 60-63) and Mei (1989) (pp. 453-463) for a depth-uniform current velocity.

A basic assumption underlying the following derivation is that the instantaneous velocity of the flow motion can be decomposed into different components related to different time and length scales of the motion. We will separate the flow into a mean part, describing a steady or slowly-varying current, and a fluctuating part which corresponds to a rapidly-varying motion. The latter component encompasses both the short-wave motion (wind waves and swell) and the purely turbulent fluctuations, which although conceptually different, can have scales of the same order of magnitude (as e.g. in a breaking wave).

To be able to separate the wave motion from the "mean" motion we need to assume that we know the time variation of the short-wave motion. In order to do so we assume that the short waves are periodic, though they can be steady or slowly

varying in time. For convenience, we also assume that the relative depth change within one wavelength is small (Svendsen and Putrevu, 1996). This requirement simplifies the problem in the sense that any conclusions drawn for a local constant depth can be generalized for any location, had the water depth been constant everywhere with exactly the local depth. The advantage of this simplification is that it allows us to use constant depth theories, such as Airy linear wave theory, to describe the wave motion.

2.1 Depth and time-averaged equations of motion

In the following we will follow an Eulerian description of the flow, i.e., describe the time-variation of the flow properties of any particular spatial element. We assume turbulent flow over a fixed bed for a fluid of constant density, ρ. For convenience, the equations are given in Cartesian coordinates (x, y, z), and tensor notation is used for the variables in the horizontal dimensions $(x, y) \equiv x_\alpha$: repeated indices imply summation and $\delta_{\alpha\beta}$ is the Kronecker delta. The vertical coordinate is represented by z, directed upwards with origin at the still water level (see Fig. 2.1). The equations of motion are given in an inertial (or nonrotating) frame of reference. Hence, we assume the time and length scales of the motion to be small enough such that the Coriolis acceleration is negligible (Rossby number $\ll 1$).

The governing equations are then given by the Reynolds equations for conservation of mass

$$\frac{\partial u_\alpha}{\partial x_\alpha} + \frac{\partial w}{\partial z} = 0\,, \tag{2.1}$$

and momentum

$$\frac{\partial u_\beta}{\partial t} + \frac{\partial u_\alpha u_\beta}{\partial x_\alpha} + \frac{\partial u_\beta w}{\partial z} = -\frac{1}{\rho}\frac{\partial p}{\partial x_\beta} + \frac{1}{\rho}\left(\frac{\partial \tau_{\alpha\beta}}{\partial x_\alpha} + \frac{\partial \tau_{z\beta}}{\partial z}\right)\,, \tag{2.2}$$

$$\frac{\partial w}{\partial t} + \frac{\partial u_\alpha w}{\partial x_\alpha} + \frac{\partial w^2}{\partial z} = -\frac{1}{\rho}\frac{\partial p}{\partial z} - g + \frac{1}{\rho}\left(\frac{\partial \tau_{\alpha z}}{\partial x_\alpha} + \frac{\partial \tau_{zz}}{\partial z}\right) . \tag{2.3}$$

In here, u_α and w are the ensemble-averaged (or turbulent-averaged) total particle velocities in the horizontal and vertical directions, respectively; p represents the pressure and $\tau_{\alpha\beta}$ are the components of the combined turbulent and viscous stress tensor, defined as:

$$\tau_{\alpha\beta} \equiv -\rho \overbrace{u'_\alpha u'_\beta} + \tau^{visc} . \tag{2.4}$$

where the overbrace indicates ensemble (or turbulent) averaging, defined such that $\overbrace{u'_\alpha} = 0$ where u'_α is the turbulent velocity component. The viscous stress tensor τ^{visc} is usually much smaller then the turbulent stress tensor for the type of flows considered here, except in the boundary layer near the solid boundaries which is out of the scope of this work. Hence, we neglect the viscous stresses in the following.

It is convenient to introduce the total volume flux Q_α defined by

$$Q_\alpha \equiv \int_{-h_o}^{\zeta} u_\alpha \, dz , \tag{2.5}$$

where $-h_o$ is the vertical coordinate of the bottom (h_o is the still water depth), and ζ is the instantaneous free-surface position. For clarity, refer to the definition sketch in Fig. 2.1. Furthermore, we divide the total particle velocity (u_α, w) into a "mean" component – the current V_α –, and an oscillatory component $u_{w\alpha}$ corresponding to the short-wave motion:

$$u_\alpha = V_\alpha + u_{w\alpha} \quad ; \quad w = W + w_w . \tag{2.6}$$

We note that the mean vertical component of the current W is usually considerably smaller than the horizontal components. This is seen in the experimental data of, e.g., Cox *et al.* (1995) for a plane beach profile. However, the order of magnitude analysis given by Putrevu and Svendsen (1997) suggest that W cannot be neglected.

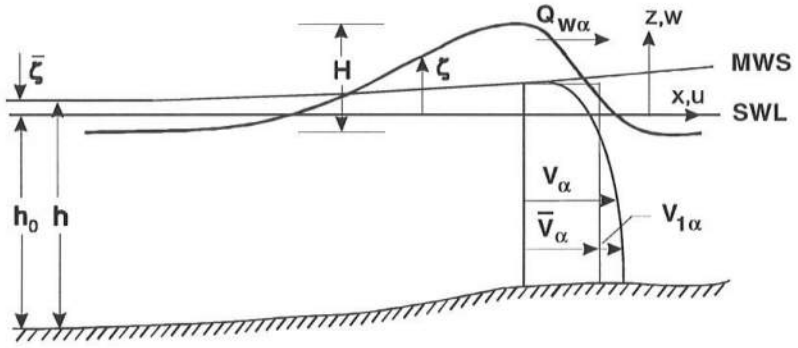

Figure 2.1: Definition sketch of the relevant variables.

Before we describe the derivation it should be mentioned that a thorough discussion of the role of the turbulent shear stresses defined by equation (2.4) is given later. However, for the purpose of our derivation, it suffices to assert that we model the turbulent Reynolds stresses using the eddy viscosity concept proposed by Boussinesq. For such, it is assumed that the turbulent stresses are proportional to the mean velocity gradients, which can be expressed by (e.g., Rodi, 1984):

$$\tau_{\alpha\beta} = \rho\,\nu_t \left(\frac{\partial V_\alpha}{\partial x_\beta} + \frac{\partial V_\beta}{\partial x_\alpha} \right) - \rho\,\frac{2}{3}\,k\,\delta_{\alpha\beta}\,, \tag{2.7}$$

and

$$\tau_{z\beta} = \rho\,\nu_t\,\frac{\partial V_\beta}{\partial z} - \rho\,\frac{2}{3}\,k\,\delta_{z\beta}\,, \tag{2.8}$$

where ν_t is the turbulent eddy viscosity and k is the turbulent kinetic energy per unit mass defined as

$$k = \frac{1}{2}\left(\widehat{u'^2} + \widehat{v'^2} + \widehat{w'^2} \right). \tag{2.9}$$

The value of ν_t is dependent on the turbulent characteristics of the flow and a closure is needed to determine its value (see section 2.4.1). The energy k is just a scalar like the pressure p and thus the second terms on the right-hand side of equations (2.7) and (2.8) can just be absorbed by the pressure gradient terms in the governing Reynolds equations.

The derivation of governing equations for the mean flow, starting from the Reynolds-averaged equations (2.1)–(2.3), is then summarized as follows:

1. We first integrate the mass conservation equation (2.1) and the horizontal momentum equation (2.2) from the bottom $-h_o$ to the instantaneous free-surface position ζ, and apply Leibniz rule to place the differential operators $\frac{\partial}{\partial x_\alpha}$ outside the integrals.

2. We then introduce the kinematic boundary conditions at the free-surface and the bottom, respectively given by

$$w(\zeta) - u_\alpha \frac{\partial \zeta}{\partial x_\alpha} = \frac{\partial \zeta}{\partial t}\,, \tag{2.10}$$

$$w(-h_o) + u_\alpha \frac{\partial h_o}{\partial x_\alpha} = 0\,, \tag{2.11}$$

into those equations to eliminate the terms that were evaluated at $z = -h_o$ and $z = \zeta$. We also make use of the dynamic boundary conditions which yield the surface and bottom shear stresses τ_β^S and τ_β^B, respectively. The dynamic boundary condition at the free-surface $z = \zeta$ reads

$$-\left(-p\,\delta_{\alpha\beta} + \tau_{\alpha\beta}\right) \frac{\partial \zeta}{\partial x_\alpha} + \tau_{z\beta} = \tau_\beta^S \, |\nabla F|\,, \tag{2.12}$$

and at the bottom $z = -h_o$ is given by

$$\tau_{\alpha\beta} \frac{\partial h_o}{\partial x_\alpha} + \tau_{z\beta} = \tau_\beta^B \, |\nabla B|\,, \tag{2.13}$$

where $\nabla F = (-\frac{\partial \zeta}{\partial x}, -\frac{\partial \zeta}{\partial y}, 1)$ and $\nabla B = (-\frac{\partial h_o}{\partial x}, -\frac{\partial h_o}{\partial y}, 1)$. Furthermore, assuming a small bottom slope and small mean free-surface slope we simplify the right-hand-side (RHS) of equations (2.12)–(2.13) by:

$$\tau_\beta^S \, |\nabla F| \approx \tau_\beta^S\,, \tag{2.14}$$

$$\tau_\beta^B \, |\nabla B| \approx \tau_\beta^B\,. \tag{2.15}$$

In the above we implicitly assume that the dynamic condition is not exactly given at the bottom, but at the top of the bottom boundary layer. In doing so, we avoid the difficulty of computing the details of the flow in the bottom boundary layer, and account only for the shear stress the boundary layer flow induces on the fluid above that layer (Putrevu and Svendsen, 1991). If we had chosen to include the proper treatment of the bottom boundary layer, then the kinematic boundary condition would read $v_\alpha = 0$ at the bottom.

3. The third step of the derivation consists of the integration of the vertical momentum equation from a level z until the free-surface ζ to obtain an expression for the pressure p at that level z, which reads,

$$\begin{aligned} p &= \rho g (\zeta - z) - \rho \left(w_w^2 + \widetilde{w'^2} \right) + \frac{\partial}{\partial t} \int_z^\zeta \rho w \, dz \\ &+ \frac{\partial}{\partial x_\alpha} \int_z^\zeta (\rho u_\alpha w - \tau_{\alpha z}) \, dz \, . \end{aligned} \tag{2.16}$$

This expression is then used in the depth-integrated equations to eliminate the pressure term, which gives rise to contributions to the radiation stress tensor. At the same time, we also evaluate the pressure at the bottom, which is similarly used in the depth-integrated horizontal momentum equations.

4. Finally, the depth-integrated equations are averaged in time over the short-wave period T. This time-averaging is defined as (indicated by an overbar):

$$\overline{\cdot} \equiv \frac{1}{T} \int_0^T \cdot \, dt \, . \tag{2.17}$$

Thus, we allow for a "mean" motion varying in a longer time scale than that of the short waves, such as in an irregular or non-stationary short-wave field. Furthermore, we assume periodicity of the short-wave motion over a "small" time scale, so that $\overline{\frac{\partial}{\partial t}} = 0$. This averaging is also done on the pressure evaluated in the previous step, which yields

$$\bar{p} = \rho g (\bar{\zeta} - z) - \rho \overline{\left(w_w^2 + \widetilde{w'^2} \right)} + \frac{\partial}{\partial x_\alpha} \overline{\int_z^\zeta (\rho u_\alpha w - \tau_{\alpha z}) \, dz}$$

$$\simeq \quad \rho\, g\,(\bar{\zeta} - z) - \rho\,\overline{\left(w_w^2 + \widehat{w'^2}\right)}\,. \tag{2.18}$$

In the above we neglected the last term because we expect that over several wave periods each water column will support itself and not transfer net weight to the neighboring columns. This step concludes the process of derivation of the governing equations, which we present below.

After proceeding through steps 1–4 of the derivation outline above, we obtain the depth and time-averaged continuity equation

$$\frac{\partial \bar{\zeta}}{\partial t} + \frac{\partial}{\partial x_\alpha}\overline{\int_{-h_o}^{\zeta} u_\alpha\, dz} = 0\,, \tag{2.19}$$

as well as the depth and time-averaged horizontal momentum equation

$$\begin{aligned}
&\frac{\partial}{\partial t}\overline{\int_{-h_o}^{\zeta} u_\beta\, dz} + \frac{\partial}{\partial x_\alpha}\overline{\int_{-h_o}^{\zeta} u_\alpha u_\beta\, dz} = -g\,(h_o + \bar{\zeta})\frac{\partial \bar{\zeta}}{\partial x_\beta} \\
&- \frac{1}{\rho}\frac{\partial}{\partial x_\alpha}\left[\overline{\int_{-h_o}^{\zeta} p\,\delta_{\alpha\beta}\, dz} - \delta_{\alpha\beta}\frac{1}{2}\rho\, g\, h^2\right] + \frac{1}{\rho}\frac{\partial}{\partial x_\alpha}\overline{\int_{-h_o}^{\zeta} \tau_{\alpha\beta}\, dz} \\
&+ \frac{\tau_\beta^S}{\rho} - \frac{\tau_\beta^B}{\rho}
\end{aligned} \tag{2.20}$$

where we kept the pressure term in terms of p for clarity, and h is defined as the total mean water depth $h = h_o + \bar{\zeta}$.

Before we present the final set of equations we apply the time-averaging definition (2.17) to the depth-integrated volume flux Q_α defined by expression (2.5), which yields

$$\bar{Q}_\alpha = \overline{\int_{-h_o}^{\zeta} u_\alpha\, dz} = \int_{-h_o}^{\bar{\zeta}} V_\alpha\, dz + \overline{\int_{-h_o}^{\zeta} u_{w\alpha}\, dz}\,, \tag{2.21}$$

where we made use of the velocity partition given by equation (2.6). For a purely oscillatory motion there is no mean transport below the wave trough level ζ_t, so that we can define:

$$\overline{u_{w\alpha}} = 0 \quad \text{below trough.} \tag{2.22}$$

Therefore, the time-averaged volume flux Q_α results from equation (2.21) as

$$\bar{Q}_\alpha = \int_{-h_o}^{\bar{\zeta}} V_\alpha \, dz + Q_{w\alpha} \,, \tag{2.23}$$

where

$$Q_{w\alpha} \equiv \overline{\int_{\zeta_t}^{\zeta} u_{w\alpha} \, dz} \,. \tag{2.24}$$

$Q_{w\alpha}$ represents the mean volume flux caused by the short-wave motion, integrated from the surface-trough level ζ_t to the instantaneous surface position ζ. It can be evaluated by any short-wave theory and it is assumed a known value in our system of modeling equations.

The depth-integrated and time-averaged equations of motion (2.19)–(2.20) can then be rewritten in terms of the mean volume flux $\bar{Q}_\alpha$, and the wave $u_{w\alpha}$ and current velocity V_α components. Introducing equation (2.23) into the continuity equation (2.19) yields

$$\frac{\partial \bar{\zeta}}{\partial t} + \frac{\partial \bar{Q}_\alpha}{\partial x_\alpha} = 0 \,. \tag{2.25}$$

Similarly, for the horizontal momentum equation we get

$$\begin{aligned} &\frac{\partial \bar{Q}_\beta}{\partial t} + \frac{\partial}{\partial x_\alpha} \int_{-h_o}^{\bar{\zeta}} V_\alpha \, V_\beta \, dz + \frac{\partial}{\partial x_\alpha} \overline{\int_{\zeta_t}^{\zeta} (\, u_{w\alpha} \, V_\beta + u_{w\beta} \, V_\alpha) \, dz} = \\ &- g \, (h_o + \zeta) \frac{\partial \bar{\zeta}}{\partial x_\beta} - \frac{1}{\rho} \frac{\partial}{\partial x_\alpha} \left[\overline{\int_{-h_o}^{\zeta} (p \, \delta_{\alpha\beta} + u_{w\alpha} \, u_{w\beta}) \, dz} - \delta_{\alpha\beta} \frac{1}{2} \rho \, g \, h^2 \right] + \\ &\frac{1}{\rho} \frac{\partial}{\partial x_\alpha} \overline{\int_{-h_o}^{\zeta} \tau_{\alpha\beta} \, dz} + \frac{\tau_\beta^S}{\rho} - \frac{\tau_\beta^B}{\rho} \,. \end{aligned} \tag{2.26}$$

Finally, we define the radiation stress tensor $S_{\alpha\beta}$ as the term in square brackets on the RHS of the momentum equation:

$$S_{\alpha\beta} \equiv \overline{\int_{-h_o}^{\zeta} (p \, \delta_{\alpha\beta} + \rho \, u_{w\alpha} \, u_{w\beta}) \, dz} - \delta_{\alpha\beta} \frac{1}{2} \rho \, g \, h^2 \,. \tag{2.27}$$

The radiation stress represent the "excess" momentum flux caused by the short waves on the mean motion (Longuet-Higgins and Stewart, 1964). This term is typically the main forcing responsible for the generation of the wave-induced currents and infra-gravity waves in the nearshore surf zone.

The momentum equation (2.26) can then be written as

$$\frac{\partial \bar{Q}_\beta}{\partial t} + \frac{\partial}{\partial x_\alpha}\int_{-h_o}^{\bar{\zeta}} V_\alpha V_\beta \, dz + \frac{\partial}{\partial x_\alpha}\overline{\int_{\zeta_t}^{\zeta} (u_{w\alpha} V_\beta + u_{w\beta} V_\alpha)\, dz} =$$

$$- g\,(h_o + \zeta)\frac{\partial \bar{\zeta}}{\partial x_\beta} - \frac{1}{\rho}\frac{\partial}{\partial x_\alpha}\left[S_{\alpha\beta} - \overline{\int_{-h_o}^{\zeta} \tau_{\alpha\beta}\, dz}\right] + \frac{\tau_\beta^S}{\rho} - \frac{\tau_\beta^B}{\rho} \; . \qquad (2.28)$$

This equation, together with the equation for conservation of mass (2.25), can be used to calculate the currents V_α and the mean surface elevation $\bar{\zeta}$ provided we know the short-wave motion (through $u_{w\alpha}$ or $Q_{w\alpha}$, and $S_{\alpha\beta}$) and the turbulent characteristics (via the depth-integrated, time-averaged, turbulent stress tensor $\tau_{\alpha\beta}$). Equation (2.28) describes the balance between the time-averaged fluid accelerations (in the LHS) and forces (in the RHS) acting on a vertical parallelepipedic water column (or control volume) of unit base dimensions. On the LHS the first term represents the local acceleration and the second and third terms are the advective accelerations; on the RHS we have from the first to the last term: the pressure gradient, the radiation stress gradient, the contribution of the turbulent stresses, and the surface and bottom shear stresses, respectively. The governing equations (2.25), (2.28) are so far exact, except for the assumptions of constant density, gently sloping bottom and free-surface, and periodic short waves ($\overline{u_{w\alpha}} = 0$, $\overline{\frac{\partial}{\partial t}} = 0$). We also neglected the viscous stresses in favor of the much larger turbulent stresses.

The integral terms in the governing equations explicitly require the knowledge of the vertical variation of the horizontal velocities V_α, both below and above the trough level. We therefore need to calculate the depth profile $V_\alpha(z)$. Once that is determined we can calculate the second and third terms in equation (2.28) by

vertical integration of products of $V_\alpha(z)$ and $u_{w\alpha}(z)$ (assumed known). We deal with the determination of the depth variation of V_α in the next section.

2.2 Vertical variation of the horizontal currents

In order to determine the vertical variation of the horizontal currents V_α we must recede the steps we did previously to determine the depth and time-averaged governing equations for the fluid motion. The following derivation has been given earlier by Svendsen and Lorenz (1989) and, more recently, in greater detail by Van Dongeren and Svendsen (1997b). Therefore, we just give again the important equations in this derivation and omit the details for brevity.

Performing the time-averaging operation onto the Reynolds equation (2.2), and splitting the particle velocity into a current and wave component (defined in equation (2.6)), we obtain:

$$\frac{\partial V_\beta}{\partial t} + \frac{\partial V_\alpha V_\beta}{\partial x_\alpha} + \frac{\partial W V_\beta}{\partial z} + \frac{\partial \overline{u_{w\alpha} u_{w\beta}}}{\partial x_\alpha} + \frac{\partial \overline{u_{w\beta} w_w}}{\partial z} =$$

$$-\frac{1}{\rho}\frac{\partial \bar{p}}{\partial x_\beta} + \frac{1}{\rho}\left(\frac{\partial \tau_{\alpha\beta}}{\partial x_\alpha} + \frac{\partial \tau_{z\beta}}{\partial z}\right) . \tag{2.29}$$

This equation can be rearranged through the substitution of the time-averaged pressure $\bar{p}$, given by equation (2.18), and the turbulent eddy viscosity model (see equations (2.7) and (2.8)). Hence, we get

$$\frac{\partial V_\beta}{\partial t} + \frac{\partial V_\alpha V_\beta}{\partial x_\alpha} + \frac{\partial W V_\beta}{\partial z} + \frac{\partial}{\partial x_\alpha}\left(\overline{u_{w\alpha} u_{w\beta}} - \delta_{\alpha\beta}\,\overline{w_w^2}\right) + \frac{\partial \overline{u_{w\beta} w_w}}{\partial z} =$$

$$-g\frac{\partial \bar{\zeta}}{\partial x_\beta} + \frac{\partial}{\partial x_\alpha}\left[\nu_t\left(\frac{\partial V_\alpha}{\partial x_\beta} + \frac{\partial V_\beta}{\partial x_\alpha}\right)\right] + \frac{\partial}{\partial z}\left(\nu_t \frac{\partial V_\beta}{\partial z}\right) . \tag{2.30}$$

In order to find the depth variation of V_α we split the current velocity into a depth-uniform $\tilde{V}_\alpha$ and a depth-varying part $V_{1\alpha}$ (Svendsen and Putrevu, 1996)

$$V_\alpha\,(x_\alpha, z) \;=\; \tilde{V}_\alpha\,(x_\alpha) \;+\; V_{1\alpha}(z)\,, \tag{2.31}$$

where $\tilde{V}_\alpha$ is defined as

$$\tilde{V}_\alpha \;\equiv\; \frac{1}{h}\overline{\int_{-h_o}^{\zeta} u_\alpha\, dz} \;=\; \frac{\bar{Q}_\alpha}{h}\,, \tag{2.32}$$

and $V_{1\alpha}$ is such that

$$\int_{-h_o}^{\tilde{\zeta}} V_{1\alpha}\, dz \;=\; -Q_{w\alpha}\,. \tag{2.33}$$

So far, no other assumptions have been made. The separation of the current velocity into two components is convenient for the following approximation of the second term in equation (2.29)

$$\begin{aligned} \frac{\partial V_\alpha V_\beta}{\partial x_\alpha} \;&=\; \left(\tilde{V}_\alpha + V_{1\alpha}\right)\frac{\partial(\tilde{V}_\beta + V_{1\beta})}{\partial x_\alpha} \\ &\simeq\; \tilde{V}_\alpha\frac{\partial \tilde{V}_\beta}{\partial x_\alpha} \;+\; \tilde{V}_\alpha\frac{\partial V_{1\beta}}{\partial x_\alpha} \;+\; V_{1\alpha}\frac{\partial \tilde{V}_\beta}{\partial x_\alpha}\,, \end{aligned} \tag{2.34}$$

where we assume that $V_{1\alpha}\frac{\partial V_{1\beta}}{\partial x_\alpha}$ is much smaller than all the other terms. In other words, we assume that both $V_{1\alpha}$ and $\frac{\partial V_{1\beta}}{\partial x_\alpha}$ are small compared to $\tilde{V}_\alpha$ or $\frac{\partial \tilde{V}_\beta}{\partial x_\alpha}$, hence we neglect the product of two small quantities. The validity of this assumption is not immediately obvious and a thorough discussion is given by Putrevu and Svendsen (1997).

Equation (2.29) then becomes an equation for $V_{1\alpha}$. We insert (2.31) into (2.29) and use the continuity equation, which yields, after rearranging

$$\begin{aligned} \frac{\partial V_{1\beta}}{\partial t} \;-\; \frac{\partial}{\partial z}\left(\nu_t\frac{\partial V_{1\beta}}{\partial z}\right) \;&=\; -\beta_\beta \;-\; \left(\frac{d\tilde{V}_\beta}{dt} \;+\; g\,\frac{\partial \bar{\zeta}}{\partial x_\beta}\right) \\ &\quad -\; V_{1\alpha}\frac{\partial \tilde{V}_\beta}{\partial x_\alpha} \;-\; \tilde{V}_\alpha\frac{\partial V_{1\beta}}{\partial x_\alpha} \;-\; W\frac{\partial V_{1\beta}}{\partial z}\,, \end{aligned} \tag{2.35}$$

where β_β is given by

$$\beta_\beta = \frac{\partial}{\partial x_\alpha}\left(\overline{u_{w\alpha}u_{w\beta}} - \delta_{\alpha\beta}\,\overline{w_w^2}\right) + \frac{\partial \overline{u_{w\beta}w_w}}{\partial z} - \frac{\partial}{\partial x_\alpha}\left[\nu_t\left(\frac{\partial V_\alpha}{\partial x_\beta} + \frac{\partial V_\beta}{\partial x_\alpha}\right)\right], \quad (2.36)$$

and $\frac{d}{dt}$ is the total derivative defined as

$$\frac{d}{dt} \equiv \frac{\partial}{\partial t} + \tilde{V}_\alpha \frac{\partial}{\partial x_\alpha}. \quad (2.37)$$

The term in parentheses in the RHS of equation (2.35) can be evaluated using the depth-integrated, time-averaged momentum equation (2.28), divided by h. Neglecting the depth-varying terms in equation (2.28), which leaves only the leading-order terms, we can use (2.28) to replace the term in parentheses on the RHS of equation (2.35). Once again, a discussion of the order of magnitude of the terms in equation (2.28) given in Putrevu and Svendsen (1997) justifies the neglect of the depth-varying terms in this step. This substitution yields

$$\frac{\partial V_{1\beta}}{\partial t} - \frac{\partial}{\partial z}\left(\nu_t \frac{\partial V_{1\beta}}{\partial z}\right) = -f_\beta - V_{1\alpha}\frac{\partial \tilde{V}_\beta}{\partial x_\alpha} - \tilde{V}_\alpha \frac{\partial V_{1\beta}}{\partial x_\alpha} - W\frac{\partial V_{1\beta}}{\partial z}, \quad (2.38)$$

where f_β represents the combined action of the short-wave forcing and upper and lower (in the water column) shear stresses:

$$f_\beta = \beta_\beta - \frac{1}{\rho h}\frac{\partial}{\partial x_\alpha}\left(S_{\alpha\beta} - \overline{\int_{-h_o}^{\zeta} \tau_{\alpha\beta}\, dz}\right) + \frac{\tau_\beta^S - \tau_\beta^B}{\rho h}. \quad (2.39)$$

Using the definition for the radiation stress tensor and the depth-integrated turbulent shear stresses, the function f_β can be simplified somewhat. For linear long waves, the short wave velocity $u_{w\beta}$ is independent of z and it turns out that so is f_β. This assumption is then utilized shortly in the depth integration of the horizontal currents.

Following Van Dongeren and Svendsen (1997b) and Putrevu and Svendsen (1997) we expand $V_{1\beta}$ as

$$V_{1\beta} = V_{1\beta}^{(0)} + V_{1\beta}^{(1)}, \quad (2.40)$$

with the assumption that $V_{1\beta}^{(1)} \ll V_{1\beta}^{(0)}$. This separation allows us to associate $V_{1\beta}^{(0)}$ with the forcing f_β, and $V_{1\beta}^{(1)}$ with the second to fourth terms on the RHS of equation (2.38), and at the same time it is assumed that the advective accelerations represented by these terms are smaller that the local forcing. Therefore, introducing equation (2.40) into (2.38) yields an equation for $V_{1\beta}^{(0)}$,

$$\frac{\partial V_{1\beta}^{(0)}}{\partial t} - \frac{\partial}{\partial z}\left(\nu_t \frac{\partial V_{1\beta}^{(0)}}{\partial z}\right) = -f_\beta \,, \tag{2.41}$$

and another for $V_{1\beta}^{(1)}$,

$$\frac{\partial V_{1\beta}^{(1)}}{\partial t} - \frac{\partial}{\partial z}\left(\nu_t \frac{\partial V_{1\beta}^{(1)}}{\partial z}\right) = -V_{1\alpha}^{(0)} \frac{\partial \tilde{V}_\beta}{\partial x_\alpha} - \tilde{V}_\alpha \frac{\partial V_{1\beta}^{(0)}}{\partial x_\alpha} - W \frac{\partial V_{1\beta}^{(0)}}{\partial z} \,. \tag{2.42}$$

These two equations are subject to the following boundary conditions:

$$\frac{\partial V_{1\beta}^{(0)}}{\partial z} = \frac{\tau_\beta^B}{\rho\, \nu_t} \qquad \text{at} \qquad z = -h_o \,, \tag{2.43}$$

$$\int_{-h_o}^{\bar{\zeta}} V_{1\beta}^{(0)}\, dz = -Q_{w\beta} \tag{2.44}$$

for $V_{1\beta}^{(0)}$; and

$$\frac{\partial V_{1\beta}^{(1)}}{\partial z} = 0 \qquad \text{at} \qquad z = -h_o \,, \tag{2.45}$$

$$\int_{-h_o}^{\bar{\zeta}} V_{1\beta}^{(1)}\, dz = 0 \tag{2.46}$$

for $V_{1\beta}^{(1)}$.

In the following we consider the special case where the time scale for variations in $V_{1\beta}^{(0)}$ and $V_{1\beta}^{(1)}$ is large enough so that the temporal acceleration terms in equations (2.41) and (2.42) can be neglected (see Van Dongeren and Svendsen, 1997b for details). Thus, for all purposes, we assume a local steady-state in the computation of the depth variation of the horizontal currents. This is in many real situations a good approximation since the vertical profiles do not change significantly anyway.

Finally, it is convenient to assume that the eddy viscosity is constant over the vertical, albeit this is not strictly necessary. As we shall see later, this assumption is supported by the few experimental data available. Therefore, the steady state version of equations (2.41) and (2.42) can be immediately integrated, subject to the boundary conditions (2.43)–(2.46), which yields the governing equations for the depth-varying profiles:

$$V_{1\beta}^{(0)} = \frac{f_\beta}{2\nu_t} z^2 + \frac{1}{\nu_t}\left(\frac{\tau_\beta^B}{\rho} + f_\beta h_o\right) z + \left[\frac{\tau_\beta^B}{2\rho\nu_t}(h_o - \bar{\zeta}) - \frac{f_\beta}{6\nu_t} h^2 - \frac{Q_{w\beta}}{h}\right], \quad (2.47)$$

$$V_{1\beta}^{(1)} = V_{1\beta}^{(1)}(\bar{\zeta}) - \int_z^{\bar{\zeta}} \frac{1}{\nu_t} \int_{-h_o}^{z} F_\beta \, dz \, dz \,, \quad (2.48)$$

where

$$F_\beta = -V_{1\alpha}^{(0)} \frac{\partial \tilde{V}_\beta}{\partial x_\alpha} - \tilde{V}_\alpha \frac{\partial V_{1\beta}^{(0)}}{\partial x_\alpha} - W \frac{\partial V_{1\beta}^{(0)}}{\partial z} \,. \quad (2.49)$$

In the above integration we utilized the fact that $f_\beta = f_\beta(x, y)$ only, i.e., it is not a function of the vertical coordinate z. We also recognize that $V_{1\beta}^{(0)}$ is a quadratic function of z that can be rewritten through the variable transformation $\xi = z + h_o$ as the following

$$V_{1\beta}^{(0)} = \frac{f_\beta}{2\,\nu_t} \xi^2 + \frac{\tau_\beta^B}{\rho\,\nu_t} \xi - \left(\frac{f_\beta}{6\,\nu_t} h^2 + \frac{\tau_\beta^B}{\rho\,\nu_t} \frac{h}{2} + \frac{Q_{w\beta}}{h}\right) . \quad (2.50)$$

We note that the vertical velocity W can be derived by integrating the local short-wave averaged continuity equation. To the order of accuracy needed in equation (2.49), W can then be approximated by (Putrevu and Svendsen, 1997)

$$W = -(z + h_o)\frac{\partial \tilde{V}_\alpha}{\partial x_\alpha} - \tilde{V}_\alpha \frac{\partial h_o}{\partial x_\alpha} \,. \quad (2.51)$$

The expressions for the vertical variation of the horizontal currents, namely equations (2.50) and (2.48), are then used to evaluate the second and third terms of the depth-integrated momentum equation (2.28) as seen in the next section.

2.3 Coupling of the depth-varying and depth-integrated equations

We will here focus our attention on the second and third terms of the depth-integrated, time-averaged momentum equation (2.28). We start by inserting the velocity separation (2.31) into those terms, which yields

$$\frac{\partial}{\partial x_\alpha}\int_{-h_o}^{\bar{\zeta}} V_\alpha\, V_\beta\, dz \;+\; \frac{\partial}{\partial x_\alpha}\overline{\int_{\zeta_t}^{\zeta} (\,u_{w\alpha}\, V_\beta \;+\; u_{w\beta}\, V_\alpha)\, dz} \;=$$
$$\frac{\partial \tilde{V}_\alpha \tilde{V}_\beta\, h}{\partial x_\alpha} \;+\; \frac{\partial}{\partial x_\alpha}\int_{-h_o}^{\bar{\zeta}} V_{1\alpha} V_{1\beta}\, dz \;+\; \frac{\partial}{\partial x_\alpha}\overline{\int_{\zeta_t}^{\zeta} (u_{w\alpha}\, V_{1\beta} + u_{w\beta}\, V_{1\alpha})\, dz}\,. \quad (2.52)$$

The first term on the RHS represents the advective acceleration of a depth-uniform current $\tilde{V}_\beta$, whereas the second and third terms are the advective accelerations of the depth-varying contributions. These integrals can be approximated by

$$\int_{-h_o}^{\bar{\zeta}} V_{1\alpha}\, V_{1\beta}\, dz \;+\; \overline{\int_{\zeta_t}^{\zeta} u_{w\alpha} V_{1\beta} + u_{w\beta} V_{1\alpha}\, dz}$$
$$\approx \int_{-h_o}^{\bar{\zeta}} V_{1\alpha}\, V_{1\beta}\, dz \;+\; V_{1\beta}(\bar{\zeta})\, Q_{w\alpha} \;+\; V_{1\alpha}(\bar{\zeta})\, Q_{w\beta}\,, \quad (2.53)$$

where we used the definition (2.24) for the short-wave volume flux. This implies we also have assumed that the current velocity above ζ_t is uniform and given by $V_{1\beta}(\bar{\zeta})$. This is clearly an approximation as the current above the trough level is not well defined. In this region there is water intermittently and thus the surface layer is occupied by two phases. As shown by Brocchini (1996) the mean properties of the flow in the surface layer are not uniquely determined, and can be related with a intermittency factor, which is unity below trough and zero above the crest level.

Following the derivation given by Putrevu and Svendsen (1997) and Van Dongeren and Svendsen (1997b) we can evaluate these integrals using the expression for $V_{1\alpha}^{(1)}$ found in the earlier section, but keeping the $V_{1\alpha}^{(0)}$ variable explicitly. The derivation is straightforward, but lengthy, and the details can be found in both references above. The result can be written as

$$\int_{-h_o}^{\bar{\zeta}} V_{1\alpha}\, V_{1\beta}\, dz \;+\; V_{1\beta}(\bar{\zeta})\, Q_{w\alpha} \;+\; V_{1\alpha}(\bar{\zeta})\, Q_{w\beta} \;=\; M_{\alpha\beta} \;+\; A_{\alpha\beta\gamma}\, \tilde{V}_\gamma$$

$$- \quad h\left(D_{\alpha\gamma}\frac{\partial \tilde{V}_\beta}{\partial x_\gamma} + D_{\beta\gamma}\frac{\partial \tilde{V}_\alpha}{\partial x_\gamma} + B_{\alpha\beta}\frac{\partial \tilde{V}_\gamma}{\partial x_\gamma}\right), \tag{2.54}$$

where the tensors A, B, D and M are defined by

$$\begin{aligned} A_{\alpha\beta\gamma} &= -\int_{-h_o}^{\bar{\zeta}} V_{1\alpha}^{(0)} \int_z^{\bar{\zeta}} \frac{1}{\nu_t}\left(\frac{\partial}{\partial x_\gamma}\int_{-h_o}^{z} V_{1\beta}^{(0)}\, dz - V_{1\beta}^{(0)}\frac{\partial h_o}{\partial x_\gamma}\right)(dz)^2 \\ &- \int_{-h_o}^{\bar{\zeta}} V_{1\beta}^{(0)} \int_z^{\bar{\zeta}} \frac{1}{\nu_t}\left(\frac{\partial}{\partial x_\gamma}\int_{-h_o}^{z} V_{1\alpha}^{(0)}\, dz - V_{1\alpha}^{(0)}\frac{\partial h_o}{\partial x_\gamma}\right)(dz)^2, \end{aligned} \tag{2.55}$$

$$\begin{aligned} B_{\alpha\beta} &= 2\,D_{\alpha\beta} - \frac{1}{h}\left[\int_{-h_o}^{\bar{\zeta}} V_{1\alpha}^{(0)} \int_z^{\bar{\zeta}} \frac{1}{\nu_t} V_{1\beta}^{(0)}\,(h_o + z)\,(dz)^2\right. \\ &+ \left.\int_{-h_o}^{\bar{\zeta}} V_{1\beta}^{(0)} \int_z^{\bar{\zeta}} \frac{1}{\nu_t} V_{1\alpha}^{(0)}\,(h_o + z)\,(dz)^2\right], \end{aligned} \tag{2.56}$$

$$D_{\alpha\beta} = \frac{1}{h}\int_{-h_o}^{\bar{\zeta}} V_{1\alpha}^{(0)} \int_z^{\bar{\zeta}} \frac{1}{\nu_t}\int_{-h_o}^{z} V_{1\beta}^{(0)}\,(dz)^3, \tag{2.57}$$

$$M_{\alpha\beta} = \int_{-h_o}^{\bar{\zeta}} V_{1\alpha}^{(0)}\, V_{1\beta}^{(0)}\, dz + V_{1\alpha}^{(0)}(\bar{\zeta})\, Q_{w\beta} + V_{1\beta}^{(0)}(\bar{\zeta})\, Q_{w\alpha}. \tag{2.58}$$

In the above no other approximations were made, except for using the previous assumption that $V_{1\beta}^{(1)} \ll V_{1\beta}^{(0)}$. The tensor $M_{\alpha\beta}$ can be related to the momentum flux correction factor $m_{\alpha\beta}$ due to the vertical variation of $V_{1\alpha}$ defined as

$$m_{\alpha\beta} = 1 + \frac{1}{\tilde{V}_\alpha \tilde{V}_\beta h}\left[\int_{-h_o}^{\bar{\zeta}} V_{1\alpha}^{(0)}\, V_{1\beta}^{(0)}\, dz + V_{1\alpha}^{(0)}(\bar{\zeta})\, Q_{w\beta} + V_{1\beta}^{(0)}(\bar{\zeta})\, Q_{w\alpha}\right], \tag{2.59}$$

which then simply reads

$$m_{\alpha\beta} = 1 + \frac{M_{\alpha\beta}}{\tilde{V}_\alpha \tilde{V}_\beta h}, \tag{2.60}$$

Hence the terms on the LHS of equation (2.52) can finally be written as

$$\begin{aligned} &\frac{\partial}{\partial x_\alpha}\int_{-h_o}^{\bar{\zeta}} V_\alpha\, V_\beta\, dz + \frac{\partial}{\partial x_\alpha}\overline{\int_{\zeta_t}^{\zeta} (\,u_{w\alpha}\, V_\beta + u_{w\beta}\, V_\alpha)\, dz} = \\ &\frac{\partial}{\partial x_\alpha}\left[m_{\alpha\beta}\tilde{V}_\alpha\tilde{V}_\beta h + A_{\alpha\beta\gamma}\tilde{V}_\gamma - h\left(D_{\alpha\gamma}\frac{\partial \tilde{V}_\beta}{\partial x_\gamma} + D_{\beta\gamma}\frac{\partial \tilde{V}_\alpha}{\partial x_\gamma} + B_{\alpha\beta}\frac{\partial \tilde{V}_\gamma}{\partial x_\gamma}\right)\right]. \end{aligned} \tag{2.61}$$

The tensors (or coefficients) A, B, D and M are expressed as a function of $V_{1\beta}^{(0)}$, which we determined earlier to be given by equation (2.47) or (2.50) under

the assumptions of quasi-steady state and vertically constant eddy viscosity. The equality given by (2.50) will then be used to evaluate explicitly the coefficients A, B, D and M. For such, we can rewrite (2.50) conveniently as

$$V_{1\beta}^{(0)} = b_1\,\xi^2 + b_2\,\xi + b_3\,, \tag{2.62}$$

where

$$b_1 = \frac{f_\beta}{2\,\nu_t}\,, \tag{2.63}$$

$$b_2 = \frac{\tau_\beta^B}{\rho\,\nu_t}\,, \tag{2.64}$$

$$b_3 = -\left(\frac{f_\beta}{6\,\nu_t}\,h^2 + \frac{\tau_\beta^B}{\rho\,\nu_t}\,\frac{h}{2} + \frac{Q_{w\beta}}{h}\right)\,. \tag{2.65}$$

A similar expression can be written for the α direction:

$$V_{1\alpha}^{(0)} = a_1\,\xi^2 + a_2\,\xi + a_3\,, \tag{2.66}$$

where a_1 , a_2 and a_3 are similar to b_1 , b_2 and b_3.

Finally, we insert equations (2.62) and (2.66) into the definitions for A, B, D and M and evaluate the depth integrals directly. Following Van Dongeren and Svendsen (1997b) this operation leads to the following forms for the coefficients:

$$\begin{aligned} A_{\alpha\beta\gamma} = & -\frac{1}{\nu_t}\left[\frac{\partial a_1\,b_1}{\partial x_\gamma}\,\frac{h^7}{63} + \left(\frac{\partial a_1\,b_2}{\partial x_\gamma} + \frac{\partial a_2\,b_1}{\partial x_\gamma}\right)\frac{h^6}{36} + \right. \\ & \left(\frac{\partial a_1\,b_3}{\partial x_\gamma} + \frac{\partial a_3\,b_1}{\partial x_\gamma}\right)\frac{h^5}{15} + \frac{\partial a_2\,b_2}{\partial x_\gamma}\,\frac{h^5}{20} + \\ & \left.\left(\frac{\partial a_2\,b_3}{\partial x_\gamma} + \frac{\partial a_3\,b_2}{\partial x_\gamma}\right)\frac{h^4}{8} + \frac{\partial a_3\,b_3}{\partial x_\gamma}\,\frac{h^3}{3}\right]\,, \end{aligned} \tag{2.67}$$

$$\begin{aligned} B_{\alpha\beta} = & -\frac{h^3}{\nu_t}\left[\frac{4}{63}\,a_1\,b_1\,h^3 + (a_1\,b_2 + a_2\,b_1)\,\frac{h^2}{12} + a_2\,b_2\,\frac{h}{10} + \right. \\ & \left.\frac{2}{15}\,(a_1\,b_3 + a_3\,b_1)\,h + \frac{1}{8}\,(a_2\,b_3 + a_3\,b_2)\right]\,, \end{aligned} \tag{2.68}$$

$$
\begin{aligned}
D_{\alpha\beta} \;=\; & \frac{1}{\nu_t}\left(a_1\, b_1\, \frac{h^6}{63} \;+\; (a_1\, b_2 \;+\; a_2\, b_1)\, \frac{h^5}{36} \right. \\
& + (a_1\, b_3 \;+\; \frac{3}{4}\, a_2\, b_2 \;+\; a_3\, b_1)\, \frac{h^4}{15} \\
& \left. + (a_2\, b_3 \;+\; a_3\, b_2)\, \frac{h^3}{8} \;+\; a_3\, b_3\, \frac{h^2}{3} \right) , \qquad (2.69)
\end{aligned}
$$

$$
\begin{aligned}
M_{\alpha\beta} \;=\; & a_1\, b_1\, \frac{h^5}{5} \;+\; (a_1\, b_2 \;+\; a_2\, b_1)\, \frac{h^4}{4} \\
& + (a_1\, b_3 \;+\; a_2\, b_2 \;+\; a_3\, b_1)\, \frac{h^3}{3} \;+\; (a_2\, b_3 \;+\; a_3\, b_2)\, \frac{h^2}{2} \;+\; a_3\, b_3\, h \\
& + (a_1\, h^2 \;+\; a_2\, h \;+\; a_3)\, Q_{w\beta} \;+\; (b_1\, h^2 \;+\; b_2\, h \;+\; b_3)\, Q_{w\alpha} \,. \qquad (2.70)
\end{aligned}
$$

The end result of the derivation above is that we determined the terms that account for the depth variation of the horizontal currents which enables us to insert them into the depth-averaged horizontal momentum equations. Equations (2.52)–(2.54) show that the advective accelerations associated with the total depth-varying currents $V_{1\alpha}$ lead to two distinct contributions to the momentum equation: (i) advective accelerations linked with the leading order depth-varying current $V_{1\alpha}^{(0)}$ and the wave-induced volume flux (the first and second terms on the RHS of (2.54)), and (ii) momentum dispersive terms (the term in parentheses on the RHS of (2.54)) that are similar in form to the turbulent stresses given by the eddy-viscosity model. Therefore, the coefficients $B_{\alpha\beta}$ and $D_{\alpha\beta}$ are the vertical mixing coefficients for momentum resulting from the depth-averaging process, similar to the mixing coefficient found by Taylor (1954) on a turbulent flow in a long straight pipe. Similarly, Elder (1959) analyzed the free-surface flow down an inclined plate, assuming a logarithmic velocity profile, which when integrated over depth yielded a dispersion coefficient of (typically) one order of magnitude larger than the eddy viscosity coefficient.

The equivalent of these results for a long straight coast was presented by

Svendsen and Putrevu (1994). They found that the term proportional to $D_{\alpha\beta}$ accounted for the largest contribution of the depth-varying terms and it was an order of magnitude larger than the turbulent dispersion mechanism. Van Dongeren and Svendsen (1997b) reached to a similar conclusion for the case of infragravity waves forced by obliquely-incident wave groups, hence confirming the importance of accounting for depth-varying currents in the study of nearshore flows.

For completeness, we write below the depth and time-averaged governing equations where we use the expressions (2.52)–(2.54) in the momentum equation given by (2.28). Thus, the continuity equation reads (where we repeat equation (2.25))

$$\frac{\partial \bar{\zeta}}{\partial t} + \frac{\partial \bar{Q}_\alpha}{\partial x_\alpha} = 0\,, \tag{2.71}$$

and the horizontal momentum balance is given by

$$\begin{aligned}
&\frac{\partial \bar{Q}_\beta}{\partial t} + \frac{\partial}{\partial x_\alpha}\left(\frac{\bar{Q}_\alpha \bar{Q}_\beta}{h} + M_{\alpha\beta} + A_{\alpha\beta\gamma}\tilde{V}_\gamma\right) \\
&- \frac{\partial}{\partial x_\alpha}\left[h\left(D_{\alpha\gamma}\frac{\partial \tilde{V}_\beta}{\partial x_\gamma} + D_{\beta\gamma}\frac{\partial \tilde{V}_\alpha}{\partial x_\gamma} + B_{\alpha\beta}\frac{\partial \tilde{V}_\gamma}{\partial x_\gamma}\right)\right] = \\
&- g\,h\frac{\partial \bar{\zeta}}{\partial x_\beta} - \frac{1}{\rho}\frac{\partial}{\partial x_\alpha}\left(S_{\alpha\beta} - \overline{\int_{-h_o}^{\zeta} \tau_{\alpha\beta}\,dz}\right) + \frac{\tau_\beta^S}{\rho} - \frac{\tau_\beta^B}{\rho}\,.
\end{aligned} \tag{2.72}$$

The model formed by these set of equations is referred to as a Quasi-3D model because it accounts for the depth variation of the currents, and constitutes an extension of the 2D-horizontal models for depth-uniform currents. Due to the complexity of this system of coupled partial differential equations no analytical solutions exist for the general case, and thus a a solution by a numerical method is sought for the applications in the later chapters.

2.4 Closure sub-models

2.4.1 Turbulence closure

As introduced earlier, we use the eddy viscosity concept to model the turbulent Reynolds stresses (see equation (2.7)). Although eddy viscosity models are one of the simplest for turbulence modeling, they can still give good results provided they allow for changes in the local turbulence structure. For example, the use of a constant eddy viscosity ν_t cannot account for changes in the turbulence, thus one should not expect it to describe correctly the details of the mean flow.

Generally we can consider $\nu_t = \nu_t(x, y, z, t)$, but a very detailed representation of such a variable would require an accurate knowledge of the turbulent flow under breaking and non-breaking waves, which is difficult to measure. However, it seems important to have a good estimate of the turbulent eddy viscosity as the depth averaged turbulent shear stresses can provide non-negligible horizontal mixing of the surf zone currents, and more important, is the fact that the dispersion mechanism described in sections 2.2 and 2.3 depends on the value of ν_t. Moreover, the local vertical variation of the horizontal currents V_α is strongly dependent on the magnitude of ν_t, but somewhat indifferent to the vertical distribution of it (Svendsen, 1984a).

In our model for the description of the vertical variation of the horizontal currents we decided not to include explicitly the bottom boundary layer, so that effectively our bottom velocity $V_{b\alpha}$ and bottom shear stresses τ_α^B should be read as if they were evaluated just above the bottom boundary layer, at $z = \delta - h_o$, where δ is the boundary layer thickness. Thus, we analyze in this section the turbulent related quantities ν_t and k just above the bottom boundary layer. We will also focus our analysis solely on the turbulent shear stresses and neglect the turbulent normal

stresses, based on the small values of the magnitude of the turbulent kinetic energy inside the surf zone (Svendsen, 1987).

Outside the breaking region, turbulence is mostly generated by the bottom boundary, but at the free surface turbulence can also be produced by wind shear (turbulent) fluctuations and interaction with the wave motion[1]. Inside the surf zone, turbulence is mainly provided by the wave breaking process. On a plane sloping beach, wave induced turbulent intensities increase after breaking to a maximum at around $h/h_b \simeq 0.6 - 0.8$, where h_b is the depth at breaking, and then decrease towards the shore as showed in the experimental results of Nadaoka and Kondoh (1982), Hattori and Aono (1985) and Okayasu (1989). Thus, *a priori*, it is clear that to cover the nearshore region with a single model of the turbulent eddy viscosity one should account for both bottom and wave generated turbulence characteristics. Such formulations are used by De Vriend and Stive (1987) and Sanchez-Arcilla *et al.* (1992)), and will be pursued in the present study. A brief review of the available eddy viscosity formulations is given below.

Empirical models

Earlier models for the depth-averaged horizontal currents on a longshore straight coast considered ν_t to vary with the cross-shore direction (e.g. Longuet-Higgins 1970a, Thornton 1970) or to be constant (Bowen 1969a). However, in those models empiricism and data fitting were used for the estimates of the eddy viscosity, which were all dependent on the local depth or local wave properties. For barred beaches Larson and Kraus (1991) and Smith *et al.* (1993) expressed the eddy

[1] For reference see Phillips (1977), p.117-134.

viscosity by the empirical formulation

$$\nu_t = \Gamma u_0 H \,, \tag{2.73}$$

where Γ is an empirical coefficient adjusted by data fitting ($\Gamma \simeq 0.1 - 1.0$), u_0 is the amplitude of the wave orbital velocity at the bottom, and H is the wave height. This parameterization gives ν_t decreasing towards zero in deep water, where the turbulence levels are much smaller than in the surf region, but it does not account for different mechanisms of turbulence generation nor the large sudden turbulent levels encountered in the breaking region.

Turbulence under wave breaking

Although several experimenters and modelers have analyzed the turbulent flow under and past breaking waves, turbulence generation, transport and decaying mechanisms are far from being completely understood. Svendsen (1987) presented a thorough review of the turbulence characteristics in the surf zone, analyzing independent experimental results of Stive (1980), Stive and Wind (1982), Hattori and Aono (1985) and Nadaoka and Kondoh (1982). Some important conclusions of his review are the following:

1. The temporal variation of the turbulent kinetic energy k (defined by equation (2.9)) over a wave period is fairly small, hence we can assume k constant over the short wave period.

2. The turbulent kinetic energy varies slightly over the water depth which suggests that a depth independent eddy viscosity ν_t is a good approximation.

More recently, Cox *et al.* (1995) presented detailed results of waves and bottom induced turbulence for spilling breakers on a gently sloping rough beach.

Those authors find the local $\nu_t(t,z)$ inside the surf zone to increase from zero at the bottom to a nearly constant value above mid-depth and up to the wave-trough level, and to be nearly constant for all the wave phases, i.e. $\nu_t(t,z)$ is roughly independent of time. Regarding the depth variation, ν_t changes significantly in the bottom boundary layer but away from it the variation is less significant. Therefore, based on this study and the conclusions of Svendsen (1984a) and Svendsen (1987), we assume for our turbulence closure that the eddy viscosity is depth-uniform and time-independent. The magnitude of it is, however, still a matter of research but it could be assessed through the estimation of the relevant turbulent length scale l and turbulent kinetic energy k which are related to ν_t by

$$\nu_t = l\sqrt{k}\,. \tag{2.74}$$

Using a best-fit estimate of an undertow model to match the data, Svendsen *et al.* (1987) estimated the turbulent length scale l to lie in the interval

$$0.25\,h < l < 0.35\,h\,. \tag{2.75}$$

This value seems appropriate as the turbulent length scale is related to the energy-containing turbulent motion, which is seen to be smaller than both the water depth and the wave height in the surf zone. Using the estimates given by Svendsen (1987) for the wave averaged turbulent kinetic energy k, and the turbulent length scale l above, the eddy viscosity ν_t inside the surf zone can then be approximated by

$$\nu_t \simeq (0.01 - 0.02)\,h\sqrt{gh}\,. \tag{2.76}$$

This result is similar to the earlier estimate of $\nu_t = 0.01h\sqrt{gh}$ given by Stive and Wind (1986). Not only is the turbulent eddy viscosity of the same order, but also the turbulent length scale is given by $0.25h < l < 0.5h$, which is similar to (2.75).

An alternative estimate for ν_t can be evaluated from the turbulence measurements in the field by George *et al.* (1994). Those authors report that turbulence

in the surf zone is only 1/4 to 1/2 of the laboratory values and their measurements suggest $u' \simeq 0.01\sqrt{gh}$. Following (Svendsen, 1987) we assume then that the relative strength of $\overline{u'^2}$, $\overline{w'^2}$ and $\overline{v'^2}$ is the same as that of a plane wake. Hence the turbulent kinetic energy can be determined by $k \simeq 1.2\,\overline{u'^2}$. Using the length scale $l = 0.3h$ a value for the eddy viscosity can easily be determined from equation (2.74) and the estimates above, yielding

$$\nu_t \simeq 0.004\, h\, \sqrt{gh}\,. \tag{2.77}$$

This estimate is indeed only 1/4 to 1/2 of the approximation (2.76), and it will be used as a guideline for the turbulence levels in the surf zone under field conditions.

Battjes (1975), based on concepts of turbulent energy dissipation and the energy cascade model, related the turbulent eddy viscosity with wave energy dissipation by breaking. Namely, the eddy viscosity is written as

$$\nu_t = l\, q\,, \tag{2.78}$$

where l is a turbulent length scale (or characteristic eddy size) and q a turbulent velocity scale. Battjes (1975) estimated $l \simeq h$, as this value being a limiting length scale for the vertical eddies, and the turbulent characteristic velocity to be given by

$$q \simeq (\frac{D}{\rho})^{1/3}\,, \tag{2.79}$$

where D is the energy dissipation rate per unit area. The combination of those two scales yields the result:

$$\nu_t = Mh(\frac{D}{\rho})^{1/3}\,, \tag{2.80}$$

where M is a constant of order one[2]. Based on comparison with laboratory data, and attributing all the surf zone mixing to turbulence, Battjes (1983) showed that in the inner surf region $q \simeq 0.8(D/\rho)^{1/3}$, i.e. $M = 0.8$.

[2] Details of the derivation are omitted here for brevity.

The above eddy viscosity model has been used in several turbulence closures in nearshore hydrodynamics models (e.g. De Vriend and Stive, 1987; Sanchez-Arcilla *et al.*, 1992; Reniers *et al.*, 1995; Özkan-Haller and Kirby, 1996). However, the values of M used by the modelers above cover a wide range from $M \sim 0.025 - 1$. This wide variability is related to the fact that in depth-uniform current models the effective turbulent eddy viscosity accounts also for the lateral dispersion mechanism induced by depth non-uniform currents.

The formulation of Battjes (1975), however, assumes an immediate transition from wave breaking dissipation into the smaller scales of turbulence where effectively the energy dissipation takes place. Recent attempts have been made to introduce a (space and time) lag between the production, due to breaking, of the turbulent energy and its dissipation (Okayasu, 1989; Nairn *et al.*, 1990). The observations of a difference between the plunging point and the point where the wave set-up commences lend support to that fact. So, the organized wave energy should not be instantly converted to turbulent energy, but part of the organized wave energy should be first converted into forward momentum flux carried by the surface roller (as indicated by Svendsen, 1984b). To account for such transmission of energy from the wave motion into the roller and then into turbulence a more detailed turbulence model would have to be considered. It cannot be simply accomplished by an eddy viscosity model. Therefore, in our turbulent model formulation we neglect this time and space lag between the production and the dissipation of energy.

Turbulence outside the breaking region

Outside the surf region very little information is available about the turbulence level and the associated eddy viscosity. We can quantify the eddy viscosity by

taking into account only bottom generated turbulence, and implicitly assuming no surface generated turbulence. For combined wave-current flows You (1994) finds

$$\nu_t = \kappa u_w^* \xi \,, \tag{2.81}$$

to be a good model for non-breaking waves, where κ is the von Karman constant ($\kappa \simeq 0.4$), u_w^* is the wave friction velocity associated with the wave motion, and $\xi = (h + z)$ is the vertical coordinate with zero at the bottom. An estimate of the wave friction velocity u_w^* is given by Nadaoka and Kondoh (1982):

$$u_w^* = \sqrt{\frac{f_w}{2}}\, u_0 \,, \tag{2.82}$$

where f_w is the wave related bottom friction coefficient.

The model equation (2.81) might give too large values of ν_t near the surface, hence a parabolic variation, such as (Coffey and Nielsen, 1984)

$$\nu_t = \kappa u_w^* \xi \left(1 - \frac{\xi}{h}\right) \,, \tag{2.83}$$

is more in agreement with the experimental data of Supharatid *et al.* (1992), who report a linear increase of ν_t from the bottom up to a certain level and then a decrease towards the water surface. The data of Supharatid *et al.* also suggests that equation (2.83) should be multiplied by a constant of $\mathcal{O}(0.1)$ in order to match the data. Similar results to those of Supharatid *et al.* had been reported previously by Sleath (1987), who finds that the constant of proportionality in equation (2.83) differs from the von Karman constant κ, and it varies between 0.06 and 0.08. Thus, it is seen from the references above that a large uncertainty is associated with the depth-varying models of ν_t as well as to the magnitude of the proportionality constant.

Contrary to the findings above, seaward of breaking, the data analysis of Cox *et al.* (1995) shows that $\nu_t(t, z)$ above the bottom boundary layer is even more

independent of z and t than shoreward of breaking, so that it is again reasonable to assume ν_t uniform over depth outside the surf region. The maximum values of ν_t over the water column found by Cox *et al.* (1995) are

$$\nu_t \simeq \begin{cases} (0.01 - 0.02)\, h\sqrt{gh}\,, & \text{inside the surf region} \\ 2 \times 10^{-4}\, h\sqrt{gh}\,, & \text{outside the surf region} \end{cases} \tag{2.84}$$

which is in agreement with (2.76) inside the surf zone. The measurements of Cox *et al.* (1995) and Nadaoka and Kondoh (1982) are some of the very few that contain analysis of turbulence both inside and outside the surf region. Due to the lack of more data, Putrevu and Svendsen (1993) quantified ν_t seaward of the breaking point by qualitative arguments based on the experimental results of Nadaoka and Kondoh (1982). Thus, Putrevu and Svendsen (1993) empirically assumed

$$\nu_t = \nu_{tb}\left[0.2 + 0.8\left(\frac{h_b}{h}\right)^4\right] \tag{2.85}$$

where ν_{tb} is the eddy viscosity at the breaking point. However, due to the degree of empiricism involved in the above estimate, we deem it more appropriate to use a relation such as (2.81) or (2.83) integrated over the depth, which is closely related to the turbulent flow characteristics at the bottom.

Combined model for turbulence inside and outside the breaking region

In the present model we use an eddy viscosity formulation that accounts both for wave-breaking and bottom generated turbulence. Outside the surf zone the model equations (2.81) and (2.83) are used as a guideline. Inside the surf zone we apply a modified Battjes (1975) model (equation (2.80)). Therefore, combining the depth-averaged equivalent of (2.83) with equation (2.80) yields

$$\nu_t = C_1\,\kappa\sqrt{\frac{f_w}{2}}\,u_0\,h + M\,h\,(\frac{D}{\rho})^{1/3}\,, \tag{2.86}$$

where we introduced the relation (2.82) for u_w^*. The coefficient C_1 accounts for the factor 1/6 that arises from the integration of (2.83) as well as for the uncertainty in the proportionality constant in that equation (see discussion above).

The first term in (2.86) represents bottom induced turbulence and it is always present, and the second term is only active in the region where breaking dissipation occurs. A smooth transition between the breaking and non-breaking regions is used. By comparing the eddy viscosity estimates from this equation with the experimental results of Nadaoka and Kondoh (1982) and the values suggested by Svendsen (1987) we use $C_1 \simeq 0.2$ and $M \simeq 0.2$ (as suggested by the length scale estimated by (2.75)).

It is important to note that the local (depth-integrated) values of the eddy viscosity enter in the evaluation of the dispersion coefficients A, B and D. The terms in the momentum equations associated with these dispersion coefficients account for most of the momentum dispersion in the model equations (2.71) and (2.72). All the coefficients A, B and D are inversely proportional to ν_t and thus we expect them to be large in regions where ν_t is small. The same applies to the depth-varying horizontal velocity $V_{1\alpha}^{(0)}$. We have found though that the use of the eddy viscosity given by (2.86) gives reasonable values both inside and outside the surf zone for all the quantities just mentioned.

Lastly, all the experimental data analyzed by Svendsen (1987) is for plane sloping beaches, and no experimental data on the turbulence structure over and past barred beaches is presently available. Nevertheless, we believe that equation (2.86) contains the physics necessary for it to be valid both inside and outside the surf region for any beach profile. It is also clear from the above review that there is a need of experimental data of the turbulence properties both inside and outside the surf region for a barred beach.

2.4.2 Bottom shear stress

Similarly to the difficulties of finding a closure for the turbulent shear stresses there is a great deal of uncertainty in the estimates of the bottom shear stress. A first question to address is the definition of the bottom shear stress. For a steady current flow the bottom shear stress can be expressed by means of a quadratic friction law:

$$\vec{\tau}_c^B = \frac{1}{2}\rho f_c \left|\vec{V}_b\right| \vec{V}_b \,, \tag{2.87}$$

where the subscript c in τ_c^B represents the "current" contribution, f_c is the current friction coefficient or drag coefficient, and $\vec{V}_b$ is the current velocity at the top of the bottom boundary layer. Similarly, for the case of a purely oscillatory flow the wave friction factor f_w can be defined by (Jonsson, 1966)

$$\vec{\tau}_w^B = \frac{1}{2}\rho f_w \left|\vec{u}_0\right| \vec{u}_0 \,, \tag{2.88}$$

where u_0 is the short-wave maximum instantaneous particle velocity evaluated at the top of the bottom boundary layer.

In the literature we find two alternative methods of defining the bed shear stress in a combined wave-current flow. Christoffersen and Jonsson (1985) and Myrhaug and Slaattelid (1990) assume

$$\vec{\tau}^B = \vec{\tau}_c^B + \vec{\tau}_w^B \,, \tag{2.89}$$

and a second definition is suggested by Bijker (1967) (cited in Visser, 1986), Jonsson *et al.* (1974), Liu and Dalrymple (1978), and Svendsen and Buhr Hansen (1988) among others,

$$\vec{\tau}^B = \frac{1}{2}\rho f_{cw} \left|\vec{u}_b\right| \vec{u}_b \,. \tag{2.90}$$

where $\vec{u}_b$ is the total velocity at the bottom. In this expression f_{cw} represents the combined wave-current friction coefficient. The first formulation (equation (2.89))

separates the two flow constituents clearly and simplifies into the well studied cases of waves alone or currents alone in the absence of one or the other component. It has the disadvantage, however, that it assumes a linear superposition of the waves and currents shear stresses alone, whereas it is well known that these do not add linearly. Alternatively, the definition of the shear stress as given by equation (2.90) does not assume a linear summation of effects, but it has the drawback of considering a single friction factor f_{cw} that must account for the two different scales of the flow, corresponding to the wave and current components. In the limiting cases of waves or currents alone f_{cw} should then revert to the factors defined for those simpler cases (Jonsson *et al.*, 1974). As mentioned in Svendsen and Buhr Hansen (1988) the important assumption behind equation (2.90) is that it applies to the instantaneous shear stress and velocities with a constant friction coefficient f_{cw}.

Since in the nearshore studies considered here we will always have a combined short-wave and current flow we follow the shear stress definition (2.90) without troubling about the limiting cases of either of those flows alone. We will further assume that $f_{cw} \simeq f_w$ because in a wave and current motion the inner bottom boundary layer close to the bed is dominated by the waves effect, and the outer boundary layer is dominated by the currents. Hence, the shear stress at the bed τ_α^B is dominated by the waves.

From dimensional analysis Jonsson (1966) showed that for pure wave motion the wave friction coefficient f_w is generally a function of the flow Reynolds number $\mathrm{Re} = \frac{u_0 a_0}{\nu}$ and the relative bed roughness $\frac{k_N}{a_0}$, where a_0 represents the amplitude of the wave orbital motion in the horizontal direction at the top of the bottom boundary layer, and k_N is the Nikuradse roughness. Additionally, for fully developed, rough turbulent flows (which occur most frequently in nature) the wave friction factor becomes only a function of the relative bed roughness: $f_w = f_w\left(\frac{k_N}{a_0}\right)$. Under that

regime a semi-empirical expression for f_w is given by Jonsson (1966). Here we prefer to use here the explicit, more commonly used, formula proposed by Swart (1974) as an approximation to Jonsson's formula:

$$f_w = \exp\left[5.213\left(\frac{a_0}{k_N}\right)^{0.194} - 5.977\right] . \tag{2.91}$$

As confirmed by measurements, this expression shows that an increase in the amplitude of wave orbital motion a_0 causes a decrease in the friction factor f_w, whereas an increase in the roughness k_N provokes an increase in f_w. Note that the above expression was calibrated using values of a_0 from linear wave theory, although breaking and broken waves vary considerably from linear waves. Thus, for consistency we use here a_0 predicted by linear theory:

$$a_0 = \frac{H}{2}\frac{g}{c\,\omega}\frac{1}{\cosh kh} , \tag{2.92}$$

where k is the short-wave wavenumber, ω is the angular short-wave frequency, and $c = \frac{\omega}{k}$ is the wave celerity. The same applies to the wave particle velocity u_0:

$$u_0 = \frac{H}{2}\frac{\omega}{\sinh kh} = g\,\omega\,a_0 . \tag{2.93}$$

We can approximate the friction coefficient for the combined wave and current flow as $f_{cw} \simeq f_w$, with f_w given by equation (2.91). The effect of the currents on f_{cw} can be accounted empirically by an increase in the bed roughness as the results of Simons *et al.* (1992) (1996) suggest. The results of these authors also indicate that the friction factor is well predicted by Swart's formula (2.91) in the case of waves alone or waves superimposed on a current motion crossing at right angles.

For current flow alone the Nikuradse roughness k_N is usually related to the bottom roughness z_0 by the relation

$$k_N = 30\,z_0 . \tag{2.94}$$

Table 2.1: Typical values of the bottom roughness z_0 for different bottom types (adapted from Soulsby, 1983)

Bottom type	z_0 (cm)
Silt/sand	0.005
Sand (unrippled)	0.04
Sand (rippled)	0.6
Sand/gravel	0.03

The ratio of the apparent bottom roughness z_a in the case of combined waves and currents relative to the bottom roughness z_0 for currents alone is found by Simons *et al.* (1992) to be within the range

$$1 < \frac{z_a}{z_0} < 20\,. \tag{2.95}$$

The above expressions apply to a fixed bed. For a movable bed in the presence of waves and currents flow You and Nielsen (1996) suggest to determine the bed roughness as

$$k_N = 30\, z_0 \left(1 + \frac{a_0\, \omega}{V_b}\right)\,. \tag{2.96}$$

However, the use of this formula implies the knowledge *a priori* of V_b which is an unknown in our problem. Thus, we do not find convenient to use this expression.

The bottom roughness z_0 can be estimated from experimental data by fitting a logarithmic velocity profile for the current $U(z) = \frac{u^*}{\kappa} \ln\left(\frac{z}{z_0}\right)$ to data. In Table 2.1 we present some values of z_0 extracted from a compilation of data given in Soulsby (1983).

Kamphuis (1975) found that k_N can be well predicted by the bottom sediment size for a fixed bed when no bed-forms are present by

$$k_N = 2\, d_{90}\,, \tag{2.97}$$

where d_{90} is the grain sediment diameter exceeded by 10% by weight of the sample. A similar formula, $k_N = 2\, d_{50}$ where d_{50} is the median grain diameter, is found by Cox *et al.* (1995) to give good agreement with estimated values of k_N using equation (2.94). In conclusion, throughout the present work we will compute k_N using both relations (2.94) and (2.97), and estimate the friction factor f_{cw} using Swart's formula (2.91) with the most reasonable result for k_N.

All the formulas for f_{cw}, k_N and z_0 above are mostly based on laboratory data, and hence a direct extrapolation to prototype conditions should be taken cautiously. Thus, we will also take guidance from measured field values of z_0 (e.g., Garcez Faria *et al.*, 1996b). Our results for f_{cw} are also consistent with the values calibrated by best-fit of modeled and measured longshore currents under field conditions (e.g., Thornton and Guza, 1986; Church and Thornton, 1993; Smith *et al.*, 1993; Thornton *et al.*, 1995; Whitford and Thornton, 1996), which fall within the approximate interval $0.003 < f_{cw} < 0.03$. Given such a wide range of f_{cw} values the estimates for the bottom shear stress τ_α^B can vary by one order of magnitude for the same wave and current velocities. Hence, a proper estimate of the friction factor and the bottom shear stress is very important in the prediction of longshore currents. Due to a significant variability of the hydrodynamic and morphologic conditions in the nearshore region, it also appears desirable to use a variable bottom friction coefficient in the computation of nearshore currents.

Here we assume that the time-averaged bottom shear stress τ_α^B can be determined from equation (2.90). The details of the derivation are omitted here for

brevity and can be found in Svendsen and Putrevu (1990). It follows straightforward from introducing the separation of the total velocity u_α into a wave $u_{w\alpha}$ and a current component V_α (see equation (2.6)) into the definition for the bottom shear stress (2.90). After time-averaging we obtain

$$\tau_\alpha^B = \frac{1}{2}\,\rho\, f_{cw}\, u_0\, (\beta_1\, V_{b\alpha} + \beta_2\, u_{0\alpha}) \;, \tag{2.98}$$

where β_1 and β_2 are defined as

$$\beta_1 = \frac{}{\left[\left(\frac{V_b}{u_0}\right)^2 + 2\,\frac{V_b}{u_0}\cos\theta\,\cos\mu + \cos^2\theta\right]^{1/2}} \;, \tag{2.99}$$

$$\beta_2 = \frac{}{\cos\theta\left[\left(\frac{V_b}{u_0}\right)^2 + 2\,\frac{V_b}{u_0}\cos\theta\,\cos\mu + \cos^2\theta\right]^{1/2}} \;, \tag{2.100}$$

and θ is the short-wave phase angle, $\theta = \omega t - \int \vec{k}\cdot\vec{dx}$, and μ is the angle between the short-wave direction (given by the wavenumber $\vec{k}$) and the current velocity at the bottom. These expressions can be simplified for the special cases of strong currents, $\frac{V_b}{u_0} \gg 1$, and weak currents, $\frac{V_b}{u_0} \ll 1$, both for currents parallel ($\mu = 0$) and orthogonal ($\mu = \frac{\pi}{2}$) to the wave direction (Liu and Dalrymple, 1978).

2.4.3 Steady-streaming induced by the bottom boundary layer

So far we have disregarded the vertical velocity variation in the bottom boundary layer. We impose a slip velocity at the top of the bottom boundary layer and calculate the bottom shear stress from expression (2.98). Since we are not interested in the details of the velocity in the bottom boundary layer and the thickness of the this layer is much smaller than the water column depth, we essentially assume the thickness to be zero and translate the calculated velocity V_b at that height to the bed surface.

Inside the surf zone the undertow vertical velocity profile is largely dominated by the forcing caused by the imbalance between the local radiation stress gradient

and the set-up gradient (as the data analysis by Stive and Wind, 1986 suggests). Outside the surf-zone, however, that imbalance is much smaller and other small terms may affect the time-averaged velocity profile. Thus, in the following we account for the Reynolds shear stress evaluated just outside the bottom boundary layer associated with the second-order wave-induced bottom streaming (Longuet-Higgins, 1956).

As mentioned by Putrevu and Svendsen (1993), in the shoaling region and outside the bottom boundary layer the terms $\frac{\partial \overline{u_{w\alpha}\, u_{w\beta}}}{\partial x_\alpha}$ and $g\frac{\partial \bar{\zeta}}{\partial x_\beta}$ in equation (2.35) are equally important. Inside the bottom boundary layer, however, those two terms can be neglected and the velocity profile is linear. At the upper limit of the boundary layer the shear stress is determined by

$$\tau_\alpha^{SB} = -\,\rho\,\overline{u_{w\alpha}\, w_w}\,. \tag{2.101}$$

This shear stress is designated by bottom-induced "steady-streaming". Longuet-Higgins (1956) determined this stress for the motion of a viscous flow in the bottom boundary layer forced by a free-surface oscillatory wave with near-bottom orbital velocity amplitude u_0. Assuming linear long wave theory Longuet-Higgins finds that the second-order steady-streaming shear stress is (generalized to 2D-horizontal)

$$\tau_\alpha^{SB} = \rho\,\frac{u_0\, u_{0\alpha}}{c}\,\sqrt{\frac{\omega\,\nu_{tb}}{8}}\,. \tag{2.102}$$

In the above equation ν_{tb} represents the (constant) eddy-viscosity inside the bottom boundary layer, which is given by Svendsen *et al.* (1987) from the analysis of experimental data as

$$\nu_{tb} \simeq 0.08\, f_{cw}^2 \left(\frac{H}{h}\right)^2 \frac{c}{k}\,. \tag{2.103}$$

The inclusion of this shear stress corrects the bottom boundary condition given by equation (2.43) which now reads

$$\frac{\partial V_{1\beta}^{(0)}}{\partial z} = \frac{\tau_\beta^B - \tau_\beta^{SB}}{\rho\,\nu_t} \qquad \text{at} \qquad z = -h_o\,. \tag{2.104}$$

Hence, the horizontal velocity distribution given by equation (2.47) or (2.50) is modified accordingly. For such we need only to substitute the bottom shear stress τ_β^B in those equations by $\tau_\beta^B - \tau_\beta^{SB}$. Hence, for example equation (2.50) is replaced by

$$V_{1\beta}^{(0)} = \frac{f_\beta}{2\,\nu_t}\,\xi^2 + \frac{\tau_\beta^B - \tau_\beta^{SB}}{\rho\,\nu_t}\,\xi - \left(\frac{f_\beta}{6\,\nu_t}\,h^2 + \frac{\tau_\beta^B - \tau_\beta^{SB}}{\rho\,\nu_t}\,\frac{h}{2} + \frac{Q_{w\beta}}{h}\right), \quad (2.105)$$

which implies also the corresponding modification of the coefficients b_1 , b_2 and b_3 (and a_1 , a_2 and a_3) given by equations (2.63)–(2.65).

As shown by Putrevu and Svendsen (1993) for the case of normal incident waves, the inclusion of the steady-streaming effect into the model equations outside the surf zone brings the model results in agreement with experimental data. Their results also show that within a wide range of variation of the ratio $\frac{\nu_{tb}}{\nu_t}$ the predicted shape of the vertical velocity profile is a robust feature which has the same trend as the observations.

As shown later, it is found in the present work that the effect of the steady-streaming term outside the surf zone is much less important for obliquely refracting incident waves than for normally incident waves (which was studied by Putrevu and Svendsen, 1993). Nevertheless, the velocity profiles do exhibit the same trend as data both inside and outside the surf zone, and we still find it important to include the steady-streaming shear stress. Furthermore, it was found that the relative importance of including τ^{SB} in the calculation of the velocity profiles outside the surf zone is strongly dependent on the values of Q_w and ν_t: the smaller the values of any of these two parameters, the larger the effect of the steady-streaming shear stress.

2.4.4 Short-wave quantities

As mentioned previously, in the present work we use linear wave theory to describe the short-wave quantities as it is the only theory readily available for 2DH general topographies, from deep to shallow water. Furthermore, we also limit our study to sea-state conditions characterized by a single monochromatic wave, and hence the time-averaged wave properties can be represented by such a periodic wave.

At any given location in the nearshore region with water depth h the wave field can be characterized by the wave period T, the wave height H, and the angle α_w between the wave orthogonal and the shore normal. For a given period T and incident wave height H_o at a seaward location of the nearshore region of interest we calculate the wave field at a shoreward location using an appropriate short-wave propagation model. For most applications in this study we use the model REF/DIF1 (Kirby and Dalrymple, 1994), which is based on the parabolic approximation of the mild-slope equation, and accounts for refraction, diffraction, shoaling and breaking phenomena (see also Kirby and Dalrymple, 1983). Other wave propagation models can be used as well, depending on the complexity of the bathymetry and degree of approximation desired. The results from this model are used to calculate the short-wave radiation stress $S_{\alpha\beta}$ and wave-induced volume flux $Q_{w\alpha}$.

A physical description of the current driving mechanism is given below. The gradient of the radiation stress tensor is the driving force for the mean wave-induced motion. This force consists of two components: a irrotational part which is unable to generate non-zero depth-averaged currents and balances the pressure gradient; and a rotational part due to non-conservative forces, which is proportional to the wave energy dissipation rate. The latter contribution is hence the one that is able to generate wave-induced nearshore currents (Longuet-Higgins, 1972). Dingemans

et al. (1987) suggest computing the driving force directly from the energy dissipation, arguing that the numerical computation of the radiation stresses derivatives can introduce spurious numerical errors that would affect the wave-induced currents. However, in the present work we found the numerical differentiation of $S_{\alpha\beta}$ not to lead to spurious errors as long as the numerical grid spacing resolves accurately the breaking point.

Using definition (2.27) the radiation stress tensor can be evaluated for any wave theory. It can be written generally as

$$S_{\alpha\beta} = \rho\, g\, P_{\alpha\beta}\, H^2\,, \tag{2.106}$$

where for linear sinusoidal waves $P_{\alpha\beta}$ is given by

$$P_{\alpha\beta} \;=\; \frac{1}{16}\left[(1\,+\,G)\;e_{\alpha\beta}\;+\;G\,\delta_{\alpha\beta}\right]\,. \tag{2.107}$$

In the equation above $e_{\alpha\beta}$ and G are given by

$$e_{\alpha\beta} \;=\; \begin{bmatrix} 2\cos^2\alpha_w + 1 & 2\sin\alpha_w\,\cos\alpha_w \\ 2\sin\alpha_w\,\cos\alpha_w & 2\sin^2\alpha_w + 1 \end{bmatrix}\,, \tag{2.108}$$

$$G \;=\; \frac{2\,k\,h}{\sinh 2\,k\,h}\,. \tag{2.109}$$

For waves propagating over relatively small water depths ($\frac{h}{L} \ll 1$) the coefficient G tends to unity.

Similarly, the wave volume flux, which is equivalent to the Stokes drift, is given by

$$Q_{w\alpha} \;=\; B_0\,\frac{g\,H^2}{c}\,\frac{k_\alpha}{k}\,, \tag{2.110}$$

where k_α is the wave number vector component in the direction x_α, $k_\alpha = k(\cos\alpha_w, \sin\alpha_w)$ and B_0 is a wave-shape parameter. For linear long waves B_0 is given by

$$B_0 \;=\; \frac{\overline{\eta^2}}{H^2}\,. \tag{2.111}$$

For sinusoidal waves $B_0 = 0.125$, but it is clearly shown in the data analysis by Hansen (1990) that the actual value varies considerably from 0.125. For non-linear, non-breaking waves it is found that $B_0 \sim 0.06$, and for broken waves $0.06 < B_0 < 0.1$. It can also be shown that for a "sawtooth"-shaped wave, which is a good approximation to a broken wave, $B_0 = 0.083$.

For shallow water waves the wave celerity is given by $c = \sqrt{gh}$ and the wave volume flux can then be written as

$$Q_{w\alpha} = B_0 \frac{H^2}{h} \sqrt{gh} \frac{k_\alpha}{k} . \tag{2.112}$$

A generalization of this result is given by Svendsen (1984a), who adds an extra term to Q_w in the surf zone that accounts for the effect of the mass of water transported shorewards by the roller riding on the front of a broken wave. Hence, an extended expression for the wave volume flux in shallow water reads

$$Q_{w\alpha} = \frac{H^2}{h} \sqrt{gh} \left(B_0 + \frac{A}{HL} \frac{h}{H} \right) \frac{k_\alpha}{k} , \tag{2.113}$$

where A represents the area of the roller in the vertical projection. Okayasu *et al.* (1986) found that A can be approximately expressed by $0.06HL$. A similar adjustment, however, could be performed in the wave radiation stresses, but more research is needed in this subject which requires a detailed analysis of the momentum and energy transfers from the wave motion to the roller motion. As an example, Svendsen and Putrevu (1993) show that the radiation stresses in the surf-zone differ quite considerably from the values given by sinusoidal wave theory.

Last, it should be noted that Putrevu and Svendsen (1992a) express the dispersion coefficient in function of Q_w for a simple vertical current profile. Rakha and Kamphuis (1997) find that the effect of the momentum dispersion due to the vertical variation of the currents is very sensitive to the value of the short-wave volume flux Q_w. Hence it is relevant to estimate properly the value of Q_w.

2.4.5 Wind-induced surface shear stress

On shallow oceans, seas and estuaries the wind shear stress can produce a surface drift of the order of 3% or 4% of the mean wind speed measured at a height of 10 m above the sea-surface (Banner and Phillips, 1974). The wind exerts a drag force on the water surface that is mainly balanced by the surface pressure gradient and bottom shear stress. The wind-induced currents are hence depth-varying with the surface velocity larger than the bottom velocity and flowing in the direction of the wind shear stress (neglecting the action of the Coriolis acceleration). In the nearshore region, however, the wind-induced currents are usually much smaller than the short-wave induced currents. Outside the surf region the wave forcing is zero, and hence the wind stress becomes an important force able to produce currents, although these currents are usually not locally generated.

The wind-induced surface shear stress is usually computed as (e.g., Church and Thornton, 1993; Smith *et al.*, 1993)

$$\tau_\alpha^S = C_D \, \rho_a \, |W| \, W_\alpha \,, \tag{2.114}$$

where C_D is the drag coefficient, ρ_a is the air density, and W is the wind velocity at the standard 10 m elevation. The wind drag coefficient C_D is calculated from the formula recommended by the WAMDI Group (1988):

$$C_D \simeq \begin{cases} 1.2875 \times 10^{-3} \,, & U < 7.5\text{m/s} \\ (0.8 + 0.065\, U) \times 10^{-3} \,, & U \geq 7.5\text{m/s} \,. \end{cases} \tag{2.115}$$

Later, in chapter 6, the wind shear stress is taken into account for the direct comparison of modeled longshore currents versus measured in the field. It is found that the inclusion of the wind stress brings the model results in slightly closer agreement with data than without that effect.

2.4.6 Tidal effects

The influence of tides on the nearshore currents have been neglected in most studies. In the absence of wind and waves, astronomical tidal currents would be the only acting currents in the nearshore zone. However, due to the continuous existence of waves it is difficult in a typical nearshore environment to isolate the tidally forced currents from the currents forced by other mechanisms. In open coastal regions the tidal currents are much smaller than those observed close to embayments and harbors, where the tidal currents can be as strong as the wave induced currents and thus need to be accounted for properly.

In the present work we are interested in simulating the time-varying currents in a region small enough such that the Coriolis acceleration can be neglected, and the tidal currents are locally spatially constant. We also focus the model applications on open coastal regions. Hence the effect of the barotropic tides is not automatically accounted for in the present model equations and has to be forced through the boundary conditions. The application of the simplified model of Clarke and Battisti (1981) for the semi-diurnal tidal component in the Mid-Atlantic continental shelf suggests that the longshore and the cross-shore coastal currents are of $\mathcal{O}(0.1\,A)$ and $\mathcal{O}(0.15\,A)$, respectively, where A is the tidal amplitude. The longshore velocity is found to be in phase with the tidal elevation and the cross-shore current in quadrature. We note that these conclusions result from a simple barotropic model, and were verified only for distances off the coast of $\mathcal{O}(10\,\mathrm{Km})$.

Recently, Thornton and Kim (1993) and Feddersen *et al.* (1996) showed clearly that in the field conditions observed at Duck, NC, the longshore currents are strongly correlated with the tidal elevation. This correlation results from the direct rise and fall of the sea level due to the semi-diurnal tidal oscillation, which increases and decreases the water depths, and hence changes the local distribution

of the wave heights and consequently the nearshore currents. The phase dependence of the wave heights and longshore currents on the tidal elevation is dependent on the beach profile.

Based on these studies, we conclude that it is sufficient in the present model applications to include only the local tidal elevation. The shelf tidal currents estimated from the model of Clarke and Battisti (1981) yield values of $\mathcal{O}(5\,\mathrm{cm\,s^{-1}})$ which are much smaller than the currents usually observed in the surf zone of $\mathcal{O}(1\,\mathrm{m\,s^{-1}})$.

Chapter 3

NUMERICAL METHOD FOR SOLVING THE GOVERNING EQUATIONS

Any numerical model encompasses the following steps: grid definition, domain discretization, application of a procedure to obtain a system of algebraic equations from the initial partial differential equations (p.d.e), and solution of the system of equations. To convert the governing p.d.e. to a system of algebraic equations the most common methods are: (i) finite differences, (ii) (Galerkin) finite elements, and (iii) spectral methods. Any of these methods can be applied to our system of governing equations (2.71)–(2.72), with both advantages and disadvantages. Due to its simplicity and ease of interpretation we adopted here the use of finite difference methods to seek a numerical solution for those equations. The models using finite difference methods are also traditionally computationally faster than those with finite elements or spectral methods, which turns out to be an important factor when performing simulations over time periods as large as 1000 times the short-wave period.

In this chapter we will describe the numerical modeling scheme used to solve the governing equations. We present the relevant details of the numerical model SHORECIRC, which solves the depth and time-averaged equations of motion (2.71)–(2.72), described in the previous chapter. This model computes the values of the time-averaged free-surface elevation $\bar{\zeta}(x, y, t)$, and the wave-averaged

velocity $V_\alpha(x, y, z, t)$ over an initially defined space, designated by model domain. A previous version of this model is given in detail by Van Dongeren and Svendsen (1997b). Here we present an updated version of that model, which includes a more accurate numerical scheme.

The vertical variation of the horizontal currents is computed exactly analytically by equation (2.47). Thus, we need only to seek a numerical solution for the flow variables in the 2D-horizontal space (x, y). Thus, the model equations (2.71)–(2.72) are discretized on a fixed orthogonal grid (Fig. 3.1), where $\bar{\zeta}$, $\bar{Q}_x$ and $\bar{Q}_y$ are computed at each gridline intersection. Other flow variables, such as h_o, are evaluated at those same locations. The grid spacings in the x and y-directions, Δx and Δy respectively, are constant over the domain. Each grid position in the x-direction is designated by i, such that $x = (i-1)\Delta x$, and $i = 1, \ldots, n_x$, where n_x is the total discretized number of points in the x–direction. Similarly, each grid location in the y-direction is written as j, such that $y = (j-1)\Delta y$, and $j = 1, \ldots, n_y$. The temporal spacing Δt corresponds to the time interval between two consequent time instants t^n of the discretized time domain, $\Delta t = t^{(n+1)} - t^n$.

3.1 Finite difference equations

The partial derivatives in the differential governing equations are approximated by finite differences. The order of approximation of the partial derivatives in the governing equations gives then the order of the finite difference scheme. This order of approximation is given by the order of the remainder term in the Taylor series expansion of the finite difference approximation to the partial derivative (Hoffman, 1992). Higher-order schemes, although computationally more intensive, have the advantage of allowing for larger spatial and temporal spacings than the lower-order schemes. For the same grid and temporal spacing, though, a lower-order scheme is

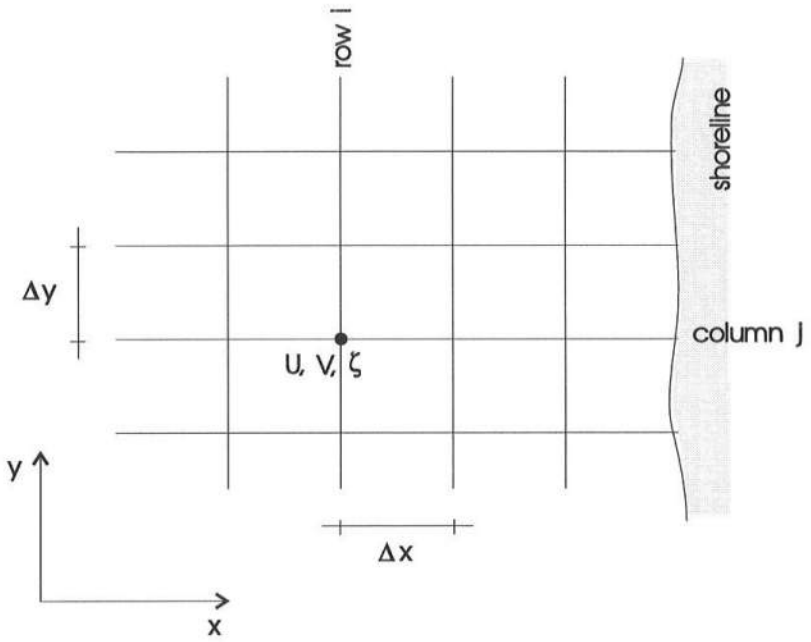

Figure 3.1: Grid definition.

faster than a higher-order scheme. Hence, the choice of the finite difference scheme and the grid spacings depends on both the requirement for the accuracy and the computational performance.

Several finite difference approximations are easily found in textbooks (e.g., Hoffman, 1992). Since we have both time and spatial derivatives we can approximate these by different orders if desired. We found that the second-order spatial scheme used by Van Dongeren and Svendsen (1997b) was not accurate enough for some applications studied here for a reasonable compromise between the total number of grid points and the grid spacing. Similarly, we found a third-order time-derivative scheme to be a good compromise between computational performance and accuracy. Hence, in the present version of the model SHORECIRC[1] the following finite

[1] Note that the version presented here is of higher order of accuracy than that given by Van Dongeren and Svendsen (1997b).

difference schemes are used:

- A third-order ($\mathcal{O}(\Delta t^3)$) Adams-Bashforth predictor method in combination with a $\mathcal{O}(\Delta t^3)$ Adams-Bashforth-Moulton corrector method for the time derivatives (Hoffman, 1992).
- Central spatial derivatives of $\mathcal{O}(\Delta x^4)$ and $\mathcal{O}(\Delta y^4)$ in the x and y-directions, respectively.

These finite difference schemes are then applied to the model equations (2.71)–(2.72). To illustrate the procedure both of those equations can be symbolically written as

$$\frac{\partial \mathbf{E}}{\partial t} = \mathbf{F} \,, \tag{3.1}$$

where the time derivative was kept in the LHS and all the other terms of any of the governing equations were put in the RHS. In equation (3.1) $\mathbf{E}$ is the vector quantity given by $\mathbf{E} = [\,\bar{\zeta}\,,\,\bar{Q}_x\,,\,\bar{Q}_y\,]^T$ and $\mathbf{F}$ is the vector corresponding to the RHS of the continuity and momentum equations (2.71)–(2.72).

In the predictor step, equation (3.1) is hence approximated by the Adams-Bashforth scheme

$$\mathbf{E}^{\star}_{i,j} = \mathbf{E}^{n}_{i,j} + \Delta t\, \alpha_0 \left(\alpha_1\, \mathbf{F}^{n}_{i,j} + \alpha_2\, \mathbf{F}^{n-1}_{i,j} + \alpha_3\, \mathbf{F}^{n-2}_{i,j}\right) + \mathcal{O}(\Delta t^3) \,, \tag{3.2}$$

where

$$\alpha_0 = 1/12 \,, \quad \alpha_1 = 23 \,, \quad \alpha_2 = -16 \,, \quad \alpha_3 = 5 \quad . \tag{3.3}$$

This equation yields the values of $\mathbf{E} = [\,\bar{\zeta}\,,\,\bar{Q}_x\,,\,\bar{Q}_y\,]^T$ at the time level $n+1$ (designated in the predictor step by $\star$) for known values of $\bar{\zeta}, \bar{Q}_x, \bar{Q}_y$ and the function $\mathbf{F}$ at previous time levels, for all the grid points i, j.

Similarly, at the corrector step the Adams-Bashforth-Moulton method reads

$$\mathbf{E}^{n+1}_{i,j} = \mathbf{E}^{n}_{i,j} + \Delta t\, \beta_0 \left(\beta_1\, \mathbf{F}^{\star}_{i,j} + \beta_2\, \mathbf{F}^{n}_{i,j} + \beta_3\, \mathbf{F}^{n-1}_{i,j}\right) + \mathcal{O}(\Delta t^3) \,, \tag{3.4}$$

where

$$\beta_0 = 1/12\,, \quad \beta_1 = 5\,, \quad \beta_2 = 8\,, \quad \beta_3 = -1 \quad . \tag{3.5}$$

In equation (3.4) we make use of the computed values of $\mathbf{F}$ at the time level $\star \equiv n+1$ from the values of $\mathbf{E}^\star$. We see then that an explicit method is used at the predictor level and an semi-implicit method is used at the corrector step. The corrector step could be applied several times consecutively until an error criterion was satisfied. However, we found that satisfactory precision is obtained by applying the corrector step only once.

Representing a general variable in the 2-dimensional space (x, y) by f, then the forth-order centered-difference partial derivatives are given by

$$\left.\frac{\partial f}{\partial x}\right|_{i,j} = \frac{f_{i-2,j} - 8\,f_{i-1,j} + 8\,f_{i+1,j} - f_{i+2,j}}{12\,\Delta x} + \mathcal{O}(\Delta x^4)\,, \tag{3.6}$$

$$\left.\frac{\partial f}{\partial y}\right|_{i,j} = \frac{f_{i,j-2} - 8\,f_{i,j-1} + 8\,f_{i,j+1} - f_{i,j+2}}{12\,\Delta y} + \mathcal{O}(\Delta y^4)\,. \tag{3.7}$$

These difference formulas are used to approximate the spatial partial derivatives in the governing equations (2.71)–(2.72). For simplicity of writing we combine the two partial derivatives into the expression

$$\left.\frac{\partial f}{\partial x_\alpha}\right|_k = \frac{\delta}{\Delta x_\alpha}\left[\gamma_{-2}\,f_{k-2} + \gamma_{-1}\,f_{k-1} + \gamma_1\,f_{k+1} + \gamma_2\,f_{k+2}\right] + \mathcal{O}(\Delta x_\alpha^4)\,, \tag{3.8}$$

where k represents the sub-indexes i or j for the partial derivatives in the x or y-directions, respectively, and

$$\delta = 1/12\,, \quad \gamma_{-2} = 1\,, \quad \gamma_{-1} = -8\,, \quad \gamma_1 = 8\,, \quad \gamma_2 = -1 \quad . \tag{3.9}$$

These finite difference equations are applied to all the interior points of the 2DH model domain. The computational molecule corresponding to the finite difference scheme is shown in Fig. 3.2. The flow variables $\bar{\zeta}$, $\bar{Q}_x$ and $\bar{Q}_y$ are computed at each grid point. At the boundaries, a different scheme has to be used because the

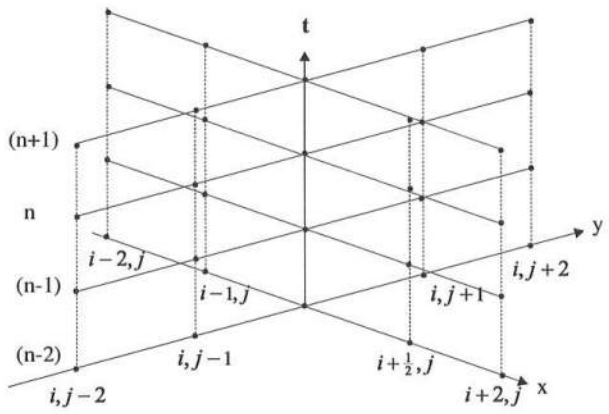

Figure 3.2: Computational molecule of the predictor-corrector $\mathcal{O}(\Delta t^3, \Delta x^4, \Delta y^4)$ scheme of SHORECIRC.

scheme (3.8) is spatially centered. An account of the finite differences scheme used at the boundary points is given later.

In the following section we analyze the stability criterion for the combined $\mathcal{O}(\Delta t^3, \Delta x^4, \Delta y^4, \Delta t \Delta x^4, \Delta t \Delta y^4)$ scheme used here. We suffice to say that the present scheme is consistent, i.e. the difference between the partial differential equations and the finite difference equations vanishes as the spatial and temporal grid spacings go to zero. Furthermore, the finite difference approximation is convergent within the limits of stability given next.

3.2 Stability analysis

We presented in the previous section the basic difference formulas that we use to build a finite difference approximation of the governing equations. Since these are only an approximation to the analytic equations we must find the limiting grid

spacings that produce a bounded solution for a set of conditions that we know to produce physically bounded solutions (which correspond to the exact solution of the governing equations). Stability analyses can only be performed for systems of linear p.d.e's, though the stability criterion obtained that way is usually also valid for the nonlinear system of equations (Hoffman, 1992). Hence we will linearize our governing equations and the respective finite difference equations. It can also be seen in Van Dongeren and Svendsen (1997b) that the forcing terms of the governing equations do not affect the stability analysis and hence we disregard them for this purpose.

We apply here the same procedure as that presented by Van Dongeren and Svendsen for the second-order spatial derivatives scheme. Furthermore, we extend the stability analysis to the two-dimensional problem as suggested by Lapidus and Pinder (1982). It turns out that the conclusions for the 2D problem can be interpreted as a geometrical extension of the 1D problem.

To abbreviate the algebra, we present only the main steps of the analysis. Hence, we consider the governing equations

$$\frac{\partial \bar{\zeta}}{\partial t} = -\frac{\partial \bar{Q}_\alpha}{\partial x_\alpha}\,, \tag{3.10}$$

$$\frac{\partial \bar{Q}_\alpha}{\partial t} = -g\,h_o\,\frac{\partial \bar{\zeta}}{\partial x_\alpha}\,. \tag{3.11}$$

Using the difference equation (3.2) for the predictor step the governing equations can then be written as

$$\bar{\zeta}^{\star}_{i,j} = \bar{\zeta}^{n}_{i,j} - \Delta t\,\alpha_0 \left(\alpha_1 \left.\frac{\partial \bar{Q}_\alpha}{\partial x_\alpha}\right|^{n}_{i,j} + \alpha_2 \left.\frac{\partial \bar{Q}_\alpha}{\partial x_\alpha}\right|^{n-1}_{i,j} + \alpha_3 \left.\frac{\partial \bar{Q}_\alpha}{\partial x_\alpha}\right|^{n-2}_{i,j} \right)\,, \tag{3.12}$$

$$\begin{aligned} \left.\bar{Q}_\alpha\right|^{\star}_{i,j} &= \left.\bar{Q}_\alpha\right|^{n}_{i,j} \\ &- \Delta t\,\alpha_0\,g\,h_o \left(\alpha_1 \left.\frac{\partial \bar{\zeta}}{\partial x_\alpha}\right|^{n}_{i,j} + \alpha_2 \left.\frac{\partial \bar{\zeta}}{\partial x_\alpha}\right|^{n-1}_{i,j} + \alpha_3 \left.\frac{\partial \bar{\zeta}}{\partial x_\alpha}\right|^{n-2}_{i,j} \right)\,, \end{aligned} \tag{3.13}$$

where we left the spatial derivatives in differential form for facility of reading. We then apply the difference formulas (3.6)–(3.7) onto those partial derivatives and obtain the finite difference equations for the predictor step.

In the corrector step we apply (3.4) to the governing equations which yields

$$\bar{\zeta}_{i,j}^{n+1} = \bar{\zeta}_{i,j}^{n} - \Delta t\, \beta_0 \left(\beta_1 \left. \frac{\partial \bar{Q}_\alpha}{\partial x_\alpha} \right|_{i,j}^{\star} + \beta_2 \left. \frac{\partial \bar{Q}_\alpha}{\partial x_\alpha} \right|_{i,j}^{n} + \beta_3 \left. \frac{\partial \bar{Q}_\alpha}{\partial x_\alpha} \right|_{i,j}^{n-1} \right) , \quad (3.14)$$

$$\begin{aligned} \bar{Q}_\alpha \Big|_{i,j}^{n+1} &= \bar{Q}_\alpha \Big|_{i,j}^{n} \\ &- \Delta t\, \beta_0\, g\, h_o \left(\beta_1 \left. \frac{\partial \bar{\zeta}}{\partial x_\alpha} \right|_{i,j}^{\star} + \beta_2 \left. \frac{\partial \bar{\zeta}}{\partial x_\alpha} \right|_{i,j}^{n} + \beta_3 \left. \frac{\partial \bar{\zeta}}{\partial x_\alpha} \right|_{i,j}^{n-1} \right) , \end{aligned} \quad (3.15)$$

where, once again, we kept the partial derivatives in differential form.

The finite difference equations for the predictor and corrector steps together can be evaluated by inserting equations (3.12)–(3.13) into equations (3.14)–(3.15), with the spatial finite differences already included too. The derivation is straightforward, but leads to lengthy equations that for reasons of space we do not present here. The procedure is similar for all the governing equations and in Appendix A we present the detailed derivation for the continuity equation as an example.

To determine the stability conditions of the our finite difference approximation we follow the von Neumann method (see, e.g. Hoffman, 1992). The numerical solution of the finite difference equations is equal to the exact solution of the same equations plus an error due to the numerical computation:

$$\bar{\zeta}_{i,j}^{n} = \bar{\zeta}^{E} \Big|_{i,j}^{n} + \eta_{i,j}^{n} , \quad (3.16)$$

$$\bar{Q}_\alpha \Big|_{i,j}^{n} = \bar{Q}_\alpha^{E} \Big|_{i,j}^{n} + q_{i,j}^{n} , \quad (3.17)$$

where the superscript E is used for the exact solution, and η and q are the errors at each grid point i, j and time level n. If the errors grow unbounded then the solution

is unstable, otherwise it is stable. These errors can be represented by Fourier series and because of linearity we only need to consider a general component of the Fourier series representation:

$$\eta_{i,j}^{n} = \eta_0 e^{I(k_m\, x_i + k_l\, y_j - \omega\, n\, \Delta t)}\,, \tag{3.18}$$

$$q_\alpha|_{i,j}^{n} = q_{0\alpha} e^{I(k_m\, x_i + k_l\, y_j - \omega\, n\, \Delta t)}\,, \tag{3.19}$$

where $x_i = (i-1)\Delta x$ and $y_j = (j-1)\Delta y$ and $I = \sqrt{-1}$. For convenience we also define the spatial phase functions

$$\theta_1 = I\, k_m\, \Delta x\,, \qquad \theta_2 = I\, k_n\, \Delta y\,, \tag{3.20}$$

and the Courant numbers

$$\nu_1 = c_0\, \frac{\Delta t}{\Delta x}\,, \qquad \nu_2 = c_0\, \frac{\Delta t}{\Delta y}\,, \tag{3.21}$$

where $c_0 = \sqrt{g h_o}$.

We then introduce the Taylor series components of the errors $\eta_{i,j}^{n}$ and $q_\alpha|_{i,j}^{n}$ at each grid location into the predictor-corrector equations satisfied by the errors. The final set of equations can then be rewritten in matrix form as

$$\mathbf{Z}^{n+1} = \mathbf{G}\, \mathbf{Z}^{n}\,, \tag{3.22}$$

where

$$\mathbf{Z}^{n+1} = [\,\eta^{n+1}\,,\, q_x^{n+1}\,,\, q_y^{n+1}\,,\, \eta^{n}\,,\, q_x^{n}\,,\, q_y^{n}\,,\, \eta^{n-1}\,,\, q_x^{n-1}\,,\, q_y^{n-1}\,]^T\,, \tag{3.23}$$

$$\mathbf{Z}^{n} = [\,\eta^{n}\,,\, q_x^{n}\,,\, q_y^{n}\,,\, \eta^{n-1}\,,\, q_x^{n-1}\,,\, q_y^{n-1}\,,\, \eta^{n-2}\,,\, q_x^{n-2}\,,\, q_y^{n-2}\,]^T\,. \tag{3.24}$$

The matrix $\mathbf{G}$ is called the amplification matrix, which is given by

$$\mathbf{G} = \begin{pmatrix} g_{11} & g_{12} & g_{13} & g_{14} & g_{15} & g_{16} & g_{17} & 0 & 0 \\ g_{21} & g_{22} & g_{23} & g_{24} & g_{25} & g_{26} & 0 & g_{28} & g_{29} \\ g_{31} & g_{32} & g_{33} & g_{34} & g_{35} & g_{36} & 0 & g_{38} & g_{39} \\ 1 & 0 & 0 & 0 & 0 & 0 & 0 & 0 & 0 \\ 0 & 1 & 0 & 0 & 0 & 0 & 0 & 0 & 0 \\ 0 & 0 & 1 & 0 & 0 & 0 & 0 & 0 & 0 \\ 0 & 0 & 0 & 1 & 0 & 0 & 0 & 0 & 0 \\ 0 & 0 & 0 & 0 & 1 & 0 & 0 & 0 & 0 \\ 0 & 0 & 0 & 0 & 0 & 1 & 0 & 0 & 0 \end{pmatrix}, \tag{3.25}$$

where the coefficients g_{ij} are given in Appendix B.

For an arbitrary Fourier component of the error to remain bounded in successive iterations we require $\|\mathbf{G}\| \leq 1$. This condition is satisfied if all the eigenvalues λ_p $(p = 1, \ldots, 9)$ of the amplification matrix $\mathbf{G}$ are bounded by unity:

$$|\lambda_p| \leq 1 \,. \tag{3.26}$$

Hence we determine the eigenvalues of the amplification matrix and check the magnitude of their absolute value. As mentioned previously, a similar analysis was presented by Van Dongeren and Svendsen (1997b) for a second-order spatial scheme and in the 1D space, which had two free parameters in the amplification matrix: ν_1 and $k_m \Delta x$. The present problem has four free parameters, ν_1, $k_m \Delta x$, ν_2 and $k_n \Delta y$, because of the addition of another spatial dimension. This makes the graphical representation of the values of $|\lambda_p|$ more difficult. We choose therefore to present first the results for the simplified 1D problem, which comes out trivially from the amplification matrix (3.25) by setting the coefficients that multiply q_y to zero.

The absolute value of the six resultant non-zero eigenvalues is shown in Fig. 3.3. All eigenvalues satisfy the stability criterion for all Courant numbers and

wave modes, except the eigenvalues λ_1 and λ_2, which have identical behavior. The stability limit of these two eigenvalues is best seen in Fig. 3.4, where we plot $|\lambda_1|$ versus ν_1 for several wave numbers $k_m\,\Delta x$. From this figure we estimate the stability criterion

$$\nu_1 = c_0\,\frac{\Delta t}{\Delta x} \leq 0.85\,. \tag{3.27}$$

which corresponds to the least stable wave, with wave number $k_m\,\Delta x = \frac{\pi}{2}$. It should be noticed that the same criterion would apply if considering the problem in the spatial dimension y instead of x as considered here, by replacing ν_1 with ν_2 and $k_m\,\Delta x$ by $k_n\,\Delta y$.

For the 2D problem we must determine nine eigenvalues which are determined numerically. As mentioned above a difficulty arises to show the stability limits given the four degrees of freedom of $|\lambda_p|$. However, using the results of the 1D problem we find that the least stable wave numbers are $k_m\,\Delta x = k_n\,\Delta y = \frac{\pi}{2}$. Hence, we fix $k_m\,\Delta x = k_n\,\Delta y = \frac{\pi}{2}$ and find the surfaces corresponding to $|\lambda_p| = f(\nu_1, \nu_2)$. A perspective view of these surfaces for the nine eigenvalues is shown in Fig. 3.5. Once again, the absolute value of the eigenvalues λ_1 and λ_2 are equal, and they are the only ones that exceed unity. For the first of these eigenvalues, we show in Fig. 3.6 the contour plot of $|\lambda_1|$, where only the contours corresponding to $|\lambda_1| \leq 1$ are drawn. As expected by geometrical reasons, the stability limit is a circle of radius $C_r \leq 0.85$, where C_r is the Courant number given by $C_r = \sqrt{\nu_1^2 + \nu_2^2}$. Hence, the stability criterion can be written as

$$C_r = c_0\,\Delta t\,\frac{\sqrt{\Delta x^2 + \Delta y^2}}{\Delta x\,\Delta y} \leq 0.85\,. \tag{3.28}$$

It should be noted that the stability criterion just derived is applicable only for the interior points of the domain where each of the flow variables is calculated from the discretized governing equations. At the 2DH domain boundaries we apply

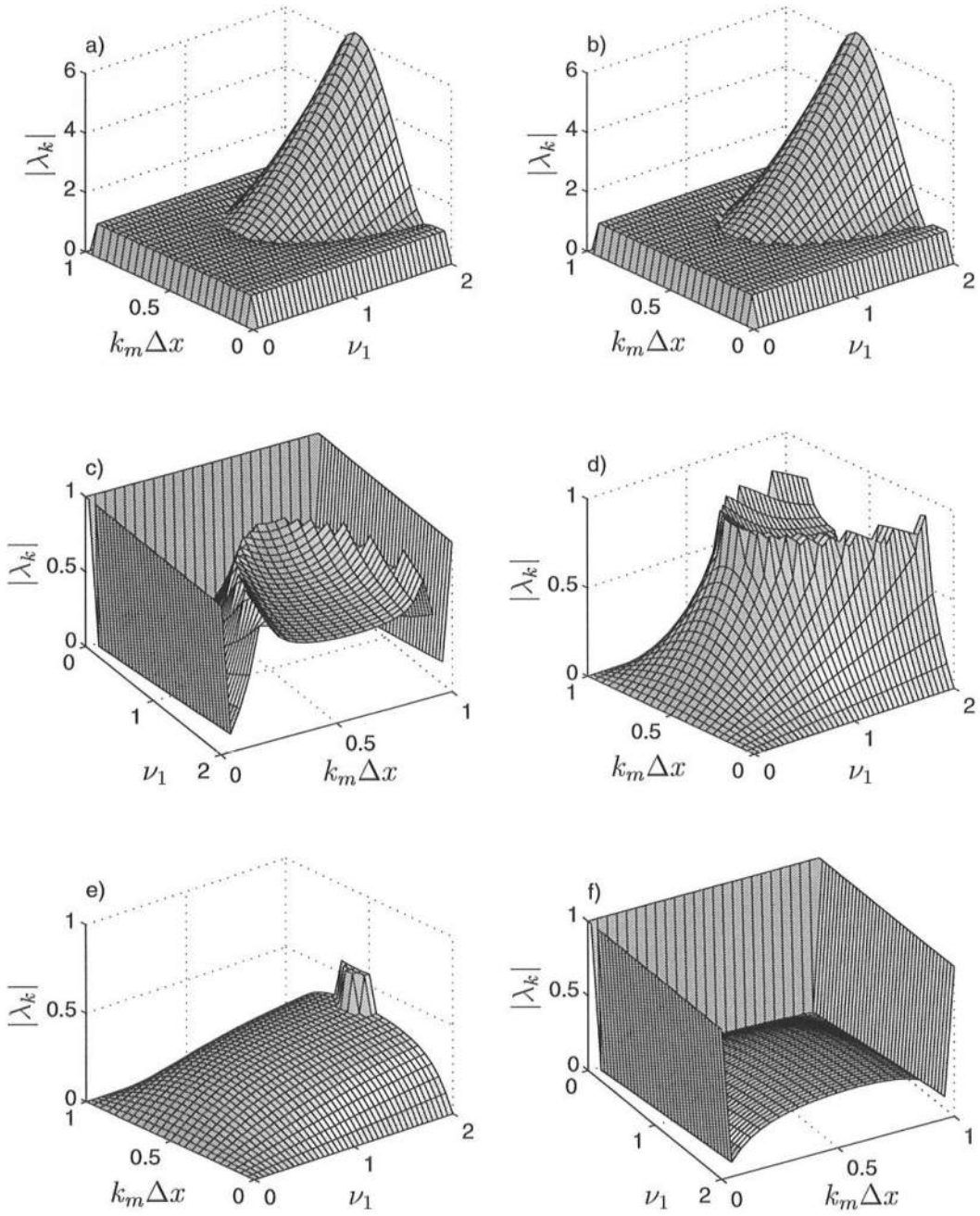

Figure 3.3: Variation of the absolute eigenvalues $|\lambda_p|$ versus the Courant number ν_1 and the wave number $k_m\Delta x$: (a) $|\lambda_1|$; (b) $|\lambda_2|$; (c) $|\lambda_3|$; (d) $|\lambda_4|$; (e) $|\lambda_5|$; (f) $|\lambda_6|$.

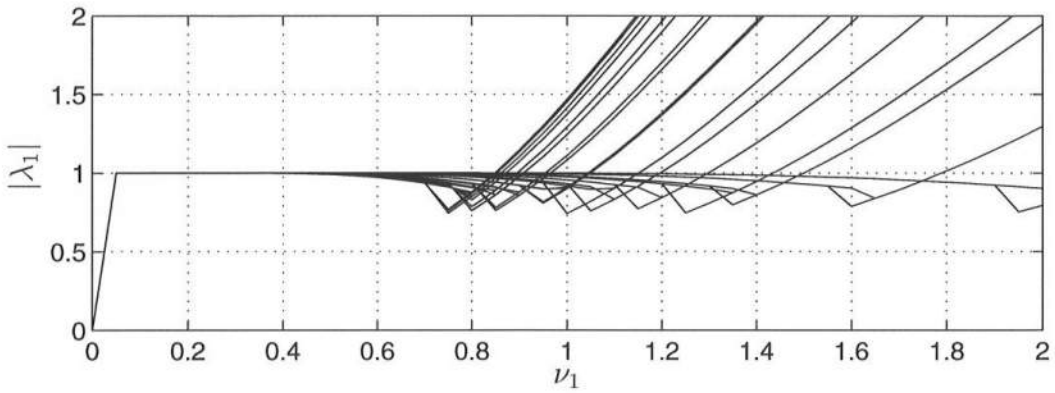

Figure 3.4: Variation of the absolute eigenvalue $|\lambda_1|$ versus the Courant number ν_1 for several values of $k_m\,\Delta x$.

boundary conditions of the Dirichlet or von Neumman type, or a combination of the two, as presented in the next section. Also, at the boundary points, and at the points immediately adjacent to those, we apply a different set of finite difference formulas for the spatial derivatives. For consistency of the order of the scheme, a fourth-order skewed (non-centered) scheme should be applied at those points. However, we found that the use of a lower-order $\mathcal{O}(\Delta x^2, \Delta y^2)$ scheme did not decrease significantly the overall accuracy of the scheme, but it improved the stability range of the model compared to that obtained by using fourth-order spatial derivatives at the boundaries.

3.3 Boundary conditions

The SHORECIRC model can be applied to a variety of different physical situations, such as the study of long waves in a flume, infragravity waves in a laboratory basin (Van Dongeren *et al.*, 1996), or nearshore currents under field conditions (Sancho *et al.*, 1996). Each of these different situations requires that we specify the boundary conditions at the domain limits and also that we set the initial

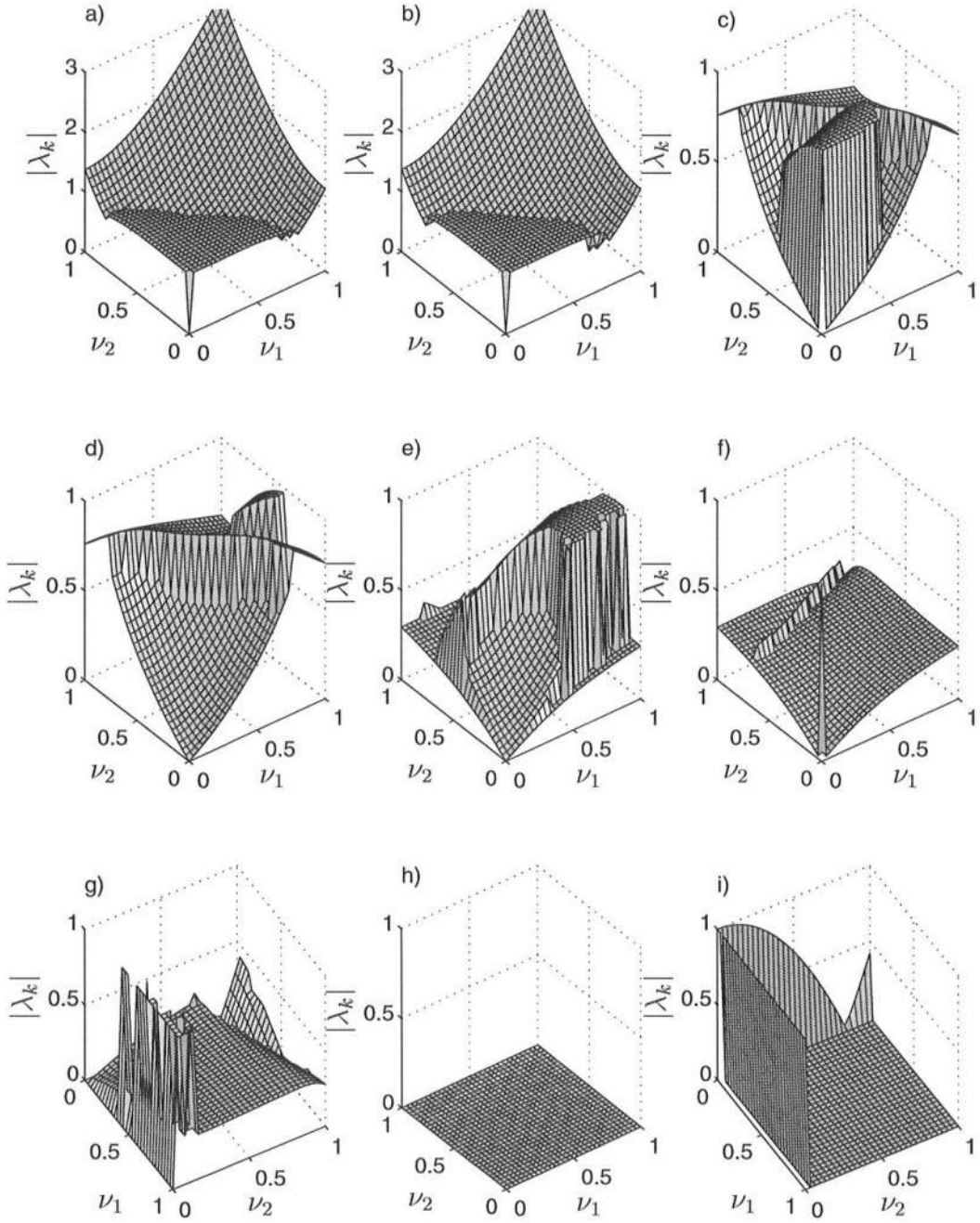

Figure 3.5: Variation of the absolute eigenvalues $|\lambda_p|$ versus the Courant numbers ν_1 and ν_2 for fixed wave numbers $k_m \Delta x, k_n \Delta y$: (a) $|\lambda_1|$; (b) $|\lambda_2|$; (c) $|\lambda_3|$; (d) $|\lambda_4|$; (e) $|\lambda_5|$; (f) $|\lambda_6|$; (g) $|\lambda_7|$; (h) $|\lambda_8|$; (i) $|\lambda_9|$.

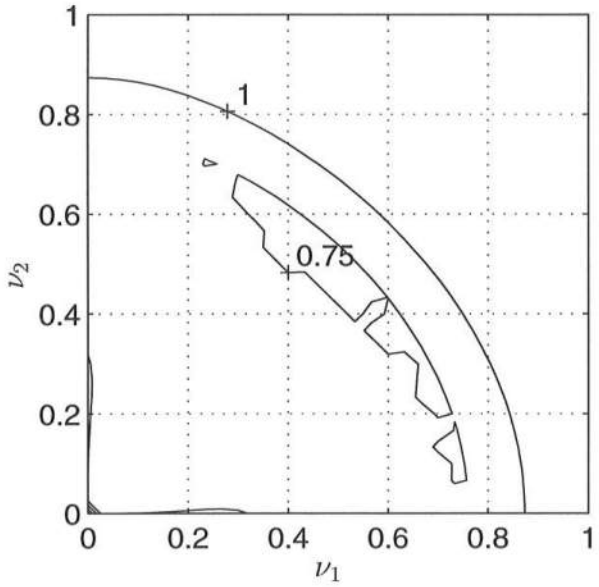

Figure 3.6: Variation of the absolute eigenvalue $|\lambda_1|$ versus the Courant numbers ν_1 and ν_2 for fixed wave numbers $k_m \Delta x, k_n \Delta y$.

condition. That is required because of the nature of the governing equations, which are of hyperbolic type, and hence we have an initial and boundary value problem.

In the present work we address mostly the study of nearshore currents under various conditions corresponding to a nearly long straight coast, using the topography at Duck, NC, for example. The model domain is thus a stretch of a coast with open boundaries at the cross-shore and seaward domain limits. The shoreward boundary is placed either over dry land, allowing thus for a moving shoreline, or is positioned fixed at a small water depth where a zero flux Dirichlet condition is applied.

Seaward boundary

At the seaward boundary we apply a generating-absorbing boundary condition developed by Van Dongeren and Svendsen (1997a). This condition makes use of the governing equations described in characteristic form. It allows a prescription of an incoming (plane) long wave along the boundary and allows the outgoing waves to leave the domain with minimum reflection. The outgoing wave is calculated using the Method of Characteristics and substituting the linear long wave relationship between the velocity and the surface elevation $Q = c\,\zeta$.

The boundary condition above applies to incoming and outgoing (long) waves. For steady or unsteady currents that do not satisfy the long wave relation $Q = c\,\zeta$ we must specify the currents at the boundary. This is because the problem is of elliptic nature and thus requires the knowledge of the currents at the domain boundaries. Since for most applications we know little about the currents at the seaward boundary, as well as outside the model domain, we let them be zero at that boundary. For that reason we also place the seaward boundary reasonably far away from the surf zone region where the currents are the strongest. Based on several computations it is recommended to locate the seaward boundary at a distance $l_x \geq 3\,x_b$ from the shoreline, where x_b is the surf zone width.

Cross-shore boundaries

The cross-shore boundaries of the physical domain are most often also open and limit the longshore domain of the coast in study. Due to the elliptical nature of the problem the currents should be specified at those boundaries as well. For the study of currents in a wave basin it is possible to specify a no flux condition or the currents measured by the recirculation system. On an open coast we need to know the nature of those currents, especially at the upstream section. At the downstream

section, a von Neumann boundary condition, such as $\frac{\partial \bar{Q}_y}{\partial y} = 0$, could be used, but we need to know the main direction of the flow *a priori*. This condition means that there is no longshore variation of the longshore current at the boundary, which is an approximation.

To overcome the problem of specifying the currents at the lateral boundaries on an open coast, and not knowing *a priori* the main direction of the flow, the domain is assumed longshore periodic so that the flow variables at one end ($y = 0$) equal those at the other end ($y = l_y$) in the longshore direction. That means

$$\bar{\zeta}(x, 0) = \bar{\zeta}(x, l_y) , \tag{3.29}$$

$$\bar{Q}_\alpha(x, 0) = \bar{Q}_\alpha(x, l_y) . \tag{3.30}$$

At the lateral boundaries, where the periodicity condition is used, we also apply the partial derivative $\frac{\partial}{\partial y}$ across the boundary using the centered space scheme (3.7) and the grid points at the other end of the domain.

In some of the examples shown later we specify the value of the currents at the cross-shore boundaries, disregarding the assumption of longshore periodicity. However, in order to have a global mass balance inside the model domain the total volume flux of the upstream current must be equal to that of the downstream current.

Shoreward boundary

At the landward boundary we apply the moving shoreline boundary condition given by Van Dongeren and Svendsen (1997b). This condition simulates the inundation and drainage of the land as the mean water level moves up and down due to long wave motions. This procedure does not account for the swash zone motion

of the short waves though (Brocchini and Peregrine, 1996).

The moving shoreline method of Van Dongeren and Svendsen (1997b) essentially accounts for the mass balance of water between the "wet" point closer to the shoreline (designated here by last "wet" point) and the shoreline itself, and considers a control volume around that "wet" node. At each time-step, the volume of water stored between the last "wet" point and the extrapolated shoreline position is calculated. This volume of water is added or subtracted by the amount of water that enters or leaves the control volume. This additional volume flux increases or decreases the free-surface elevation at the last "wet" node, and hence we determine the new shoreline position by the intersection of the bottom surface with the surface given by free-surface gradient determined at the last "wet" point and previous time level. The position of the shoreline at the new time level will then control whether other grid points get "wet" or "dry". For details of the method see the reference above. Finally, it should be noted that the model domain limit is actually located landward of the maximum high water mark (the position of the maximum run-up) and the flow variables are set to zero at those locations, which are "dry".

A second type of shoreward boundary condition is often used throughout this work. We set a fixed shoreline at a small water depth (typically of the order of 5 cm) and prescribe a no-flux condition at that boundary:

$$\bar{Q}_x(l_x, y) = 0\,, \tag{3.31}$$

where $x = l_x$ is the shoreline location. For the longshore velocity V (or the longshore volume flux $\bar{Q}_y$) we specify $\bar{Q}_y(l_x, y) = 0$ as well. This condition is an approximation because at this boundary there could be a slip velocity. The specification of the correct longshore current at this landward boundary would require knowledge of the swash zone motion though, and it should include the contribution of the mass

and momentum fluxes due to this motion (Brocchini, 1996). In the present work, however, we do not address this contribution.

Last, Özkan-Haller and Kirby (1997) find that for the prediction of shear instabilities of the longshore currents the use of a moving shoreline gives very similar results to those of having a fixed shoreline with the no flux boundary condition (3.31). This means that the effect of the shoreline runup and rundown of the mean flow properties away from the shoreline is negligible, and thus it is a good approximation to use (3.31).

Initial condition

As seen before, the governing equations (2.71)–(2.72) are time-dependent and can describe time-varying phenomena (in a time scale much longer than that of the short wave period). The SHORECIRC model gives time series of the dependent variables for the period of simulation desired. Hence we can in principle describe non-steady sea states, such as the evolution of a calm flow field (where the currents are nearly zero) to a current condition correspondent to highly energetic waves (cold start). This, however, would require the knowledge of the sea-state conditions at every moment in order calculate a time-varying wave forcing.

Instead, in the applications presented herein we consider a stationary wave field for the period of time of the duration of the simulation. This simplification is due to the present unavailability of a time-varying wave model to provide the wave forcing in a general situation, and thus the use of a monochromatic wave model (REFDIF) in our simulations. For most applications we use a single periodic wave train, or the linear superposition of several sinusoidal waves, and compute the steady short-wave induced forcing caused by that wave field.

In order apply the numerical model we must start from an initial state. That can, in principle, be any arbitrary state — the steady wave forcing will then cause the flow to accelerate and adjust until it reaches an equilibrium between the driving forces, the dissipative forces, and the flow accelerations. In a steady state solution the local acceleration is zero, and in a global perspective of the nearshore region as a whole the bottom friction over this region equals the total short-wave forcing.

In practice, the numerical solution of the equations of motion can diverge from the physical solution if the initial condition is not well-behaved. The modeling of a sudden impulse force on a body of water can cause accelerations that are so large that numerical instabilities develop due to the nonlinear terms. Hence, to avoid this type of problems we choose the initial condition:

$$\bar{\zeta} = \bar{Q}_x = \bar{Q}_y = 0 \tag{3.32}$$

for every point in the model domain. We designate this condition as a "cold start". The wave forcing is also set equal to zero at the start of the computation, and then is increased at a chosen rate until it reaches the representative value of steady wave field we want to simulate. This "ramping" of the wave forcing induces a transient motion in a form of a long wave that is absorbed at the seaward boundary by the absorbing-generating boundary condition. After that transient propagates out of the model domain the flow field approaches the conditions we want to model.

3.4 Numerical instabilities

The stability analysis in section 3.2 indicated a limiting Courant number for which the numerical solution of the finite difference equations would be stable. That limit was calculated from the linearized mass and momentum equations, and assumes the governing equations to have a bounded solution. The last assumption

is, however, not valid if instead of considering the linear equations we model the non-linear long wave equations (unforced and frictionless). These equations are known to not have a permanent form solution as the waves will steepen and pitch forward progressively as they advance in space. The forward pitching will eventually pass the vertical position and at this stage the free-surface elevation is multivalued and a single-valued solution no longer exists.

Due to the nonlinearity, high frequency harmonics are generated with the steepening of the waves and become progressively more energetic. The high frequency waves have a short wave length that could physically be smaller than the Nyquist frequency associated with the spatial discretization. This situation poses numerical difficulties and the numerical solution can become unstable as energy is transferred into the high frequency waves. However, waves shorter than $2\Delta x$ or ($2\Delta y$ in the y-direction) can not be resolved by the grid system, but such waves can be generated by physical (nonlinearities) or numerical (roundoff and truncation) mechanisms. Since these waves can not be resolved numerically, their energy will appear at longer wavelengths by aliasing (Shapiro, 1970). This process will transfer energy that should not be transferred from high-frequency waves to low-frequency waves. It is thus important to reduce the amplitude of the high-frequency spurious waves, so that their energy is not moved back to the low-frequency components.

To prevent the growth of high-frequency waves we apply a numerical filter that removes ideally only the shortest resolvable wave component. The details of the numerical filter are given by Shapiro (1970) and we employ here that technique to the computed values of $\bar{\zeta}$ and $\bar{Q}_\alpha$ at every certain number of time-steps. The filter presented by that author is considered a "quasi-ideal" low-pass filter as it removes the $2\Delta x$ wavelength components leaving at the same time the other wavelengths almost unfiltered. If that were not accomplished then the successive applications of

the numerical smoother would remove energy from unwanted physical wavelengths.

In brief, the filtered (smoothed) general variable $\dot{Z}$ is related to the original unsmoothed variable Z by the response function ρ:

$$\rho = \frac{\dot{Z}}{Z} \,. \tag{3.33}$$

The "ideal" response function ρ is given for the 1D problem by (Shapiro, 1970):

$$\rho\,(\lambda, n) = 1 - \sin^{2n}\left(\frac{\pi\,\Delta x}{\lambda}\right) \,, \tag{3.34}$$

where λ is the spatial wavelength of a sinusoidal component of Z, and n is the order of the filter. The higher the order n, the closer ρ approaches unity for wavelengths other then $\lambda = 2\,\Delta x$; for this wavelength the response function is zero as desired. The response function for the 2D problem is the product of the individual response functions for each direction given by (3.34).

It should be noted that we do not find it necessary to apply the numerical filter for every type of physical problem presented here. Hence, given any physical problem simulated herein, we have attempted a simulation without the numerical smoother and we redo the simulation applying the filter only if instabilities arise. As a result of several tests, for the most unstable situations, we find it convenient to apply the 16th-element filter operator ($n = 8$) in the cross-shore direction for the $\bar{Q}_x$ and $\bar{Q}_y$ variables at every time-step. For the free-surface elevation $\bar{\zeta}$ we apply the same filter only at every 10 time-steps. Since the gradients in the longshore direction are usually smaller than the gradients in the cross-shore direction, we use a lower-order filter (8th-element operator, $n = 4$) in the longshore direction. In this direction we apply the smoother for $\bar{Q}_x$ and $\bar{Q}_y$ at every time-step, and for $\bar{\zeta}$ at every 10 time-steps. For more stable simulations we apply the 16th-element filter in the x-direction, and the 8th-element filter in the y-direction, but less frequently than stated above.

Chapter 4

A SIMPLIFIED MODEL FOR CURRENTS OVER WEAKLY LONGSHORE NONUNIFORM TOPOGRAPHIES

On a longshore nonuniform beach the current patterns can be very complicated due to nonuniformities of the topography and wave conditions, and larger scale variations of the forcing mechanisms. The dominating flow is usually a longshore current and various simplifying situations have been considered for the prediction of such currents. The first longshore current models (shortciteNPBowen69,LH70a, 1970a; Thornton, 1970) assumed a longshore uniform bathymetry and a steady, depth-uniform distribution of the longshore currents. The currents were a result of a balance between the wave radiation stress, the bottom friction and turbulent mixing. Later studies by Putrevu and Svendsen (1992a) and Svendsen and Putrevu (1994) concluded that the nonlinear interaction between depth-varying cross- and longshore currents causes a dispersive mixing effect, which largely dominates the turbulent lateral mixing in the nearshore region. More recently, Kobayashi *et al.* (1997) confirmed that the dispersive mixing is significant for regular waves, but they also found it to be secondary for irregular waves.

A second class of longshore current models relaxed the assumption of longshore uniform topography. Mei and Liu (1977) considered normally-incident waves

breaking on a bottom topography that varied weakly in the longshore direction and analyzed the effect of those longshore bottom variations on the nearshore circulation. An extension of that work was given by Wu and Liu (1984), who considered, at second-order, the effects of the nonlinear inertial terms (the convective accelerations) and studied waves incident at an oblique angle. Those authors found the effects of the nonlinear convective terms to grow with increasing amplitude and angle of the incident wave.

The work by Putrevu *et al.* (1995), (referred to as POS from here on) is an extension of the work of Mei and Liu (1977). POS proposed a simple model accounting for the terms analyzed by Mei and Liu (1977) — the wave forcing, the bottom friction and the longshore pressure gradient — plus the effect of dispersive mixing mentioned above. They also considered obliquely-incident waves and in their examples it is shown that, for a weak longshore bottom variation and small angles of incidence, the longshore pressure gradient becomes important and contributes significantly to the forcing of the longshore currents. For larger angles of incidence, however, the contribution of the longshore pressure gradient diminishes relative to the wave radiation stress. Using the model equations of POS Reniers *et al.* (1995) also find that including the longshore pressure gradient, due to local longshore bottom variations, greatly improves their model results agreement with field data.

In an example application of the SHORECIRC model (described in the previous section) for depth-uniform currents, Sancho *et al.* (1995) predicted that in a barred beach with a rip-channel the longshore pressure gradient forcing is of the same magnitude as the longshore radiation stress forcing. A similar situation had been predicted in the simplified model for rip-currents given by Dalrymple (1978). Further investigation of the longshore currents over a barred beach, and the role of the pressure gradient will be pursued here.

We analyze in detail the range of validity of the assumptions in POS by comparing the results from their semi-analytical solution with the results of SHORECIRC. Two specific beach configurations are used to illustrate the accuracy and limitations of the POS model. One is a plane beach with a longshore sinusoidal modulation, and the other a barred beach with a variation in the bar height simulating a rip-channel. We also make use of the model SHORECIRC as a tool to evaluate the importance of each term in the governing equations and assist us in the understanding of their contribution to the nearshore flow. We find that, in the cross-shore and longshore momentum equations for nearshore circulation, in general the leading order terms are of different orders of magnitude and a new extension of the POS model is presented here, which consistently includes all terms of the same order.

4.1 Model equations

In the following we will nondimensionalize the governing equations (2.25) and (2.28), prior to the coupling between the depth-varying and depth-integrated equations, written in terms of the current velocities. For completeness, we rewrite those equations explicitly in the x- and y-directions as

$$\frac{\partial \bar{\zeta}}{\partial t} + \frac{\partial}{\partial x}\left(\overline{\int_{-h_o}^{\zeta} U\,dz} + Q_{wx}\right) + \frac{\partial}{\partial y}\left(\overline{\int_{-h_o}^{\zeta} V\,dz} + Q_{wy}\right) = 0\,, \tag{4.1}$$

$$\begin{aligned}
&\frac{\partial}{\partial t}\left(\overline{\int_{-h_o}^{\zeta} U\,dz}\right) + \frac{\partial}{\partial y}\left(\overline{\int_{-h_o}^{\zeta} UV\,dz} + U(\bar{\zeta})\,Q_{wy} + V(\bar{\zeta})\,Q_{wx}\right) \\
&+ \frac{\partial}{\partial x}\left(\overline{\int_{-h_o}^{\zeta} U^2\,dz} + 2U(\bar{\zeta})\,Q_{wx}\right) + g\,(h_o + \bar{\zeta})\,\frac{\partial \bar{\zeta}}{\partial x} \\
&+ \frac{1}{\rho}\left(\frac{\partial S_{xx}}{\partial x} + \frac{\partial S_{yx}}{\partial x}\right) + \frac{1}{\rho}\frac{\partial}{\partial y}\left(\overline{\int_{-h_o}^{\zeta} \tau_{yx}\,dz}\right) + \frac{\tau_x^B - \tau_x^S}{\rho} = 0\,,
\end{aligned} \tag{4.2}$$

$$\frac{\partial}{\partial t}\left(\overline{\int_{-h_o}^{\zeta} V\,dz}\right) + \frac{\partial}{\partial x}\left(\overline{\int_{-h_o}^{\zeta} UV\,dz} + V(\bar{\zeta})\,Q_{wx} + U(\bar{\zeta})\,Q_{wy}\right)$$

$$+\frac{\partial}{\partial y}\left(\overline{\int_{-h_o}^{\zeta} V^2\,dz}+2V(\bar{\zeta})\,Q_{wy}\right)+g\,(h_o+\bar{\zeta})\,\frac{\partial\bar{\zeta}}{\partial y}$$
$$+\frac{1}{\rho}\left(\frac{\partial S_{xy}}{\partial x}+\frac{\partial S_{yy}}{\partial y}\right)+\frac{1}{\rho}\frac{\partial}{\partial x}\left(\overline{\int_{-h_o}^{\zeta}\tau_{xy}\,dz}\right)+\frac{\tau_y^B-\tau_y^S}{\rho}=0\,. \qquad (4.3)$$

It is useful to first rederive the solution of POS while clarifying the assumptions for the benefit of the later discussion. For simplicity, the following assumptions are introduced:

1) the flow is considered steady;

2) turbulent and surface shear stresses are neglected;

3) waves are assumed to approach the coast at a small angle α_b with the shore normal, such that $\sin\alpha_b \ll 1$ and $\cos\alpha_b \simeq 1$;

4) refraction is neglected in the wave height estimates due to assumption 3);

5) short-wave related quantities are determined by linear long wave theory.

The POS model is based on a set of nondimensional variables. We follow the nomenclature of POS everywhere, except when otherwise noted. Thus, the following nondimensional variables are introduced:

$$\begin{aligned} x' &= \frac{x}{L_x}\,,\\ y' &= \frac{y}{L_y}\,,\\ h' &= \frac{h}{h_b}\,,\\ U' &= \frac{U}{\mu\,c_b}\,,\\ V' &= \frac{V}{\kappa\,c_b}\,, \end{aligned}$$

$$
\begin{aligned}
Q'_{wx} &= \frac{\bar{Q}_{wx}}{\mu\, c_b\, h_b}\,, \\
Q'_{wy} &= \frac{\bar{Q}_{wy}}{\mu\, \sin\alpha_b\, c_b\, h_b}\,, \\
\tau'_x &= \frac{\tau^B_x}{\rho\, f_w\, \mu\, c_b^2}\,, \\
\tau'_y &= \frac{\tau^B_y}{\rho\, f_w\, \kappa\, c_b^2}\,, \\
\zeta' &= \frac{\bar{\zeta}}{\mu\, h_b}\,, \\
S'_{xx} &= \frac{S_{xx}}{\rho\, \mu\, c_b^2\, h_b}\,, \\
S'_{xy} &= \frac{S_{xy}}{\rho\, \mu\, \sin\alpha_b\, c_b^2\, h_b}\,, \\
S'_{yy} &= \frac{S_{yy}}{\rho\, \mu\, c_b^2\, h_b}\,.
\end{aligned}
$$

In the above we have not only chosen the nondimensionalization to try to make all quantities $\mathcal{O}(1)$, but we have also chosen it to capture some relevant parameters: L_x, L_y, μ, κ and the characteristic water depth, h_b, wave celerity, c_b, and wave angle $\sin\alpha_b$ at the breaking point. Furthermore, note that we divided similar variables such as Q_{wx} and Q_{wy} by different quantities, in order to accommodate for waves approaching the coast with a small angle of incidence ($\sin\alpha_b \ll 1$ and $\cos\alpha_b \simeq 1$). Finally, we introduce f_w as the bottom friction coefficient.

The scalars L_x and L_y are length scales that characterize the topographical variations in the x and y directions, respectively. For a bottom topography that varies weakly in the longshore direction we assume that $\frac{L_x}{L_y} \ll 1$, and for a longshore uniform coast we get $\frac{L_x}{L_y} = 0$. Thus, the ratio $\frac{L_x}{L_y}$ is an asymptotic parameter which can go to zero, or be $\mathcal{O}(1)$ in the situation of equal length scales of the bottom variations in the x and y directions (as on a beach with significant longshore variations). For a nearly plane beach the ratio $\frac{L_x}{L_y}$ can be simply related to the depth

gradient ratio by $\frac{L_x}{L_y} = \frac{\partial h}{\partial y}/\frac{\partial h}{\partial x}$. However, for a barred beach with rip-channels, the choice of the characteristic length scales, L_x and L_y, and their ratio is less obvious. This is discussed later.

An additional small parameter ν can be defined as

$$\nu = \frac{h_b}{L_x}\,, \tag{4.4}$$

which for a planar beach is equivalent to the bottom slope, h_x. Typical values are of the order 0.01-0.1.

The nondimensional parameter κ enters in the previous nondimensionalization and it is related with the longshore velocity by

$$V_{max} \sim \kappa \sqrt{g h_b}\,. \tag{4.5}$$

Laboratory and field data (Putnam *et al.*, 1949; Galvin and Eagleson, 1965; Visser, 1991; Reniers *et al.*, 1995) indicate that the parameter κ is essentially of $\mathcal{O}(\sin\alpha_b)$, but depends on several variables related to the wave and flow field. For example, a theoretical solution for steady uniform longshore currents (Longuet-Higgins, 1970b) shows that $\kappa \propto h_x \gamma \frac{\sin\alpha}{f_w}$. So, the parameter κ tends to zero for nearly normal incident waves or for h_x going to zero.

The parameter μ appearing in several of the nondimensional quantities above is a small coefficient, $\mu \sim 0.05 - 0.2$, which differs from the other small parameters in that it does not go to zero for known situations. The quantity μ replaces the parameter δ of the original POS derivation. A separate symbol is adopted here because, unlike in POS (see their equation (14)), we do not want to link μ (their δ) with κ: μ is a small number, whereas κ is an asymptotically small parameter. The parameter μ formally accounts for the smallness of several dimensionless flow variables: an example is $Q_{wx} = \mu c \frac{H^2}{h}$ with $\mu \sim 0.1 - 0.2$ (Svendsen, 1984a). Similarly, for typical

values of the undertow we expect $\frac{U}{c} = \mathcal{O}(0.05 - 0.1) = \mathcal{O}(\mu)$. For the maximum setup ζ_{max} at the shoreline, analysis of field data by Longuet-Higgins and Stewart (1963) have shown that $\frac{\bar{\zeta}_{max}}{h_b} \sim 0.15 = \mathcal{O}(\mu)$. This result is also confirmed by the theoretical analysis and laboratory data of Bowen *et al.* (1968), Stive and Wind (1982) and Okayasu (1989). Finally, for the longshore component of the radiation stress S_{xy} we find $S_{xy} \sim \frac{\gamma^2}{8}\,\rho \sin\alpha\, c^2\, h$, which means in this case $\mu \sim \frac{\gamma^2}{8} \simeq 0.06$. Hence, μ is a number that typically has a magnitude of $\mathcal{O}(10^{-1})$.

Substituting the nondimensional quantities and the parameter ν defined by (4.4) into the (steady-state) governing equations (4.1)–(4.3) then gives those equations in nondimensional form expressed in terms of the parameters $\frac{L_x}{L_y}$, ν, κ, $\sin\alpha_b$, and the number μ. For the continuity equation we get:

$$\frac{\partial}{\partial x'}\left(\overline{\int_{-h'_o}^{\zeta'} U'\,dz'} + Q'_{wx}\right) + \frac{L_x}{L_y}\frac{\kappa}{\mu}\frac{\partial}{\partial y'}\left(\overline{\int_{-h'_o}^{\zeta'} V'\,dz'} + \frac{\mu}{\kappa}\sin\alpha_b\, Q'_{wy}\right) = 0\,, \tag{4.6}$$

and for the x- and y-momentum equations we get, respectively,

$$\begin{aligned}
&\mu\frac{\partial}{\partial x'}\left(\overline{\int_{-h_o}^{\zeta'} U'^2\,dz'} + 2U'(\bar{\zeta}')\,Q'_{wx}\right)\\
&+\frac{L_x}{L_y}\kappa\frac{\partial}{\partial y'}\left(\overline{\int_{-h'_o}^{\zeta'} U'V'\,dz'} + \frac{\mu}{\kappa}\sin\alpha_b\,U'(\bar{\zeta}')\,Q'_{wy} + V'(\bar{\zeta}')\,Q'_{wx}\right)\\
&+h'\frac{\partial\bar{\zeta}'}{\partial x'} + \frac{\partial S'_{xx}}{\partial x'} + \frac{L_x}{L_y}\sin\alpha_b\frac{\partial S'_{yx}}{\partial y'} + \frac{f_w}{\nu}\tau'_x = 0\,,
\end{aligned} \tag{4.7}$$

$$\begin{aligned}
&\kappa\frac{\partial}{\partial x'}\left(\overline{\int_{-h_o}^{\zeta'} U'V'\,dz'} + V'(\bar{\zeta}')\,Q'_{wx} + \frac{\mu}{\kappa}\sin\alpha_b\,U'(\bar{\zeta}')\,Q'_{wy}\right)\\
&+\frac{L_x}{L_y}\frac{\kappa^2}{\mu}\frac{\partial}{\partial y'}\left(\overline{\int_{-h'_o}^{\zeta'} V'^2\,dz'} + \frac{\mu}{\kappa}\sin\alpha_b\,2V'(\bar{\zeta}')\,Q'_{wy}\right)\\
&+\frac{L_x}{L_y}h'\frac{\partial\bar{\zeta}'}{\partial y'} + \sin\alpha_b\frac{\partial S'_{xy}}{\partial x'} + \frac{L_x}{L_y}\frac{\partial S'_{yy}}{\partial y'} + \frac{\kappa}{\mu}\frac{f_w}{\nu}\tau'_y = 0\,,
\end{aligned} \tag{4.8}$$

This system of equations is equivalent to that of POS's equations (17)–(19) with δ replaced by μ. However, in contrast to the equations given in POS, the momentum equations here have been divided by a common factor, so that the relative

magnitude of the terms in the two equations remains the same.

4.1.1 Lower-order equations for nearly longshore uniform topographies

The nondimensional governing equations above can be simplified in different ways depending on the restrictions put on the parameters. In the following we will recover the analytical model given by POS. First, based on the previous assessments, we choose to consider situations where $\mathcal{O}(\nu) = \mathcal{O}(\kappa) = \mathcal{O}(\sin\alpha_b)$, so that all these asymptotic parameters can be represented simply by one of them (we choose ν). We also consider the friction parameter such that $\frac{\kappa}{\mu}\frac{f_w}{\nu} = \mathcal{O}(\sin\alpha_b)$, which results from the balance between the radiation stress component $\frac{\partial S_{xy}}{\partial x}$ and the bottom shear stress τ_y^B in the simplest longshore current model of Longuet-Higgins (1970b). For a nearly longshore uniform coast we typically have

$$\frac{L_x}{L_y} \ll 1\,, \tag{4.9}$$

hence we assume $\frac{L_x}{L_y} = \mathcal{O}(\nu)$. Introducing these assumptions into the governing equations (4.6)–(4.8) we can rewrite them in terms of two single parameters, ν and μ, the first going asymptotically to zero and second being just a small number of $\mathcal{O}(0.1)$. Therefore the continuity equation reads

$$\frac{\partial}{\partial x'}\left(\overline{\int_{-h'_o}^{\zeta'} U'\,dz'} + Q'_{wx}\right) + \frac{\nu^2}{\mu}\frac{\partial}{\partial y'}\left(\overline{\int_{-h'_o}^{\zeta'} V'\,dz'} + \mu\,Q'_{wy}\right) = 0\,, \tag{4.10}$$

and for the x- and y-momentum equations we get, reordering the terms by orders of magnitude,

$$\begin{aligned} & h'\frac{\partial\bar{\zeta}'}{\partial x'} + \frac{\partial S'_{xx}}{\partial x'} + \mu\left[\frac{\partial}{\partial x'}\left(\overline{\int_{-h_o}^{\zeta'} U'^2\,dz'} + 2U'(\bar{\zeta}')\,Q'_{wx}\right) + \tau'_x\right] \\ + \;& \nu^2\left[\frac{\partial}{\partial y'}\left(\overline{\int_{-h'_o}^{\zeta'} U'V'\,dz'} + V'(\bar{\zeta}')\,Q'_{wx}\right) + \frac{\partial S'_{yx}}{\partial y'}\right] \\ + \;& \nu^2\,\mu\frac{\partial}{\partial y'}\left(U'(\bar{\zeta}')\,Q'_{wy}\right) = 0\,, \end{aligned} \tag{4.11}$$

$$\nu \left[\frac{\partial}{\partial x'} \left(\overline{\int_{-h_o}^{\zeta'} U'V' \, dz'} + V'(\bar{\zeta}') \, Q'_{wx} \right) + h' \frac{\partial \bar{\zeta}'}{\partial y'} + \frac{\partial S'_{xy}}{\partial x'} + \frac{\partial S'_{yy}}{\partial y'} + \tau'_y \right]$$
$$+ \nu \mu \frac{\partial}{\partial x'} \left(U'(\bar{\zeta}') \, Q'_{wy} \right) + \frac{\nu^3}{\mu} \frac{\partial}{\partial y'} \left(\overline{\int_{-h'_o}^{\zeta'} V'^2 \, dz'} \right)$$
$$+ \nu^3 \frac{\partial}{\partial y'} \left(2V'(\bar{\zeta}') \, Q'_{wy} \right) = 0 \, . \tag{4.12}$$

Under these constraints we notice that the largest terms in the x-momentum equation (4.11) are one order of magnitude larger than the leading order terms in the y-momentum equation (4.12). This shows that for small angles of incidence and for $L_x \ll L_y$ the forces in the cross-shore direction are much larger than the longshore forces. For this situation POS proposed a simplified model which retained only the leading order terms of each equation. We then get (in dimensional variables) for the continuity equation:

$$\frac{\partial}{\partial x} \left(\overline{\int_{-h_o}^{\zeta} U \, dz} + Q_{wx} \right) = 0 \, , \tag{4.13}$$

and for the x and y-momentum equations:

$$g \, (h_o + \bar{\zeta}) \frac{\partial \bar{\zeta}}{\partial x} + \frac{1}{\rho} \frac{\partial S_{xx}}{\partial x} = 0 \, , \tag{4.14}$$

$$\frac{\partial}{\partial x} \left(\overline{\int_{-h_o}^{\zeta} UV \, dz} + V(\bar{\zeta}) \, Q_{wx} \right)$$
$$+ \frac{1}{\rho} \left(\frac{\partial S_{xy}}{\partial x} + \frac{\partial S_{yy}}{\partial y} \right) + \frac{\tau_y^B}{\rho} + g \, (h_o + \bar{\zeta}) \frac{\partial \bar{\zeta}}{\partial y} = 0 \, . \tag{4.15}$$

which is equivalent to equations (25)–(27) in POS except for the S_{yy} term in equation (4.15) that was left out.

By retaining only the terms of $\mathcal{O}(1)$ in the x-momentum equation (4.11) POS neglected the terms of $\mathcal{O}(\mu)$ in that equation, which is likely to be of the order of the leading terms in the y-momentum equation (4.12), which are of $\mathcal{O}(\nu)$. Consequently, these two equations are solved with different orders of accuracy.

Secondly, we notice that at the leading order shown in (4.13) the simplified continuity equation yields a solution of zero net averaged volume flux ($\bar{Q}_x = 0$) for a zero cross-shore flux boundary condition at the shoreline. Thus, at this order, the local short-wave averaged volume flux is completely balanced by the undertow return current. However, as mentioned in POS, an approximation for the second term on the left-hand-side of equation (4.6) can be determined and provide a correction to the first order flow. This is done by using the solution of equation (4.15) to calculate $\frac{\partial V}{\partial y}$, and hence the second term in the complete continuity equation (4.6). Then $\bar{Q}_x$ can be determined through the integration of that same equation yielding to second order (in dimensional form):

$$\bar{Q}_x = \overline{\int_{-h_o}^{\zeta} U\, dz} + Q_{wx} = -\int_0^x \frac{\partial}{\partial y}\left(\overline{\int_{-h_o}^{\zeta} V\, dz} + Q_{wy}\right) dx' \,, \tag{4.16}$$

where the boundary condition $\bar{Q}_x(0, y) = 0$ has been used. Note that the $\bar{Q}_x$ found this way is a second order quantity satisfying the boundary condition of no flux at the shore and equation (4.1) for the conservation of mass.

Lastly, based on the findings about the dispersive mixing effect due to depth-varying currents (Svendsen and Putrevu, 1994), POS introduces the following approximation for the first term of the longshore momentum equation (4.15):

$$\frac{\partial}{\partial x}\left(\overline{\int_{-h_o}^{\zeta} UV\, dz} + V(\bar{\zeta})\, Q_{wx}\right) = \frac{\partial}{\partial x}\left(D_c h \frac{\partial \tilde{V}}{\partial x}\right) \tag{4.17}$$

where D_c is a dispersion coefficient, which varies in the cross-shore direction, and $\tilde{V}$ is the depth-averaged longshore current. Svendsen and Putrevu (1994) estimated that inside the surf zone D_c could be given by:

$$D_c \simeq 0.2\, h_o \sqrt{g\, h_o}\,. \tag{4.18}$$

Therefore, the model equation (4.14) is solved to determine the setup $\bar{\zeta}$, and equation (4.15) with the first term represented by equation (4.18) is used to calculate the depth-averaged longshore current $\tilde{V}$.

4.1.2 Consistent lower-order model equations

It will be shown in a following section that the Putrevu *et al.* (1995) model can give inaccurate predictions even at the lowest order. Hence, a new extension of this model is presented which consistently includes all terms of the same order, and it is shown that the results of this revised model compare favorably with the complete SHORECIRC's solution.

A model that retains all the terms in the governing equations correct to $\mathcal{O}(\mu)$ and $\mathcal{O}(\nu, \kappa)$, instead of retaining only the terms of $\mathcal{O}(\nu, \kappa)$ as in POS, is given below. This arises from the recognition that μ is really not asymptotically small, but in many cases still small enough to make $\frac{\nu^2}{\mu}$ in the continuity equation (4.10) of the same magnitude as other ν-terms.

Thus, we consider a revised model consisting of the following equations:

$$\frac{\partial(\tilde{U}h)}{\partial x} + \frac{\partial(\tilde{V}h)}{\partial y} = 0\,, \tag{4.19}$$

$$\frac{\partial(\tilde{U}^2h)}{\partial x} + g\,(h_o + \bar{\zeta})\,\frac{\partial\bar{\zeta}}{\partial x} + \frac{1}{\rho}\,\frac{\partial S_{xx}}{\partial x} + \frac{\tau_x^B}{\rho} = 0\,, \tag{4.20}$$

$$\begin{aligned}\frac{\partial(\tilde{V}\tilde{U}h)}{\partial x} &+ \frac{\partial}{\partial x}\left(D_c h\frac{\partial\tilde{V}}{\partial x}\right) + g\,(h_o + \bar{\zeta})\,\frac{\partial\bar{\zeta}}{\partial y} \\ &+ \frac{1}{\rho}\left(\frac{\partial S_{xy}}{\partial x} + \frac{\partial S_{yy}}{\partial y}\right) + \frac{\tau_y^B}{\rho} = 0\,.\end{aligned} \tag{4.21}$$

These equations essentially correspond to the addition of the cross-shore bottom shear stress and the cross-shore nonlinear advective acceleration terms which, according to equation (4.11), both have a magnitude of μ times the leading terms. To be consistent we have also included the term of $\mathcal{O}(\frac{\nu^2}{\mu})$ in the continuity equation (4.10), which is the second term in equation (4.19) above. Note that the first term

of equation (4.21) is already included in the POS model equation (4.15), although it turns out to be zero because $\tilde{U} = 0$ at first order in the perturbation scheme followed in the POS model.

The model given by equations (4.19)–(4.21) is referred to herein as the extended (POS) model. Although the terms added in this model equations (relative to those of POS) are small, they are of the same order as some of the retained terms in the longshore momentum balance and thus can be important under certain physical conditions as shown later.

4.1.3 Simplified SHORECIRC model

In the following sections we present a comparison between the results of (i) the POS model (see equations (4.14), (4.15)); (ii) the extended model (given by (4.19)–(4.21)); and (iii) the results of a simplified version of the full SHORECIRC model as follows. Rewritten in terms of $(\tilde{U}, \tilde{V})$, this version essentially corresponds to the nonlinear shallow-water equations with dispersive mixing, which reads:

$$\frac{\partial \bar{\zeta}}{\partial t} + \frac{\partial (\tilde{U}h)}{\partial x} + \frac{\partial (\tilde{V}h)}{\partial y} = 0\,, \tag{4.22}$$

$$\begin{aligned} \frac{\partial \tilde{U}h}{\partial t} &+ \frac{\partial (\tilde{U}^2 h)}{\partial x} + \frac{\partial (\tilde{U}\tilde{V}h)}{\partial y} \\ &+ g\,(h_o + \bar{\zeta})\,\frac{\partial \bar{\zeta}}{\partial x} + \frac{1}{\rho}\left(\frac{\partial S_{xx}}{\partial x} + \frac{\partial S_{yx}}{\partial y}\right) + \frac{\tau_x^B}{\rho} = 0\,, \end{aligned} \tag{4.23}$$

$$\begin{aligned} \frac{\partial \tilde{V}h}{\partial t} &+ \frac{\partial (\tilde{V}\tilde{U}h)}{\partial x} + \frac{\partial (\tilde{V}^2 h)}{\partial y} + \frac{\partial}{\partial x}\left(D_c h \frac{\partial \tilde{V}}{\partial x}\right) \\ &+ g\,(h_o + \bar{\zeta})\,\frac{\partial \bar{\zeta}}{\partial y} + \frac{1}{\rho}\left(\frac{\partial S_{xy}}{\partial x} + \frac{\partial S_{yy}}{\partial y}\right) + \frac{\tau_y^B}{\rho} = 0\,. \end{aligned} \tag{4.24}$$

This system is derived from the original model equations (4.1)–(4.3) by neglecting the turbulent and surface shear stresses. In order to be able to compare

with the POS model we have also assumed that the only contribution from the depth-varying velocities is given as in that model. Thus, by keeping only the same dispersive term as in the POS model, we focus the comparison between the two models on the effect of the second order terms that depend only on the depth-averaged quantities. This model is in this chapter referred to as SHORECIRC model, although the equations (4.22)–(4.24) only represent a simplified version of that model. Since the numerical model SHORECIRC is time-dependent we continue the computations until it reaches steady-state.

In order to establish a relevant basis for comparing the circulation models it has been assumed that the short-wave forcing for both models is given by the same simplified wave height calculation used in POS, even though this may not always be realistic. Hence, we use the energy equation $\frac{\partial}{\partial x}(E\,c_g) = D$ with the energy dissipation rate determined as that in a bore. Similarly, we use the linear bottom shear stress relation $\tau_\alpha^B = \rho\, f_w\, u_0\, V_\alpha$ as in POS, with $f_w = 0.01$ in all computations except when otherwise mentioned.

For simplicity POS further assumed that all the longshore bottom perturbations occur inside the surf zone region only. The bottom variation is divided into

$$h_o(x,y) = h_{oL}(x) + \epsilon h_1(x,y)\,, \tag{4.25}$$

where ϵ is a small parameter, ($\epsilon \ll 1$), and h_{0L} stands for a longshore uniform depth. For both applications in this paper we restrict the longshore bottom perturbation to the form

$$h_1(x,y) = h_{0L}(x)\, F_x(x)\, F_y(y)\,, \tag{4.26}$$

where $F_x(x)$ and $F_y(y)$ are arbitrary functions. In the following two sections we apply the model equations described in this section to study the nearshore currents

over a quasi-planar beach and a barred beach. All of the above models are solved numerically through the finite difference method given in chapter 3.

4.2 Currents on a nearly plane beach

In the first example we compare the results of the simplified POS model to the results obtained by the more complete SHORECIRC for the nearshore currents over a slightly modified plane beach. This is the same example that was used in POS with a topography given by a sinusoidally longshore varying plane beach. The deviation from the plane beach with a 1/30 slope is characterized by the depth variation parameter ϵ defined in equation (4.25), and is confined to the surf zone. For the current application the depth as defined in equation (4.25) reads:

$$h_{0L}(x') = h_b + h_x(x' - x'_b)\,, \tag{4.27}$$

$$h_1(x', y) = h_{0L}\,\exp\left[-5\left(\frac{x' - x'_M}{x'_M}\right)^2\right]\,\sin\left(\frac{2\pi y}{l_y} + \frac{\pi}{2}\right)\,, \tag{4.28}$$

where $h_x = 1/30$ is the cross-shore depth gradient, the subscript b refers to the breaking point, x' stands for the seaward oriented cross-shore direction with origin at the shore, and x'_M is the the position of the maximum bottom perturbation amplitude. The parameters l_x and l_y are the cross-shore and longshore computational domain lengths, respectively. For the following computations we have chosen $x'_M = \frac{x'_b}{2}$, $x'_b = 30h_b$, $l_x = 3x'_b = 90h_b$, and $l_y = 180h_b$. To obtain good computational accuracy the grid spacings in the cross-shore and longshore directions are $\triangle x = h_b$ and $\triangle y = 2h_b$, respectively.

Fig. 4.1 shows the bottom contours for the bathymetry defined above, with a depth variation parameter of $\epsilon = 0.1$. At a constant cross-shore position, the water depth is the largest at $y = 0$ and $y = l_y$, and the smallest at the middle section $y = l_y/2$. The $(x, y) = (0, 0)$ is the seaward-upstream boundary point in the model

domain. $x = 0$ is the seaward boundary, where the absorbing-generating boundary condition is used. We also impose $\tilde{V} = 0$ at that boundary, in order to find a solution to the POS model equation (4.15). The shoreline boundary is at $x/l_x = 1$, where we follow POS and use a zero velocity condition $\tilde{U} = \tilde{V} = 0$. Finally, for the numerical solution, we use periodicity at the cross-shore boundaries $y = 0$ and $y = l_y$. This means we basically simulate an infinite coast with a spatially periodic domain.

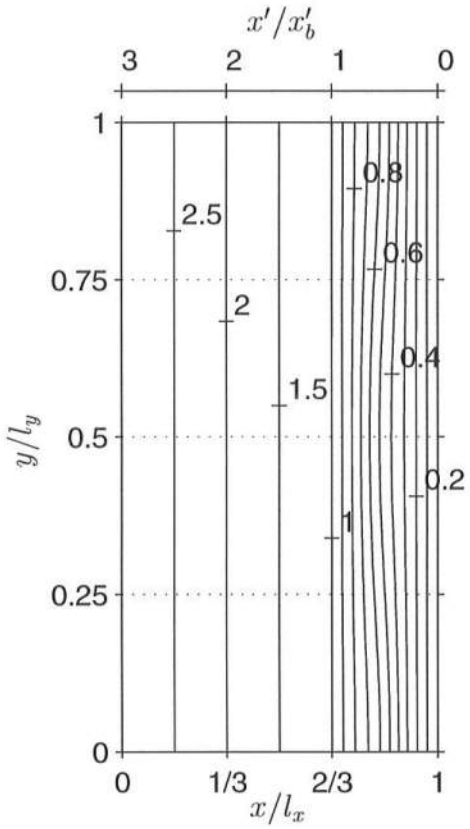

Figure 4.1: Depth contours of the nearly plane beach for a longshore depth variation parameter $\epsilon = 0.1$.

The ratio of the characteristic length scales L_x and L_y can be clearly identified for a nearly plane beach in function of the depth gradients as $L_y/L_x = \frac{\partial h}{\partial x}/\frac{\partial h}{\partial y}$. Using equations (4.25)–(4.28) the maximum depth gradients can be estimated as $h_x = \frac{h_b}{x'_b}$

and $h_y = \epsilon\, h_0(x'_M)\,\frac{2\pi}{l_y}$. Hence for the present choice of values, the above depth gradients are related by $h_x = \frac{6}{\pi\,\epsilon}\,h_y$, which for $\epsilon = 0.1$ yields $L_y/L_x = 20$. This ratio indicates that the basic assumption of the POS model $L_x \ll L_y$ is valid.

In Fig. 4.2 (top panel) we show the normalized wave height variation, $\frac{H}{H_b}$, inside the surf zone against the normalized cross-shore location, $\frac{x'}{x'_b}$, at four longshore locations ($y = 0$, $y = \frac{l_y}{4}$, $y = \frac{l_y}{2}$, $y = \frac{3l_y}{4}$) for the depth variation parameter $\epsilon = 0.1$. The bottom panel of Fig. 4.2 shows the bottom variation at the same longshore positions. The wave height to water depth ratio at breaking is $\gamma = 0.5$, and the short wave period is $T = 15.66\sqrt{h_b/g}$, which corresponds to $T = 5$ s for $h_b = 1$ m. The results show that at the position of the crest ($y = \frac{l_y}{2}$) of the longshore bottom perturbation, where the water depth is smaller, the energy dissipation by breaking is larger than at the other sections and thus the wave height is smaller. The inverse happens at $y = 0$.

Fig. 4.3 and 4.4 show the results of the comparison between the steady-state solution of SHORECIRC and POS of setup and longshore current variation for an incident wave angle $\alpha_b = 5°$, and bottom friction coefficient $f_w = 0.01$. Fig. 4.3 shows the setup $\bar{\zeta}$ (top panel) and longshore current $\tilde{V}$ (bottom panel) predictions at the same four longshore positions as the wave height distribution ($y = 0$, $y = \frac{l_y}{4}$, $y = \frac{l_y}{2}$, $y = \frac{3l_y}{4}$). The lines correspond to the results of POS model, and the symbols correspond to SHORECIRC results. Both models predict the same qualitative variation of the setup: higher setup in the shallower depth at $y = \frac{l_y}{2}$ and lower setup in the deeper longshore location at $y = 0$. The longshore surface elevation gradient, $gh\frac{\partial\bar{\zeta}}{\partial y}$, is nearly the same in both models, but a higher mean setup is predicted by SHORECIRC at all longshore locations. This turns out to be due to the contribution of second-order terms in the x-momentum equation (4.11) as explained later. The largest second-order term in the x-momentum equation is

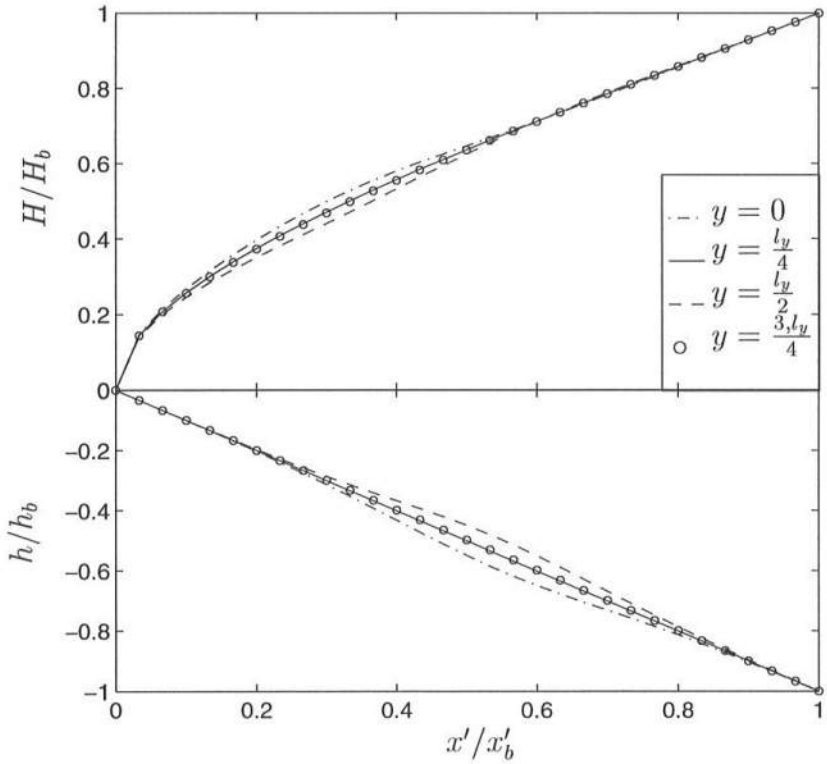

Figure 4.2: Wave height and bottom cross-shore variations over the nearly plane beach for a depth variation parameter $\epsilon = 0.1$. The four longshore positions are $y = 0$, $y = \frac{l_y}{4}$, $y = \frac{l_y}{2}$, $y = \frac{3l_y}{4}$ (see Figure 4.1 for depth contours).

the bottom shear stress, τ_x^B, which acts in the same direction as the cross-shore component of the wave radiation stress. Thus, as τ_x^B reinforces $\frac{\partial S_{xx}}{\partial x}$, the cross-shore pressure gradient term is larger in the presence of τ_x^B (given by SHORECIRC results) than its value when τ_x^B is neglected (as given by POS results). The resulting larger cross-shore pressure gradient then induces a higher overall mean setup.

In the bottom panel of Fig. 4.3 we see that both models predict a significant deviation from a longshore uniform current profile. This is mainly due to the effect of the longshore pressure gradient. The maximum and minimum of the longshore

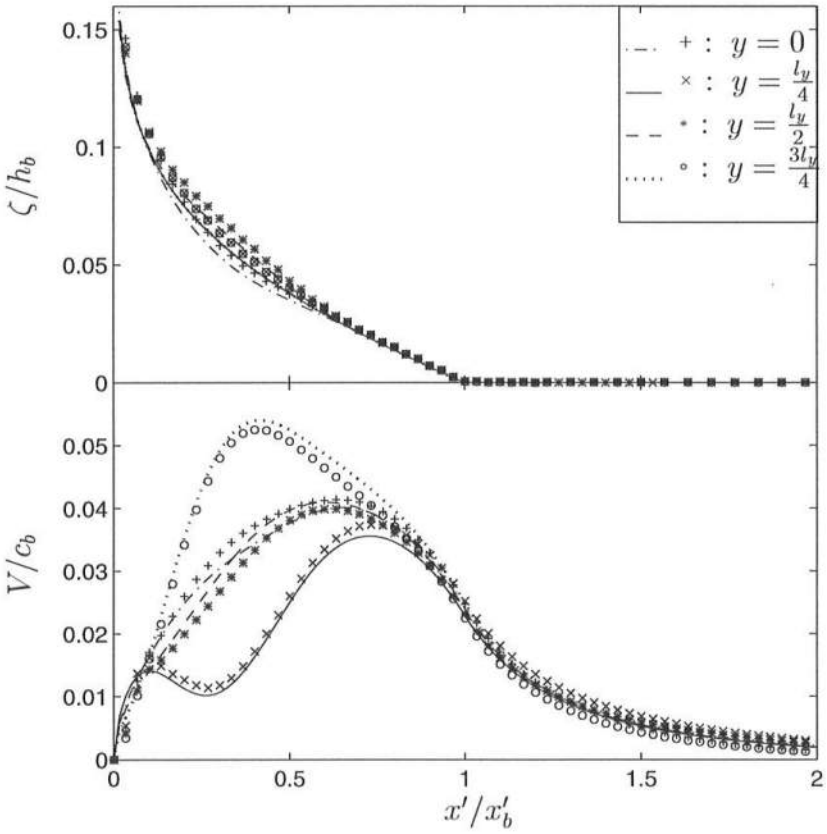

Figure 4.3: Comparison between the POS model (lines) and the SHORECIRC model results (symbols) for a depth variation parameter $\epsilon = 0.1$ and incident wave angle $\alpha_b = 5°$. The four longshore positions are $y = 0$, $y = \frac{l_y}{4}$, $y = \frac{l_y}{2}$, $y = \frac{3l_y}{4}$. Top panel: mean surface elevation $\bar{\zeta}$; bottom panel: depth-averaged longshore currents $\tilde{V}$.

currents are slightly overpredicted by the POS model, relative to the predictions of SHORECIRC, but the overall good agreement indicates that, in this case, the simplified POS model include all the important terms of the governing equations. A careful analysis of the differences between the two models indicates, however, that at $y = 0$ and $y = \frac{l_y}{2}$ the longshore pressure gradient is zero in both models and the observed differences between the two model predictions are due to an inertial effect of the nonlinear accelerations.

In Fig. 4.4a and 4.4b we show the resulting spatial distribution of the depth-averaged velocity vectors, $\vec{V}$, as predicted by the POS model and the SHORECIRC model, respectively. These figures give an overview of the flow and the effect of the longshore pressure gradient. Closer inspection of the longshore currents estimated by both models shows that SHORECIRC's results are more longshore uniform than those from the POS model. Also, there is a longshore phase shift of the current extrema predicted by SHORECIRC relative to the POS model calculation: the maximum (and minimum) longshore currents shoreward of x_b' predicted by SHORECIRC are shifted downstream relative to that predicted by the POS model. These results confirm the earlier findings of Wu and Liu (1984) on the uniformizing effect of the nonlinear convective accelerations.

We also performed similar tests for stronger longshore sinusoidal bottom perturbations, with the depth variation parameter $\epsilon = 0.2$ and $\epsilon = 0.3$, and for larger angles of incidence, such as $\theta_b = 20°$. The agreement between the two models for this larger angle is similar to that found for the case of $\theta_b = 5°$. These tests showed that the deviation between the POS model and the SHORECIRC in the prediction of the mean surface elevation $\bar{\zeta}$ are relatively independent of ϵ and θ_b, and are caused mainly by neglecting the bottom shear stress in the x–momentum equation in the POS model. Conversely, the differences in the estimation of $\tilde{V}$ grow

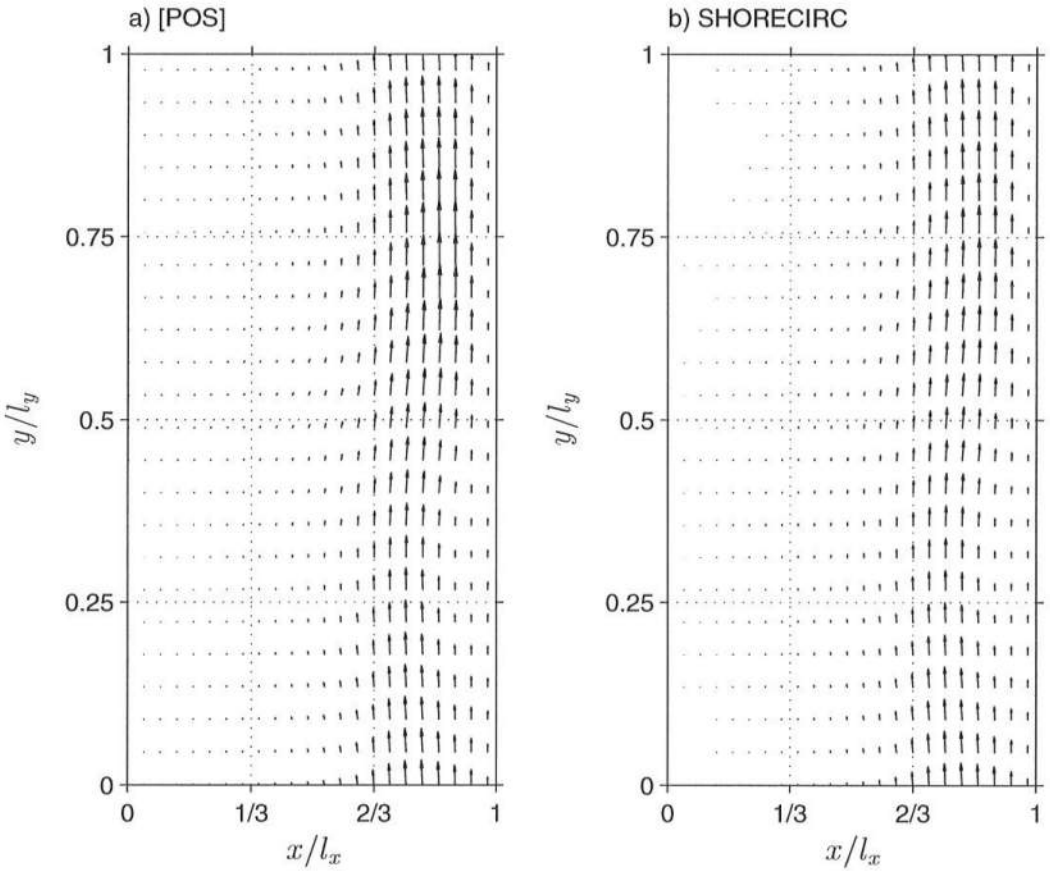

Figure 4.4: Depth-averaged current vectors $\vec{V}$ over the nearly plane beach for a depth variation parameter $\epsilon = 0.1$ and incident wave angle $\alpha_b = 5°$: (a) POS model results; (b) SHORECIRC model results.

both with increasing ϵ and decreasing θ_b.

In Fig. 4.5 we present the comparison between the depth-averaged current vectors, $\vec{V}$, determined by the modified POS and SHORECIRC models for a bottom perturbation $\epsilon = 0.3$, which implies that $L_y/L_x \approx 6$, and an incident wave angle $\alpha_b = 5°$. Although $\epsilon = 0.3$ is not small, it is noted that the current pattern predicted by the two models is quite similar. Both models show a relatively strong backwards current in a region near the shore (see Fig. 4.1 for similar topography). However, one can also see that the extrema are slightly accentuated in the POS solution.

In conclusion, for a nearly planar beach with a longshore sinusoidal modulation the results indicate that even for a relatively large longshore bottom variation parameter ($\epsilon = 0.3$) the POS model performs well against the SHORECIRC model. The POS model includes the longshore pressure gradient term, $gh\frac{\partial \bar{\zeta}}{\partial y}$, and the longshore gradient of the longshore radiation stress, $\frac{\partial S_{yy}}{\partial y}$, which can be fairly important in the estimation of the longshore currents. The nonlinear advective accelerations, and the bottom shear stress in the x–momentum direction are formally second-order terms that can locally cause the linear solution of POS to deviate from the solution of the complete nonlinear shallow water equations.

4.3 Currents on a nearly longshore uniform barred beach

As a second example we analyze the nearshore currents over a longshore varying barred beach. The longshore bottom perturbation is characterized by a slight depression in the bar crest, similar to the formation of a rip-channel. The bottom topography used in the present example is analogous to that used by Sancho *et al.* (1995), except that the rip-channel is smaller, and it is also similar to the barred beach often encountered at the FRF experimental station in Duck, NC (see,

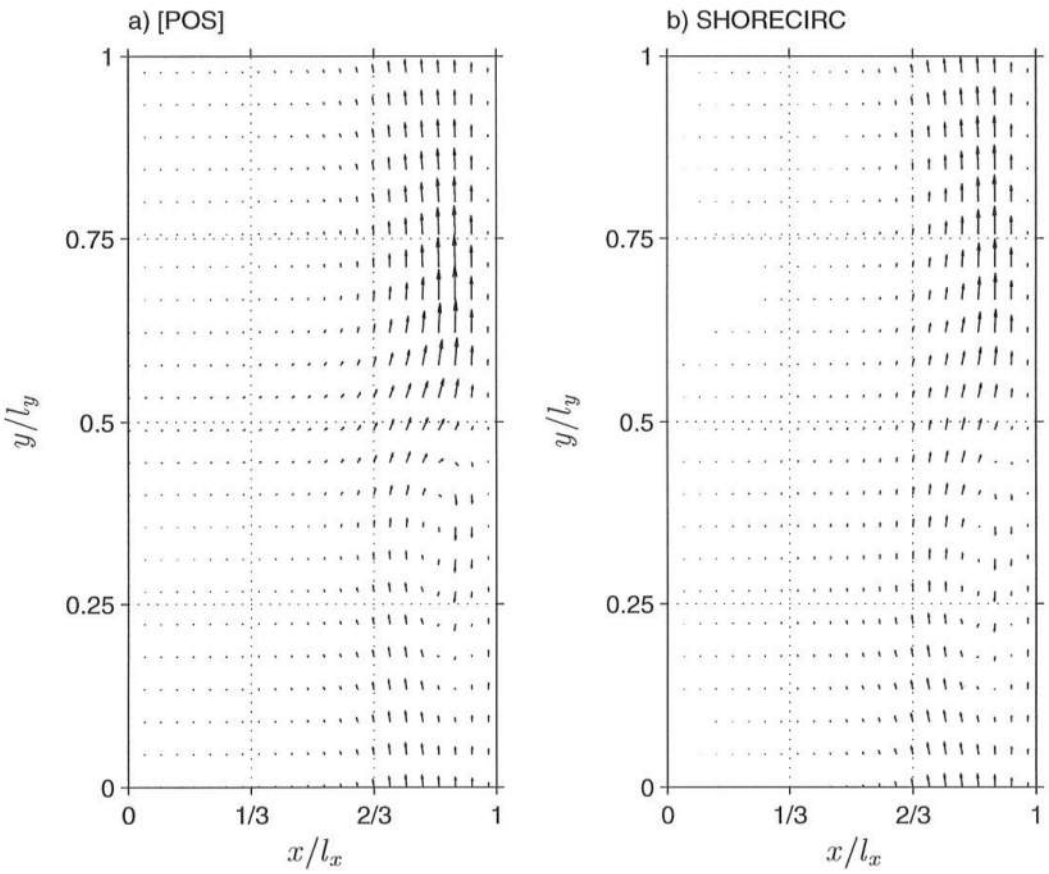

Figure 4.5: Depth-averaged current vectors $\vec{V}$ over the nearly plane beach for a depth variation parameter $\epsilon = 0.3$ and incident wave angle $\alpha_b = 5°$: (a) POS model results; (b) SHORECIRC model results.

e.g., Thornton and Kim, 1993; Reniers *et al.*, 1995). By curve fitting to measured bathymetric profiles at that beach, the depth of the longshore uniform section of the beach can be given by the following analytical expression:

$$h_{0L}(X') = \begin{cases} 0.55\, l_c^{0.35}\,(X' - \frac{10}{l_c})^{0.35} - F_1\,, & 0.125 \le X' \le \frac{l_x}{l_c} \\ h_{0L}\,|_{X'=0.125} \; -0.06\, l_c\,(\frac{15}{l_c} - X') - F_1\,, & 0 \le X' < 0.125 \end{cases} \tag{4.29}$$

with

$$F_1 = \frac{l_c}{150}\left(\frac{30}{l_c} + X'\right) \exp\left[-15\left(\frac{1 - X'}{1 - \frac{l_x}{l_c}}\right)^2\right], \tag{4.30}$$

where $X' = \frac{x'}{l_c}$ is a normalized seaward oriented cross-shore coordinate with origin at the shoreline, l_c is the bar crest position relative to the shoreline, and l_x is the cross-shore domain length. For the following computations we use $l_c = 120$ m, $l_x \simeq 3.17\, l_c$ (380 m), and $l_y \simeq 3.33\, l_c$ (400 m). The depth at the crest of the bar is $h_c \simeq 1.18$ m, and the numerical grid spacings are $\triangle x \simeq 4.24 h_c$ (5 m) and $\triangle y \simeq 8.48 h_c$ (10 m).

The longshore topography-variation functions F_x and F_y, defined in equation (4.26), are given by:

$$F_x(x') = \exp\left[b\left(\frac{x'_M - x'}{x'_M}\right)^2\right], \tag{4.31}$$

$$F_y(y) = \operatorname{sech}\left[a\left(y - \frac{l_y}{2}\right)\right], \tag{4.32}$$

with $x'_M \simeq 0.92\, l_c$ (110 m) and $b = -12$. Several topographies are examined with different values of a.

A perspective view of the beach configuration for the example with $\epsilon = 0.1$ is shown in Fig. 4.6. (As before, ϵ is the parameter controlling the strength of the longshore bottom perturbation). The rip-channel is located at $y = \frac{l_y}{2}$ and across the bar crest. As a further illustration, the bottom panel of Fig. 4.7 shows the cross-shore profiles of the barred beach at the longshore straight section, $y = 0$,

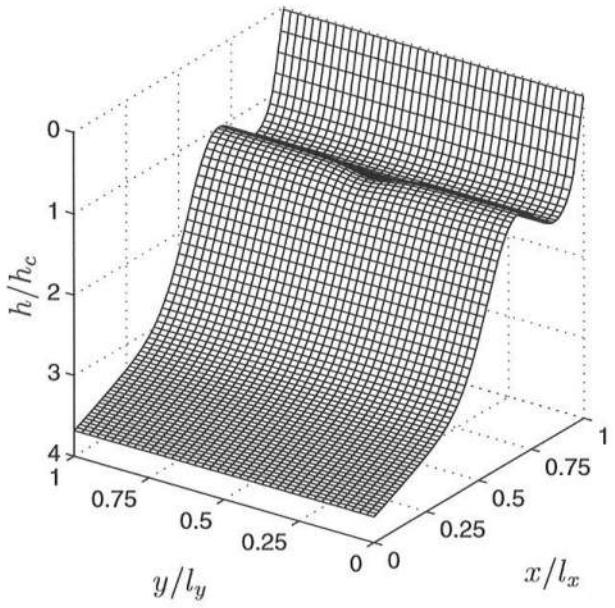

Figure 4.6: Perspective view of the longshore varying barred beach for a longshore depth variation parameter $\epsilon = 0.1$, and $a = \frac{4.8}{l_c}$ corresponding to $L_y \simeq 2.5\, L_x$.

and at the rip-channel, $y = \frac{l_y}{2}$. The maximum absolute longshore depth variation is $\triangle h = 0.1\, h\, |_{x'_M} \simeq 0.1 h_c$ at $x' = x'_M$. Physically, this corresponds to a very small bottom variation over a reasonable longshore length scale: in a typical case (at Duck) with $h_c = 1.2$ m the absolute longshore depth variation of the rip-channel is only $\triangle h \simeq 0.12$ m, which is of the same height or even smaller than that of a sand mega-ripple.

In order to discuss the applicability of the POS model it is convenient to briefly discuss the length scales associated with this bathymetry. The width w_r of the rip-channel is dependent on the parameter a in equation (4.32). From F_y we can define a characteristic longshore length scale L_y based on the maximum longshore depth gradient and vertical extent of bottom variation. The result gives $L_y = \frac{2}{a}$,

hence the width of the rip-channel is defined as $w_r = 2L_y$. For the example shown in Figure 4.6 we have chosen $a = \frac{4.8}{l_c}$, which implies $L_y \simeq 0.42 l_c$. The cross-shore length scale L_x can be defined in multiple ways. The crest-to-trough distance (roughly $l_c/2$), or the surf zone width (x_b') are two examples. However, to be consistent with the definition for L_y we can also define L_x based on the depth variation of the rip-channel and the cross-shore depth gradient in that region, which gives $L_x \simeq 1.67\,\epsilon\, l_c$. Hence, for $\epsilon = 0.1$ that gives $L_x \simeq 0.17 l_c$ and so the horizontal length scales are related by $L_y \simeq 2.5 L_x$. Note that we chose the length scales consistently, but if we had chosen L_x as the crest-to-trough distance ($\sim 0.5 l_c$) then we would have obtained $L_y \simeq L_x$.

The assessments above indicate that the bathymetry with $a = \frac{4.8}{l_c}$ has a ratio of length scales given by $1 < \frac{L_y}{L_x} < 2.5$, depending on the definition for L_x. Hence, it does not strictly satisfy the requirement of the POS model that $L_y \gg L_x$, although it has a minor longshore depth variation (~ 0.12 m) over a large longshore distance (~ 100 m). This topography is relevant, however, since we are interested in determining the applicability of the POS model for a realistic barred beach.

Again, the wave conditions have been chosen so that the breaker line is longshore uniform seaward of the bar crest as shown by the dashed line in Fig. 4.7. The important variables are $x_b' \simeq 1.42\, l_c$ (170 m), $\frac{x}{l_x} = 0.55$, $h_b \simeq 1.78 h_c$ (2.1 m) and $H_b = 0.5\, h_b$. The wave height variation along two cross-shore sections at $y = 0$ and $y = \frac{l_y}{2}$, for an incident short wave of period $T = 14.4\sqrt{h_c/g}$ (5 s), is given in the top panel of Fig.4.7. Note that the wave height decays rapidly over the bar-crest, and then remains nearly constant over the bar-trough until it reaches shallower depths, where strong energy dissipation again occurs. Thus, the radiation stresses forcing is strong over the bar-crest and at the beach face, and very weak over the trough.

In the computations of the longshore currents over this beach the dispersion coefficient used is slightly different from the one given by equation (4.18). In order

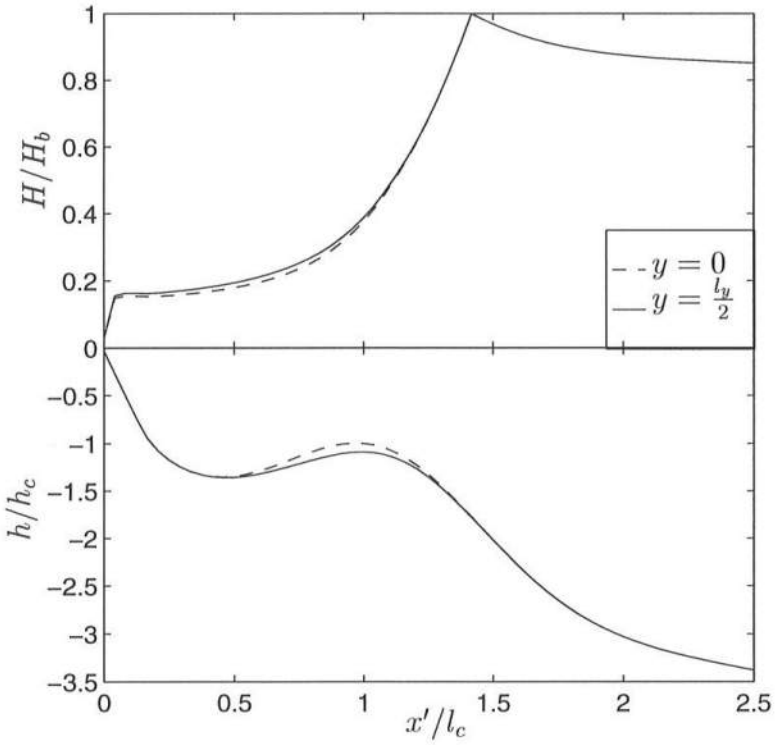

Figure 4.7: Wave height and bottom cross-shore variations over the barred beach at two longshore positions ($y = 0$, $y = \frac{l_y}{2}$), for a depth variation parameter $\epsilon = 0.1$, and $a = \frac{4.8}{l_c}$, $L_y \simeq 2.5\, L_x$.

to represent the fact that the vertical variation of the currents is smaller outside the surf region we use an empirical distribution that decays outside the breaking point (similar to the one for the eddy viscosity given by equation (2.84)):

$$D_c = \begin{cases} D_{cb}\left[0.2 + 0.8\left(\frac{h_b}{h}\right)^2\right], & x' > x'_b \\ 0.1\, h\sqrt{g\, h}\,, & x' \leq x'_b \end{cases} \tag{4.33}$$

with D_{cb} the dispersion coefficient at breaking, $x' = x'_b$. Note that to get realistic vertical profiles for the barred beach, in the computation of the dispersive mixing we have reduced the coefficient 0.2 in equation (4.18) to 0.1. The bottom friction coefficient used for these computations is $f_w = 0.01$.

The spatial distribution of the depth-averaged velocity vectors, as predicted by the POS and the SHORECIRC models, for an incident wave angle $\alpha_b = 5°$, is presented in Fig. 4.8. We see that contrary to the first example, the current patterns calculated by the two models for the present topography are surprisingly different from each other. The modified POS model (with the second order correction for $\bar{Q}_x$) predicts a strong rip current of $U_{max} \simeq 3\,\mathrm{ms}^{-1}$, whereas SHORECIRC estimates $U_{max} = 0.06\,\mathrm{ms}^{-1}$ only. The strong rip predicted by the POS model results from the concentration of mass flux at the rip-channel, caused by longshore flowing currents towards that location. The SHORECIRC results in Fig. 4.8b show longshore currents that dominate over the cross-shore currents, and are nearly longshore uniform. At the rip-channel and slightly downstream of it there is a noticeable cross-shore current component, but it does not resemble a rip-current.

In Fig. 4.9 we present the results of the POS model without the (second order) correction for $\bar{Q}_x$. Comparing Fig. 4.9 and 4.8a with 4.8b we can conclude that both versions of the POS model give results that are radically different from the results of the more complete SHORECIRC model. Furthermore, the values of

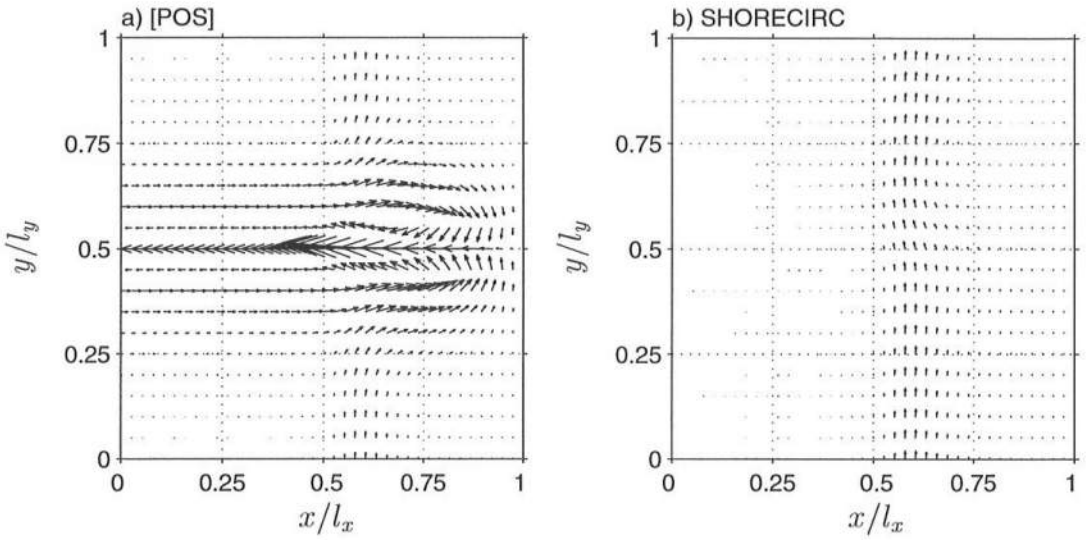

Figure 4.8: Depth-averaged current vectors $\vec{V}$ over the barred beach for a depth variation parameter $\epsilon = 0.1$, $a = \frac{4.8}{l_c}$, $L_y \simeq 2.5\, L_x$, and incident wave angle $\alpha_b = 5°$: (a) POS model results; (b) SHORECIRC model results.

$\frac{\partial \bar{Q}_y}{\partial y}$ calculated from the POS solution are not small as the nondimensional equation (4.10) suggests.

Inspection of the setup predictions for the present computations (see top panel of Fig. 4.10) shows that the POS model predicts a setup that varies somewhat in the longshore direction, which results in a longshore pressure gradient much stronger than that of the SHORECIRC model. In the latter, the setup is mostly longshore uniform. This is better illustrated in Fig. 4.11 (top panel) which shows the longshore variation of the setup at $x' = 0.294 x'_b$. The equivalent variation of the longshore currents at the same cross-shore location is shown in Fig. 4.11 (bottom panel), and we see that the strong pressure gradients in POS cause a reversion of the longshore currents on the downstream side of the rip-channel, whereas SHORECIRC results are unidirectional and nearly longshore uniform. It turns out that the differences in the setup calculations are all due to the different cross-shore momentum

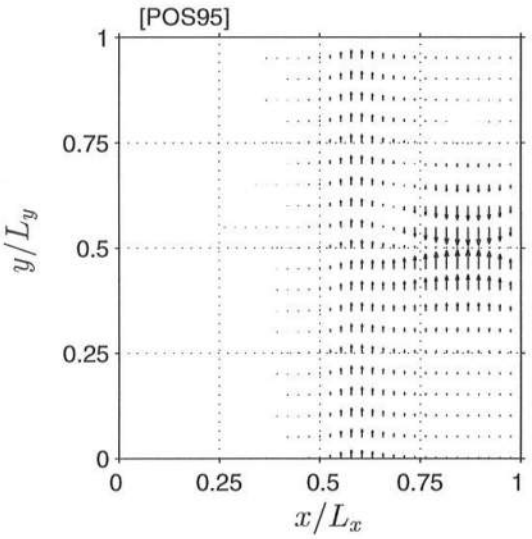

Figure 4.9: Depth-averaged current vectors $\vec{V}$ over the barred beach for a depth variation parameter $\epsilon = 0.1$ and incident wave angle $\alpha_b = 5°$: POS model results without cross-shore flow.

equations of each model.

A numerical experiment for the same bottom configuration ($\epsilon = 0.1$), but a larger angle of incidence, $\theta_b = 20°$, shows a flow pattern similar to the previous example, except that the overall longshore currents are larger due to an increase in the longshore forcing. We have also conducted a numerical experiment with a perturbation in the bar corresponding to $\epsilon = 0.02$ only, and found a similar trend as for $\epsilon = 0.1$, though naturally weaker. This confirms the conclusions of the past section that, within the range $\epsilon < 0.3$, the amplitude of the bottom perturbation does not affect the performance of the POS model when compared to the SHORECIRC model.

As a second example we choose a case with a longer value of L_y, where the application of the POS model does not generate a rip-current. This case corresponds to $a = \frac{1.8}{l_c}$, which means $L_y \simeq 1.1\, l_c$. The cross-shore length scale is the same as

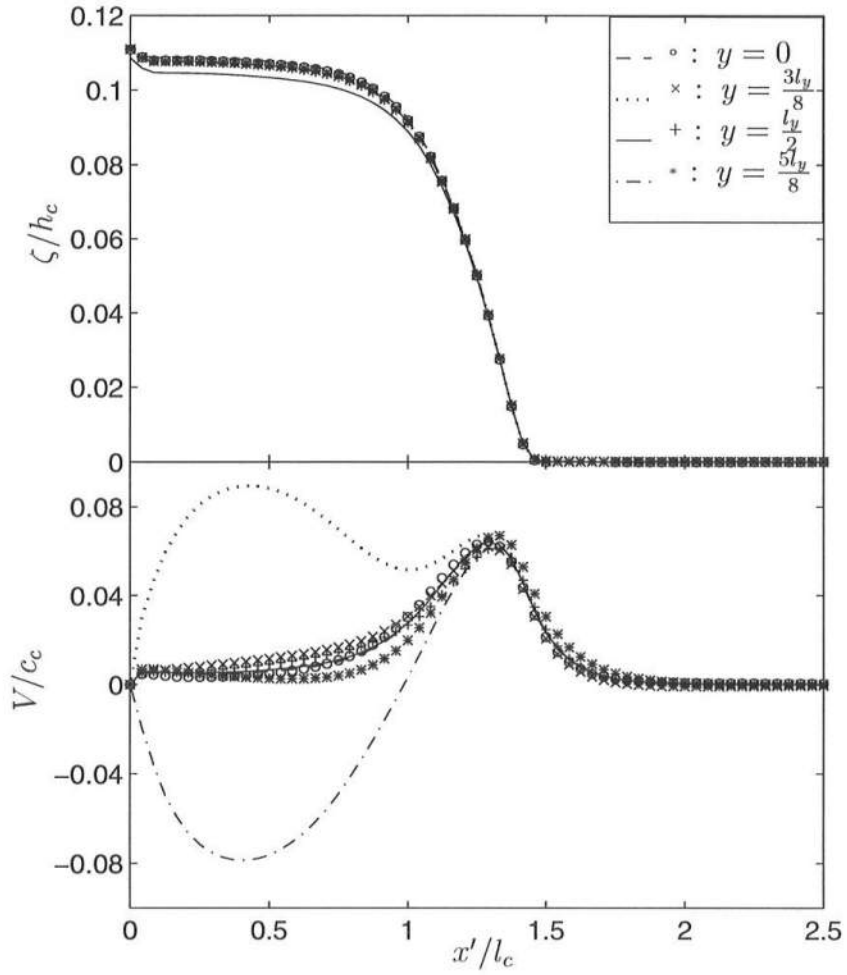

Figure 4.10: Comparison between the POS model (lines) and the SHORECIRC model results (symbols) over the barred beach at four longshore positions ($y = 0$, $y = \frac{3l_y}{8}$, $y = \frac{l_y}{2}$, $y = \frac{5l_y}{8}$), for a depth variation parameter $\epsilon = 0.1$, $a = \frac{4.8}{l_c}$, $L_y \simeq 2.5\, L_x$, and incident wave angle $\alpha_b = 5°$: (top) mean surface elevation $\bar{\zeta}$; (bottom) depth-averaged longshore currents $\tilde{V}$.

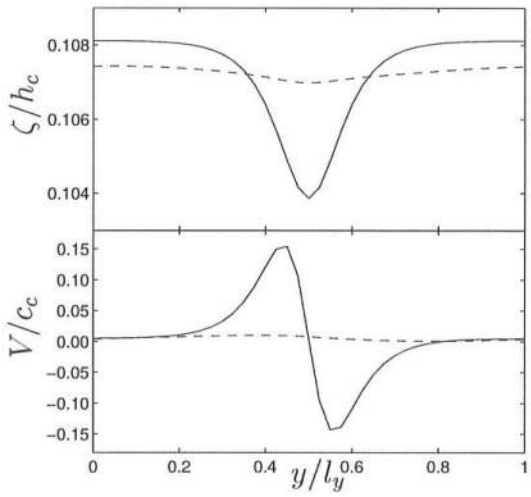

Figure 4.11: Longshore variation of $\frac{\bar{\zeta}}{h_b}$ and $\frac{\bar{V}}{c_b}$ at $x' = 0.294\, x'_b$ predicted by the POS model (solid line) and the SHORECIRC model (dashed line), for a depth variation parameter $\epsilon = 0.1$, $a = \frac{4.8}{l_c}$, $L_y \simeq 2.5\, L_x$, and incident wave angle $\theta_b = 5°$.

before, $L_x \simeq 1.67\, \epsilon\, l_c$, which for $\epsilon = 0.1$ gives $L_x \simeq 0.17\, l_c$ and so the horizontal length scales are related by $L_y \simeq 6.6 L_x$. We note that the rip-channel width $w_r \simeq 2.2\, l_c$ is quite large, though comparable with that of surveyed bathymetric profiles (e.g., Sancho *et al.*, 1995).

The results for the flow predicted by the two models for the smoother longshore bottom variation (i.e., over a longer length scale) is given in Fig. 4.12. Note that for this simulation the longshore domain length is $l_y = 10\, l_c$, and $l_x = 3.17\, l_c$ as before. The comparison between the depth-averaged velocities in Fig. 4.12 indicates that even for a barred beach with a milder rip-channel the POS model still predicts the formation of a rip-current due to an excessively large longshore pressure gradient (compared to that from SHORECIRC), whereas the SHORECIRC model predicts again a nearly longshore uniform flow. The differences between the two models are

concentrated over a distance approximately equal to $3\,l_c$, which is larger than the rip-channel width.

The example just shown indicates that the POS model can not be applied to study the longshore currents over a barred beach with a realistic longshore bottom perturbation. The key to the large differences between the two models is that the POS model overestimates the longshore pressure gradient, which locally causes excessively large gradients in the longshore currents and hence large cross-shore currents. This pattern is seen in all the examples and is attenuated with the increase of the ratio $\frac{L_y}{L_x}$. Conversely, mainly due to the contribution of the convective accelerations, the flow predicted by SHORECIRC appears to ignore local bottom perturbations. It is therefore relevant to analyze the predictions for the barred beach of the extended (POS) model, given by equations (4.19)–(4.21), which consistently retains all the terms in the governing equations at the same order.

In Fig. 4.13 and 4.14 we show the nearshore currents obtained for the same physical situation as that presented in Fig. 4.6–4.11, with the model equations (4.19)–(4.21) of the extended model, which include the above mentioned terms. These results should be compared to those in Fig. 4.8–4.10 which correspond to the full SHORECIRC and the POS models. It is clearly seen that the addition of the two small terms in the x–momentum equation dramatically changes the predicted flow pattern. The results from the extended model in Fig. 4.13 agree much better with those of SHORECIRC than the results of the POS model shown in Fig. 4.9. The flow around the rip-channel exhibits similar features as predicted by SHORECIRC, although there is a slightly larger longshore variation in the flow. As Fig. 4.14 shows this change between the behavior of POS and the extended-POS model is associated with a greatly reduced longshore variation in the setup and hence, in the longshore

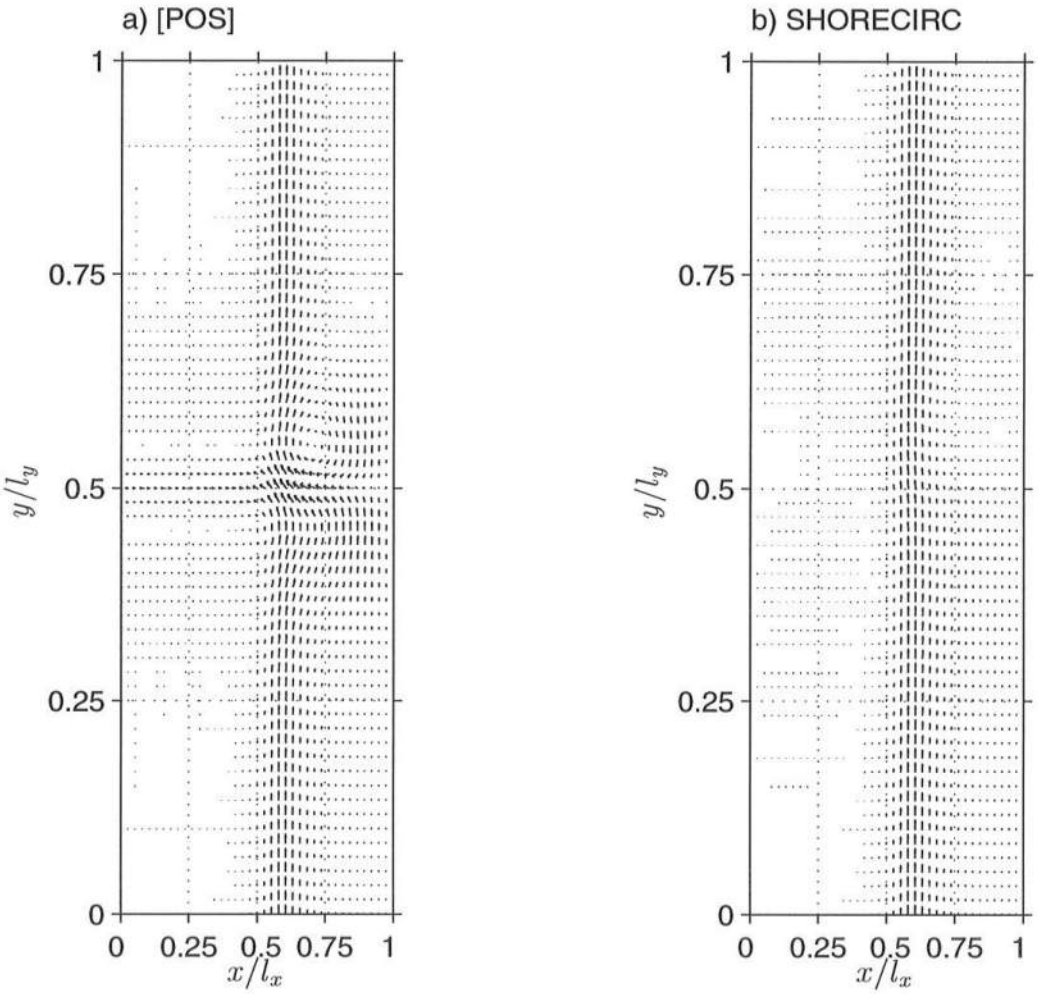

Figure 4.12: Depth-averaged current vectors $\vec{V}$ over a smoother barred beach ($L_y = 1.1\, l_c$) for a depth variation parameter $\epsilon = 0.1$, $a = \frac{1.8}{l_c}$, $L_y \simeq 6.6\, L_x$, and incident wave angle $\theta_b = 5\,\text{deg}$: (a) POS model results; (b) SHORECIRC model results.

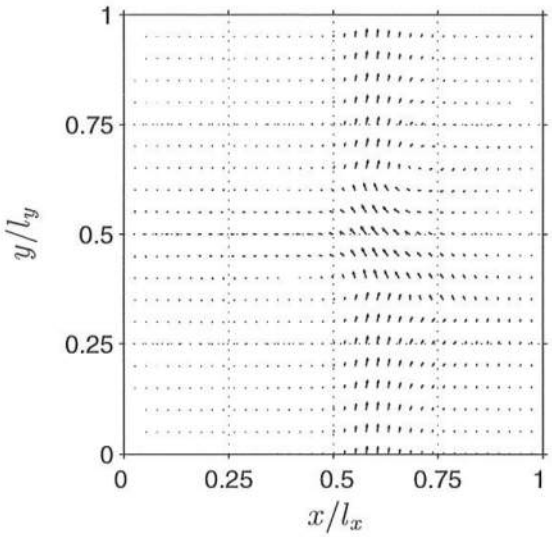

Figure 4.13: Depth-averaged current vectors $\vec{V}$ over the barred beach for a depth variation parameter $\epsilon = 0.1$, $a = \frac{4.8}{l_c}$, $L_y \simeq 2.5\, L_x$, and incident wave angle $\alpha_b = 5°$: results of extended (POS) model, which includes all second-order terms.

pressure gradient. Thus, the inclusion of the $\mathcal{O}(\mu)$ terms in the x-momentum equation greatly improves the predictions when using SHORECIRC as a reference.

The comparison between the results of the SHORECIRC model and the extended set of equations shown in Fig. 4.13 also indicates that there are still considerable differences in the longshore velocities near the rip-channel. Hence, we find that, even for a seemingly small realistic bottom perturbation, the lower order terms that are neglected in the extended-POS model relative to the SHORECIRC model equations can be locally important. Specifically, the results indicate that the depth-averaged convective acceleration in the y-momentum equation (4.21) is not negligible, and it turns out to be of the same order as the longshore pressure gradient term.

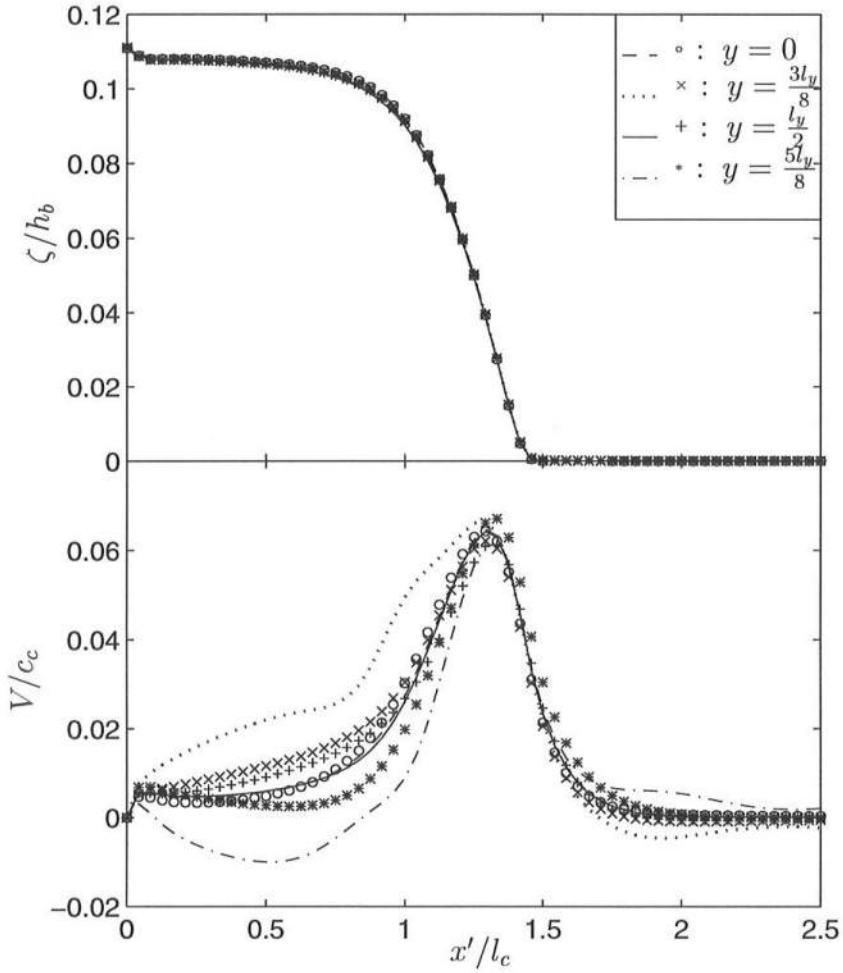

Figure 4.14: Comparison between the extended model (lines) and the SHORE-CIRC model results (symbols) over the barred beach at four longshore positions ($y = 0$, $y = \frac{3l_y}{8}$, $y = \frac{l_y}{2}$, $y = \frac{5l_y}{8}$), for a depth variation parameter $\epsilon = 0.1$, $a = \frac{4.8}{l_c}$, $L_y \simeq 2.5\, L_x$, and incident wave angle $\alpha_b = 5°$: (top) mean surface elevation $\bar{\zeta}$; (bottom) depth-averaged longshore currents $\tilde{V}$.

4.4 Discussion

The causes for the sensitivity and potential inaccuracy of the POS model turn out to be subtle. It appears from the computations that the POS model is particularly prone to give misleading results in the case with a barred beach with a (even gentle) rip-channel, but also that the depth of that channel is less important than its width.

It is believed that one factor contributing to this is that the forces (i.e., the terms) in the longshore direction are an order of magnitude smaller than the cross-shore forces (see equations (4.11) and (4.12)). This is further enhanced by the fact that the longshore pressure gradient $\frac{\partial \bar{\zeta}}{\partial y}$ in equations (4.12) and (4.15) may be even ϵ times smaller than the other terms in the y–momentum equation, as is also illustrated by the longshore $\bar{\zeta}$–variation shown in Figure 4.11. A final factor then comes from the way in which $\frac{\partial \bar{\zeta}}{\partial y}$ is determined in the POS model. The $\frac{\partial \bar{\zeta}}{\partial y}$ term in (4.15) is calculated as the y–derivative of $\bar{\zeta}$, which itself is determined by the cross-shore integration of equation (4.14) (see POS equations (B4) and (B5)). These equations can be written as

$$\bar{\zeta}(x,y) = -\frac{1}{\rho\, g}\int_{x_b}^{x} \frac{1}{h}\frac{\partial S_{xx}}{\partial x}\, dx \;+\; \bar{\zeta}(x_b)\,, \tag{4.34}$$

and

$$\frac{\partial \bar{\zeta}}{\partial y} = -\frac{1}{\rho\, g}\int_{x_b}^{x} \frac{\partial}{\partial y}\left(\frac{1}{h}\frac{\partial S_{xx}}{\partial x}\right) dx\,, \tag{4.35}$$

Since here the values of $\bar{\zeta}$ are much larger than the longshore variation in $\bar{\zeta}$, that means that $\frac{\partial \bar{\zeta}}{\partial y}$ is determined as a small difference between two relatively large numbers. That yields high sensitivity to small innacuracies, that can come from the simplified way in which the cross-shore wave height variation is determined. As the results in Figures 4.3 and 4.10 show, such relatively small ($\mathcal{O}$(3-5%)) errors do occur in the values of $\bar{\zeta}$. In particular, on the barred beach these errors create values

of $\frac{\partial \bar{\zeta}}{\partial y}$ over the trough which are 5-10 times larger than the correct values. At the same time, the longshore wave forcing over the trough is nearly zero due to lack of wave breaking, which means that the longshore pressure gradient is the dominating driving force. The consequence is the unrealistic convergence of the flow in the trough towards the rip-channel predicted by the POS model that creates the strong rip-current (see Figures 4.8 and 4.10). Hence, the inaccuracy occurs primarily in the trough behind the bar, which may also explain why the depth of the rip-channel is less important, and why a good agreement was obtained for the quasi-planar beach.

For the barred beach it turns out that both the nonlinear inertial terms and the bottom shear stress in the cross-shore direction can affect the cross-shore momentum balance of equation (4.14) significantly. The effect of these terms is sufficient to suppress the rip-currents that are predicted by the POS model. These terms lead to a local increase of the set-up in the neighborhood of the rip-channel, which reduces the longshore pressure gradient that would otherwise have been predicted. The correction to the momentum equations provided by these seemingly small terms, however, improves the accuracy of the model predictions quite noticeably.

It should be noted that there is no advantage in using the model equations (4.19)–(4.21) as an alternative to using the full model equations (4.22)–(4.24). The use of the system (4.19)–(4.21) also precludes the derivation of a simple semi-analytical solution as in POS because these equations can no longer be decoupled as was done by those authors. The important feature about the extended model is that it shows that including consistently second-order terms greatly improved the POS model prediction ability.

In all the examples analyzed in this chapter the wave height was calculated using the simplified energy equation given by POS, with the energy dissipation rate calculated by the bore dissipation model. Although for a quasi-planar beach the

use of the bore dissipation model has proven to be satisfactory (Svendsen, 1984b), its validity has not been confirmed for a barred beach. Since the radiation stress gradients are directly proportional to the energy dissipation rate, a different wave breaking model could yield a different distribution of the wave forcing. A local modification of the radiation stress alters the local ratio between the gradient of that stress and the local pressure gradient and thus, the response of the flow to these forcing mechanisms may be changed if a different wave model is used. The results in this chapter are based on the assumption that the angle of incidence α_b is small. For larger α_b the wave forcing will be stronger and the longshore pressure gradient has a more limited effect on the longshore flow.

Based on the results presented here, we conclude that even when the basic assumptions of gentle longshore variations of the semi-analytical POS model seem to be satisfied the predictions of that model may be grossly inaccurate. In the next chapter we will further explore some of the ideas analyzed here. We will continue the study of nearshore currents on weakly longshore varying barred beaches, and show that several different flow situations can occur for slight variations of the topography and/or the hydrodynamic conditions.

Chapter 5

NUMERICAL EXPERIMENTS ON THE EFFECT OF SOME PHYSICAL MECHANISMS

In this chapter we present several numerical tests aimed to emphasize the role of some mechanisms in the nearshore currents. In the past chapter we showed by comparison with the semi-analytic model of Putrevu *et al.* (1995) that the longshore pressure gradient can be quite a substantial force for the longshore currents in the nearshore region, in addition to the forcing provided by the radiation stress gradients. These forces were mainly balanced by the bottom friction and the dispersive mixing due to the vertical variation of the currents. In this chapter we analyze in greater detail the separate effects of the longshore pressure gradient, the bottom friction, and the dispersive mixing in the prediction of the nearshore circulation over a longshore varying barred beach.

Another issue that is relevant in nearshore currents is whether, on a beach of a general topography, the observed (or predicted) longshore currents are stable or unstable, which in the latter situation can lead to the so-called shear waves (Oltman-Shay *et al.*, 1989; Bowen and Holman, 1989). Several recent analytical and numerical studies addressed this mechanism with various degrees of complexity of the problem (e.g., Putrevu and Svendsen, 1992b; Dodd *et al.*, 1992; Church *et al.*, 1992; Allen *et al.*, 1996; Özkan-Haller and Kirby, 1996, 1997). These studies gave insight into the shear wave dynamics, and comparisons with field data collected

during the SUPERDUCK experiment showed a good agreement of the predicted versus the observed range of frequencies and wavelengths at which these motions were stronger (0.001–0.01 Hz, and 100–500 m, respectively).

It was also found that shear waves contribute significantly to the lateral mixing in the surf zone (Putrevu and Svendsen, 1992b; Church *et al.*, 1992; Özkan-Haller and Kirby, 1996). In a comparison of model predictions against field data for the SUPERDUCK experiment, Özkan-Haller and Kirby find that shear waves provide a mixing mechanism similar to that of the Reynolds stresses (averaged over the time-scale of the infra-gravity wave motions). Hence, the effect of shear waves on the time-mean longshore currents is essentially similar to that of the dispersive mixing. However, whilst the dispersive mixing is likely to be present all the time due to the depth variation of the currents, the mixing associated with the shear waves is only effective when these are present. We are thus interested in examining the lateral mixing provided by these two conceptually different mechanisms.

In order to address the study of shear waves over a longshore non-uniform barred beach we find convenient though to first investigate the dynamics of these motions over a longshore uniform plane beach. The example pursued in the following section shows the results from SHORECIRC for same plane beach as that studied by Allen *et al.* (1996) and Özkan-Haller and Kirby (1997). Furthermore, we use this example to test the accuracy of our numerical model versus the results of other modelers for an unsteady motion. Hence, the plane beach is considered a "benchmark" test for the performance of SHORECIRC.

5.1 Shear waves on a plane beach

Shear (or vorticity) waves are perturbations (instabilities) of the longshore currents. Bowen and Holman (1989) suggest that these waves are unstable perturbations of the cross-shore shear of the mean longshore current. The perturbation of the current leads to a longshore progressive wave, where the restoring force is the potential vorticity. The free-surface displacement associated with these perturbations is usually limited to the $\mathcal{O}(1\,\mathrm{cm})$ for typical beach topographies (Özkan-Haller and Kirby, 1997). The speed at which shear waves propagate in the direction of the longshore currents have been observed (and predicted) to be between 30% and 70% of that of the maximum mean longshore current (Oltman-Shay *et al.*, 1989; Bowen and Holman, 1989; Putrevu and Svendsen, 1992b; Dodd *et al.*, 1992). Hence they are found to be dynamically dependent of the mean longshore current.

Shear waves are also seen to be slightly dispersive, with the waves of longer wavelengths traveling slower than the waves of shorter wavelengths. Observations of Oltman-Shay *et al.* (1989) indicate that the free-surface displacement and the cross-shore velocities in the frequency range of shear waves are in phase, but the longshore and cross-shore velocities are near quadrature.

Although most natural beaches can exhibit complicated bottom contours, it is interesting to analyze the development and propagation of shear waves on a plane beach, as some of the aforementioned features can be predicted on such a simpler topography. Hence, we choose to investigate the nonlinear shear instabilities on a 1/20 sloping beach, with the same characteristics as that studied by Allen *et al.* (1996) and Özkan-Haller and Kirby (1995, 1997).

5.1.1 Model equations

The model equations for the present test are the forced nonlinear shallow-water equations for depth-uniform currents,

$$\frac{\partial \bar{\zeta}}{\partial t} + \frac{\partial}{\partial x}\left(\tilde{U}h\right) + \frac{\partial}{\partial y}\left(\tilde{V}h\right) = 0\,, \tag{5.1}$$

$$\begin{aligned}\frac{\partial}{\partial t}\left(\tilde{U}h\right) &+ \frac{\partial}{\partial x}\left(\tilde{U}^2h\right) + \frac{\partial}{\partial y}\left(\tilde{U}\tilde{V}h\right) \\ &+ g\left(h_o+\bar{\zeta}\right)\frac{\partial \bar{\zeta}}{\partial x} + \frac{1}{\rho}\left(\frac{\partial S_{xx}}{\partial x}+\frac{\partial S_{yx}}{\partial y}\right) + \frac{\tau_x^B}{\rho} = 0\,,\end{aligned} \tag{5.2}$$

$$\begin{aligned}\frac{\partial}{\partial t}\left(\tilde{V}h\right) &+ \frac{\partial}{\partial x}\left(\tilde{U}\tilde{V}h\right) + \frac{\partial}{\partial y}\left(\tilde{V}^2h\right) \\ &+ g\left(h_o+\bar{\zeta}\right)\frac{\partial \bar{\zeta}}{\partial y} + \frac{1}{\rho}\left(\frac{\partial S_{xy}}{\partial x}+\frac{\partial S_{yy}}{\partial y}\right) + \frac{\tau_y^B}{\rho} = 0\,,\end{aligned} \tag{5.3}$$

which are easily retrieved from the time-averaged and depth-integrated equations of motion derived in section 2.1. Note that these equations are the same as (4.22)–(4.24) without the dispersion mixing.

We consider a longshore uniform beach such that $\frac{\partial S_{yx}}{\partial y} = \frac{\partial S_{yy}}{\partial y} = 0$. Furthermore, for the purpose of the comparison with the results of Allen *et al.* (1996) and Özkan-Haller and Kirby (1997), we first assume the short-wave forcing in the cross-shore direction to be in balance with the setup gradient, and in the longshore direction it balances the bottom shear stress associated with the time-mean longshore current V_S by a linear model ($\tau_{yS}^B = \rho\mu V_S$):

$$\frac{1}{\rho}\frac{\partial S_{xx}}{\partial x} = -g\left(h_o+\bar{\zeta}_S\right)\frac{\partial \bar{\zeta}_S}{\partial x}\,, \tag{5.4}$$

$$\frac{1}{\rho}\frac{\partial S_{xy}}{\partial x} = -\frac{\tau_{yS}^B}{\rho} = -\mu V_S\,. \tag{5.5}$$

In the above expressions the subscript S in $\bar{\zeta}_S$ and τ^B_{yS} stands for the time-steady components of $\bar{\zeta}$ and τ^B_y. The time-steady components are the contribution to the total variables that are in balance with the short-wave forcing. Hence, defining

$$\bar{\zeta} = \bar{\zeta}_S + \eta\,, \tag{5.6}$$

$$\tau^B_y = \tau^B_{yS} + \tau'^B_y\,, \tag{5.7}$$

and using the longshore uniformity of the forcing, the governing equations (5.2)–(5.3) can be rewritten as:

$$\frac{\partial}{\partial t}\left(\tilde{U}h\right) + \frac{\partial}{\partial x}\left(\tilde{U}^2 h\right) + \frac{\partial}{\partial y}\left(\tilde{U}\tilde{V}h\right) + g\,h\,\frac{\partial \eta}{\partial x} + \frac{\tau^B_x}{\rho} = 0\,, \tag{5.8}$$

$$\frac{\partial}{\partial t}\left(\tilde{V}h\right) + \frac{\partial}{\partial x}\left(\tilde{U}\tilde{V}h\right) + \frac{\partial}{\partial y}\left(\tilde{V}^2 h\right) + g\,h\,\frac{\partial \eta}{\partial y} + \frac{\tau^B_y - \tau^B_{yS}}{\rho} = 0\,. \tag{5.9}$$

Following Özkan-Haller and Kirby (1997) we neglect the contribution of the steady setup $\bar{\zeta}_S$ to the mean water level in the equations above, so that $h = h_o + \eta$ is the total water depth excluding the setup[1]. For simplification, the bottom shear stresses are assumed linear functions of $\tilde{U}$ and $\tilde{V}$

$$\tau^B_x = \rho\,\mu\,\tilde{U}\,, \tag{5.10}$$

$$\tau^B_y = \rho\,\mu\,(\tilde{V} - V_S)\,, \tag{5.11}$$

with a constant friction coefficient $\mu = 0.006$. Hence, we are at first solving exactly the same model equations as Özkan-Haller and Kirby, and a slightly modified set of that solved by Allen *et al.* (1996), who further introduce the rigid lid approximation.

[1] This was observed by those authors not to alter the pattern of the flow anywhere, except close to the shoreline.

The steady current V_S is the result of the balance between the longshore component of the radiation stress and the bottom friction τ_{yS}^{B}. Like the previous modelers, V_S is an input parameter and is assumed to be given by

$$V_S = C\, x'^2 \exp\left[-\left(\frac{x'}{\alpha}\right)^3\right], \tag{5.12}$$

where x' is the seaward oriented cross-shore axis, and C and α are chosen such that the maximum of V_S is 1 m/s and occurs at $x' = x'_b = 90$ m.

5.1.2 Results for standard grid values

In this section we present the results of SHORECIRC over a plane beach, using the set of equations (5.1), (5.8) and (5.9). The beach slope is $h_x = 1/20$, and we choose the longshore domain length equal to that of the most unstable wavelength calculated from linear instability theory, $l_y = 5x'_b$ (Allen *et al.*, 1996). At the lateral boundaries we use longshore periodicity. In the cross-shore direction the domain length is $l_x = 4x'_b$. At the seaward boundary $x' = l_x$ we set the absorbing-generating boundary condition, and at the shoreline $x' = 0$ we place a no flux boundary condition at a small water depth $h_o = 0.01$ m. We note that a similar treatment of the shoreline is utilized by Özkan-Haller and Kirby (1997), as those authors found minor differences between the results obtained by including the shoreline runup and those from calculations with a wall boundary at the shore.

The initial condition is given by:

$$\eta = 0\,, \tag{5.13}$$

$$\tilde{U} = \epsilon U'\,, \tag{5.14}$$

$$\tilde{V} = V_S + \epsilon V'\,, \tag{5.15}$$

where U' and V' are the velocities from the computed linear instability analysis using the solution of Putrevu and Svendsen (1992b), and $\epsilon = 4.5\times10^{-2}$. We point out that

we found through our computations that the nonlinear shear wave instabilities, after the initial development, were rather insensitive to the initial condition. However, the simulation time for those instabilities to grow depends on the initial condition. As an example, for a random perturbation of the initial velocities U' and V', it was found that the time for the shear waves to reach the same energetic motion as that for the linear unstable perturbation of U' and V' was four times as large.

The grid spacings for the present calculations are the same as those used by Allen *et al.*, namely $\triangle x = \triangle y = \frac{x'_b}{18} = 5$ m. We choose the time spacing $\triangle t$ corresponding to the Courant number $C_r = 0.8$, which is lower than the limiting Courant number $C_r = 0.85$ calculated in section 3.2.

Fig. 5.1a shows the current vectors of the initial velocity field, with the maximum $\tilde{V} = 1$ m/s at $\frac{x}{l_x} = 0.75$. The solid dots represent the location of the grid-points for which time series are shown. Notice that the velocity perturbations $\epsilon U'$ and $\epsilon V'$ from the basic state are so small, that they are imperceptible at this scale. Fig. 5.1b shows the instantaneous current vectors at $t \simeq 3.5$ hr. The comparison of the two plots evidences the growth of the instabilities into shear waves, which cause the currents to meander and form vortices.

Time series of $\eta, \tilde{U}$ and $\tilde{V}$ at $\frac{x}{l_x} = 0.75$ and $\frac{y}{l_y} = 0.5$ are given in Fig. 5.2. It is seen that the amplitude of the shear waves grows quasi-exponentially in about 3.5 hr, and then remains quasi-steady, oscillating around a mean value. This modulated amplitude is clearly seen for all the three variables, but it is stronger for the velocity components than for the free-surface variation. It is also visible that the higher amplitude disturbances have larger periods, which confirms previous observations. The free-surface oscillations have an absolute maximum around 5 mm, hence confirming the validity of the rigid-lid assumption used by Allen *et al.* (1996). In Fig. 5.3 and 5.4 we present the time series at the same location obtained by

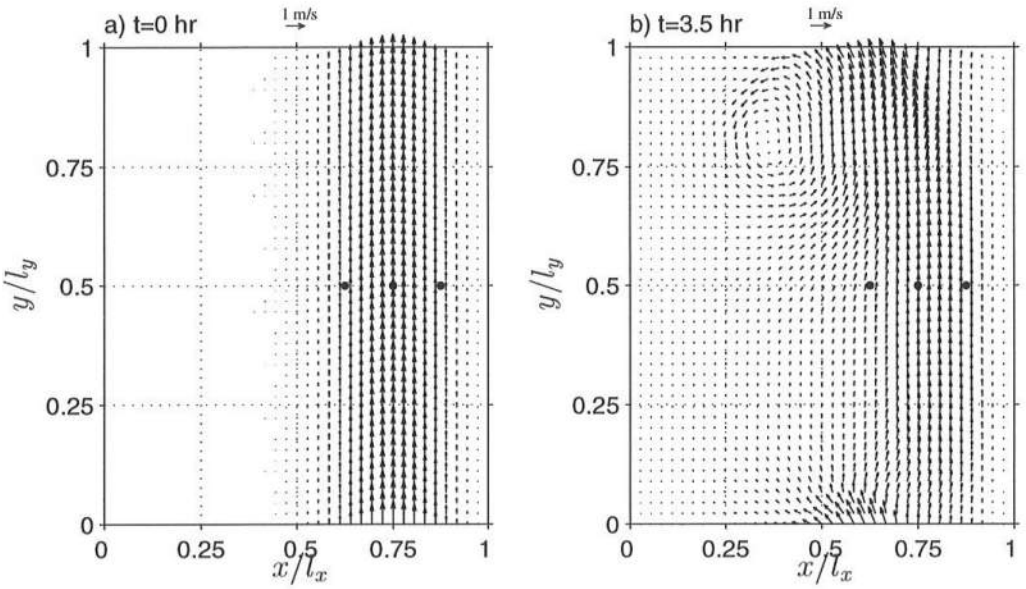

Figure 5.1: Depth-averaged current vectors over a plane beach at two instants of time: (a) $t = 0$ hr ; (b) $t \simeq 3.5$ hr.

Özkan-Haller and Kirby (1997) and Allen *et al.* (1996), respectively. Though they differ in some details, the similarity between our results and those of Özkan-Haller and Kirby is encouraging. It should be mentioned that Özkan-Haller and Kirby use a pseudospectral numerical model, which has a zero truncation error for the spatial derivatives. The solution presented here and that of Özkan-Haller and Kirby differ mainly on the initial time for the disturbance to grow, and also exhibit slightly different values of the peak period. The period of the oscillations in our solution ($T \simeq 870$ s) is slightly smaller than that predicted by those authors ($T \simeq 920$ s), which suggests that our shear waves travel faster (since the wavelength in these computations is determined by the fixed longshore domain length).

A closer comparion of Fig. 5.2 and 5.3 shows that the low-frequency oscillations are the same in both cases. Second, we notice that the cross-shore and

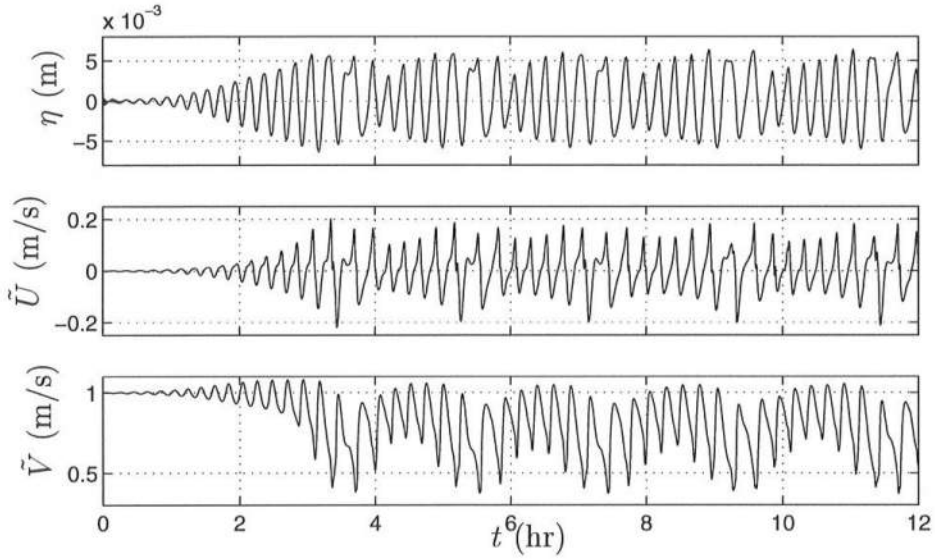

Figure 5.2: Time series of $\eta, \tilde{U}$ and $\tilde{V}$ at $\frac{x}{l_x} = 0.75$ and $\frac{y}{l_y} = 0.5$.

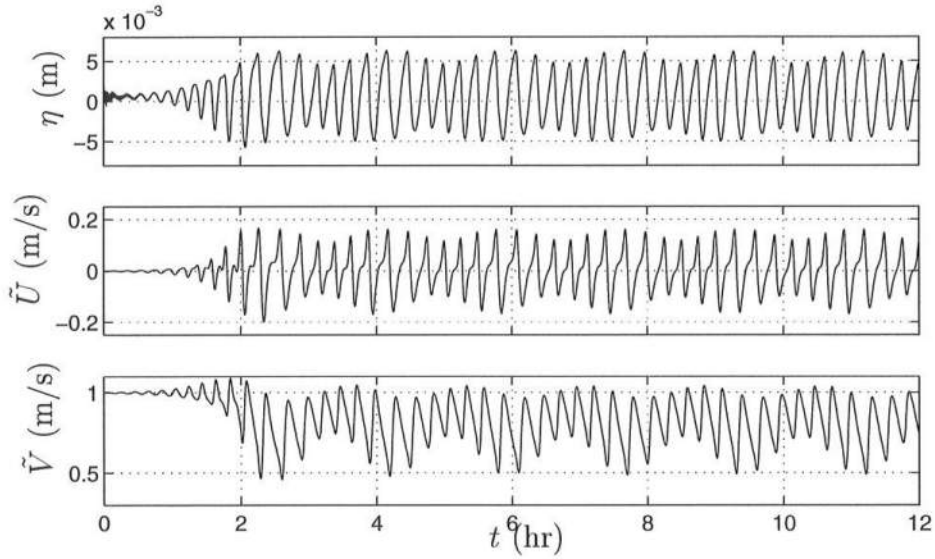

Figure 5.3: Time series of $\eta, \tilde{U}$ and $\tilde{V}$ at $\frac{x}{l_x} = 0.75$ and $\frac{y}{l_y} = 0.5$ from Özkan-Haller and Kirby (1997) simulations (courtesy of H.T. Özkan-Haller).

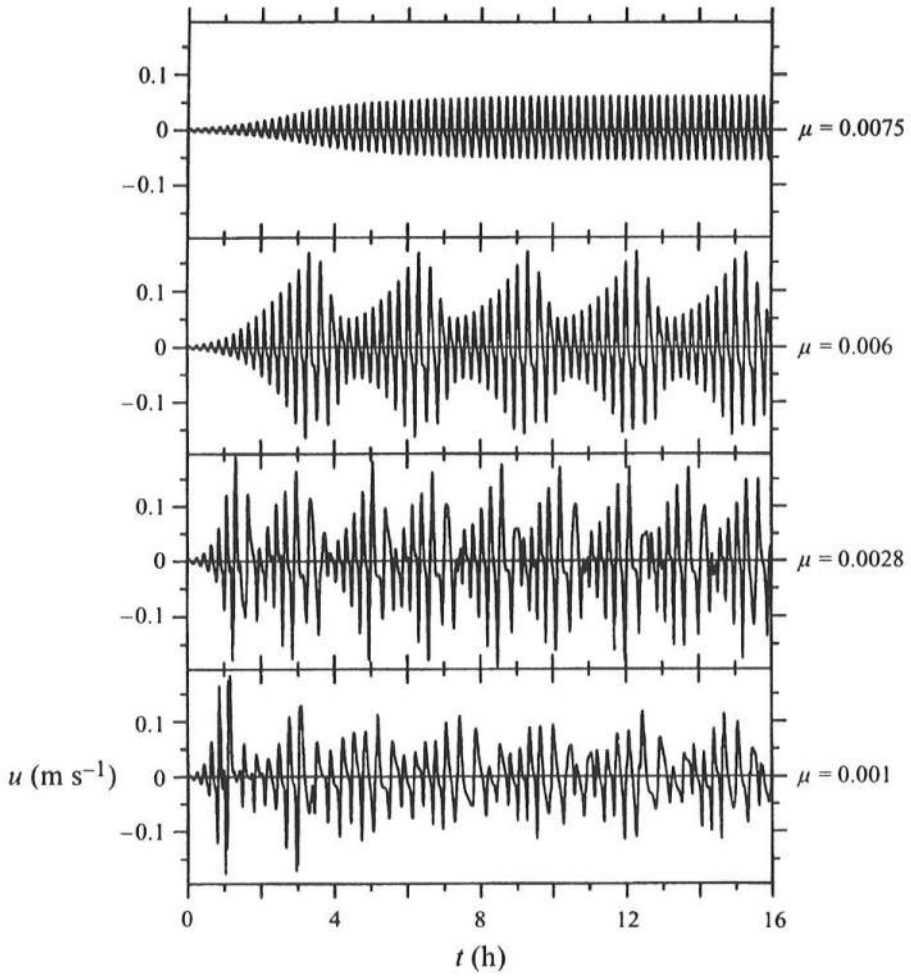

Figure 5.4: Time series of $\tilde{U}$ at $\frac{x}{l_x} = 0.75$ and $\frac{y}{l_y} = 0.5$ for different values of the friction factor from Allen *et al.* (1996) simulations (courtesy of H.T. Özkan-Haller).

longshore velocities are skewed in the same direction in the results of the two models. The differences between the time series of the two simulations after the initial growth is that both $\tilde{U}$ and $\tilde{V}$ are slightly more regular in Fig. 5.3.

The time series of $\tilde{U}$ predicted by Allen *et al.* (1996) for the same friction value $\mu = 0.006$ are shown in the second panel (from the top) of Fig. 5.4. The period of those shear waves is estimated as $T \simeq 800$ s. It also appears that the cross-shore velocity amplitudes are slightly smaller than those calculated by SHORECIRC and Özkan-Haller and Kirby. Nevertheless, the overall magnitude and time variation of the velocities are seen to agree fairly well. We recall that the model of Allen *et al.* (1996) uses the rigid-lid assumption, which from this comparison appears to influence the predictions of $\tilde{U}$.

The frequency spectra corresponding to the time series of $\eta, \tilde{U}$ and $\tilde{V}$ at $\frac{x}{l_x} = 0.75$ and $\frac{y}{l_y} = 0.5$, from the present model computations, are shown in Fig. 5.5. The spectra are obtained from a 12.1 hr record starting at $t \simeq 4.8$ hr, using a Bartlett smoothing with five segments, each of them with 4096 points and a sampling rate of $10\triangle t = 2.128$ s. The spectral estimates indicate that the peak frequency is $f_p = 0.00115$ Hz, or $T = 870$ s. Note that the vertical axis scale for the surface elevation spectrum $S(\eta)$ is 1000 times smaller than the axis for the velocity spectra, $S(\tilde{U}), S(\tilde{V})$. The energy associated with $\tilde{V}$ at the peak frequency is slightly larger than that of $\tilde{U}$. This means that the amplitude of the shear waves in the cross-shore direction is smaller than that in the longshore direction (this observation can also be inferred from the time series in Fig.5.2). We note, however, that this is not always true for other locations in the model domain: $S(\tilde{U})$ is larger than $S(\tilde{V})$ for locations some distance seaward from the maximum longshore velocity at $\frac{x}{l_x} = 0.75$.

It has been suggested (Bowen and Holman, 1989) that the phase spectra between the measured time-series of $\eta, \tilde{U}$ and $\tilde{V}$ at a given location can be used

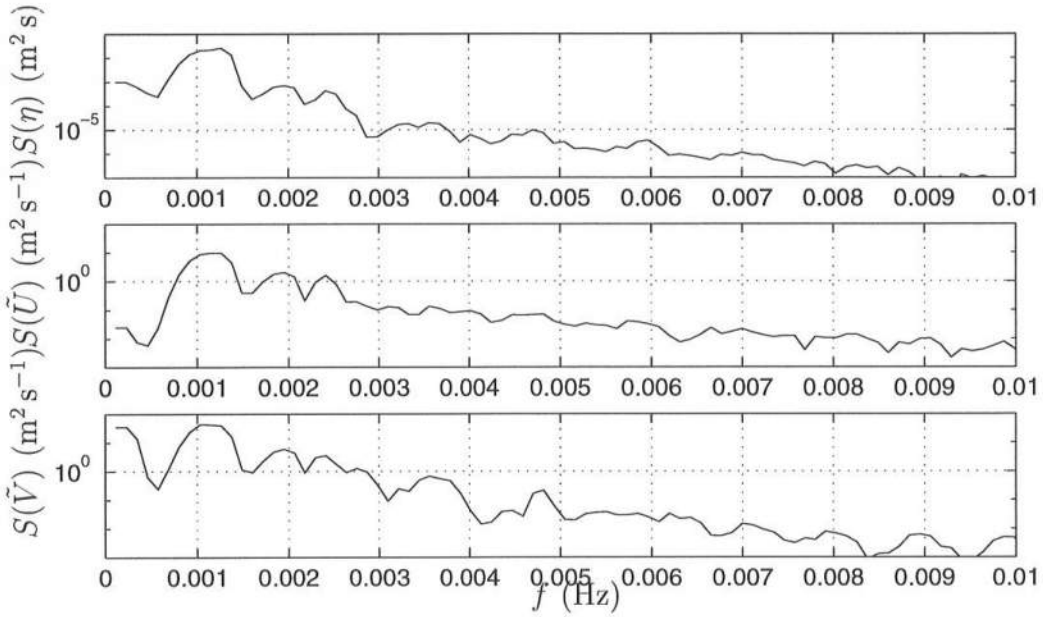

Figure 5.5: Frequency spectra of the time series of $\eta, \tilde{U}$ and $\tilde{V}$ at $\frac{x}{l_x} = 0.75$ and $\frac{y}{l_y} = 0.5$.

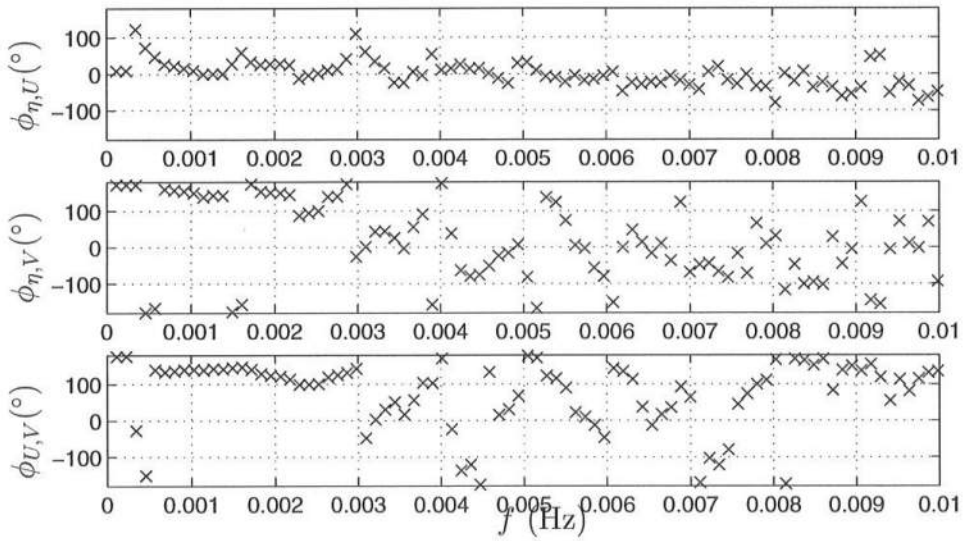

Figure 5.6: Phase spectra from the time series at $\frac{x}{l_x} = 0.75$ and $\frac{y}{l_y} = 0.5$ of: (a) $\eta, \tilde{U}$; (b) $\eta, \tilde{V}$; (c) $\tilde{U}, \tilde{V}$.

to identify the presence of shear waves. Therefore, next we will briefly analyze the phase difference spectra between the signals corresponding to $\eta(t), \tilde{U}(t), \tilde{V}(t)$. For a stationary random process the cross-correlation between two generic time sequences f_1 and f_2 is defined as (Newland, 1993)

$$C_{12}(\tau) \equiv \langle f_1(t)\, f_2(t+\tau) \rangle \ , \tag{5.16}$$

where $\langle\rangle$ represents the expected value operator. The cross-spectral density function is given by

$$\Phi_{12}(\omega) \equiv \int_{-\infty}^{\infty} C_{12}(\tau)\, e^{i\omega\tau}\, d\tau \ = \ F_1^*(\omega)\, F_2(\omega) \ , \tag{5.17}$$

where F_1 and F_2 are the spectral densities of f_1 and f_2, and $*$ represents the complex conjugate. We define the transfer function $H(\omega)$ as

$$H(\omega) \equiv \frac{\Phi_{12}(\omega)}{\Phi_{11}(\omega)} \ , \tag{5.18}$$

where $\Phi_{11}(\omega)$ is the autocorrelation spectrum. The phase difference $\phi(\omega)$ between two signals at each frequency can be calculated from the transfer function as

$$\phi(\omega) = \arctan\left(\frac{\Im\mathrm{m}[H(\omega)]}{\Re\mathrm{e}\,[H(\omega)]}\right) \ . \tag{5.19}$$

Before presenting the phase spectra, it should be remarked that the coherence between the time series of measured (in the field) $\tilde{U}$ and $\tilde{V}$ is much stronger than that with surface elevation records (Oltman-Shay *et al.*, 1989). Hence it is more relevant to examine the coherence and phase difference between the two velocity records, though we start first with the analysis of the phase spectra between η and $\tilde{U}$, and η and $\tilde{V}$. The phase difference between the free-surface elevation η and the cross-shore velocity $\tilde{U}$ is shown in Fig.5.6 (top panel). In the frequency range $0.0005 < f < 0.003$ Hz where the time-series are coherent (coherence larger than 0.8) we observe that η and $\tilde{U}$ are nearly in phase or at most 45° out of phase. This phase relation is in agreement with that calculated by Oltman-Shay *et al.* (1989) from

the analysis of field data. Conversely, the phase difference between the free-surface elevation η and the longshore velocity $\tilde{V}$, shown in Fig.5.6 (center), is between 90° and 180° and at the peak frequency is approximately 140°.

More relevant, though, is the phase difference between $\tilde{U}$ and $\tilde{V}$ shown in Fig.5.6 (bottom panel). In the frequency range $0.0005 < f < 0.003$ Hz where the motions are coherent, $\tilde{U}$ and $\tilde{V}$ are out of phase by 140°, with $\tilde{U}$ lagging $\tilde{V}$. We note that this phase relation is different from those observed by Oltman-Shay *et al.* (1989), who indicate a near quadrature (90°) phase between $\tilde{U}$ and $\tilde{V}$. One possible reason for this difference is that (as we will see later) the phase difference changes with the cross-shore position. Therefore, since the beach topography in the present simulation and that of Oltman-Shay *et al.* are very different, it is equivalent to say that the relative locations of the points at which the time-series are taken are also different. Second, the results of Oltman-Shay *et al.* are from the analysis of field data where other mechanisms such as the dispersive mixing are also present, which maybe responsible for changing the relative phase spectra.

The phase difference between $\tilde{U}$ and $\tilde{V}$ can also be calculated from the results from the linear stability analysis. As mentioned above, the initial perturbed velocities are calculated using the solution of Putrevu and Svendsen (1992b). We can therefore reconstruct a time series for that solution for the velocities corresponding to a given amplitude, which contains the phase information, as:

$$V' = \frac{1}{h}\,\Re\mathrm{e}\left[\frac{\partial \psi}{\partial x}\, e^{i\,(k\,y\,-\omega\,t)}\right], \tag{5.20}$$

$$U' = -\frac{1}{h}\,\Re\mathrm{e}\left[i\,k\,\psi\, e^{i\,(k\,y\,-\omega\,t)}\right], \tag{5.21}$$

where $\psi(x)$ is the complex function related with the stream function $\Psi(x, y, t)$ by

$$\Psi = \Re\mathrm{e}\left[\psi(x) e^{i\,(k\,y\,-\omega\,t}\right]. \tag{5.22}$$

For each location (x,y) and a given wavenumber k and angular frequency ω we determine the time series of U' and V', which are just sinusoidal functions, and then calculate the phase difference between the two. Thus, we find that at $\frac{x}{l_x} = 0.75$ and $\frac{y}{l_y} = 0.5$ the phase difference between U and V for the wavenumber corresponding to the maximum instability ($k = 1.4 \times 10^{-2}\mathrm{m}^{-1}$, $\omega = 9.084 \times 10^{-2}\mathrm{s}^{-1}$) is $-10°$, with V lagging U. Hence, there is a considerable difference between the phase lag predicted by the nonlinear model and the linear stability model.

To further illustrate the growth and propagation of shear waves we also present in Fig.5.7 the time series of $\eta, \tilde{U}$ and $\tilde{V}$ at $\frac{x}{l_x} = 0.875$ and $\frac{y}{l_y} = 0.5$, which corresponds to a point located halfway between the shoreline line and the position of the maximum of $\tilde{V}_S$ seen in Fig.5.1. The range of the vertical scales in the three time series is the same as that for the time series shown in Fig.5.2. Comparing the two plots, we notice that the amplitudes of both $\tilde{U}$ and $\tilde{V}$ are smaller at the location $\frac{x}{l_x} = 0.875$ than at $\frac{x}{l_x} = 0.75$. Hence, the shear wave energy is considerably smaller in the region corresponding to the inner surf zone. At this location the results also exhibit a modulation of the amplitudes. The phase spectra at this same location is shown in Fig. 5.8. At the peak frequency, the free-surface elevation leads the cross-shore velocity by 50°, and lags the longshore velocity by 50°. The longshore and cross-shore velocities are nearly in quadrature, with a phase lag of 100°. Hence, the phase difference between the three time series at a point inside the surf zone ($\frac{x}{l_x} = 0.875$) is somewhat different from that at the position of the maximum initial velocity ($\frac{x}{l_x} = 0.75$). We also note that at this location the phase difference between U and V from the linear stability model is $-85°$, which means that it is approximately 180° out of phase from the nonlinear model predictions.

The time series of the free-surface elevation, and cross-shore and longshore currents at a third location, $\frac{x}{l_x} = 0.625$ and $\frac{y}{l_y} = 0.5$ are shown in Fig. 5.9. This

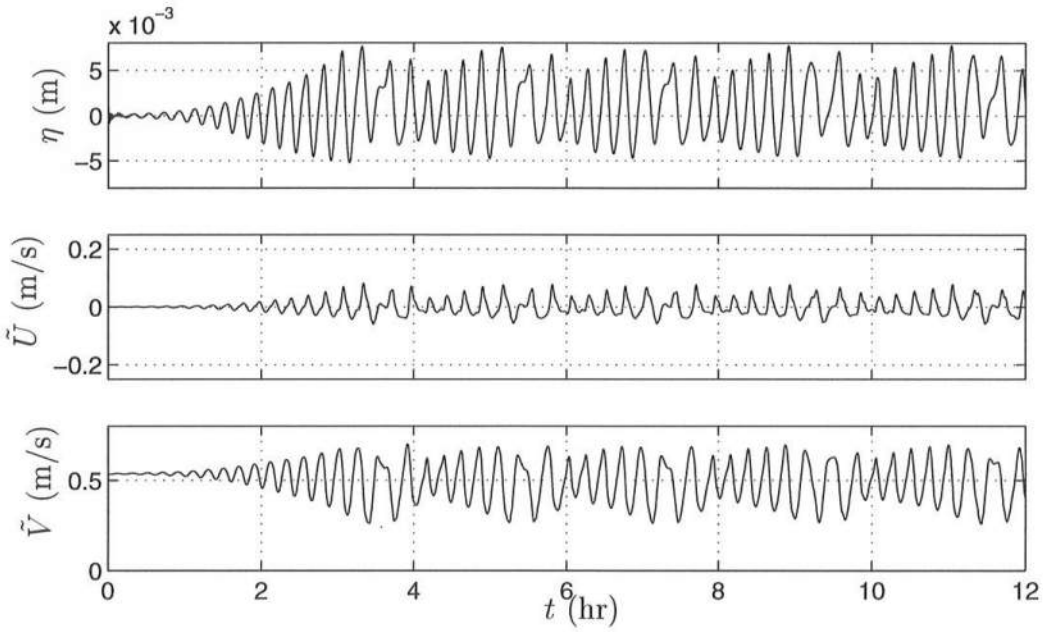

Figure 5.7: Time series of $\eta, \tilde{U}$ and $\tilde{V}$ at $\frac{x}{l_x} = 0.875$ and $\frac{y}{l_y} = 0.5$.

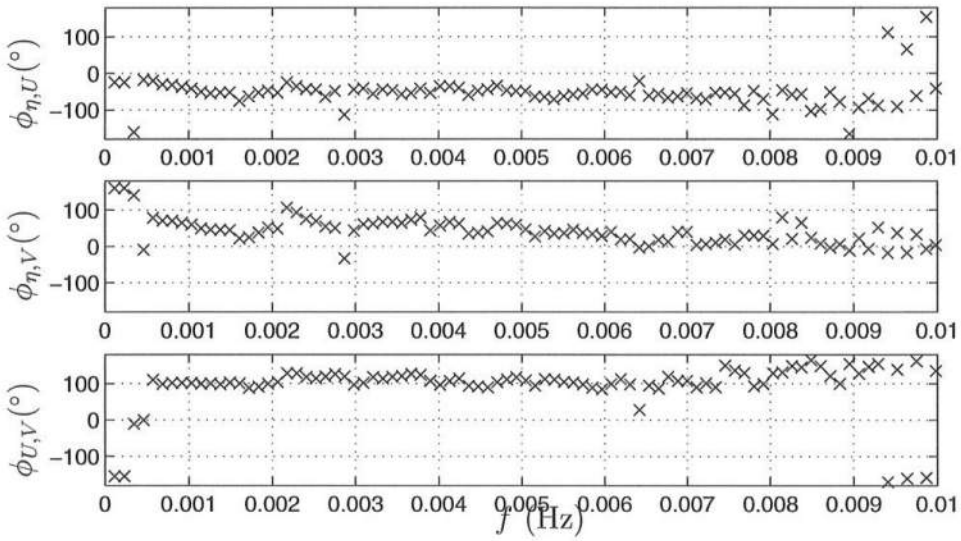

Figure 5.8: Phase spectra from the time series at $\frac{x}{l_x} = 0.875$ and $\frac{y}{l_y} = 0.5$ of: (a) $\eta, \tilde{U}$; (b) $\eta, \tilde{V}$; (c) $\tilde{U}, \tilde{V}$.

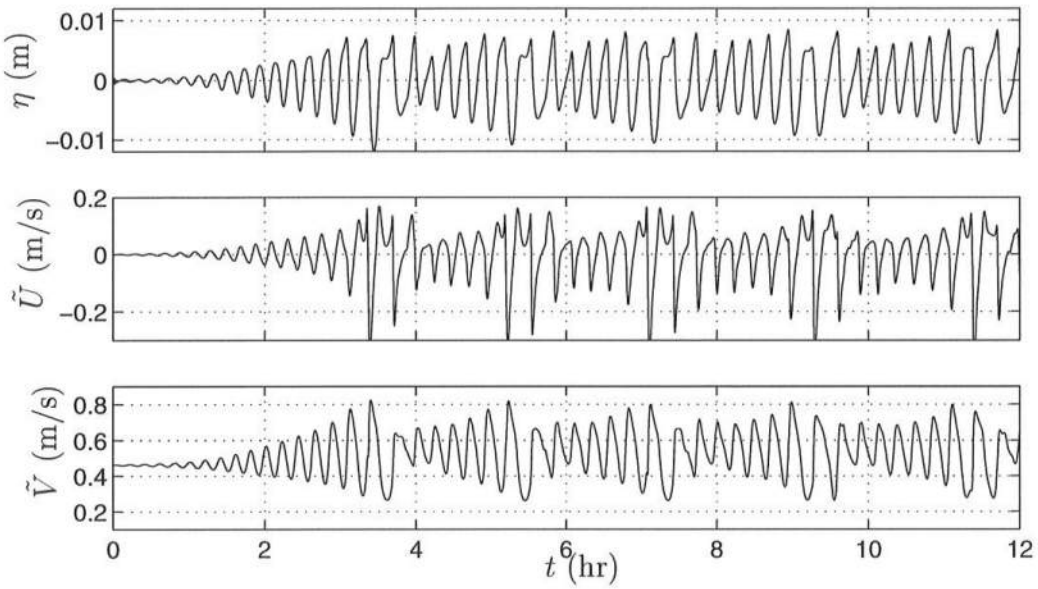

Figure 5.9: Time series of $\eta, \tilde{U}$ and $\tilde{V}$ at $\frac{x}{l_x} = 0.625$ and $\frac{y}{l_y} = 0.5$.

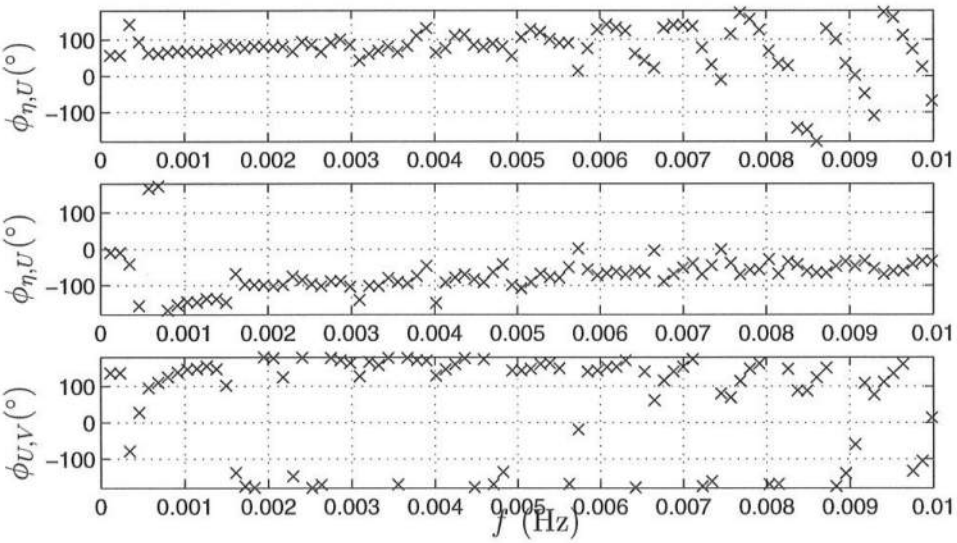

Figure 5.10: Phase spectra from the time series at $\frac{x}{l_x} = 0.625$ and $\frac{y}{l_y} = 0.5$ of: (a) $\eta, \tilde{U}$; (b) $\eta, \tilde{V}$; (c) $\tilde{U}, \tilde{V}$.

point, shown in Fig. 5.1, is located seaward of the maximum of V_S. This is where the largest shear on the cross-shore profile of the longshore current occurs and we expect a stronger shear wave energy. As noted by Putrevu and Svendsen (1992b), the strength of the instability increases with increasing shear on the seaward face. Comparing the results in Fig. 5.9 with those in Fig. 5.2 we observe that both the free-surface displacement and the cross-shore velocity at $\frac{x}{l_x} = 0.625$ are more energetic than those observed at $\frac{x}{l_x} = 0.75$ and at $\frac{x}{l_x} = 0.875$. The amplitude of the longshore current at $\frac{x}{l_x} = 0.625$ is comparable with that at $\frac{x}{l_x} = 0.75$. Thus, the conclusions reached by Putrevu and Svendsen (1992b) and others are confirmed by our results.

For completeness, the phase spectra at the same location, $\frac{x}{l_x} = 0.625$ and $\frac{y}{l_y} = 0.5$, are shown in Fig. 5.10. Once again we find the phase relations between the three time series at this location different from those at the other cross-shore locations in particular for the free-surface elevation. Focusing on the relation between $\tilde{U}$ and $\tilde{V}$, the phase difference at the peak frequency is 150°, which should be compared to the $-60°$ calculated by the linear stability model. It is interesting to note that the phase angle of the nonlinear model at this location (150°) is quite similar to that found at the position of the maximum longshore velocity, $\frac{x}{l_x} = 0.75$ (140°). However, this is likely to be fortuitous as the results from the linear analysis do not show the same feature.

In brief conclusion, due to the nonlinear nature of the motion, our results indicate that there is not a simple relationship for the phase difference between U and V at different locations. Therefore, contrary to the suggestion of Bowen and Holman (1989), this indicates that it is not sufficient to analyze phase spectra in order to extract from field data information on the shear wave motion.

Given this detailed view of the shear wave motion over a plane beach it is interesting also to analyze the effect it produces on the mean longshore current. The

initial longshore current profile is described by equations (5.12) and (5.15), which form a quasi-uniform flow in the longshore direction as seen in Fig. 5.1a. As the instabilities grow in amplitude, energy is transferred from the mean motion to the shear waves. Hence, the instantaneous plot of the currents can deviate considerably from the longshore uniform situation as seen in Fig. 5.1b. This transfer of energy occurs continuously, and as the meandering currents grow in amplitude they eventually release vortices that detach from the background current.

The transfer of energy from the mean motion to shear waves is associated with a transfer of momentum. This is identical to the situation found in a turbulent motion where energy and momentum is converted to the small scale eddies. Hence, shear waves cause a dispersion of momentum which will modify the background time-mean (averaged over the duration of the simulation) longshore current profile. In Fig. 5.11a we plot the initial cross-shore profile of longshore current at $\frac{y}{l_y} = 0.5$ (solid line) versus the current profile obtained by time-averaging $\tilde{V}$ over the entire period of simulation ($t = 12$ hr), (dashed line). The maximum of the time-averaged $\tilde{V}$ is approximately 20% smaller than that of the initial current distribution. The time-mean current seaward of $\frac{x}{l_x} < 0.65$ is larger than the initial current, indicating that there is a transfer of mean momentum from the region of the maximum of the V_S to the offshore.

In Fig. 5.11b and 5.11c we show the cross-shore distribution of the terms of the time-averaged x and y–momentum equations. These are obtained from equations (5.8)–(5.9) averaged over the period of simulation. When interpreting this figure it is recalled that we have assumed that the cross-shore gradients of the radiation stress and mean setup balance each other. Hence these large terms do not appear in the balance in Fig. 5.11. In the cross-shore direction, the main terms that balance each other are the pressure gradient $gh\frac{\partial \eta}{\partial x}$ and the convective acceleration $\overline{\frac{\partial}{\partial x}\left(\tilde{U}^2 h\right)}$, which

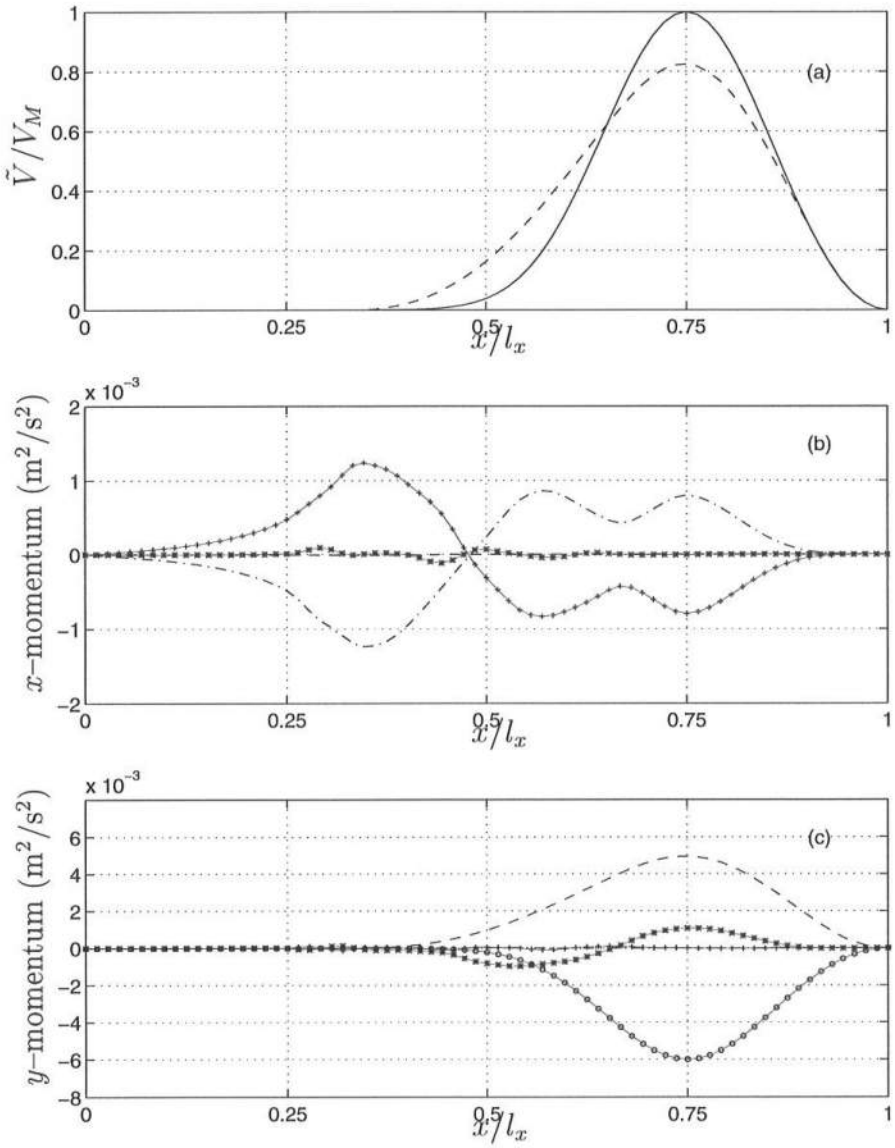

Figure 5.11: Cross shore distribution at $\frac{y}{l_y} = 0.5$ of: (a) Initial (——) and time-averaged (– –) $\tilde{V}$; (b) Terms in the x–momentum balance: $gh\frac{\partial \eta}{\partial x}$ (– ·), $\overline{\frac{\partial}{\partial x}\left(\tilde{U}^2 h\right)}$ (+), $\overline{\frac{\partial}{\partial y}\left(\tilde{U}\tilde{V}h\right)}$ (∗), $\frac{\tau_x^B}{\rho}$ (– –); (c) Terms in the y–momentum balance: $gh\frac{\partial \eta}{\partial y}$ (– ·), $\overline{\frac{\partial}{\partial y}\left(\tilde{V}^2 h\right)}$ (+), $\overline{\frac{\partial}{\partial x}\left(\tilde{U}\tilde{V}h\right)}$ (∗), $\frac{\tau_y^B}{\rho}$ (– –), $-\frac{\tau_{yS}^B}{\rho}$ (○) .

were zero at the initial condition. Due to the development of shear instabilities these two terms contribute to the mixing in the cross-shore direction. In the longshore direction, we essentially have $\overline{\frac{\partial}{\partial x}\left(\tilde{U}\tilde{V}h\right)}+\frac{\tau_y^B}{\rho}-\frac{\tau_{yS}^B}{\rho}=0$, where the overbar represents the time-averaging over the period of the simulation where the shear waves had become quasi-stationary (i.e., $t > 4$ hr). The balance in the y–momentum equation means that the forcing represented by $-\frac{\tau_{yS}^B}{\rho}$ is balanced by the bottom friction $\frac{\tau_y^B}{\rho}$ and the mixing provided by the shear wave motion $\overline{\frac{\partial}{\partial x}\left(\tilde{U}\tilde{V}h\right)}$. We note that the motion at the end of the simulated time (for the time-averaging calculation) is not the same as that at the beginning, and thus a question arises whether the time-averaging procedure is valid. It can be seen that the time-averaged terms in the momentum equations sum to nearly zero which validates the concept of analyzing the time-mean values over the simulation time. Therefore, the terms $gh\frac{\partial\eta}{\partial y}$ and $\overline{\frac{\partial}{\partial y}\left(\tilde{V}^2h\right)}$ in the longshore momentum equation are nearly zero because the motion is nearly periodic in time (and in the longshore direction, which implies $\frac{\partial}{\partial y}\simeq 0$), and we averaged over a long enough number of periods such that the residual time derivative is negligible.

From Fig. 5.11c it can be seen that the mixing due to the shear wave motion transfers momentum from the forcing in the region $\frac{x}{l_x} > 0.65$ (positive sign of $\overline{\frac{\partial}{\partial x}\left(\tilde{U}\tilde{V}h\right)}$) to the region $\frac{x}{l_x} < 0.65$ (negative sign of $\overline{\frac{\partial}{\partial x}\left(\tilde{U}\tilde{V}h\right)}$). This accounts for the increase in the longshore current seaward of $\frac{x}{l_x}=0.65$ as seen in Fig. 5.11a. A similar conclusion is reached by Özkan-Haller and Kirby (1997) by looking at the longshore average of the momentum equations, after reaching an equilibrium periodic shear wave motion.

In summary, we analyzed the development of shear waves on a plane beach, which compared well with the results of Özkan-Haller and Kirby (1997) and Allen *et al.* (1996) for the same physical situation. For a standard grid size our model

results agree favorably with those of Özkan-Haller and Kirby, who solve the same set of equations. The agreement with the simulations of Allen *et al.* is not as good, and one explanation could be that these authors assume rigid-lid in their model equations, which we believe can influence some details in the development of the instabilities. In the next section we check the accuracy of our numerical computations by showing through examples the effect the grid size has on the predicted currents for the physical conditions simulated here.

5.1.3 Variation of the spatial and temporal resolution

To examine the numerical accuracy of the scheme, and sensitivity of the simulations to the grid size it is convenient to use the simple setting of the model equations and physical domain of the previous example. First, we reduce the temporal spacing relative to that used for the previous results, and then we change the spatial grid dimensions using the combinations listed in Table 5.1. The physical domain, model equations, initial and boundary conditions for the present computations are the same as in the previous section.

Simulation A in Table 5.1 corresponds to the model parameters used in the examples in the previous section, which we designated by "standard grid" simulation. We will compare here the time series of $\tilde{U}$ and $\tilde{V}$ from simulations B–F at the location $\frac{x}{l_x} = 0.75$ and $\frac{y}{l_y} = 0.5$, with those of the results for the standard grid (simulation A). Simulation B is obtained for the same model parameters as A, except for the value of the Courant number C_r, which is halved. The results indicate that the time series of the simulations A and B (not shown) are indistinguishable from each other, and thus we conclude that halving the Courant number, i.e., the time-spacing Δt, does not change the accuracy of the computations.

Table 5.1: Values of the parameters used in numerical accuracy tests for the simulation of shear waves over a plane beach

Simulation	Δx (m)	$\frac{x_b'}{\Delta x}$	Δy (m)	$\frac{x_b'}{\Delta y}$	C_r
A	5	18	5	18	0.8
B	5	18	5	18	0.4
C	2.5	36	2.5	36	0.8
D	10	9	10	9	0.8
E	5	18	10	9	0.8
F	2.5	36	5	18	0.8

In Fig. 5.12 we show the comparison between the time series of $\tilde{U}$ and $\tilde{V}$ for the results of simulation A (thick line) and simulation C (thin line). The spatial grid-spacings in simulation C are 1/2 of those for the standard simulation (A). It can be seen in Fig. 5.12 that there are small deviations between the two time series, but the overall agreement is good, which suggests that a further reduction of the grid size will not increase the accuracy. Conversely, the results of simulations A (thick line) and D (thin line) shown in Fig. 5.13 are quite different from each other. The spatial grid-spacings for simulation D are twice as large as those of A, and four times the spacings used in C. It is seen in Fig. 5.13 that the largest deviations occur for the longshore currents: the period of the shear waves from simulation D is slightly shorter than that from A, and the period of the amplitude modulation is also different. Thus, we conclude from this comparison that doubling the grid spacing relative to the standard grid results changes the dynamics of the shear waves.

The results for simulations E and F, versus A, are presented in Fig. 5.14 and 5.15, respectively. Both computations E and F have a grid-spacing in the longshore

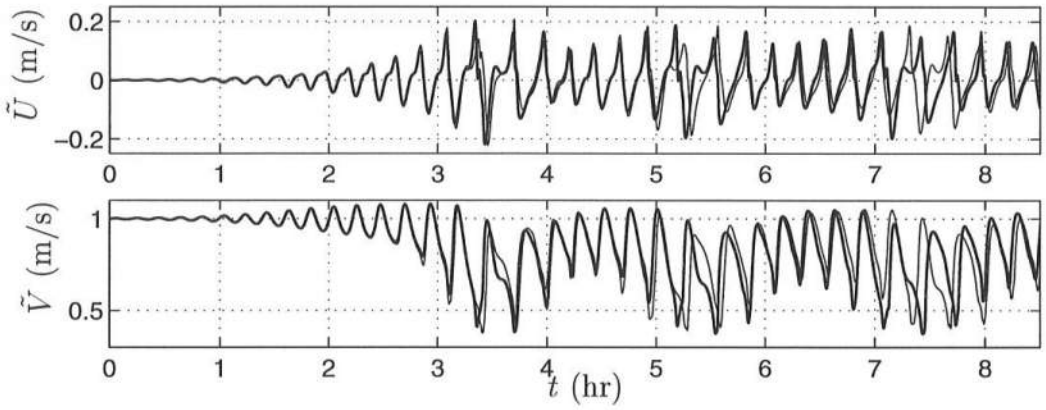

Figure 5.12: Time series of $\tilde{U}$ and $\tilde{V}$ at $\frac{x}{l_x} = 0.75$ and $\frac{y}{l_y} = 0.5$ from simulation A (thick line) and simulation C (thin line), (see Table 5.1 for details of parameters).

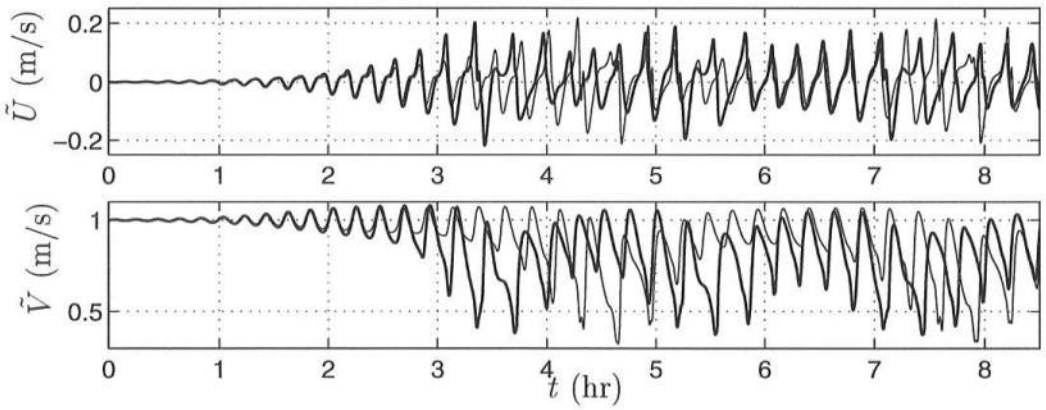

Figure 5.13: Time series of $\tilde{U}$ and $\tilde{V}$ at $\frac{x}{l_x} = 0.75$ and $\frac{y}{l_y} = 0.5$ from simulation A (thick line) and simulation D (thin line), (see Table 5.1 for details of parameters).

direction (Δy) which is twice the spacing in the cross-shore direction (Δx), (refer to Table 5.1). Simulation E has Δx equal to the value used in A, and simulation F has Δy equal to the value used in A. The comparison between the results from simulations E and F with the results from A shows once again a different dynamical behavior of the shear waves at $\frac{x}{l_x} = 0.75$ and $\frac{y}{l_y} = 0.5$. The time series of $\tilde{U}$ and $\tilde{V}$ in Fig. 5.14 are quite similar until $t \sim 4.5$ hr, but after this time the two series diverge with the modulation period of E much larger than that of A. For the comparison in Fig. 5.15 the agreement deteriorates after about 5 hr of simulation, where the largest differences are also in the modulation period.

A non-negligible discrepancy is found between the results from simulations A and F (5.15), which is somewhat inconsistent with the good agreement between A and C (5.12). Also, we find no particular pattern for the differences between simulations A and D, E. A possible explanation is that shear waves are an instability phenomena, which can have different growth rates depending on the simulation conditions, which are intrinsically different for all computations because the numerical discretization is different.

Overall, for all the time series corresponding to simulations A–F and shown in Fig. 5.12–5.15, we find the shear wave period to be quite consistent, and varying between 830 and 900 s. The shear wave propagation velocity c_S for all computations is within the interval $0.5 < \frac{c_S}{V_{SM}} < 0.54$, where V_{SM} is the maximum of the initial longshore current profile. This result is consistent with the values found by Allen *et al.* (1996) and Özkan-Haller and Kirby (1997). Therefore, though the details of the shear waves vary with the grid spacing, the global properties of the physical solution are identical for all the simulations.

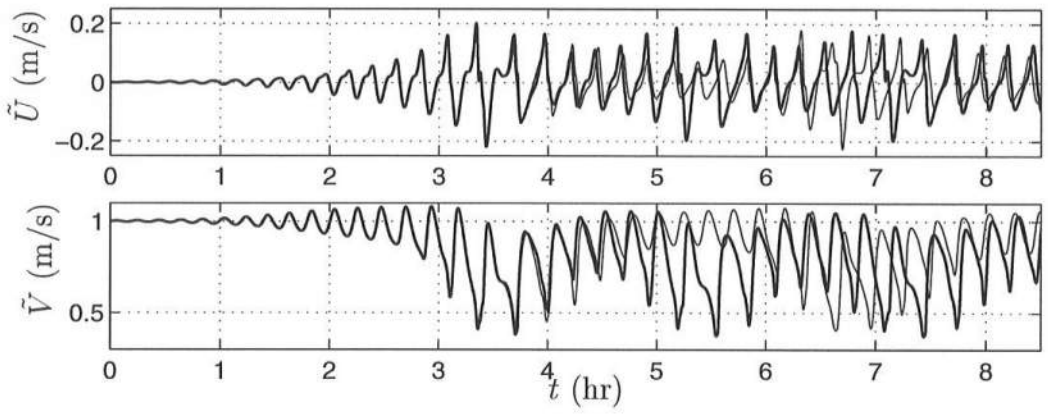

Figure 5.14: Time series of $\tilde{U}$ and $\tilde{V}$ at $\frac{x}{l_x} = 0.75$ and $\frac{y}{l_y} = 0.5$ from simulation A (thick line) and simulation E (thin line), (see Table 5.1 for details of parameters).

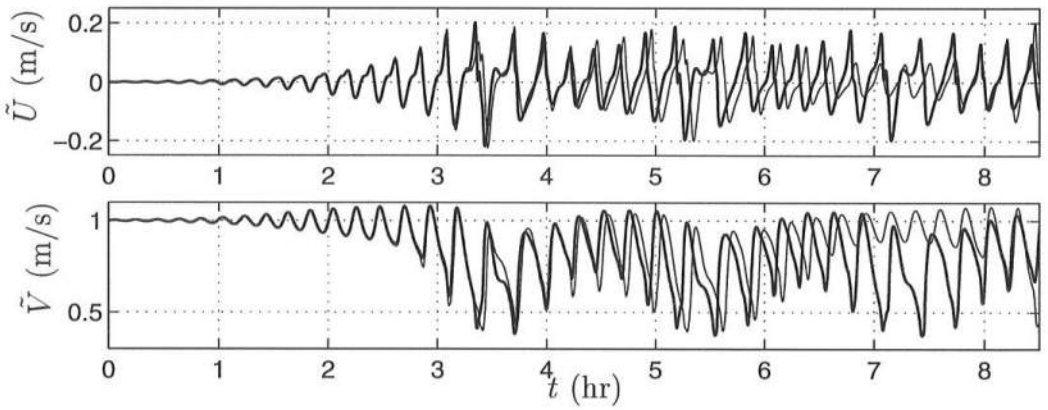

Figure 5.15: Time series of $\tilde{U}$ and $\tilde{V}$ at $\frac{x}{l_x} = 0.75$ and $\frac{y}{l_y} = 0.5$ from simulation A (thick line) and simulation F (thin line), (see Table 5.1 for details of parameters).

5.2 Mixing mechanisms on a barred beach

We have so far either neglected, or utilized a simplified model, to account for the dispersion effect due to the vertical variation of the horizontal currents. In this section we study in detail the effect of including in the model equations the interaction terms linked with the three-dimensionality of the problem.

In the example analyzed here, we choose to consider the longshore varying barred beach with a small rip-channel studied in section 4.3, and we also extend the computational region in the longshore direction. For the example studied in that section the dispersive terms were approximated by an enhanced turbulent viscosity. In the following application we model the complete governing equations (2.71)–(2.72) with and without the vertical interaction terms.

The present situation differs from those given by Svendsen and Putrevu (1994), Rodriguez *et al.* (1994), Garcez Faria *et al.* (1995) and Van Dongeren and Svendsen (1997b), among others, who included the vertically-induced momentum mixing but considered only a longshore uniform coast of a small dimension. Their solutions (except the one of Van Dongeren and Svendsen) were steady, which means that they do not account for shear wave motions. The conditions simulated by Van Dongeren and Svendsen corresponded to infragravity waves forced by obliquely-incident wave groups on a longshore uniform plane beach. Conversely, Özkan-Haller and Kirby (1996) studied the nearshore motion over a long straight barred beach with a length long enough for shear waves to develop, but approximated the 3D dispersion mechanism by an enhanced eddy viscosity model. The study of Deigaard *et al.* (1994) does include a longshore varying barred beach of a dimension long enough to allow for shear wave disturbances, and their model is only 2DH (depth-averaged currents only).

The present simulation bridges several of the above studies as we apply the fully quasi-3D model to a longshore nonuniform barred beach, which stretches for a considerable longshore distance. The role of the mixing induced by the vertically-varying currents is studied and compared with the mixing provided by the shear waves.

5.2.1 Model equations

The governing equations and closure models for the subsequent example are briefly given as follows. The equations for conservation of mass and momentum are identical to equations (2.71)–(2.72), without the surface shear stress, which then read

$$\frac{\partial \bar{\zeta}}{\partial t} + \frac{\partial \bar{Q}_\alpha}{\partial x_\alpha} = 0\,, \tag{5.23}$$

$$\begin{aligned}
&\frac{\partial \bar{Q}_\beta}{\partial t} + \frac{\partial}{\partial x_\alpha}\left(\frac{\bar{Q}_\alpha\,\bar{Q}_\beta}{h} + M_{\alpha\beta} + A_{\alpha\beta\gamma}\,\tilde{V}_\gamma\right) \\
&- \frac{\partial}{\partial x_\alpha}\left[h\left(D_{\alpha\gamma}\,\frac{\partial \tilde{V}_\beta}{\partial x_\gamma} + D_{\beta\gamma}\,\frac{\partial \tilde{V}_\alpha}{\partial x_\gamma} + B_{\alpha\beta}\,\frac{\partial \tilde{V}_\gamma}{\partial x_\gamma}\right)\right] = \\
&- g\,h\,\frac{\partial \bar{\zeta}}{\partial x_\beta} - \frac{1}{\rho}\,\frac{\partial}{\partial x_\alpha}\left(S_{\alpha\beta} - \overline{\int_{-h_o}^{\zeta} \tau_{\alpha\beta}\,dz}\right) - \frac{\tau_\beta^B}{\rho}\ .
\end{aligned} \tag{5.24}$$

where the tensors $A_{\alpha\beta\gamma}$, $B_{\alpha\beta}$, $D_{\alpha\beta}$ and $M_{\alpha\beta}$ are dependent of the vertical variation of the horizontal velocities and given by equations (2.55)–(2.58) or (2.67)–(2.70). As discussed in sections 2.1 and 2.4.1 the turbulent shear stresses are given by

$$\tau_{\alpha\beta} = \rho\,\nu_t\left(\frac{\partial V_\alpha}{\partial x_\beta} + \frac{\partial V_\beta}{\partial x_\alpha}\right)\,, \tag{5.25}$$

and the eddy viscosity ν_t is calculated by

$$\nu_t = C_1\,\kappa\sqrt{\frac{f_w}{2}}\,u_0\,h + M\,h\,(\frac{D}{\rho})^{1/3}\,. \tag{5.26}$$

In this expression we choose $M = 0.1$ and C_1 will vary with the simulations and is thus given later. The bottom shear stress is computed according to

$$\tau_\alpha^B = \frac{1}{2}\rho\, f_{cw}\, u_0\, (\beta_1\, V_{b\alpha} + \beta_2\, u_{0\alpha}) \ , \tag{5.27}$$

where u_0 is wave orbital velocity at the bottom determined from linear wave theory (see equation (2.93)), and the friction factor is $f_{cw} = 0.006$. The radiation stresses $S_{\alpha\beta}$ are determined using linear wave theory from equations (2.106)–(2.109), and $Q_{w\alpha}$ is evaluated by equation (2.113) with $A = 0.07\,HL$ and $B_0 = 0.125$, which corresponds to the use of linear wave theory. Note that a better representation for B_0 in the surf zone implies the use of a lower value (see discussion in section 2.4.4), but we chose to use the value $B_0 = 0.125$ in order to be consistent with the use of linear wave theory. The wave field is obtained from the REF/DIF1 model.

5.2.2 Results without dispersive mixing

We are interested in discussing the strength of the dispersive mixing versus that of the shear wave mixing. Therefore, we start with the presentation of the results of a simulation without the dispersive mixing terms in the model equations (5.23)–(5.24), i.e., we consider the situation where $A_{\alpha\beta\gamma}$, $B_{\alpha\beta}$, $D_{\alpha\beta}$ and $M_{\alpha\beta}$ are all equal to zero. Hence, for this simulation, the only terms in the model equations that are able to provide mixing are the turbulent shear stresses[2]. These are modeled by equation (5.26) with $C_1 = 0.75$, which is slightly larger than the expected values $C_1 \sim 0.2$. (Note that lower values of C_1 will be used later). Also, because we consider depth-uniform currents, then $V_{b\alpha}$ in equation (5.27) is equal to the depth-averaged current $\tilde{V}_\alpha$.

[2] The shear wave action is only seen as a mixing term when we look at the time-averaged quantities over a long period of time.

We consider the longshore currents over the barred beach, with a small longshore perturbation similar to a rip-channel, that was considered in section 4.3. Hence, the still water depth h_o is given by

$$h_o(x, y) = h_{0L} \, (1 + \epsilon \, F_x \, F_y) \ , \tag{5.28}$$

with h_{0L}, F_x and F_y defined by equations (4.29)–(4.32). As for the case in section 4.3, we choose $x'_M \simeq 0.92 \, l_c$, $a = \frac{4.8}{l_c}$, $b = -12$, and $\epsilon = 0.1$ (refer to that section for definitions of the variables).

The relevant parameters to define the bathymetry and domain size are the crest to shoreline distance $l_c = 120$ m, and the domain lengths in the cross-shore and longshore directions, $l_x = 4 \, l_c$, and $l_y = 16 \, l_c$, respectively. The depth at the crest of the longshore uniform section of the bar is $h_c \simeq 1.18$ m, and the numerical grid spacings are $\triangle x \simeq 4.24 h_c$ (5 m) and $\triangle y \simeq 8.48 h_c$ (10 m). The time step $\triangle t$ is calculated from the Courant number $C_r = 0.8$. For the present simulation we use periodicity at the lateral boundaries $y = 0$ and $y = 16 \, l_c$, the generating-absorbing condition (without incoming waves) at the seaward boundary $x = 0$, and a zero velocity condition ($\tilde{V} = \tilde{U} = 0$) at the shoreward boundary ($x = 4 \, l_c$) at a small water depth $\frac{h}{h_c} = 0.025$. The initial condition for the simulations is a "cold start", and the short-wave forcing is "ramped" smoothly until it reaches the steady state value in approximately $t = 400$ s.

A perspective view of the beach configuration given above is shown in Fig. 5.16. Although barely noticeable, there is a rip-channel located at $\frac{y}{l_c} = 8$ and across the bar crest. In dimensional units, the maximum absolute longshore depth variation is only $\triangle h \simeq 0.12$ m, which is of the same height or even smaller than that of a sand mega-ripple. As defined in chapter 4, the width of the rip-channel is $w_r = \frac{4}{a} = 0.84 \, l_c$ (100 m). The existence of this longshore variation in the bar geometry will, as seen

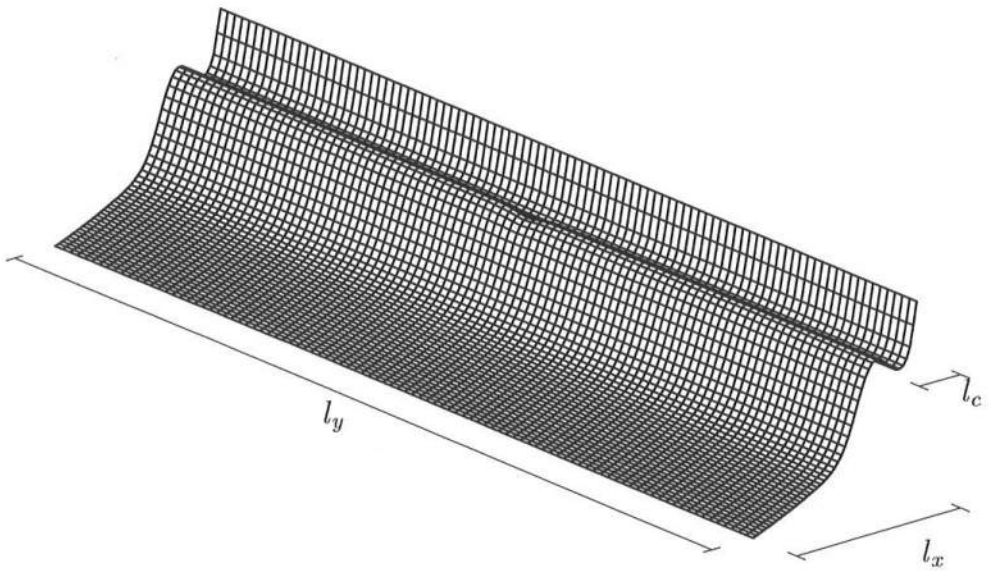

Figure 5.16: Perspective view of the barred beach for the computational example in section 5.2.

later, enhance the growth of shear waves. It can also contribute to significant modifications of the wave field as will be demonstrated in section 5.3.

The incident wave conditions are chosen so that the wave height at the seaward boundary ($x = 0$) is $H_o = 0.9\,h_c$ (1.06 m) and the incident wave angle is $\alpha_{w0} = 7.5°$ with the shore normal direction x. The wave period is $T = 14.4\sqrt{h_c/g}$ (5 s). The wave field is calculated using REF/DIF1, where a breaking criterion $H_b/h_b = 0.78$ is used. A contour plot of the predicted wave heights and wave angles for the given incident wave conditions and bathymetry is given in Fig. 5.17. For reference the bathymetric contours are also given. Fig. 5.18 shows the cross-shore variation of the normalized wave height H/H_b (top panel) at the longshore uniform beach section ($y = 0$) and over the rip-channel ($y = 8\,l_c$). Both figures show that the wave field is nearly longshore uniform with breaking occuring at $x/l_c = 2.75$ (or in the seaward oriented coordinate system $x'/l_c = 1.25$). The short-wave angle at

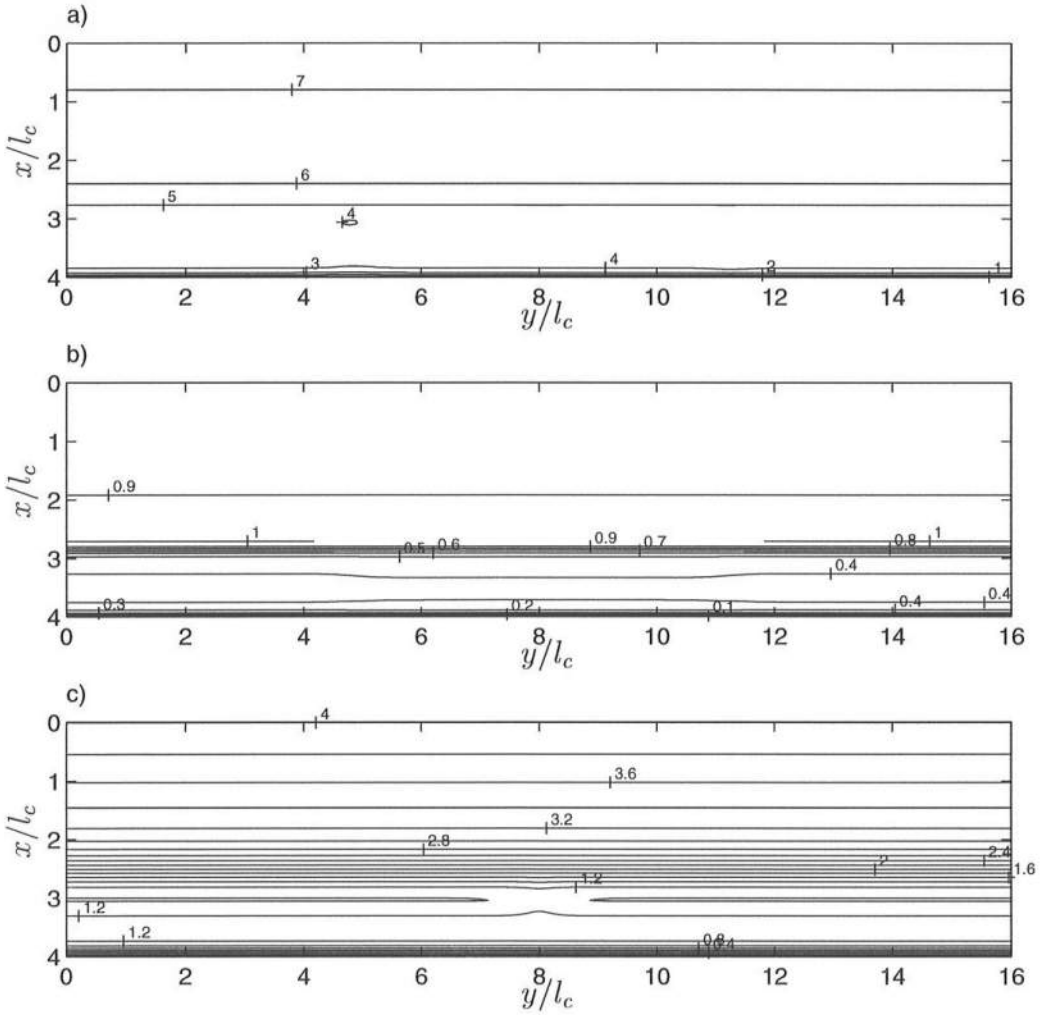

Figure 5.17: Contour plots of: a) wave angle $\alpha_w(^\circ)$; b) wave height H/H_b; and c) still water depth h_o/h_c.

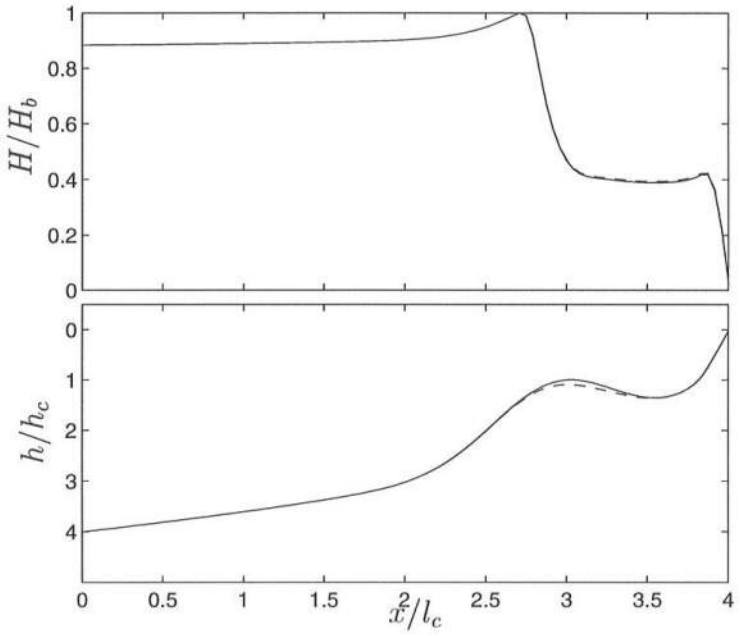

Figure 5.18: Wave height and bottom cross-shore variations over the barred beach at two longshore positions: $y = 0$ (solid line) and $y = 8\,l_c$ (dashed line).

the breaking point is $\alpha_{wb} \simeq 5°$. Wave breaking is intense just before and over the bar crest, and then the waves reform slightly past the bar-crest and propagate over the bar-trough before a second breaking occurs at the foreshore slope of the beach face. Thus, the radiation stresses forcing is strong over the bar-crest and at the beach face, and essentially zero over the trough, where no dissipation takes place.

Fig. 5.19 shows the instantaneous depth-averaged velocity vectors at four different times during the simulation. The first three pictures are at early stages of the computation, and show how the growth of shear waves starts at the rip-channel location. Looking consecutively at plots (a), (b) and (c) shear instabilities develop continuously at $y = 8\,l_c$, where the small channel is, and propagate with the longshore current downstream. The longshore periodicity is clearly seen in plot (b),

where the initial shear instabilities have moved past $y = 16\,l_c$ and are at that instant located at $y \simeq 1\,l_c$. Between subplots (c) and (d) there is a significant time lapse (3.6 hr). We see that during this time the predicted predominant wavelength of the shear waves has increased considerably, which means that vortices have merged. This frequency downshift is similar to that observed by Özkan-Haller and Kirby (1997) of subharmonic transition between shear wavelengths. The increase in wavelength is accompanied by an increase in the shear wave period as it will be seen in the time series plots. To further illustrate the dynamics of the shear waves, Fig. 5.20 shows the plots of the vorticity density ($\Psi = \frac{\partial \tilde{V}}{\partial x} - \frac{\partial \tilde{U}}{\partial y}$). The light shadings indicate positive vorticity and the dark areas negative vorticity. In Fig. 5.19(c) and 5.20(a) it is seen that the vortices at $t = 1680$ s are very periodic and concentrated near the bar-crest. In fact, the vortices at $t = 1680$ s have larger vorticity (in absolute value) than at the latter stages. At $t = 14693$ s, when vortex pairing has already occured, the nearshore currents and the associated vorticity are significantly more irregular, and we notice that the vortices extend further shorewards and seawards from the bar-crest than at the early stages. The linear stretches of the vorticity that can be seen in some longshore locations in Fig. 5.20(b) are an indication of a typical longshore current profile at those locations. It is interesting to note that Özkan-Haller and Kirby (1997) have found for most of their computations that the vortices released by the shear instabilities travel further seawards than in the present situation. This is most likely to be caused by the lower friction values used by those authors relative to ours. Other computations (not shown here) for the present topography with lower friction coefficients indicated that the vortices extended further offshore, in a similar fashion with the results of Özkan-Haller and Kirby.

Time series of the normalized cross-shore velocity $\tilde{U}/c_c$ and longshore velocity $\tilde{V}/c_c$ at different locations are given in Fig. 5.21 and 5.22, where $c_c = \sqrt{gh_c} \simeq 3.4$ m/s. The first of these two figures depicts times series at three locations along

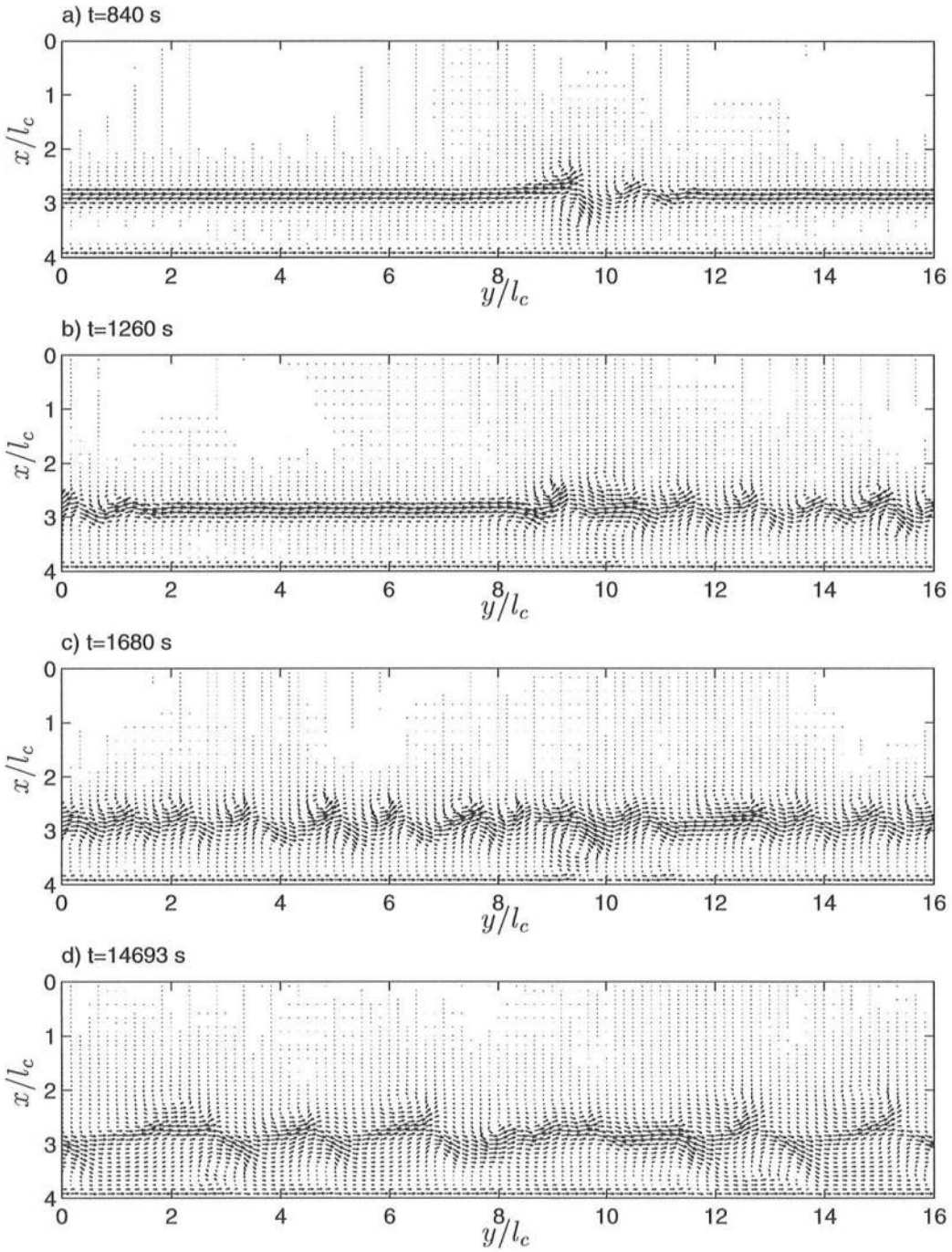

Figure 5.19: Depth-averaged current vectors at four instants of the simulation, for the case without dispersive mixing.

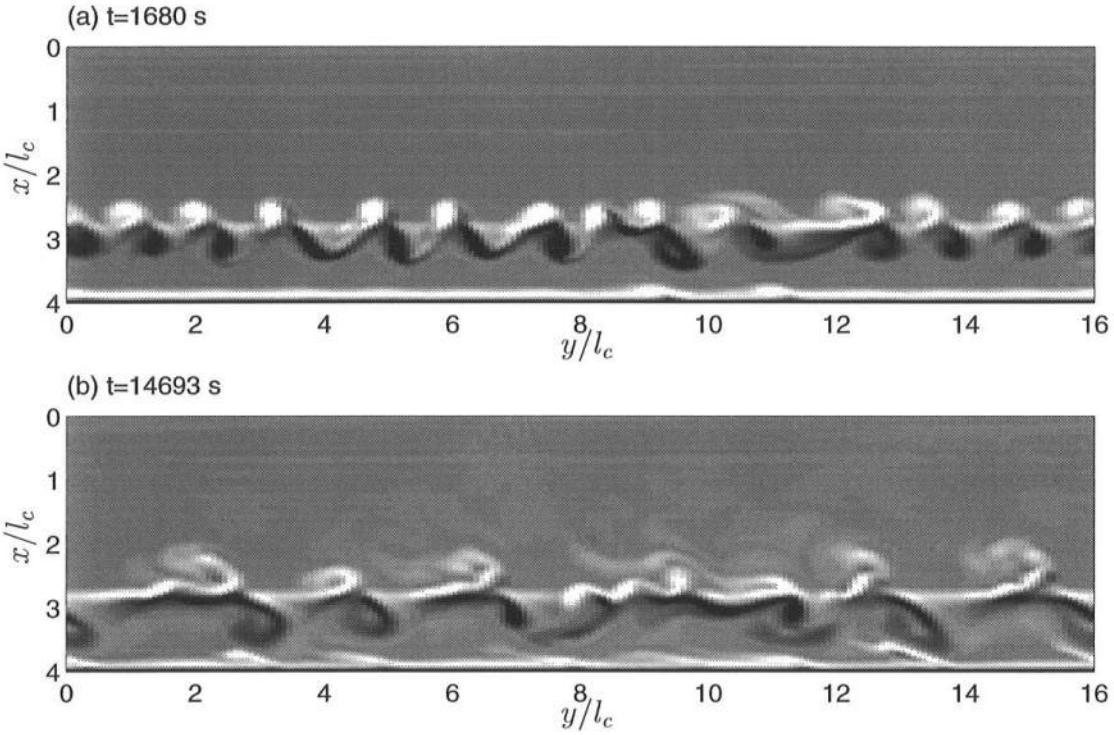

Figure 5.20: Density plots of the vorticity at two instants of the simulation, for the case without dispersive mixing. (Negative and positive vorticities correspond to dark and light shadings).

the rip-channel (seaward of the bar-crest, over the bar-crest and over the bar-trough), and the second shows the time series at the same cross-shore locations, but at $y = 0$, which corresponds to the mid-distance between multiple rip-channels (because of the lateral periodicity condition). Focusing on the time series of $\tilde{U}/c_c$ in Fig. 5.21 it is first observed that the velocity magnitudes at the different cross-shore positions are different, indicating that shear waves are more intense seaward and over the bar-crest. Second, we notice that the predominant shear wave period changes around $t = 4000$ s, and that even after that time the shear waves have a broad frequency band. Third, is appears that the predominant period at the seaward location $x = 2.5\,l_c$ is significantly larger than that at the trough location $x = 3.5\,l_c$. Hence, the dynamics in those two regions appear to be different. The time series of $\tilde{V}/c_c$ shown in Fig. 5.21 confirm the above observations. It is also seen that the magnitudes of the deviations from the mean of $\tilde{V}/c_c$ are comparable to those of $\tilde{U}/c_c$.

Turning the attention to Fig.5.22, we notice the same features as in Fig.5.21. However, the dynamics of the shear waves at this location ($y = 0$) are somewhat different from those at $y = 8\,l_c$, indicating that the shear waves did not merely propagate downstream from $y = 8\,l_c$. Because the present shear waves are very dynamic, vortices are formed and destroyed along the meandering currents, which change the local signature of these instabilities.

From the time series and frequency spectra (not shown) of $\tilde{U}$ and $\tilde{V}$ we can estimate the peak period of the shear disturbances. For the present simulation we find that at $y = 0$, $x = 3\,l_c$ the peak period is approximately within the range $700 < T < 1400$ s. The shear wavelength can also be approximately estimated from Fig. 5.19 and the values are within $2.3\,l_c < L < 3.2\,l_c$. Hence, we can estimate the shear wave velocity as $c_S = \frac{L}{T}$ which gives $c_S \simeq 0.08$–$0.12\,c_c$ or (in dimensional units) $c_S \simeq 0.27 - 0.40$ m/s. Note that the maximum time-averaged longshore current is

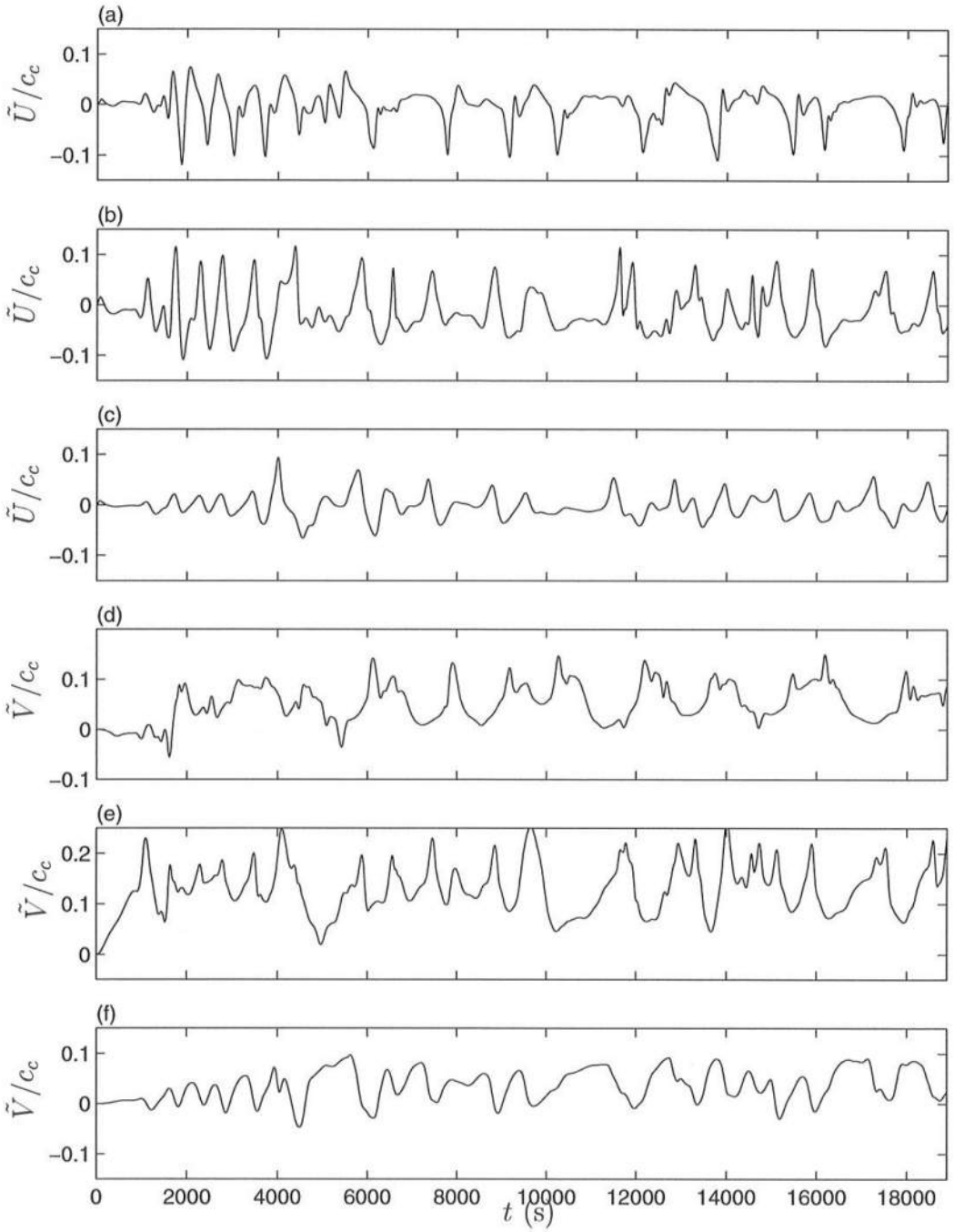

Figure 5.21: Time series of $\tilde{U}/c_c$ (3 upper plots) and $\tilde{V}/c_c$ (3 lower plots), where $c_c = (g\,h_c)^{0.5} \simeq 3.4$ m/s, for the case without dispersive mixing, at $y = 8\,l_c$ and: (a),(d) $x = 2.5\,l_c$; (b),(e) $x = 3\,l_c$; (c),(f) $x = 3.5\,l_c$.

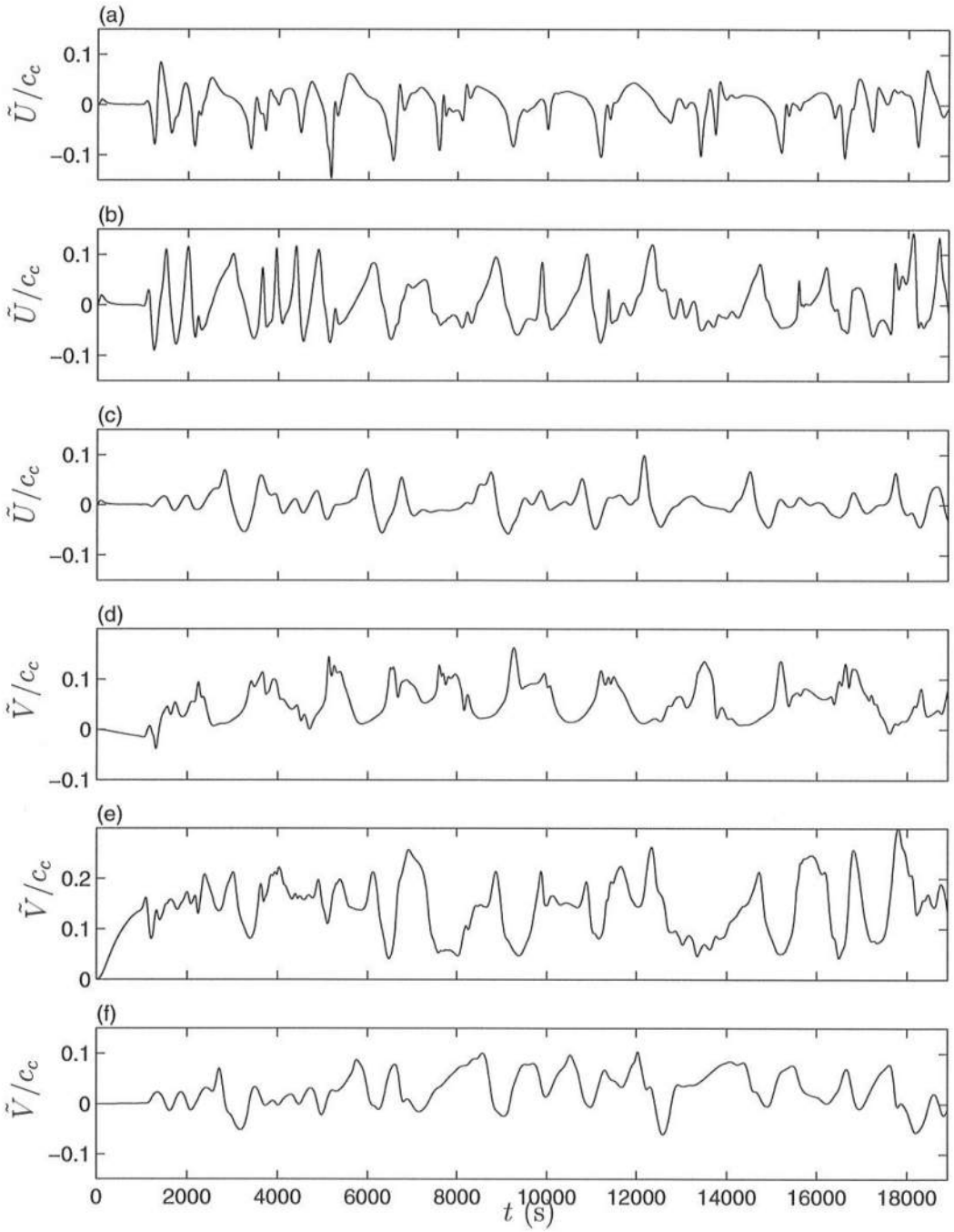

Figure 5.22: Time series of $\tilde{U}/c_c$ (3 upper plots) and $\tilde{V}/c_c$ (3 lower plots), where $c_c = (g\,h_c)^{0.5} \simeq 3.4$ m/s, for the case without dispersive mixing, at $y = 0$ and: (a),(d) $x = 2.5\,l_c$; (b),(e) $x = 3\,l_c$; (c),(f) $x = 3.5\,l_c$.

$\tilde{V}_M = 0.18\, c_c$, and hence the ratio of the shear wave celerity and the maximum longshore current is between 0.44 and 0.67, which is comparable to that suggested by field measurements (Oltman-Shay *et al.*, 1989; Dodd *et al.*, 1992).

Time-averaged properties of the flow field are shown in Fig. 5.23. The time-averaging is performed over the period of time starting at $t = 4000$ s until the time at the end of the simulation (see Fig. 5.22 for reference). The depth-averaged velocity vectors shown in Fig. 5.23a indicate a slight variation of the flow at the region of the rip-channel ($y = 8\, l_c$). This is confirmed by the velocity contours of $\tilde{U}/c_c$ and $\tilde{V}/c_c$ in subplots (c) and (d), respectively. The maximum depth-averaged cross-shore velocity is oriented seaward and has a magnitude of $0.025\sqrt{g\, h_c}$, which in dimensional units is ~ 0.10 m/s. Note that the depth-averaged cross-shore current away from the rip-channel is zero, which means that the wave-induced shoreward mass flux is locally balanced by the return current (undertow). The results show that even a small rip-channel is able to disturb the otherwise longshore uniform flow significantly. Last, Fig. 5.23b shows that the longshore variation of the mean free-surface elevation $\frac{\bar{\zeta}}{h_c}$ is negligible.

It is relevant to point out that, although there is a slight depression in the bottom topography simulating a rip-channel, rip-currents are not predicted for the current conditions. This is due to the fact that the wave field as well as the mean surface elevation are very homogeneous in the longshore direction. It will be seen in section 5.3 that a change in the above properties will cause the formation of rip-currents over the rip-channel.

The cross-shore profiles of the time-averaged mean surface elevation, cross-shore and longshore (depth-averaged) velocities at four different longshore locations

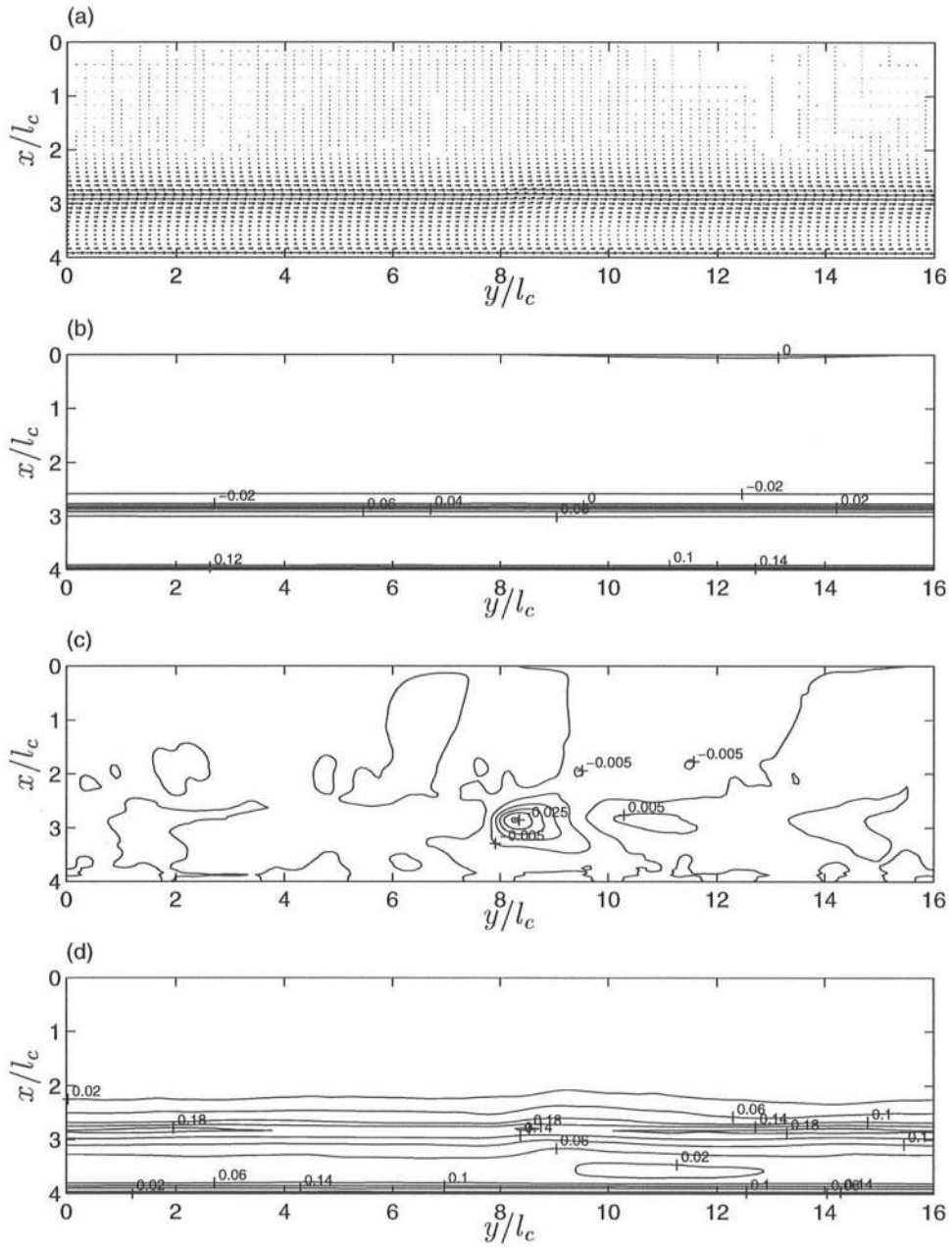

Figure 5.23: Time-averaged flow field for the case without dispersive mixing: a) depth-averaged velocity vectors. (b), (c), (d) Contour plots of: b) mean free-surface elevation $\bar{\zeta}/h_c$; c) cross-shore velocity $\tilde{U}/c_c$; d) longshore velocity $\tilde{V}/c_c$.

($\frac{y}{l_c} = 0$, $\frac{y}{l_c} = 7$, $\frac{y}{l_c} = 8$, $\frac{y}{l_c} = 9$) are shown in Fig. 5.24. The mean free-surface elevation is fairly longshore uniform, but the profiles of $\tilde{U}$ and $\tilde{V}$ vary with the location. The largest variations are observed, as expected, around the the rip-channel but are more pronounced slightly downstream of it due to the inertial acceleration as demonstrated soon. The figure for the longshore current shows the "classical" double-peaked distribution caused by the breaking over the bar and at the foreshore, but it also shows a significant current in the trough where the wave-induced forcing is zero. It turns out that this non-negligible current is forced by the redistribution of the wave-induced forcing by shear waves.

It is therefore interesting to analyze the contribution of each of the terms in the momentum equations (5.23)–(5.25), not accounting for the dispersive mixing terms. For such, let us consider the momentum balance of the time-averaged (over the period of simulation) governing equations, as we did in section 5.1. Fig. 5.25 shows the cross-shore distribution of the magnitude of each of the terms far away from the rip-channel ($y = 0$), in the x–momentum equation (top) and y–momentum equation (center). For the x–momentum balance the only two significant terms are the wave-forcing $\frac{1}{\rho}\frac{\partial S_{xx}}{\partial x}$ and the pressure term $gh\frac{\partial \bar{\zeta}}{\partial x}$. In the y–momentum balance there are other important contributions, though. In the region of breaking over the bar the wave-forcing $\frac{1}{\rho}\frac{\partial S_{xy}}{\partial x}$ is balanced by the bottom shear stress and the mixing provided by the shear waves, which is represented by the time-averaged convective accelerations $\overline{\frac{\partial}{\partial y}\left(\frac{\bar{Q}_y^2}{h}\right)}$ and $\overline{\frac{\partial}{\partial x}\left(\frac{\bar{Q}_x\bar{Q}_y}{h}\right)}$. The magnitude of $\overline{\frac{\partial}{\partial x}\left(\frac{\bar{Q}_x\bar{Q}_y}{h}\right)}$ is quite large, which means that most of the mixing is provided by the interaction between $\tilde{U}$ and $\tilde{V}$; the contribution of the interaction of $\tilde{V}$ with itself is much smaller due to the quasi-longshore uniformity of the motion studied here. In the trough region all the terms are relatively small, but the momentum mixing due to the shear waves is able to transfer momentum from the breaking zone to the trough region.

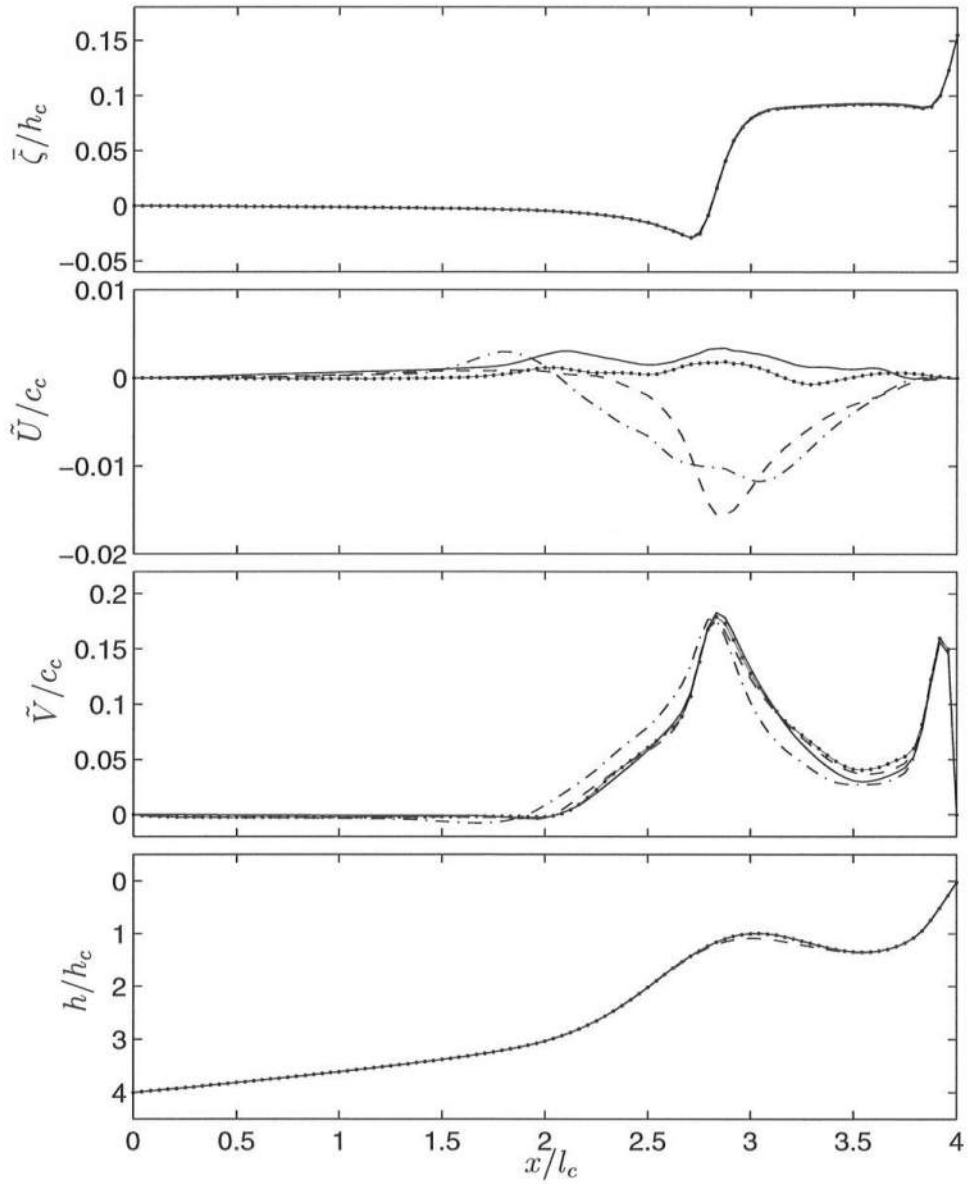

Figure 5.24: Cross shore distribution at $\frac{y}{l_c} = 0$ (——), $\frac{y}{l_c} = 7$ (–•–), $\frac{y}{l_c} = 8$ (– –), and $\frac{y}{l_c} = 9$ (– ·), for the case without dispersive mixing, of time-averaged flow properties: (a) $\bar{\zeta}/h_c$; (b) $\tilde{U}/c_c$; (c) $\tilde{V}/c_c$; (d) h_o/h_c .

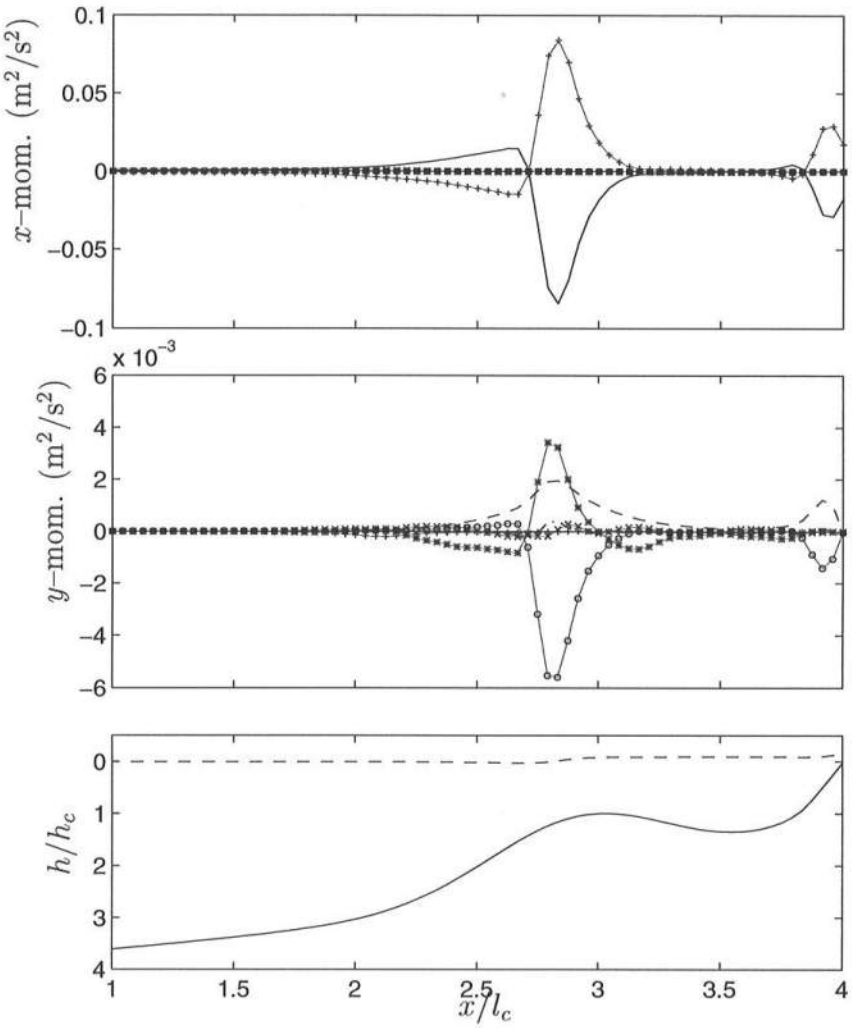

Figure 5.25: Cross shore distribution at $y = 0$ of (time-averaged): (a) Terms in the x–momentum balance: $gh\frac{\partial \bar{\zeta}}{\partial x}$ (+), $\frac{1}{\rho}\frac{\partial S_{xx}}{\partial x}$ (——), $\frac{1}{\rho}\frac{\partial S_{yx}}{\partial y}$ (○), $\overline{\frac{\partial}{\partial x}\left(\frac{\bar{Q}_x^2}{h}\right)}$ (×), $\overline{\frac{\partial}{\partial y}\left(\frac{\bar{Q}_x\bar{Q}_y}{h}\right)}$ (∗), – turb. mixing (– ·), $\frac{\tau_x^B}{\rho}$ (– –); (b) Terms in the y–momentum balance: $gh\frac{\partial \bar{\zeta}}{\partial y}$ (+), $\frac{1}{\rho}\frac{\partial S_{yy}}{\partial y}$ (——), $\frac{1}{\rho}\frac{\partial S_{xy}}{\partial x}$ (○), $\overline{\frac{\partial}{\partial y}\left(\frac{\bar{Q}_y^2}{h}\right)}$ (×), $\overline{\frac{\partial}{\partial x}\left(\frac{\bar{Q}_x\bar{Q}_y}{h}\right)}$ (∗), – turb. mixing (– ·), $\frac{\tau_y^B}{\rho}$ (– –); (c) bottom variation (——), and mean surface elevation (– –) .

The cross-shore distribution of the terms in the time-averaged momentum balance at the rip-channel ($y = 8\,l_c$) is shown in Fig. 5.26. At this longshore location the wave-forcing is nearly the same as at $y = 0$, but the distribution of the convective accelerations in the y–momentum is quite different. The term $\overline{\frac{\partial}{\partial y}\left(\frac{\bar{Q}_y^2}{h}\right)}$ is no longer negligible compared to $\overline{\frac{\partial}{\partial x}\left(\frac{\bar{Q}_x\bar{Q}_y}{h}\right)}$, although it has the opposite sign, and thus the sum of these two terms at this cross-section is similar to that at $y = 0$. Hence, the bottom shear stress profile at $y = 8\,l_c$ is only slightly different from that at $y = 0$, which means that the longshore current is similar (as depicted in Fig. 5.24). This change in the distribution of the convective accelerations from one longshore location to the other is due to existence of the rip-channel, which enhances the contribution of the longshore gradients ($\frac{\partial}{\partial y}$) of the flow variables. Last, we notice that at both cross-sections the longshore pressure gradient $gh\frac{\partial \bar{\zeta}}{\partial y}$ is negligible. We find though that at $y = 7\,l_c$ (not shown) the magnitude of the longshore pressure gradient in the trough region is comparable to that of the bottom friction and shear-waves induced mixing.

In summary, we have seen in this example that, without the dispersive mixing, strong shear waves are predicted for the present conditions. For the chosen incoming wave characteristics on the barred beach the longshore current (cross-shore) profile has a double peak, and a relatively weak but not negligible current in the trough region caused by the mixing provided by the shear waves dispersion.

5.2.3 Results with dispersive mixing

A second set of simulations was then carried out where the dispersive terms, which account for the depth variation of the horizontal currents, were no longer neglected. Thus, in this subsection we use the full SHORECIRC model to study the nearshore currents over the same barred beach with a rip-channel, and governed

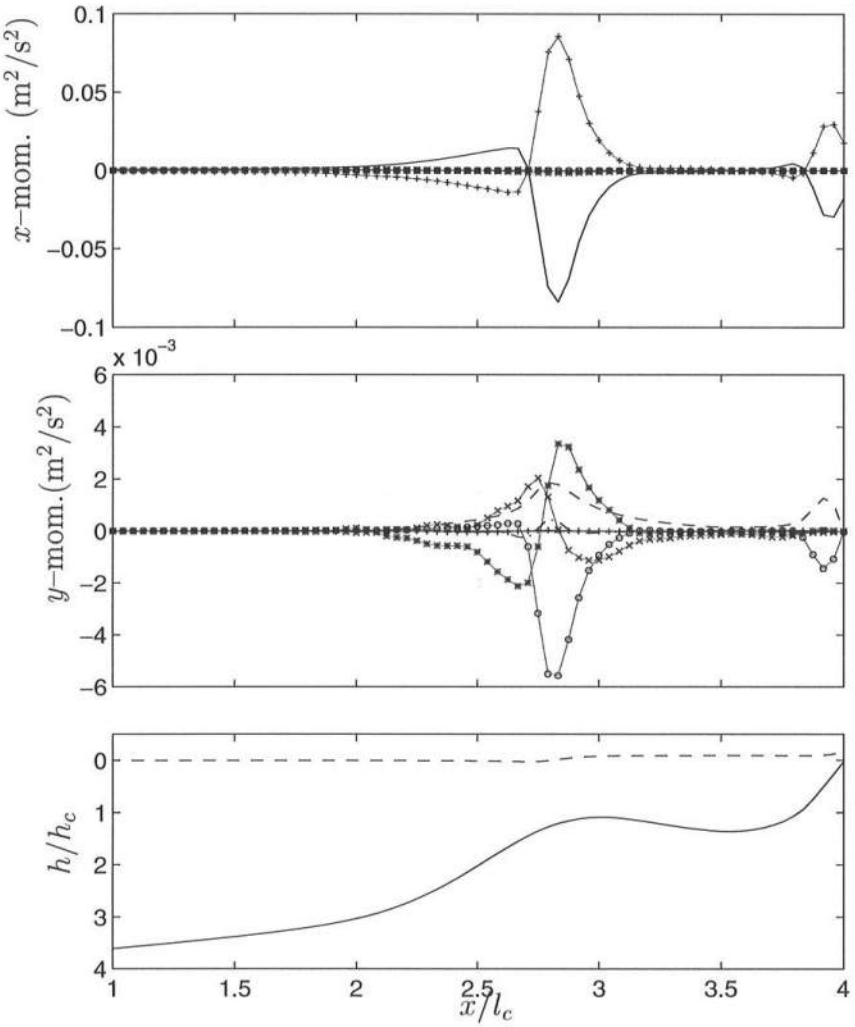

Figure 5.26: Cross shore distribution at $y = 8\,l_c$ of (time-averaged): (a) Terms in the x–momentum balance: $gh\frac{\partial \bar{\zeta}}{\partial x}$ (+), $\frac{1}{\rho}\frac{\partial S_{xx}}{\partial x}$ (——), $\frac{1}{\rho}\frac{\partial S_{yx}}{\partial y}$ (○), $\overline{\frac{\partial}{\partial x}\left(\frac{\bar{Q}_x^2}{h}\right)}$ (×), $\overline{\frac{\partial}{\partial y}\left(\frac{\bar{Q}_x\bar{Q}_y}{h}\right)}$ (∗), – turb. mixing (– ·), $\frac{\tau_x^B}{\rho}$ (– –); (b) Terms in the y–momentum balance: $gh\frac{\partial \bar{\zeta}}{\partial y}$ (+), $\frac{1}{\rho}\frac{\partial S_{yy}}{\partial y}$ (——), $\frac{1}{\rho}\frac{\partial S_{xy}}{\partial x}$ (○), $\overline{\frac{\partial}{\partial y}\left(\frac{\bar{Q}_y^2}{h}\right)}$ (×), $\overline{\frac{\partial}{\partial x}\left(\frac{\bar{Q}_x\bar{Q}_y}{h}\right)}$ (∗), – turb. mixing (– ·), $\frac{\tau_y^B}{\rho}$ (– –); (c) bottom variation (——), and mean surface elevation (– –) .

by the complete set of equations (5.23)–(5.25). The turbulent mixing and bottom shear stress are modeled as before, with $C_1 = 0.75$ and $f_{cw} = 0.006$. The bathymetry and wave field variables are given in Fig. 5.16–5.18. The results presented in the following should be compared with those in the previous subsection, and show the changes caused by the dispersive mixing.

The instantaneous velocity field of the depth-averaged currents at four different times is shown in Fig. 5.27. As in Fig 5.19 a perturbation of the longshore velocity is started at the rip-channel. However, at $t = 1680$ s (see Fig 5.19c, and Fig 5.27b) the magnitude of the shear waves is seen to be much smaller than in the case without dispersive mixing. Even at $t = 2519$ s the shear waves have not developed yet all over the domain. Hence, there is an initial growth of shear waves triggered by the rip-channel at the initial stages of the simulation. This growth only continues up to a certain point and it takes a longer time for the present case for shear waves to be formed everywhere. A comparison of the velocity vectors at $t = 14693$ s for the two simulations reveals that the shear waves for the case with dispersive mixing remain quite regular and periodic, whereas in the case without the dispersion the shear wave motion develops into a flow pattern that could resemble large scale turbulence.

Times series of the nondimensional cross-shore and longshore depth-averaged velocities at the rip-channel axis ($y = 8\,l_c$) and three cross-shore locations are given in Fig. 5.28. Notice that the velocity range in these plots is slightly less than one-half of that for the plots in Fig. 5.21. Hence, comparing the two figures, we confirm that the magnitude of the shear waves predicted for the case with dispersive mixing is considerably smaller than that for the case without. Second, we notice that the amplitude of the variations in the longshore velocity $\tilde{V}/c_c$ at $x = 2.5\,l_c$ is much smaller than that at $x = 3\,l_c$. This result is in contrast with the similar magnitudes

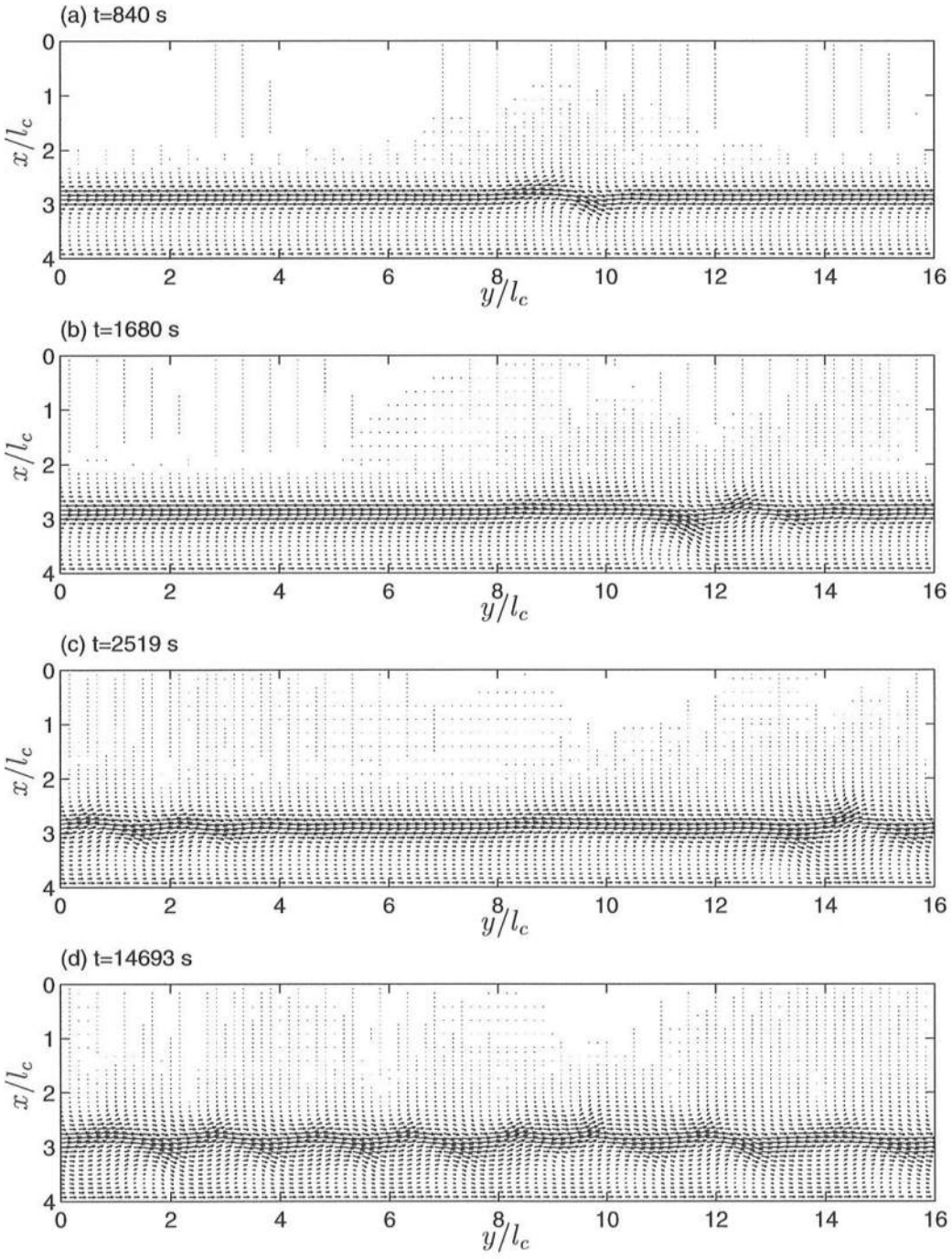

Figure 5.27: Depth-averaged current vectors at four instants of the simulation, for the case with dispersive mixing.

of the velocity variations found previously at the same locations for the case without dispersive mixing (Fig. 5.21). Thus, the shear waves for the case with dispersive mixing are almost non-existent seaward of the bar crest, which means they are concentrated over the bar crest. From Fig. 5.28 it is also observed that the shear waves in the presence of dispersive mixing are very periodic, unlike the results in Fig. 5.21. The period of the shear waves is $T \simeq 530$ s, and the wavelength is $L \simeq 2\,l_c$, which means that the shear wave celerity is $c_S \simeq 0.13\,c_c$ or (in dimensional units) $c_S \simeq 0.45$ m/s. The ratio of the shear wave celerity over the maximum depth-averaged longshore current is then $\frac{c_S}{V_M} \simeq 0.65$. In summary, these plots show that the inclusion of the vertical dispersive mixing limits the growth of the shear wave instabilities.

It is therefore interesting to look at the distribution of the time-mean variables (averaged over the period of simulation). The contour plots of the flow variables are similar to those shown in Fig. 5.23, and thus we turn to the more revealing cross-shore profiles shown in Fig. 5.29. From the top to the bottom the graphs represent the cross-shore variation of $\bar{\zeta}/h_c$, $\tilde{U}/c_c$, $\tilde{U}/c_c$ and h_o/h_c at the longshore locations $\frac{y}{l_c}=0$, $\frac{y}{l_c}=7$, $\frac{y}{l_c}=8$, $\frac{y}{l_c}=9$. This figure indicates that the longshore velocity is quite longshore uniform with the largest variation slightly downstream of the rip-channel location. The longshore current profile exhibits a double-peak, but also a non-negligible velocity in the trough region. The maximum is located at $x \simeq 2.85\,l_c$, which is slightly shoreward of the breaking point location ($x = 2.75\,l_c$). The latter location coincides with the position of the minimum set-down, (REF/DIF1 does not account for any "spatial-lag" transition between the transfer of momentum from the short-wave motion to the mean flow motion).

A comparison between the time-averaged, depth-averaged longshore current, $\tilde{V}/c_c$, for the case with and without dispersive mixing is shown in Fig. 5.30. In

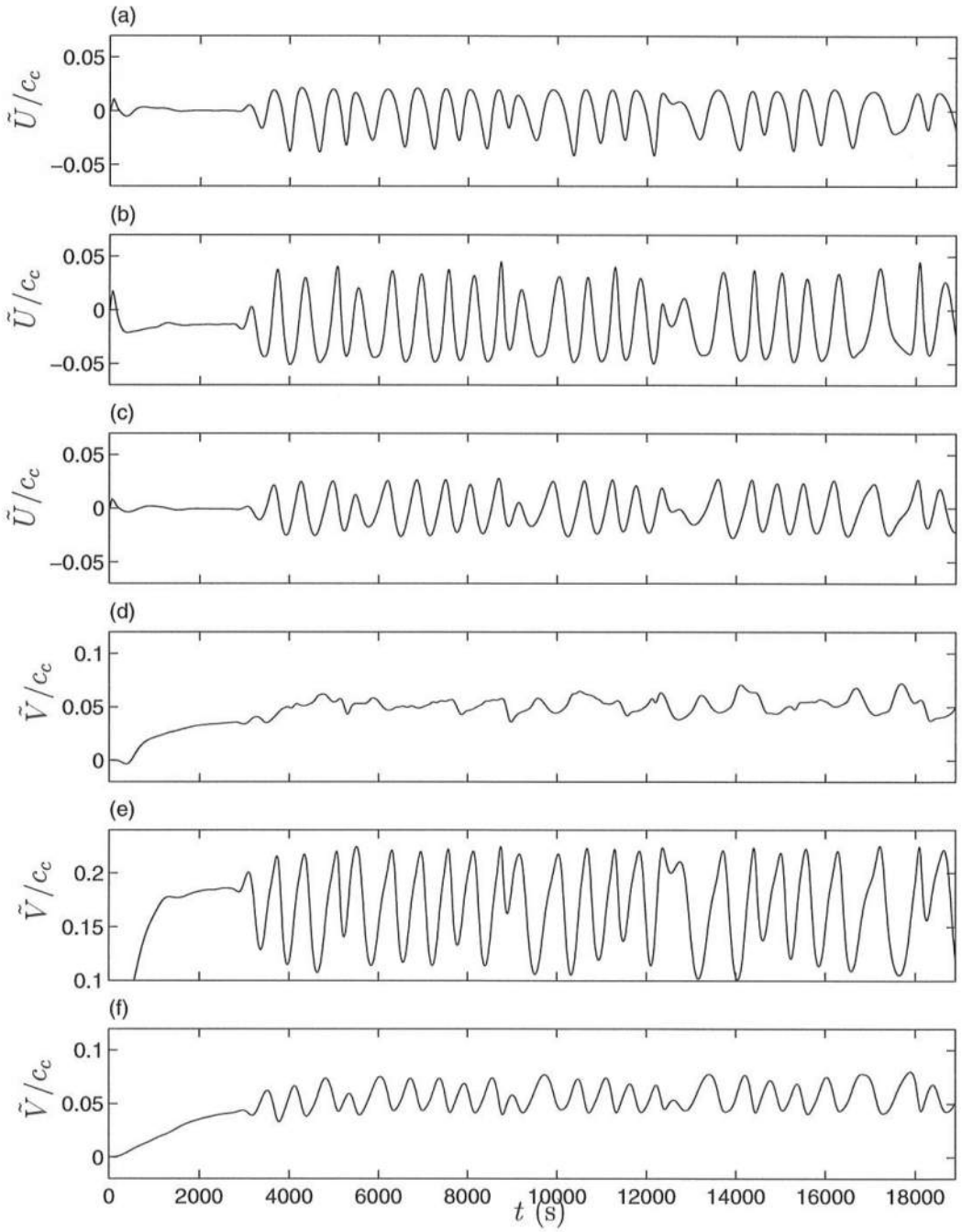

Figure 5.28: Time series of $\tilde{U}/c_c$ (3 upper plots) and $\tilde{V}/c_c$ (3 upper plots), where $c_c = (g\,h_c)^{0.5} \simeq 3.4$ m/s, for the case with dispersive mixing, at $y = 0$ and: (a),(d) $x = 2.5\,l_c$; (b),(e) $x = 3\,l_c$; (c),(f) $x = 3.5\,l_c$.

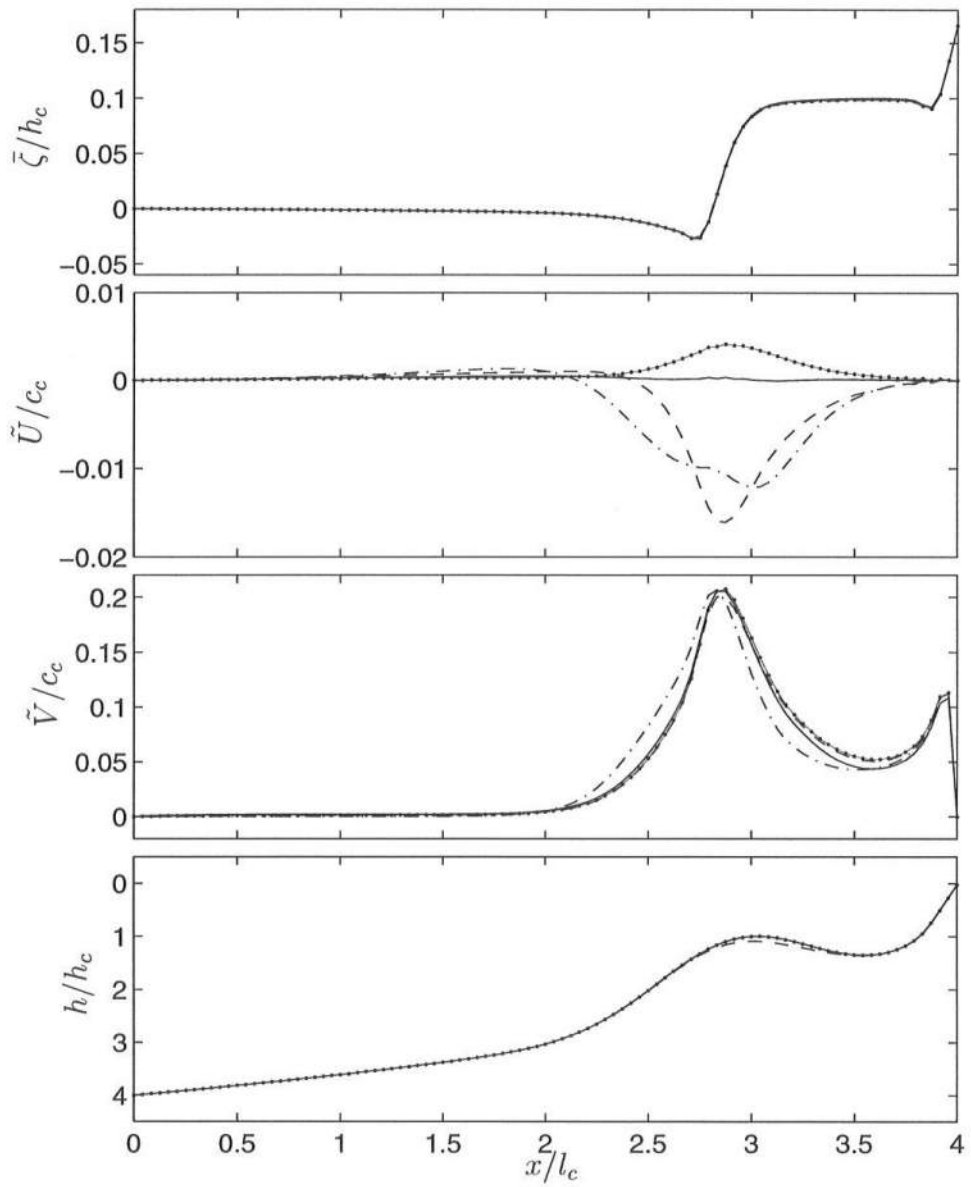

Figure 5.29: Cross shore distribution at $\frac{y}{l_c} = 0$ (——), $\frac{y}{l_c} = 7$ (–•–), $\frac{y}{l_c} = 8$ (– –), and $\frac{y}{l_c} = 9$ (– ·), for the case without dispersive mixing, of time-averaged flow properties: (a) $\bar{\zeta}/h_c$; (b) $\tilde{U}/c_c$; (c) $\tilde{V}/c_c$; (d) h_o/h_c .

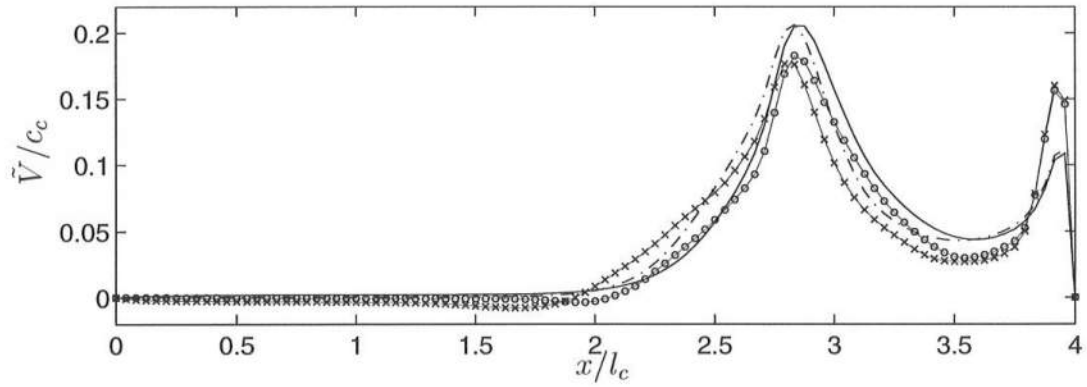

Figure 5.30: Cross shore distribution of (time-averaged) $\tilde{V}/c_c$ with the dispersive mixing at $\frac{y}{l_c} = 0$ (——) and $\frac{y}{l_c} = 9$ (– ·), and without the dispersive mixing at $\frac{y}{l_c} = 0$ (–○–) and $\frac{y}{l_c} = 9$ (–×–).

this figure is plotted the cross-shore distribution of $\tilde{V}/c_c$ at two longshore locations ($\frac{y}{l_c} = 0, \frac{y}{l_c} = 9$). First, we notice the overall similarity between the current profiles for the two situations. In one case, the mixing is solely provided by the shear wave motion, which is very energetic. In the second scenario, the mixing is provided by the vertical variation of the currents and by a weak shear wave motion. Second, it can be seen that the depth-averaged velocities for the case with the 3D-mixing are larger than those for the case without, except near the shoreline. Hence, it appears that the cross-shore integrated longshore flow in one situation is larger than in the other, which could seem to contradict the global balance of forces over the entire domain:

$$\int_0^{l_y} S_{xy}(0,y)\,dy = \int_0^{l_x}\int_0^{l_y} \tau_y^B\,dx\,dy\,. \tag{5.29}$$

Closer analysis of the longshore velocities for the case with the dispersive mixing reveals that because they vary over the depth, the velocity at the bottom V_b is smaller than the depth-averaged velocity $\tilde{V}$. It therefore requires a larger value of $\tilde{V}$ to generate the bottom shear stress required to satisfy (5.29).

The vertical variation of the horizontal currents has been used to calculate the dispersive mixing terms. At a first approximation, the vertical profile $V_{1\alpha}^{(0)}(z)$ of the horizontal currents is given by expression (2.47), where depth-uniform eddy viscosity and local steady-state were assumed. Equation (2.47) is therefore valid at each time-step, but it can also be used to compute the time-averaged (over the whole simulation) vertical profile from the known time-averaged values of $\tilde{V}_\alpha$ and the bottom shear stress.

The local depth variation of time-averaged (over the period of simulation) current $V_\alpha = \tilde{V}_\alpha + V_{1\alpha}^{(0)}$ (normalized by $c_c = \sqrt{g\,h_c}$) at several locations along the middle of the rip-channel ($y = 8\,l_c$) is given in Fig. 5.31. For reference the breaking point is indicated as "B.P.", and the dashed line represents the mean free-surface elevation. As mentioned previously, the current velocities are not defined above the wave-trough level, but we assume that the value at the trough can be extended up to the mean free-surface elevation. The top-panel of Fig. 5.31 shows "typical" undertow profiles in the bar-crest region. In the trough region the cross-shore velocities are sheared with the (absolute) maximum close at the free-surface. Seaward of the breaking region the undertow profiles show less vertical variation those given by (Putrevu and Svendsen, 1993), which means that the contribution of the steady-streaming is smaller here. The vertical profiles of the longshore current (shown in the bottom panel) are almost depth-uniform, but still exhibit a slight vertical shear from the bottom to the top in the direction of the mean longshore flow. Hence, as mentioned above, the velocity at the bottom is smaller than the depth-averaged velocity. It is convenient to mention that the vertical variation at the same and other longshore locations of the time-averaged and the instantaneous velocities are similar to those just presented.

The cross-shore distribution of the terms in the time-averaged momentum

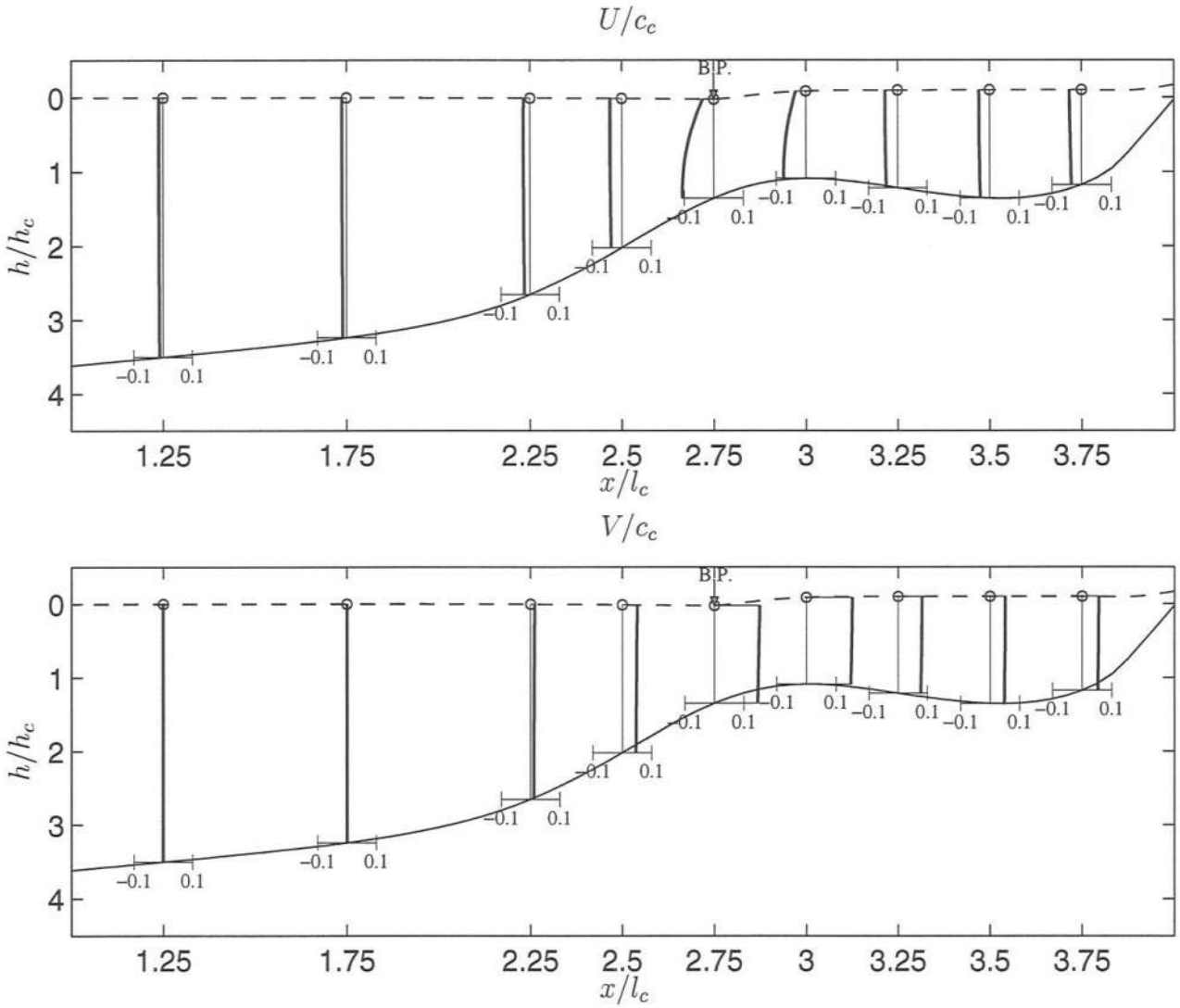

Figure 5.31: Cross-shore variation of the vertical profiles of (time-averaged) U/c_c and V/c_c at $y = 8\,l_c$.

balance at $y = 0$ is shown in Fig. 5.32. Note that the terms in the momentum equations that are generated by the depth variation of the currents are here combined together as a single term, which we designate by dispersive mixing term. For the x–momentum we notice that the dispersive mixing gives a small contribution around the two breaking points, but the main balance is still governed by the cross-shore component of the radiation stress and pressure gradient. In the y–momentum four terms are important: the wave-forcing $\frac{1}{\rho}\frac{\partial S_{yx}}{\partial y}$, the bottom friction $\frac{\tau_x^B}{\rho}$, the dispersive mixing, and the shear wave mixing given by the term $\overline{\frac{\partial}{\partial x}\left(\frac{\tilde{Q}_x\tilde{Q}_y}{h}\right)}$. Compared to Fig. 5.25 it is observed that the shear wave mixing is reduced in the present simulation and is partly replaced by the dispersive mixing. In the trough region, a detailed analysis of the magnitude of the terms reveals that the bottom shear stress and the dispersive mixing are the two dominating terms, which means that the shear wave mixing is negligible in that region.

Last, it is of interest to evaluate the magnitude of the dispersive coefficients $D_{\alpha\beta}$ and $B_{\alpha\beta}$ in equation (5.24). The terms containing these coefficients were found by Svendsen and Putrevu (1994) and Van Dongeren and Svendsen (1997b) to give the largest contribution to the momentum mixing. Furthermore, the studies of Van Dongeren and Svendsen suggest that B_{xx} and D_{xx} are the largest and thus we compare the magnitude of them with the value of the turbulent eddy viscosity ν_t[3]. Therefore, in Fig. 5.33 we have plotted the cross-shore distribution of $\frac{D_{xx}}{h_o\sqrt{g\,h_o}}$, $\frac{B_{xx}}{h_o\sqrt{g\,h_o}}$ and $\frac{\nu_t}{h_o\sqrt{g\,h_o}}$ at several longshore positions $2\,l_c$ apart, and at a given time of the simulation. First, we notice that the eddy viscosity ν_t is one order of magnitude smaller than the mixing coefficients D_{xx} and B_{xx}. Inside the surf zone, the ratio D_{xx}/ν_t is approximately 5, which is of the same order, but smaller than, the estimate

[3] Note that Van Dongeren and Svendsen find that the terms associated with $M_{\alpha\beta}$ can also be important, but the tensor $M_{\alpha\beta}$ can not be directly compared with $D_{\alpha\beta}$ and $B_{\alpha\beta}$ because it has different dimensions.

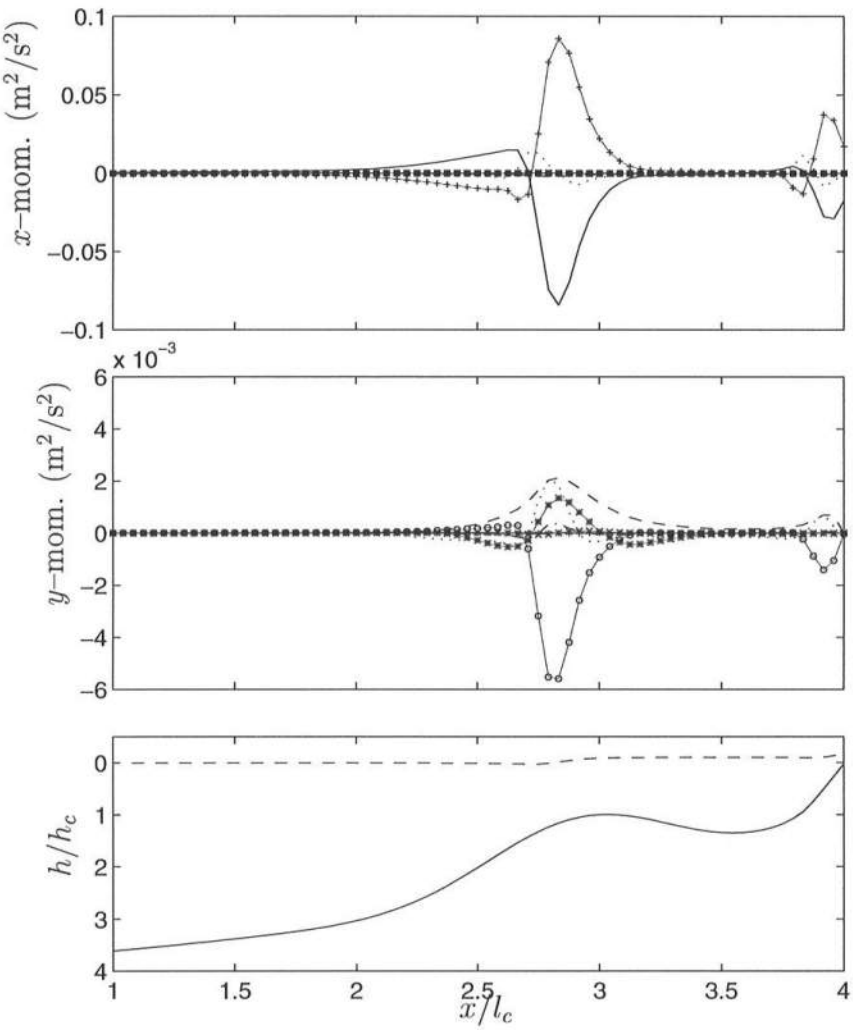

Figure 5.32: Cross shore distribution at $y = 0$ of (time-averaged): (a) Terms in the x–momentum balance: $gh\frac{\partial \bar{\zeta}}{\partial x}$ (+), $\frac{1}{\rho}\frac{\partial S_{xx}}{\partial x}$ (——), $\frac{1}{\rho}\frac{\partial S_{yx}}{\partial y}$ (○), $\overline{\frac{\partial}{\partial x}\left(\frac{\bar{Q}_x^2}{h}\right)}$ (×), $\overline{\frac{\partial}{\partial y}\left(\frac{\bar{Q}_x\bar{Q}_y}{h}\right)}$ (∗), – turb. mixing (–), $\frac{\tau_x^B}{\rho}$ (——), – dispersive mixing (···); (b) Terms in the y–momentum balance: $gh\frac{\partial \bar{\zeta}}{\partial y}$ (+), $\frac{1}{\rho}\frac{\partial S_{yy}}{\partial y}$ (——), $\frac{1}{\rho}\frac{\partial S_{xy}}{\partial x}$ (○), $\overline{\frac{\partial}{\partial y}\left(\frac{\bar{Q}_y^2}{h}\right)}$ (×), $\overline{\frac{\partial}{\partial x}\left(\frac{\bar{Q}_x\bar{Q}_y}{h}\right)}$ (∗), – turb. mixing (– ·), $\frac{\tau_y^B}{\rho}$ (– –), – dispersive mixing (···); (c) bottom variation (——), and mean surface elevation (– –) .

$D_{xx} \approx 20\,\nu_t$ given by Svendsen and Putrevu (1994). However, the ratio D_{xx}/ν_t is approximately 50 in the bar-trough, due to the fact that the eddy viscosity in that region does not have a wave breaking contribution. Second, the results show that D_{xx} is about the same value as B_{xx} over the bar-crest, and larger over the trough. The coefficient B_{xx} has a local maximum near the shoreline, in the location where the second breaking occurs. This suggests that the dispersive mixing is stronger nearer the shoreline, which is confirmed by inspecting the vertical current profiles at those locations. Furthermore, we notice that all the coefficients vary little with the longshore location, despite the fact that these are instantaneous values and hence reflect some longshore variation due to the shear wave motion.

In summary the present simulation indicates that the inclusion of the depth variation of the currents provides an effective mixing in the breaking region, that carries momentum from there to the bar-trough region where breaking is absent, and to the region outside the surf zone. Using an eddy viscosity parameterization estimated from the turbulence due to breaking and the bottom friction, we find reasonable values of the mixing coefficient compared to the values found by other authors. This conclusion strengthens the importance of accounting for the depth-varying currents in a nearshore current model. We also find that the action of the depth-varying currents is to provide some mixing which reduces the dynamics of shear waves.

5.2.4 Sensitivity analysis to variations in the eddy viscosity

The eddy viscosity is one of the parameters in the computations to which a significant uncertainty is attached. It is therefore important to examine the influence of the eddy viscosity values on the estimates of the vertical profiles $V_{1\alpha}$ of the currents, and thus on the estimates of the dispersive mixing. An example identical to

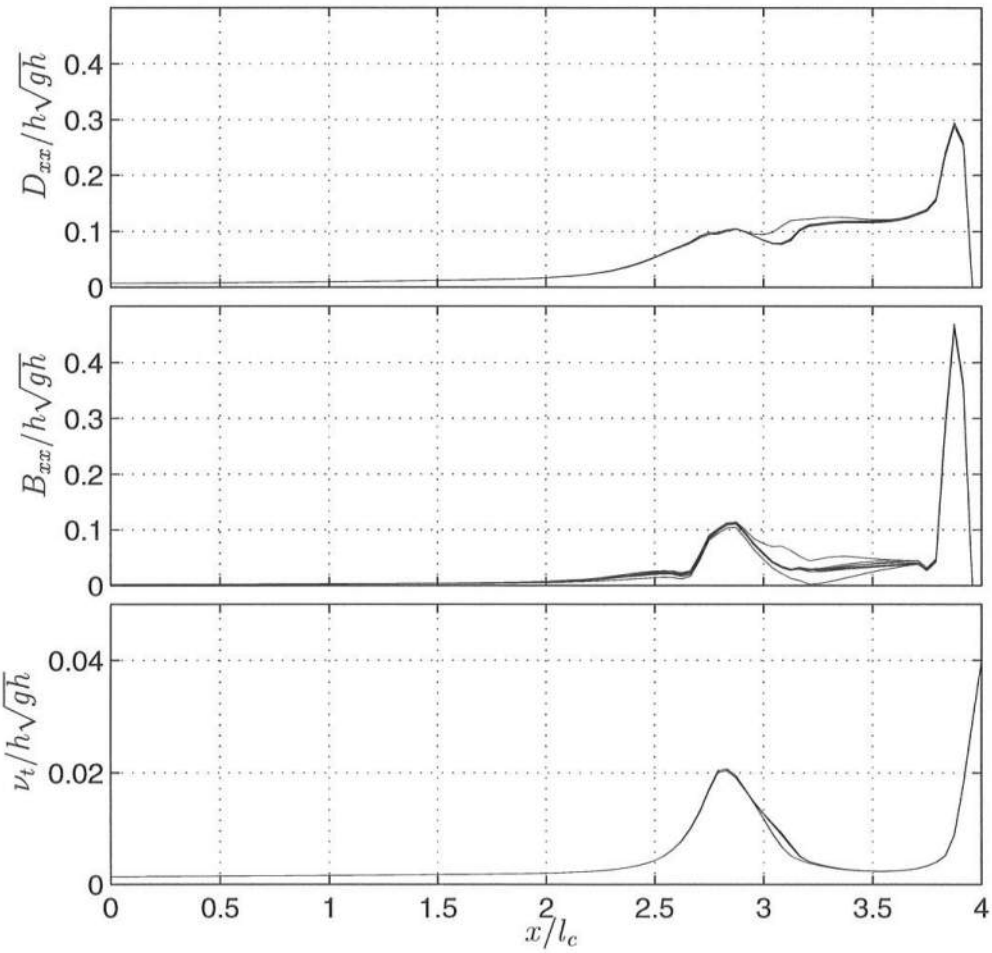

Figure 5.33: Cross shore distribution at several longshore locations $2\,l_c$ apart of: (a) $\frac{D_{xx}}{h_o\sqrt{g\,h_o}}$; (b) $\frac{B_{xx}}{h_o\sqrt{g\,h_o}}$; (c) $\frac{\nu_t}{h_o\sqrt{g\,h_o}}$.

the examples presented in subsections 5.2.1–5.2.3 is shown here, where the coefficient C_1 in the eddy viscosity formula (5.26) is changed from $C_1 = 0.75$ to 0.25, whereas M remains equal to 0.1 as before. This means that ν_t is reduced approximately 20% in the region where breaking occurs, and thus we expect the dispersive mixing to increase in that region. In fact, the choice $C_1 = 0.25$ is closer to the estimates based on the physical processes discussed in section 2.4.1, whereas $C_1 = 0.75$ is slightly larger than the expected values.

The time series of the non-dimensional current velocities, obtained from SHORECIRC for the present parameters, at three cross-shore locations and at $y = 8\, l_c$ are shown in Fig. 5.34. The velocity scales are the same as those in Fig. 5.28, and, as expected, the comparison between the two figures indicates that the shear waves for the present simulation are less energetic than those for the case with $C_1 = 0.75$. Thus, we conclude that an apparent small change in the eddy viscosity coefficient (which affects mainly the non-breaking region) can affect significantly the dynamics of the nearshore currents.

The time-mean cross-shore profiles of the the mean surface elevation $\bar{\zeta}/h_c$, the depth-averaged cross-shore current $\tilde{U}/c_c$, and the depth-averaged longshore current $\tilde{V}/c_c$ at four longshore locations are shown in Fig. 5.35. The general trend is similar to that observed in Fig. 5.24 and 5.29, but the maximum of the longshore current (see third panel) is slightly larger than the maxima for the previous simulations, due to a greater vertical variation of the longshore current and thus the bottom velocity is smaller than the depth-averaged velocity. Hence, it can be expected that the dispersive mixing is larger for the present case with $C_1 = 0.25$ than for the simulation with $C_1 = 0.75$. This can be seen in Fig. 5.36, where we plot the magnitude of the terms in the (long) time-averaged momentum equations. In the x–momentum equation, we find again that the balance is mainly between the radiation

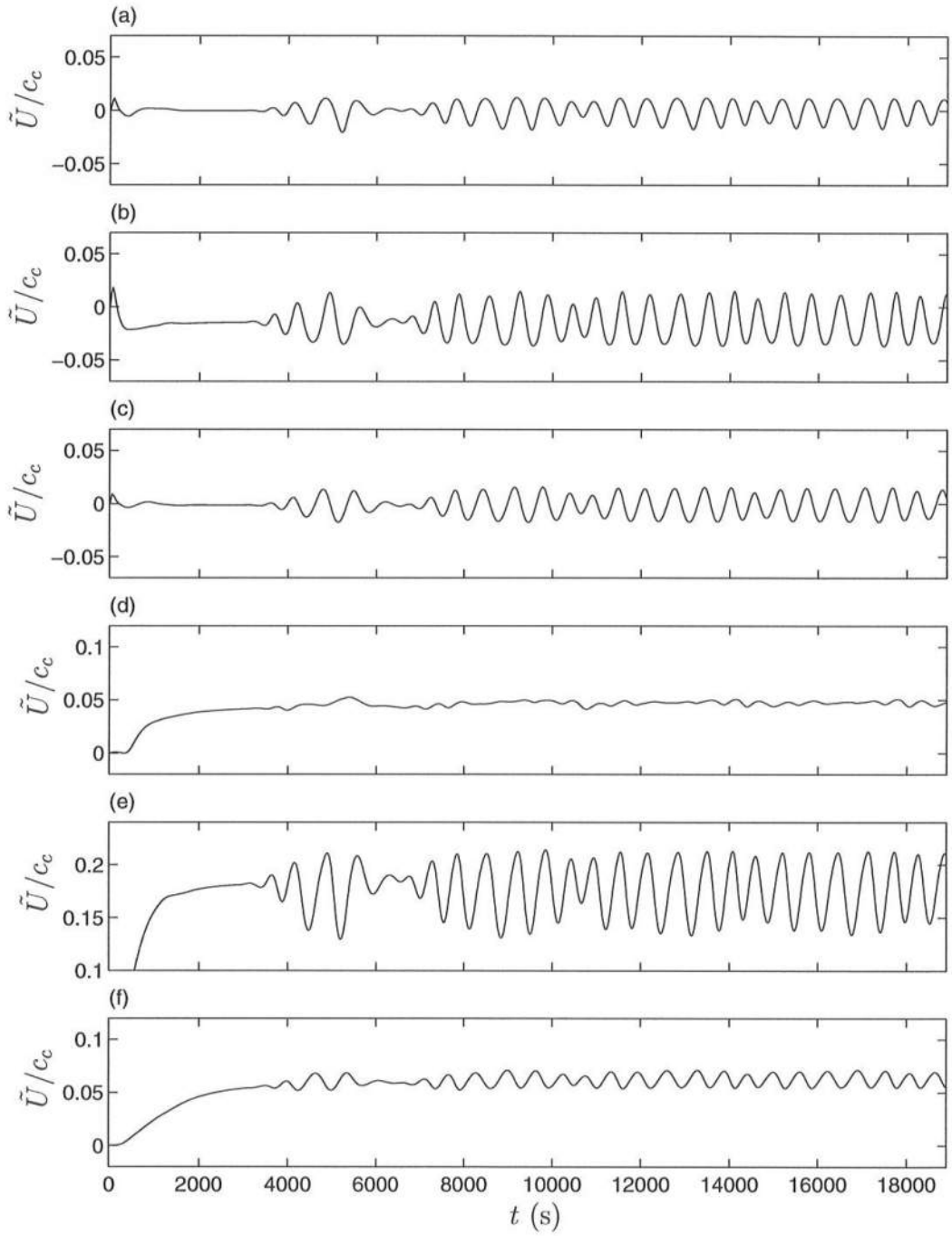

Figure 5.34: Time series of $\tilde{U}/c_c$ (3 upper plots) and $\tilde{V}/c_c$ (3 upper plots), where $c_c = (g\,h_c)^{0.5} \simeq 3.4$ m/s, for the case with lower eddy viscosity, at $y = 0$ and: (a),(d) $x = 2.5\,l_c$; (b),(e) $x = 3\,l_c$; (c),(f) $x = 3.5\,l_c$.

stress gradient and the setup gradient, with a small but not negligible contribution due to the dispersive mixing. In the y–momentum balance the dispersive mixing is seen to be locally quite large in the region where breaking first occurs, and the magnitude of it is comparable with that of the bottom shear stress. In the bar-trough region, these are the only two active terms (in the time-averaged sense). Comparing Fig. 5.36 with Fig. 5.32 we notice that the dispersive mixing is larger for the present case, and the shear wave mixing is substantially smaller. The bottom friction has similar magnitudes.

A better quantification of the dispersive mixing effect can be seen in Fig. 5.37, where the cross-shore distribution of the mixing coefficients D_{xx}, B_{xx} and ν_t at eight longshore locations are shown. The mixing coefficients D_{xx} and B_{xx} for the present simulation are, in the surf zone, approximately twice as large as the correspondent mixing coefficients for the case with $C_1 = 0.75$, shown in Fig. 5.33. This variation contrasts with the variation of just 20% in the value of ν_t over the crest from one case to the other. Inside the surf zone, the ratio D_{xx}/ν_t for this case is 10, which is closer to that of Svendsen and Putrevu (1994). Over the bar-trough that ratio is $D_{xx}/\nu_t = 200$. It is also convenient to point out that based on their results, Svendsen and Putrevu suggested that $D_{xx} \approx 0.2\, h_o \sqrt{g\, h_o}$ inside the surf zone. For the present simulation this can be seen to be a good approximation over and shoreward of the bar-crest. Seaward of the bar-crest the value of D_{xx} is about 25% of the value in the surf region, which validates the expression (4.33) used in chapter 4.

Fig. 5.33 and 5.37 give an indication of the dependence of D_{xx} and B_{xx} on the values of ν_t, and also show that innacuracies in the estimates of ν_t will reflect on the values of the mixing coefficients and thus, on the total amount of dispersive mixing provided by the vertical variation of the currents. It is therefore quite important to have a good model for the eddy viscosity parameterization, and more data is needed

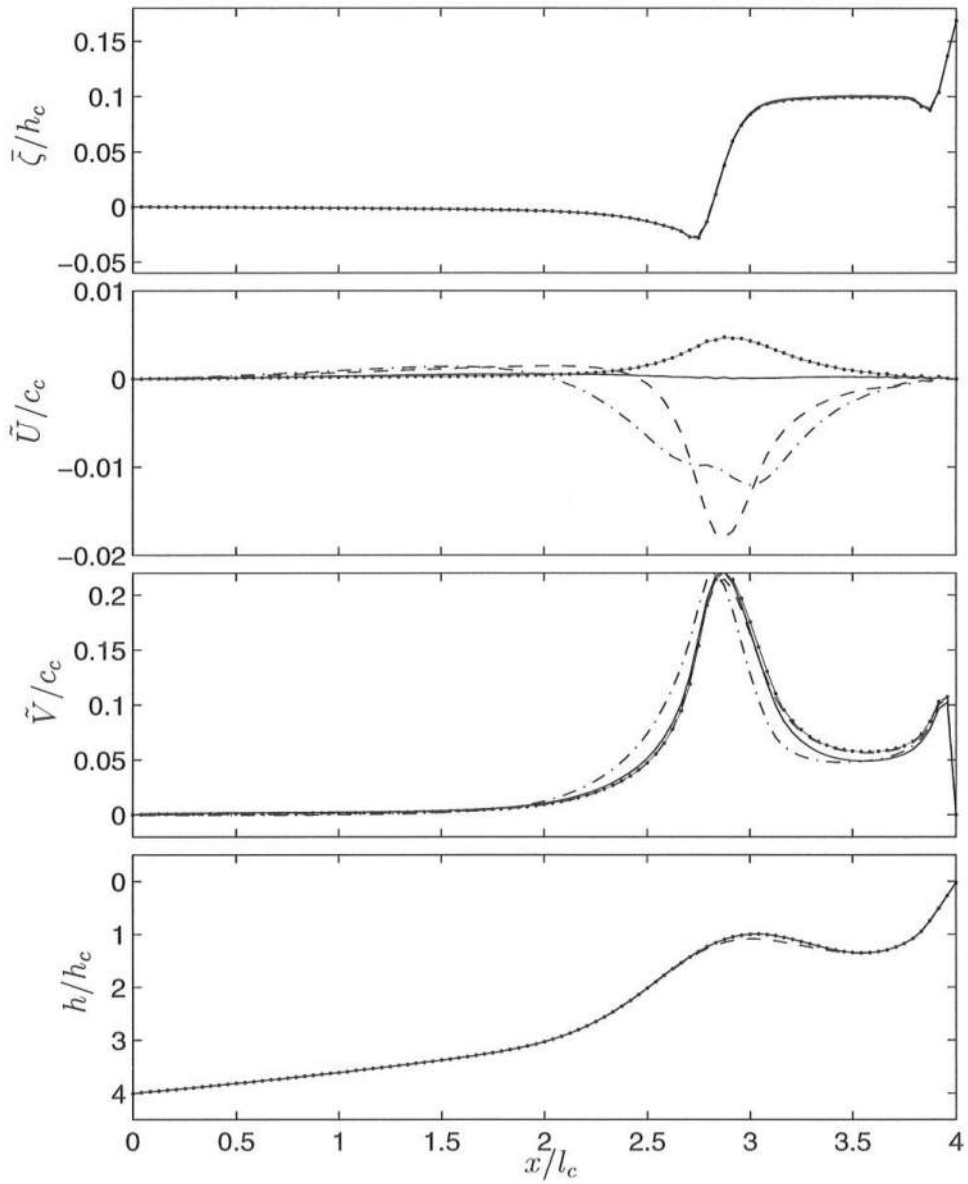

Figure 5.35: Cross shore distribution at $\frac{y}{l_c} = 0$ (——), $\frac{y}{l_c} = 7$ (– • –), $\frac{y}{l_c} = 8$ (– –), and $\frac{y}{l_c} = 9$ (– ·), for the case with lower eddy viscosity, of time-averaged flow properties: (a) $\bar{\zeta}/h_c$; (b) $\tilde{U}/c_c$; (c) $\tilde{V}/c_c$; (d) h_o/h_c .

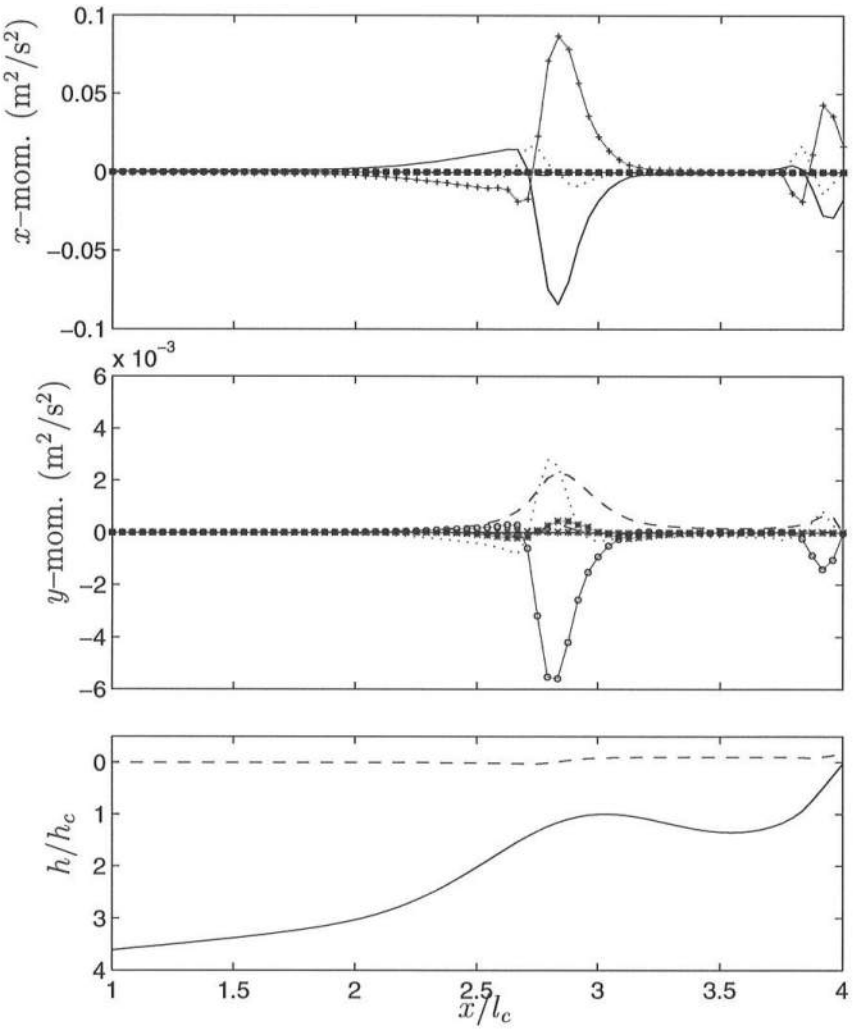

Figure 5.36: Cross shore distribution at $y = 0$ of (time-averaged): (a) Terms in the x–momentum balance: $gh\frac{\partial \bar{\zeta}}{\partial x}$ (+), $\frac{1}{\rho}\frac{\partial S_{xx}}{\partial x}$ (——), $\frac{1}{\rho}\frac{\partial S_{yx}}{\partial y}$ (○), $\overline{\frac{\partial}{\partial x}\left(\frac{\bar{Q}_x^2}{h}\right)}$ (×), $\overline{\frac{\partial}{\partial y}\left(\frac{\bar{Q}_x\bar{Q}_y}{h}\right)}$ (∗), – turb. mixing (– –), $\frac{\tau_x^B}{\rho}$ (——), – dispersive mixing (···); (b) Terms in the y–momentum balance: $gh\frac{\partial \bar{\zeta}}{\partial y}$ (+), $\frac{1}{\rho}\frac{\partial S_{yy}}{\partial y}$ (——), $\frac{1}{\rho}\frac{\partial S_{xy}}{\partial x}$ (○), $\overline{\frac{\partial}{\partial y}\left(\frac{\bar{Q}_y^2}{h}\right)}$ (×), $\overline{\frac{\partial}{\partial x}\left(\frac{\bar{Q}_x\bar{Q}_y}{h}\right)}$ (∗), – turb. mixing (– ·), $\frac{\tau_y^B}{\rho}$ (– –), – dispersive mixing (···); (c) bottom variation (——), and mean surface elevation (– –) .

for the turbulence levels over barred beaches in order to validate our eddy viscosity model.

For a value of $C_1 = 0.1$ we find that shear waves are still predicted and that $D_{xx} \approx 12\nu_t$ inside the surf zone. Hence, we find a certain stability of the ratio D_{xx}/ν_t for a reasonable range of the values of C_1. Another test was performed where we chose $C_1 = 0.25$ as before, but $M = 0.05$ in equation (5.26) instead of $M = 0.1$. This implies that we reduced the eddy viscosity to one-half in the breaking region, and thus $\nu_t \simeq 0.1 h_o \sqrt{g\, h_o}$. Under these circumstances the dispersive mixing turns out to be large enough to completely eliminate the generation of shear instabilities. The vertical velocity profiles also exhibit a larger curvature mainly over the bar-crest, both in the cross-shore and longshore directions.

Thus, in summary, the development of shear instabilities is seen to be strongly dependent on the value of ν_t through the amount of mixing provided by the dispersion due to the vertical variation of the currents. We point out that these results indicate that the mixing provided by shear waves in the absence of dispersion is equivalent to the mixing provided by the dispersion mechanism only (when present), or the combined mixing provided by the two effects. It will also be seen in chapter 6 that a combination of mixing from the shear instabilities and vertical dispersion dominates the total mixing for the simulation of currents under field conditions. We find that the present eddy viscosity formulation seems to be fairly realistic in face of the values estimated from field or laboratory data, and moreover, to give a reasonable variation of the current velocities over the depth.

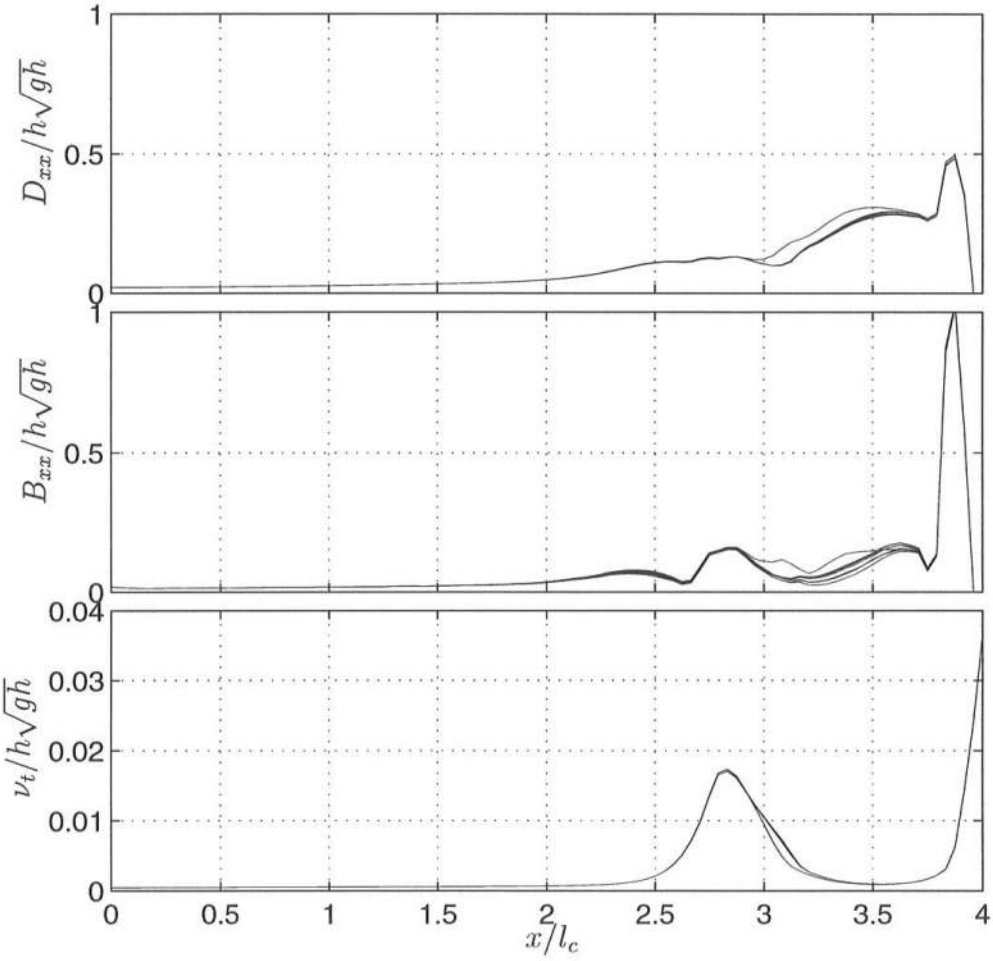

Figure 5.37: Cross shore distribution, at several longshore locations $2\,l_c$ apart, of: (a) $\frac{D_{xx}}{h_o\sqrt{g\,h_o}}$; (b) $\frac{B_{xx}}{h_o\sqrt{g\,h_o}}$; (c) $\frac{\nu_t}{h_o\sqrt{g\,h_o}}$.

5.3 The effect of the wave field and the longshore pressure gradient: prediction of rip-currents on a barred beach

It was demonstrated in chapter 4 that the inclusion of the longshore pressure gradient in a simple (one-line) longshore current model (Putrevu *et al.*, 1995) could have a dramatic effect in the velocity field. Conversely, the use of the complete SHORECIRC model illustrated that the longshore pressure gradient was overestimated in the model of Putrevu *et al.*, and that the nonlinear advective accelerations and bottom shear stress can affect the flow even in a simple case of a quasi-longshore uniform topography. The flow pattern predicted by SHORECIRC under that situation was mostly uniform in the longshore direction.

For the same quasi-longshore uniform barred beach the results in the previous section showed other dynamics of a predominantly longshore uniform flow. Only minor deviations of longshore uniformity in the time-averaged flow are seen in, e.g., Fig. 5.23. In contrast, a very uneven longshore current was predicted by Sancho *et al.* (1995), which was attributed to the existence of a large longshore pressure gradient. That is seen to drive a longshore current with the maximum over the bar-trough, unlike the double-peaked current profile we obtained in the examples in the section 5.2. The results of Sancho *et al.* also illustrate the formation of a rip-current, which is not seen for the examples analyzed here so far. The longshore variation in the topography of the example used by Sancho *et al.* is substantially larger than that of the examples in section 5.2. Thus, a few questions arise: Can rip-currents be predicted for the topography studied in section 5.2 (see Fig. 5.16)? Can the longshore pressure gradient also cause a substantial modification of the longshore current profile for such weaker topographic longshore perturbation?

Notice that in the literature we find several references to the formation of rip-currents caused by the longshore pressure gradient due to longshore uneven wave

fields (Arthur, 1962; Bowen, 1969b; Sonu, 1972; Haller *et al.*, 1997). Therefore, in this section we link our previous findings to the formation of rip-currents and discuss the importance of the longshore pressure gradient relative to that of other mechanisms.

The model equations for the following example are the same as for the examples in section 5.2, namely, equations (5.23)–(5.27). We first present the results for depth-uniform currents (no dispersive mixing) and then for depth-varying currents.

5.3.1 Depth-uniform currents

The beach topography is also the same as the previous (Fig. 5.16), but extended seaward, and is given by equations (4.29)–(4.32) with $l_c = 120$ m, $x'_M \simeq 0.92\, l_c$, $a = \frac{4.8}{l_c}$, $b = -12$, $\epsilon = 0.1$ and $w_r = \frac{4}{a} = 0.84\, l_c$ (100 m). The domain size is $l_x = 6\, l_c$ and $l_y = 16\, l_c$ which means that we extended the previous bathymetry further offshore in order to accommodate for the formation of rip-currents flowing over a larger cross-shore distance. The grid sizes are $\triangle x \simeq 4.24 h_c$ and $\triangle y \simeq 8.48 h_c$, where $h_c \simeq 1.18$ m is the depth at the bar-crest. The Courant number C_r is 0.8 ($\triangle t \simeq 0.488$ s). The boundary conditions are the same as used in section 5.2.

The wave field is obtained from the model REF/DIF1. The initial wave height is chosen such that wave breaking occurs over the bar everywhere except over the rip-channel, where the water depth is larger and thus the waves break only on the beach face itself (see Fig. 5.38). At the seaward boundary ($x = 0$) the wave height is $H_o = 0.64\, h_c$ (0.76 m) and the incident wave angle is $\alpha_{w0} = 8°$, which gives a wave angle $\alpha_{wb} = 5°$ at the breakpoint over the bar. The wave period is $T = 14.4\sqrt{h_c/g}$ (5 s). The results from REF/DIF1 shown in Fig. 5.38 and 5.39 also indicate that refraction is important around the rip-channel, modifying the initial

incident wave direction by $\pm 15°$.

The cross-shore profile of the wave height over the bar (at $y = 0$) and over the rip-channel ($y = 8\,l_c$) is given in Fig. 5.39. The breakpoint for the current wave conditions over the linear portion of the bar is at $x' = l_x - x = l_c$, whereas over the rip-channel breaking only starts at $x' = 0.2\,l_c$, i.e., it only occurs over the last 25 m on the beach face. These two figures indicate the difference in wave conditions over the rip-channel and over the bar, which is likely to induce a strong differential in wave forcing. Note that although the wave model predictions may not be accurate, a similar trend in the wave height variation over the channel and the bar has been observed in laboratory experiments (Haller *et al.*, 1997).

Time-averaged properties of the flow

We will discuss first the time-averaged characteristics of the predicted flow. The time-averaged (over a period of 2.1 hr) flow is illustrated in Fig. 5.40, where we present the spatial distribution of the depth-averaged currents $\tilde{V}_\alpha$ (top panel), and the below-trough mean current $V_{m\alpha}$ (bottom panel). The later corresponds to the total mass flux minus the wave-induced mass flux, averaged over the depth, and hence is representative of a measured current below trough level. These results correspond to a simulation with a bottom friction coefficient of $f_{cw} = 0.006$ and the eddy viscosity parameters $C_1 = 0.75$ and $M = 0.1$[4].

Focusing on Fig. 5.40(a), we notice that two circulation cells form around the rip-current, centered at the bar-crest. The width of the rip increases slowly towards offshore, as the result from a small turbulent dispersion as well as the dispersion caused by fluctuations of the rip (see later). Notice that for this particular

[4] These are the same values as used for the test in subsection 5.2.2.

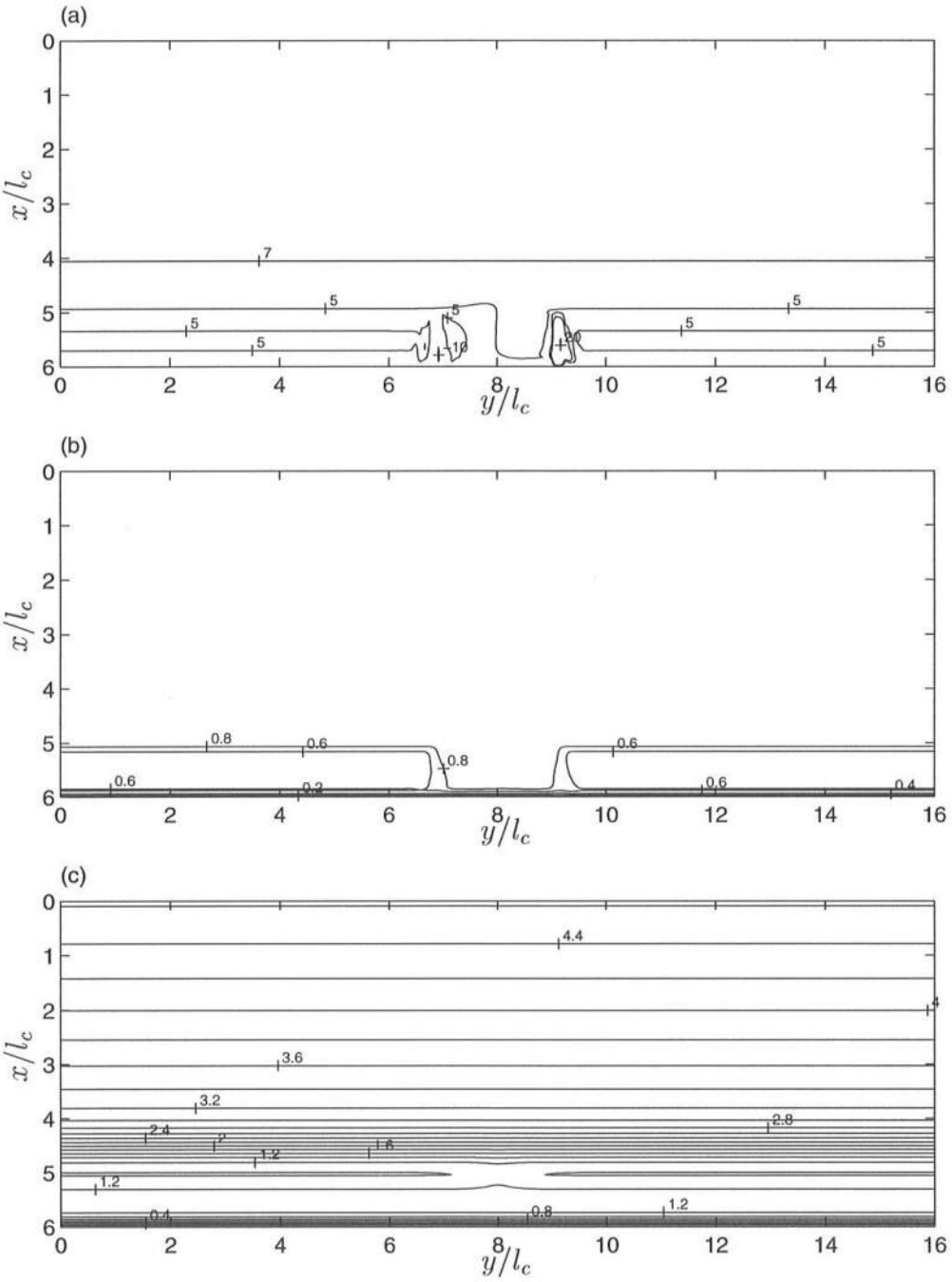

Figure 5.38: Contour plots of: a) wave angle $\alpha_w(^\circ)$; b) wave height H/H_b; and c) still water depth h_o/h_c.

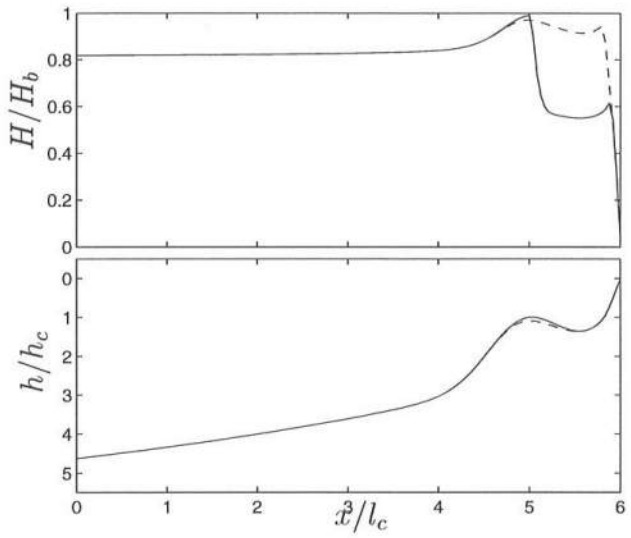

Figure 5.39: Wave height and bottom cross-shore variations over the barred beach at two longshore positions: $y = 0$ (solid line) and $y = 8\,l_c$ (dashed line).

simulation the rip-current is small but not negligible next to the seaward boundary, suggesting that boundary effects may be limiting the progression of the rip-current further offshore. Also, the rip-current axis makes a small angle with the shore normal direction due to the obliquely incoming short-waves. At each side of the rip, water flows onshore forming a closed circuit (for mass conservation). The longshore current flows towards the rip-channel at both sides of the rip, even though waves are approaching at an oblique angle of incidence locally against the currents (note in Fig. 5.38 that $\alpha = -10°$ and $20°$ at the upstream and downstream sections of the rip-channel). A smaller circulation cell is present close to the shoreline at $y = 7\,l_c$ due to a local peak in the wave angle and hence in the radiation stress forcing. In subplot (b) we observe classical undertow currents away from the rip-channel, and other features similar to the previous plot.

For reference, Fig. 5.41 shows the spatial distribution of the time-averaged

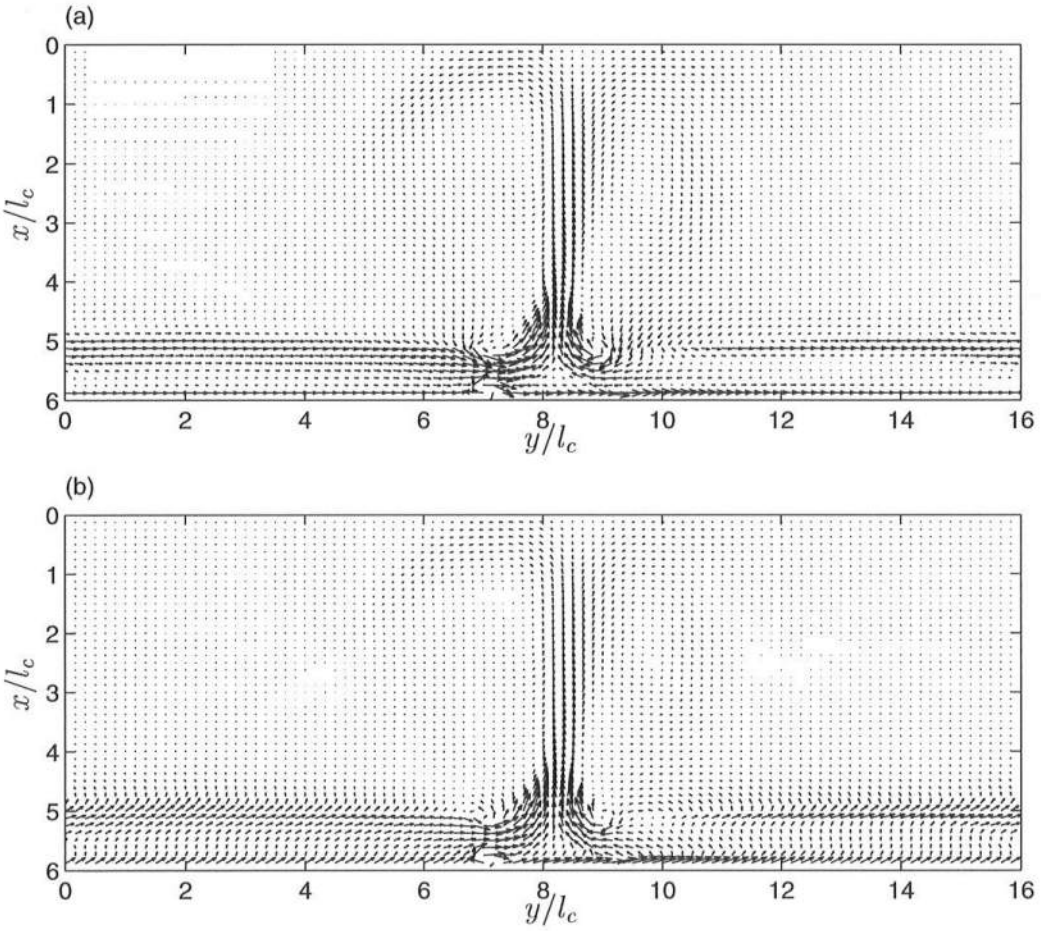

Figure 5.40: Time-averaged flow field for case with depth-uniform currents: a) total depth-averaged velocity vectors, $\vec{V}$; b) below-trough depth-averaged velocity vectors $\vec{V}_m$.

flow variables $\bar{\zeta}, \tilde{U}, \tilde{V}$. The maximum velocity at the rip-current is $0.2\sqrt{g\,h_c}$ (0.70 m/s). The longshore currents (see subplot (c)) vary substantially in the longshore and cross-shore directions and can be quite large over the trough. The top panel of Fig. 5.41 shows the distribution on the mean surface elevation $\bar{\zeta}/h_c$. From this figure it can be inferred that there is an appreciable longshore variation of the surface elevation in a region of width $\sim 2\,l_c$ centered at the rip-channel. Consequently, the longshore gradient of the mean surface elevation will be an important term locally around the rip.

The cross-shore variations of the normalized, time-averaged $\bar{\zeta}, \tilde{U}, \tilde{V}$ at four longshore locations ($\frac{y}{l_c}=0$, $\frac{y}{l_c}=7$, $\frac{y}{l_c}=8$, $\frac{y}{l_c}=9$) are plotted in Fig. 5.42. First, we observe that $\bar{\zeta}$ away from the rip-channel (solid line) is much larger than $\bar{\zeta}$ in the region of the rip-channel, indicating clearly the existence of a longshore pressure gradient. At the center of the rip (dashed line) the mean free-surface increases almost linearly from $\frac{x}{l_c}=5$ to $\frac{x}{l_c}=5.8$, and then rises sharply towards the shoreline. Over the bar, $\bar{\zeta}$ presents the typical "terraced" variation of a double breaking region. Notice that a similar trend for the mean surface elevation over and away from the rip-channel has been measured in laboratory conditions (Haller *et al.*, 1997). Subplot (b) shows that the variation of $\tilde{U}/c_c$ has a maximum (in magnitude) along the rip-channel axis, and over the bar crest. The rip-current is nearly constant seaward of the location $x = 3.5\,l_c$ until the proximity of the seaward boundary. Away from the rip-channel the depth-averaged cross-shore velocity is nearly zero suggesting that the short-wave induced mass flux is carried seaward by the undertow current.

The variability of the longshore velocity profiles at the four cross-sections predicted for the present conditions (Fig. 5.42c) contrasts with the quasi-longshore uniform profiles seen for the previous examples (see e.g., Fig. 5.24c). Here, at $y = 0$ (solid line) the longshore current velocity profile exhibits the "classical" double-peak

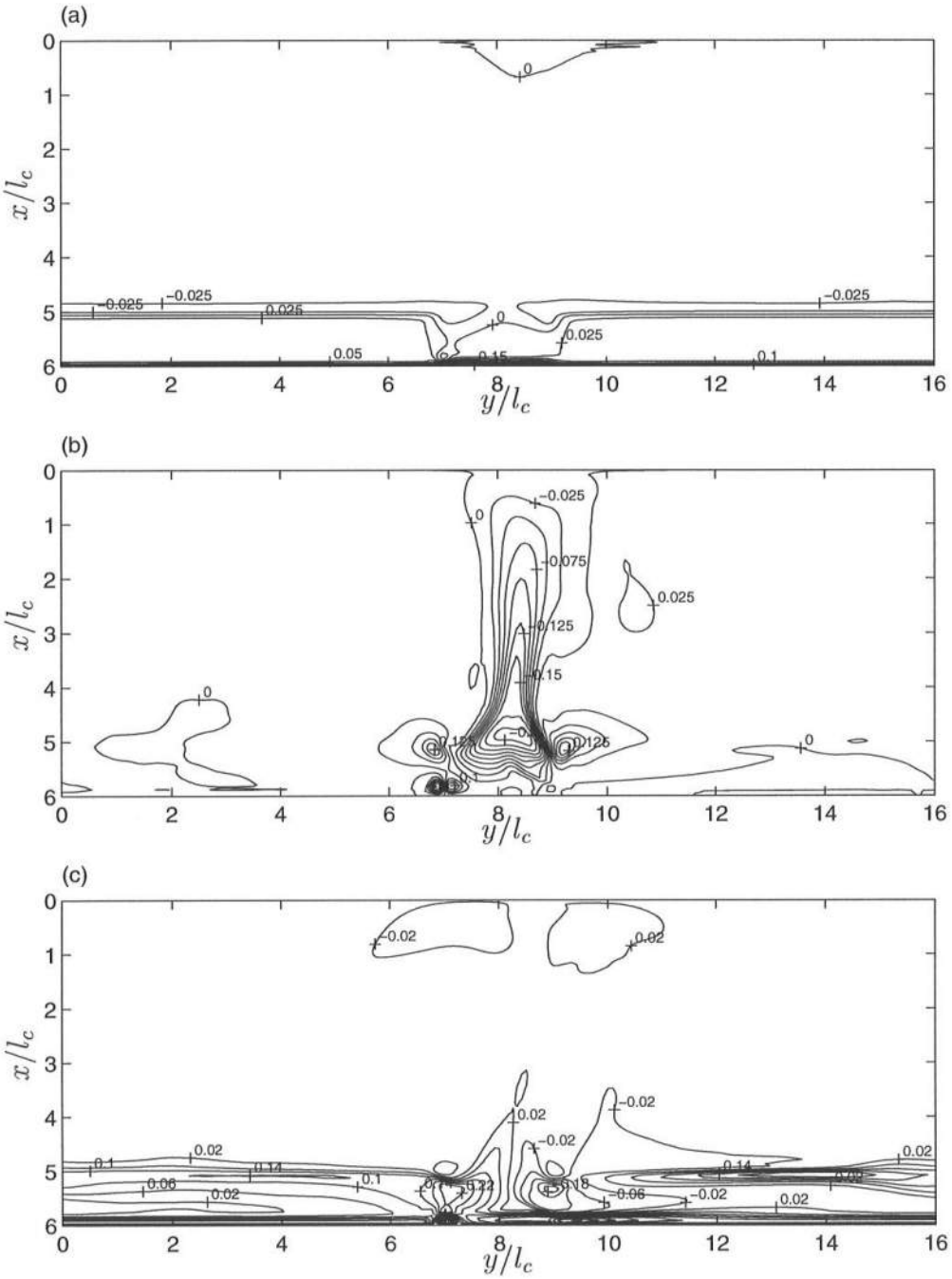

Figure 5.41: Time-averaged flow field for case with depth-uniform currents. Contour plots of: a) mean free-surface elevation $\bar{\zeta}/h_c$; b) cross-shore velocity $\tilde{U}/c_c$; c) longshore velocity $\tilde{V}/c_c$.

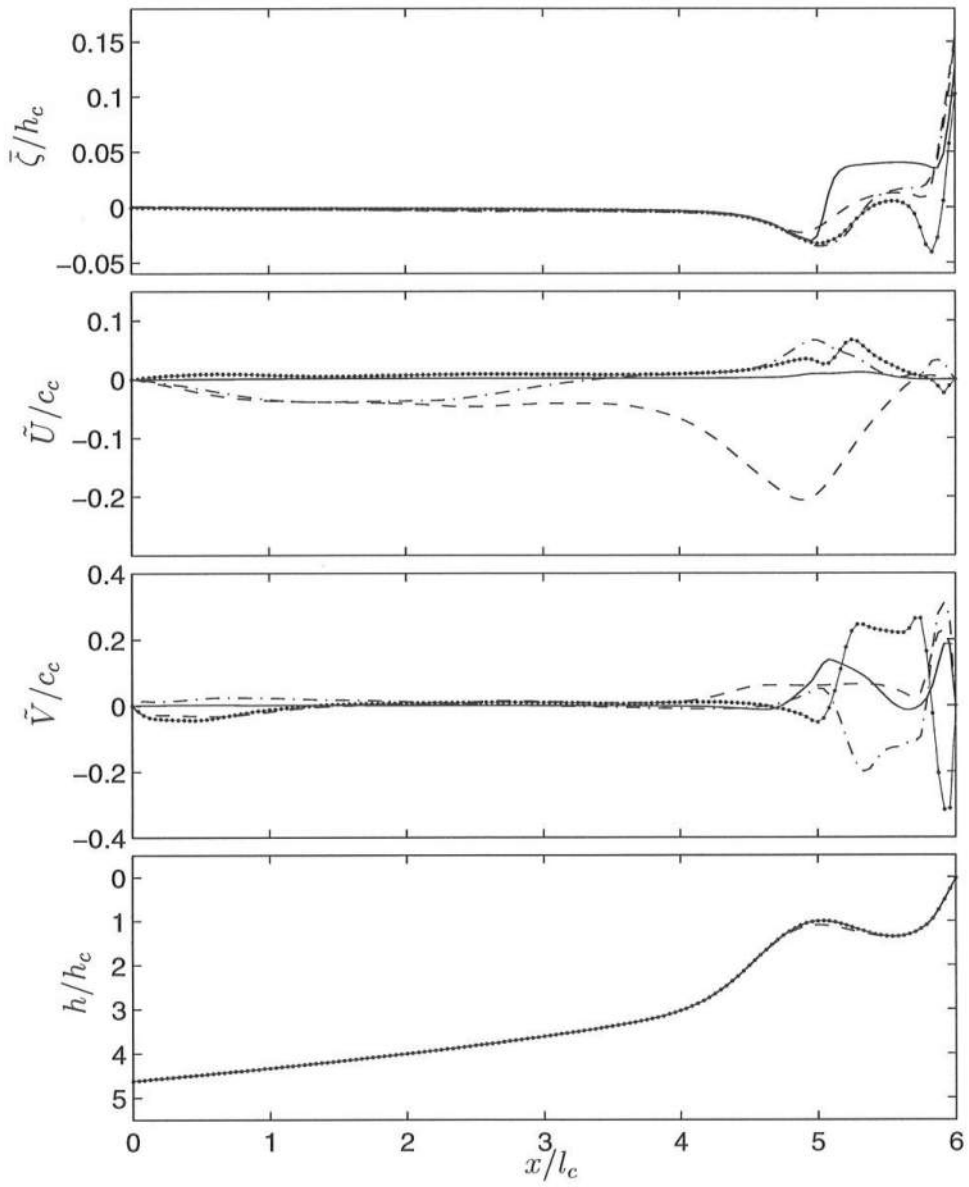

Figure 5.42: Cross shore distribution at $\frac{y}{l_c} = 0$ (——), $\frac{y}{l_c} = 7$ (·—·), $\frac{y}{l_c} = 8$ (– –), and $\frac{y}{l_c} = 9$ (– ·), for the case with depth-uniform currents, of: (a) $\bar{\zeta}/h_c$; (b) $\tilde{U}/c_c$; (c) $\tilde{V}/c_c$; (d) h_o/h_c .

shape, whereas at the sections immediately downstream ($y = 7\,l_c$) and upstream ($y = 9\,l_c$) of the channel the velocity profiles have a peak in the direction of the rip-channel over the trough region, and a secondary, narrower, maximum in the opposite direction close to the shoreline. (Note that the secondary peak at $y = 7\,l_c$ is caused by the local vortex next to the shoreline observed in Fig. 5.40).

The change in shape of the longshore current profile with the distance from the rip-channel is best seen in Fig. 5.43. The currents upstream of the rip are represented in the top panel, and downstream of the rip in the lower panel. Focusing on the upstream cross-sections, and progressing in the downstream direction, we notice that it is not until $y = 6\,l_c$ that pronounced differences can be observed in the current profiles. At that section the velocity over the trough is significantly larger than at the other sections. Over the rip-channel ($y = 6\,l_c$) the longshore current is not zero due to the oblique angle of incidence of the incoming waves. At the downstream locations (subplot (b)), the velocity profiles change dramatically with the position. At $y = 10\,l_c$ there is a small peak over the crest, a counter-current (negative) over the trough, and a large sharp peak near the shoreline. At $y = 12\,l_c$ and $y = 14\,l_c$ the peak over the bar-crest is significantly larger than at the other locations, and the second peak at the shoreline is of comparable magnitude. At $y = 16\,l_c$ the current profile has almost reached the quasi-longshore uniform solution, which appears to be recovered at the locations $2 < \frac{y}{l_c} < 4$ where the current profile is nearly constant. For all positions, the sharp peak near the shoreline in the current velocity profiles is due to intensive wave breaking in that region (see Fig. 5.39).

Still considering time-averaged motion only, Fig. 5.44 shows the cross-shore variation of the terms in the x and y–momentum equations at the section further away from the rip-channel ($y = 0$) and over the rip-channel ($y = 8\,l_c$). Notice the difference in order of magnitude of the vertical scales of the figures for the x and

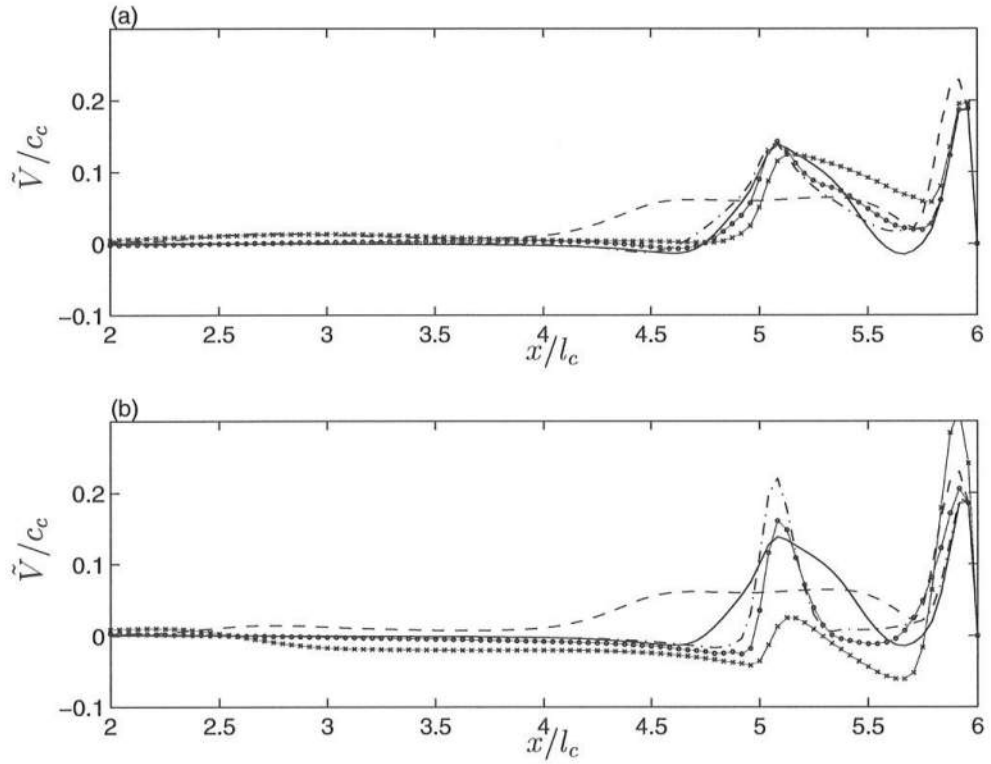

Figure 5.43: Cross shore distribution of $\tilde{V}/c_c$, at different longshore positions, for the case with depth-uniform currents: (a) $\frac{y}{l_c} = 0$ (——), $\frac{y}{l_c} = 2$ (– ·), $\frac{y}{l_c} = 4$ (– • –), $\frac{y}{l_c} = 6$ (– × –), $\frac{y}{l_c} = 8$ (– –); (b) $\frac{y}{l_c} = 8$ (– –), $\frac{y}{l_c} = 10$ (– × –), $\frac{y}{l_c} = 12$ (– • –), $\frac{y}{l_c} = 14$ (– ·), $\frac{y}{l_c} = 16$ (——).

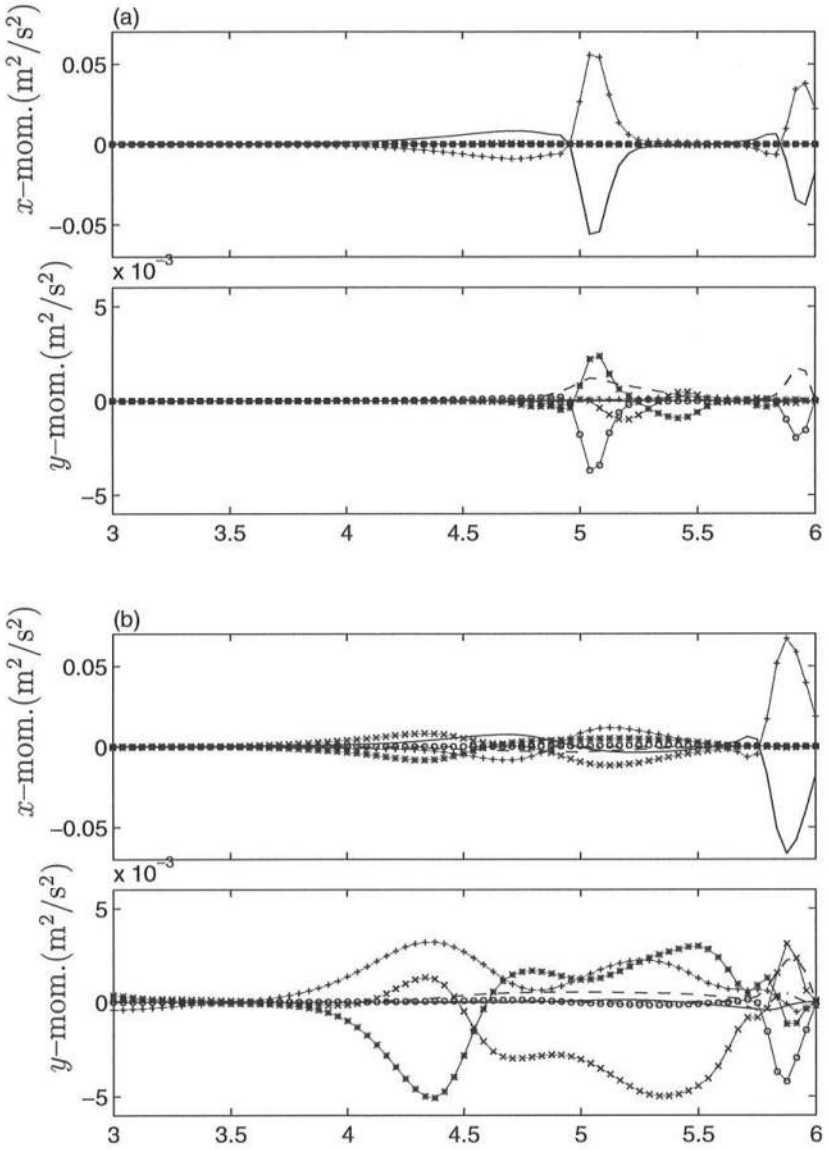

Figure 5.44: Cross shore distribution at (a) $y = 0$, and (b) $y = 8\,l_c$ of the terms in the (time-averaged) momentum equations. Terms in the x–momentum balance: $gh\frac{\partial \bar{\zeta}}{\partial x}$ (+), $\frac{1}{\rho}\frac{\partial S_{xx}}{\partial x}$ (——), $\frac{1}{\rho}\frac{\partial S_{yx}}{\partial y}$ (○), $\overline{\frac{\partial}{\partial x}\left(\frac{\bar{Q}_x^2}{h}\right)}$ (×), $\overline{\frac{\partial}{\partial y}\left(\frac{\bar{Q}_x\bar{Q}_y}{h}\right)}$ (∗), – turb. mixing (– ·), $\frac{\tau_x^B}{\rho}$ (– –). Terms in the y–momentum balance: $gh\frac{\partial \bar{\zeta}}{\partial y}$ (+), $\frac{1}{\rho}\frac{\partial S_{yy}}{\partial y}$ (——), $\frac{1}{\rho}\frac{\partial S_{xy}}{\partial x}$ (○), $\overline{\frac{\partial}{\partial y}\left(\frac{\bar{Q}_y^2}{h}\right)}$ (×), $\overline{\frac{\partial}{\partial x}\left(\frac{\bar{Q}_x\bar{Q}_y}{h}\right)}$ (∗), – turb. mixing (– ·), $\frac{\tau_y^B}{\rho}$ (– –).

y–momentum terms. In the x–momentum at $y = 0$ the main balance is between the wave radiation stress and the cross-shore pressure gradient. In the y–momentum the primary terms are the radiation stress ($\circ$), the bottom friction ($-\ -$), and a mixing provided by the time-averaged, depth-uniform convective accelerations[5]. Thus, at this location the effective terms are the same as seen previously. At $y = 8\,l_c$ (lower subplots) we notice first that the magnitude of some terms in the y–momentum, namely the time-averaged convective accelerations and longshore pressure gradient, is quite large seaward of the bar-crest, where the rip-current forms. The wave forcing is seen to be important only close to the shore. In the x–momentum the magnitude of the bottom shear stress ($--$) is seemingly small, but a closer analysis reveals that it has the magnitude 4×10^{-3} m^2/s^2, which is of the order of the largest terms in the y–momentum equation. This picture demonstrates the complexity of the balance in the momentum equations next to a rip-current.

In order to evaluate the importance of the longshore pressure gradient over the trough we present in Fig. 5.45 the terms in the momentum equations at $y = 6\,l_c$ and $y = 10\,l_c$. For the first location (upstream of the rip-channel), the longshore pressure gradient is negative and with a significant magnitude over the trough, confirming that it is an important driving force for the large longshore currents observed over the trough. The convective accelerations are equally large, and appear to nearly cancel each other in that region, and hence the main balance is between $gh\frac{\partial \bar{\zeta}}{\partial y}$ and $\frac{\tau_y^B}{\rho}$, which supports the conjecture of the importance of the pressure gradient. However, at the downstream location (lower panel) the inverse situation is observed: the longshore pressure gradient is positive and drives a current towards the rip over the trough, in the direction opposite of the main longshore current. Notice that at this location the longshore current is nearly zero (see bottom panel of Fig. 5.43),

[5] It will be shown later that this mixing originates from the existence of shear wave motions, in a similar fashion to the examples in the previous section.

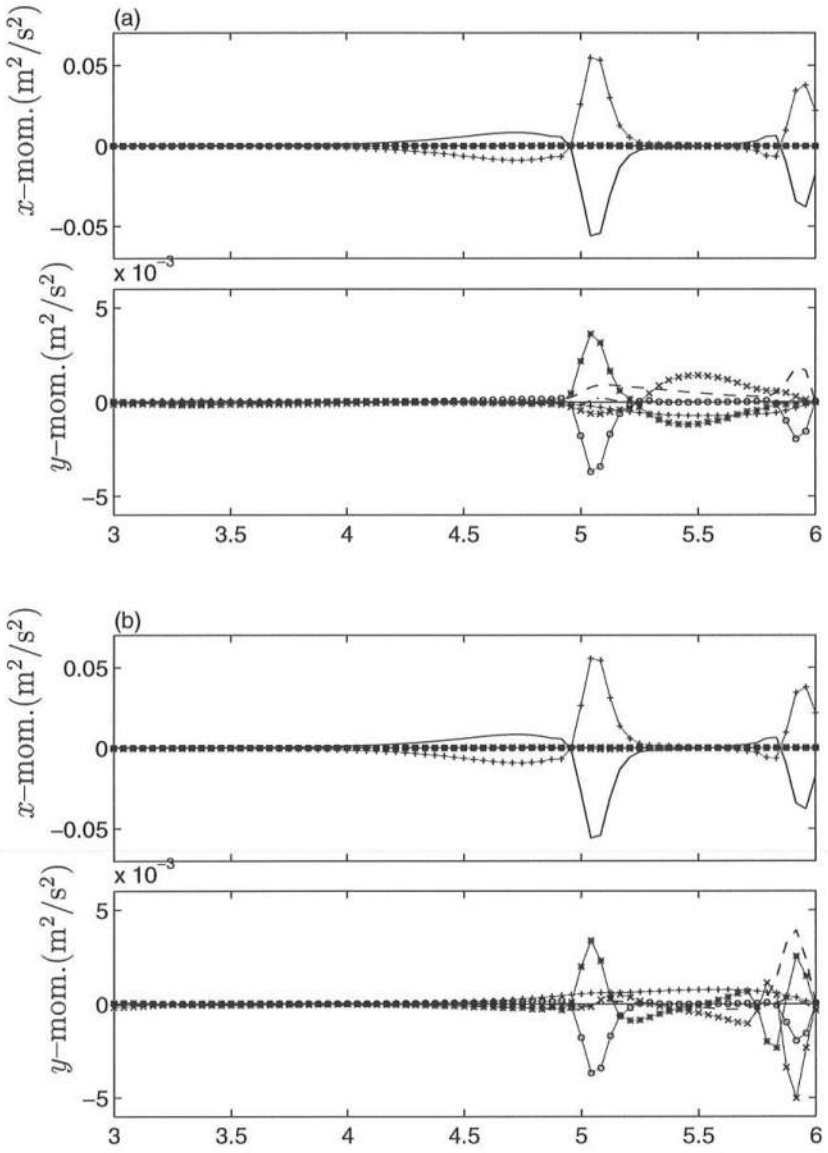

Figure 5.45: Cross shore distribution at (a) $y = 6\,l_c$, and (b) $y = 10\,l_c$ of the terms in the (time-averaged) momentum equations. Terms in the x–momentum balance: $gh\frac{\partial \bar{\zeta}}{\partial x}$ (+), $\frac{1}{\rho}\frac{\partial S_{xx}}{\partial x}$ (——), $\frac{1}{\rho}\frac{\partial S_{yx}}{\partial y}$ (○), $\overline{\frac{\partial}{\partial x}\left(\frac{\bar{Q}_x^2}{h}\right)}$ (×), $\overline{\frac{\partial}{\partial y}\left(\frac{\bar{Q}_x\bar{Q}_y}{h}\right)}$ (∗), – turb. mixing (– ·), $\frac{\tau_x^B}{\rho}$ (– –). Terms in the y–momentum balance: $gh\frac{\partial \bar{\zeta}}{\partial y}$ (+), $\frac{1}{\rho}\frac{\partial S_{yy}}{\partial y}$ (——), $\frac{1}{\rho}\frac{\partial S_{xy}}{\partial x}$ (○), $\overline{\frac{\partial}{\partial y}\left(\frac{\bar{Q}_y^2}{h}\right)}$ (×), $\overline{\frac{\partial}{\partial x}\left(\frac{\bar{Q}_x\bar{Q}_y}{h}\right)}$ (∗), – turb. mixing (– ·), $\frac{\tau_y^B}{\rho}$ (– –).

and hence the bottom shear stress is quite small. This means that the longshore pressure gradient in this region does not generate a strong longshore current, and is balanced by the convective accelerations. These are seen to be large and are linked to the large variations in direction of the mean flow seen in Fig. 5.42.

Time-varying properties of the flow

We have so far looked at the characteristics of the mean flow. However, the current velocities for the present simulation are very dynamic and exhibit different patterns at different locations. Fig. 5.46 and 5.47 show the time series of the cross-shore and longshore (depth-uniform) velocities respectively, at five locations along the shore and over the bar-crest ($x = 5\,l_c$). Both the cross-shore and longshore velocities are seen to vary dramatically with the position, depending whether this is located upstream or downstream of the rip-channel. At the closer sections downstream of the rip ($y = 10\,l_c$ and $y = 12\,l_c$) we observe that the motion is steady. Further away ($y = 0$), somewhat periodic shear waves have developed, which appear to become more unstable and irregular at $y = 6\,l_c$. Secondly, the magnitude of the cross-shore velocity disturbances (Fig. 5.46) is equivalent to that of the longshore perturbations (Fig. 5.47), although the two figures have slightly different vertical scales. At $y = 0$ the period of the shear waves is initially $\sim$440 s, and later a sub-harmonic transition occurs and the period is $\sim$800 s. The shear waves are seen to travel with a speed of $c_S \simeq 0.05-0.07\,c_c$, which corresponds to $c_S \simeq 0.17-0.25$ m/s in dimensional units. Notice also the irregularity of both $\tilde{U}/c_c$ and $\tilde{V}/c_c$ at $y = 6\,l_c$.

The time series of the cross-shore and longshore velocities at several locations along the centerline of the rip-channel ($y = 8\,l_c$) are shown in Fig. 5.48 and 5.49, respectively. These figures illustrate that the predicted rip-currents are unsteady

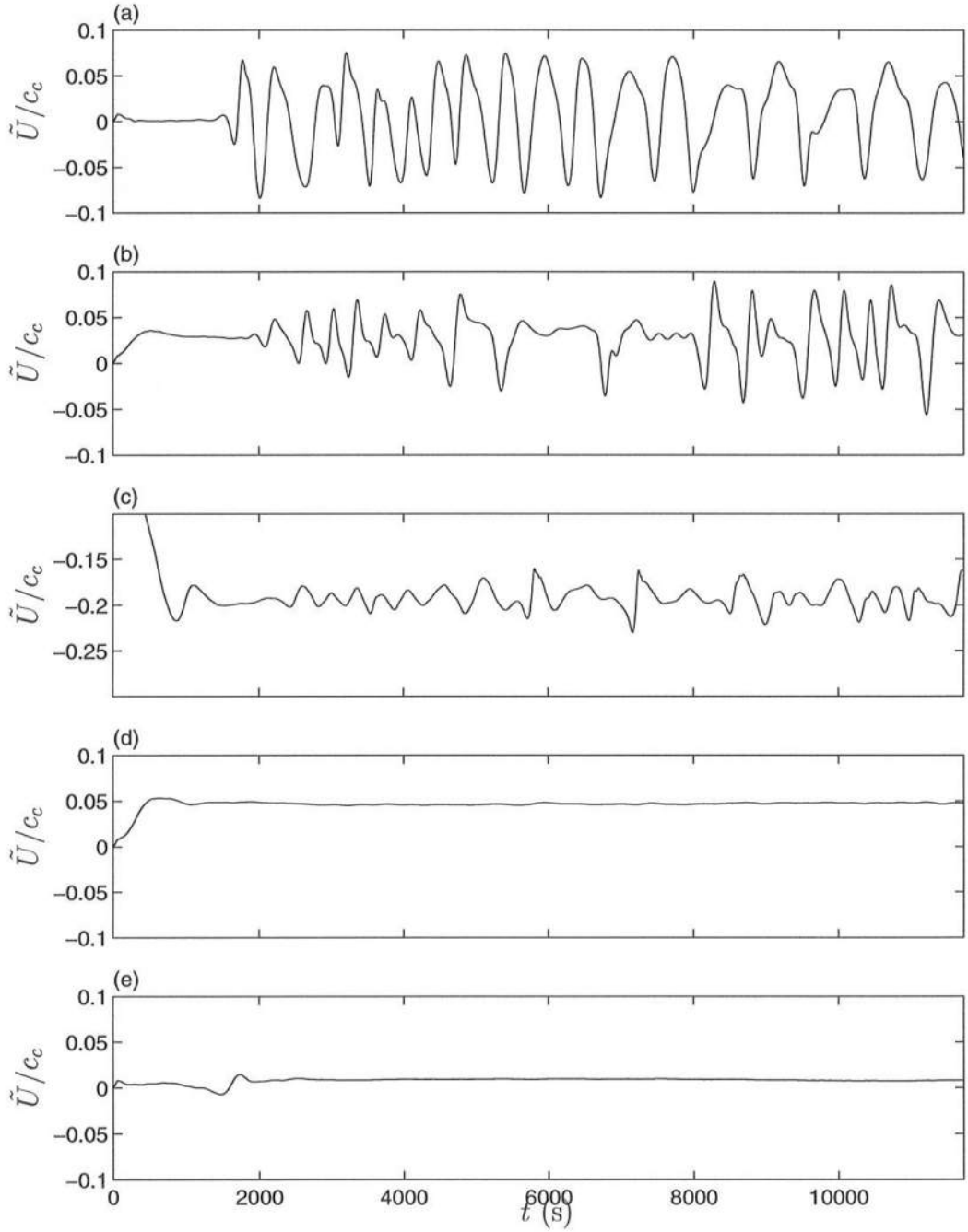

Figure 5.46: Time series of $\tilde{U}/c_c$, where $c_c = (g\,h_c)^{0.5} \simeq 3.4$ m/s, for the case with depth-uniform currents, at $x = 5\,l_c$ and: (a) $y = 0$; (b) $y = 6\,l_c$; (c) $y = 8\,l_c$; (d) $y = 10\,l_c$; (e) $y = 12\,l_c$. (See Fig. 5.40 for locations).

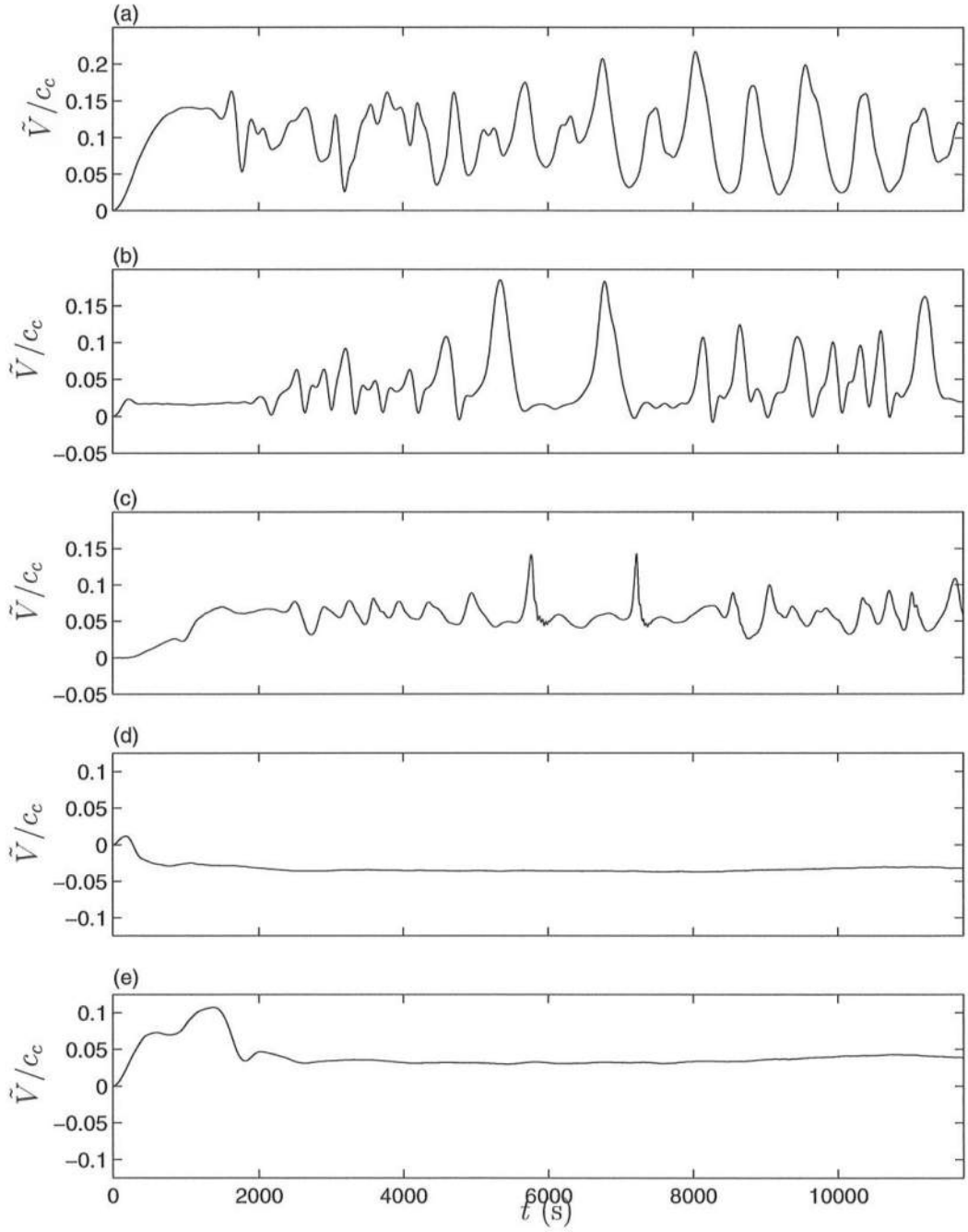

Figure 5.47: Time series of $\tilde{V}/c_c$, where $c_c = (g\,h_c)^{0.5} \simeq 3.4$ m/s, for the case with depth-uniform currents, at $x = 5\,l_c$ and: (a) $y = 0$; (b) $y = 6\,l_c$; (c) $y = 8\,l_c$; (d) $y = 10\,l_c$; (e) $y = 12\,l_c$. (See Fig. 5.40 for locations).

and somewhat periodic. The most energetic periods are seen to range between $400 < T < 450$ s, but there are also appreciable variations in the time series at a much lower frequency. The lower frequency oscillations are more significant at the rip-current "head" (positions $x = 3\,l_c$ and $x = 4\,l_c$) than at the rip-current "neck" (positions $x = 4.5\,l_c$ and $x = 5\,l_c$). A detailed analysis of the spatial variations of the currents over the time reveals that the higher frequency oscillations are associated with a meandering motion of the rip-currents (see Fig. 5.50), which are initially nearly steady (see the time series in subplots (d) and (e) in Fig. 5.48 between $1000 < t < 2500$ s) and then get unstable. In contrast, the longer period variations are related to a "side-to-side" shift of the rip-current, and with the passage of vortices released by the unstable rip over a certain location.

Fig. 5.50 shows three "snapshots" of the depth-averaged current velocities. In the first plot ($t = 1950$ s) the rip-current has not developed fully, but we notice already vortex shedding at the sides of the rip, and even the generation of vortices that separate from the rip and travel independently. At this stage shear waves have begun to form and exhibit a short wavelength (together with the shorter period as seen previously). At $t = 5860$ s a meandering rip-current is fully developed and vortices are seen at each side. The shear waves have a longer wavelength which indicates that a subharmonic transition occurred. The flow at $t = 9760$ s presents similar characteristics as at $t = 5860$ s, though a larger longshore current is observed at the seaward boundary. The two lower plots show clearly that the motion is steady downstream of the rip-channel until $y = 14\,l_c$ and then shear waves start to form, due to the strong seaward-shear of the longshore current profile. For all plots the flow over the trough, in the region adjacent to the rip-channel, is towards the rip from both sides which confirms the importance of the longshore pressure gradient as a driving force in that region.

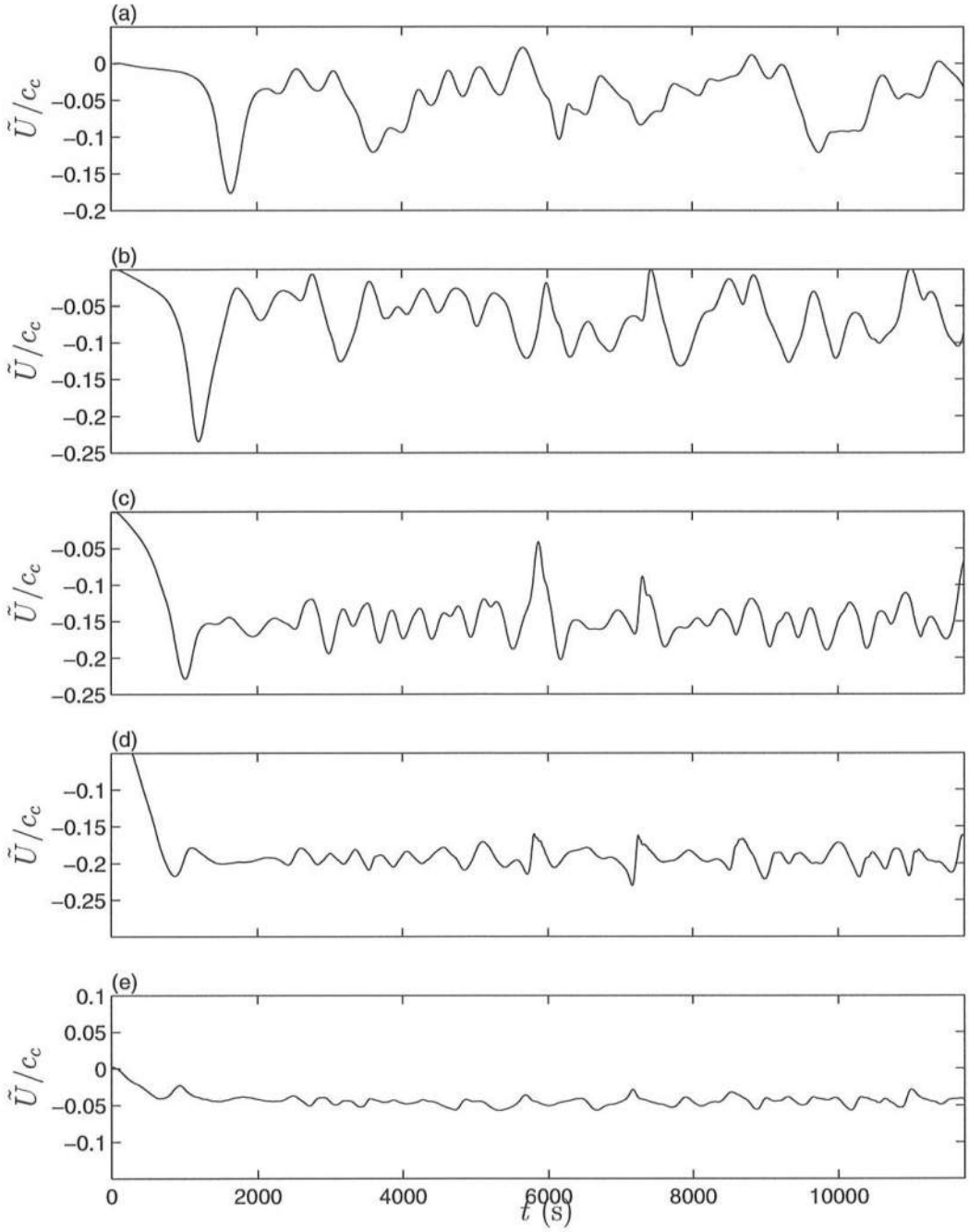

Figure 5.48: Time series of $\tilde{U}/c_c$, where $c_c = (g\,h_c)^{0.5} \simeq 3.4$ m/s, at $y = 8\,l_c$ and: (a) $x = 3\,l_c$; (b) $x = 4\,l_c$; (c) $x = 4.5\,l_c$; (d) $x = 5\,l_c$; (e) $x = 5.5\,l_c$. (See Fig. 5.40 for locations).

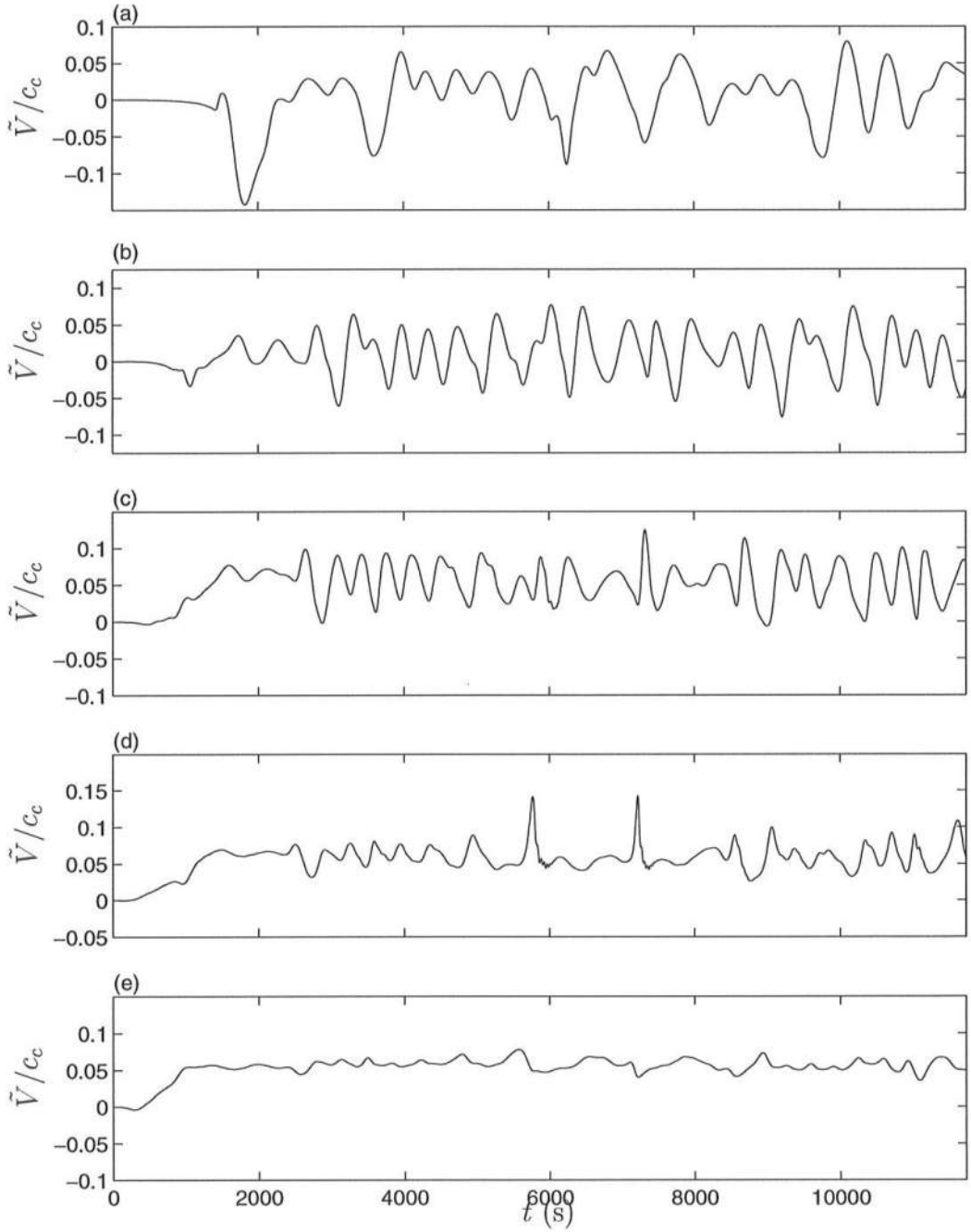

Figure 5.49: Time series of $\tilde{V}/c_c$, where $c_c = (g\,h_c)^{0.5} \simeq 3.4$ m/s, at $y = 8\,l_c$ and: (a) $x = 3\,l_c$; (b) $x = 4\,l_c$; (c) $x = 4.5\,l_c$; (d) $x = 5\,l_c$; (e) $x = 5.5\,l_c$. (See Fig. 5.40 for locations).

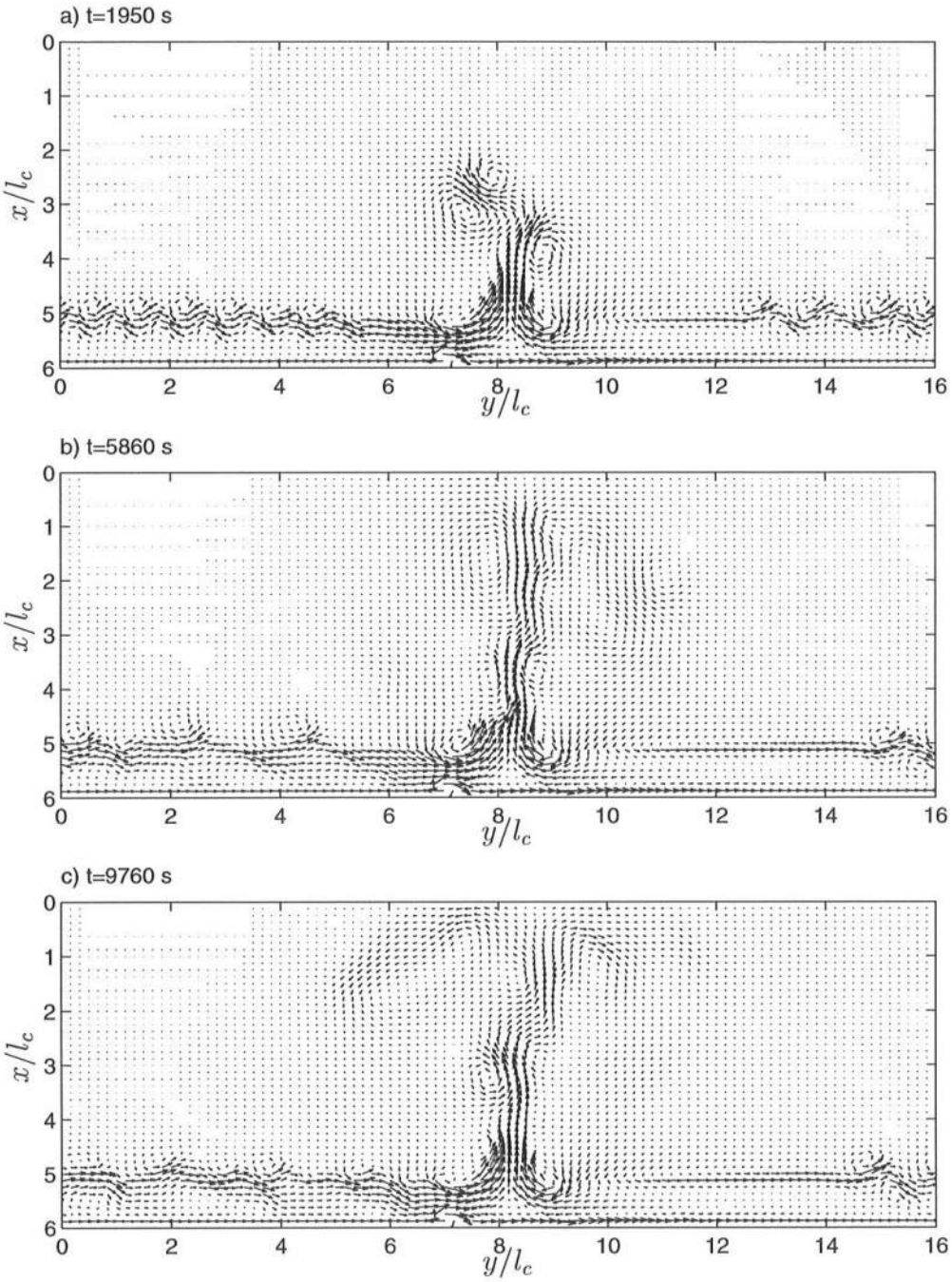

Figure 5.50: Depth-averaged current vectors at three instants of the simulation, for the simulation with depth-uniform currents. (See Fig. 5.38 for the wave field properties).

The plots of the time series (Fig. 5.48 and 5.49) and the instantaneous velocities (Fig. 5.50) show that the rip-current is very dynamic and exhibits several features common with the shear waves. Results from other computations with slightly different model parameters showed a similar pattern, and we found that the shorter period of the rip-currents oscillations was mostly constant and around $T = 450$ s. For the shear waves though, (Fig. 5.46 and 5.47) we observe a downshift of the period from $T = 440$ s to $T = 800$ s, which is similar to the period observed for the simulations in section 5.2 with a different incident wave field. A hydrodynamic instability mechanism is common to the two flow types — the shear waves and the rip-currents. For the shear waves a linear analysis of the instability mechanism is given by Bowen and Holman (1989), whereas the rip-currents are similar to a jet flow and a linear instability analysis can be found in Drazin and Reid (1982) for certain simplifying situations. Long period oscillations of rip-currents have also been observed by Shepard and Inman (1950), Sonu (1972), and Haller *et al.* (1997). The observations of Shepard and Inman were conducted at the Scripps Beach at La Jolla, CA, and the authors indicated the presence of "major fluctuations in the onshore-offshore current ... on an average of 7.8 min (480 s) ...". Other phenomena such as wave groupiness, wave-current interaction, and obliquely incident multiple wave trains can also provide a mechanism for unstable rips, but the present computations show that for a steady wave forcing and no wave-current interaction, unstable rip-currents can be formed as well. Also, the fact that the period of both the shear waves oscillations and the rip-currents predicted in our simulations is of the same order of magnitude suggests that these phenomena have a similar origin.

Similar to the shear waves "mixing" (in the long time-averaged sense), it is suspected that the meandering rip-currents can also induce a mixing. In the following, the time-averaging designation refers to an averaging over the period of the simulation (several hours). (The second overbar in the expression below indicates

the long time-averaging). The shear stress (mixing) caused by the meandering rip-currents can be computed from the difference between the time-averaged convective accelerations in the momentum equations and the similar terms computed from the time-averaged values, namely:

$$\begin{aligned}\sigma_x &= \overline{\frac{\partial}{\partial x}\left(\frac{\bar{Q}_x^2}{h}\right)} - \frac{\partial}{\partial x}\left(\frac{\overline{\bar{Q}}_x^2}{\bar{h}}\right) \\ &+ \overline{\frac{\partial}{\partial y}\left(\frac{\bar{Q}_x\bar{Q}_y}{h}\right)} - \frac{\partial}{\partial y}\left(\frac{\overline{\bar{Q}}_x\overline{\bar{Q}}_y}{\bar{h}}\right)\end{aligned} \tag{5.30}$$

for the x–momentum, and similar for the y–momentum. It turns out that σ_x is very small ($\mathcal{O}(10^{-4})$ m^2/s^2) for the present situation, which indicates that the mixing along the axis of the rip-channel is negligible. This leads to the conclusion that the magnitude of the advective accelerations seen in Fig. 5.44 are not associated with a mixing, but solely with the flow acceleration necessary to change the direction and magnitude of the currents in that region. This result is in agreement with the simplified analysis given by Arthur (1962), who gives an account of the effect of the inertial forces along a rip-current. The effect is to decrease the width of the rip as the water depth increases, due to conservation of potential vorticity (in the absence of dissipation, which is not the case here). In the presence of friction we can expect that the inertial accelerations will still be important, but the rip-current can broaden.

In this section we saw that the modification of the wave field over the bar promoted the generation of rip-currents over the rip-channel, forced by a longshore pressure gradient that drives the longshore "feeder" currents towards the rip. Shear waves and unstable rip-currents are seen to be predicted, which suggests that a complexity of multiple flow types can be present simultaneously in field conditions (as documented by Sonu, 1972). Over the rip-channel, the velocity fluctuations are much smaller than just upstream of it, which means that the existence of the

rip-current destroys the structure and development of the shear waves. Finally, it should be noted that we did not include the effect of wave-current refraction in the wave model REF/DIF1. It is clear that for the present situation it is likely that waves will refract in strong opposing currents. However, for this particular situation of waves propagating on strong opposing currents a more suitable wave model is needed. This could change the results of the present computations, but the overall conclusions are expected to remain valid.

5.3.2 Depth-varying currents

It is interesting to examine the results of the full quasi-3D model for the case just studied, where we assumed depth-uniform currents. Hence, for the following study, the wave conditions and beach geometry are the same as in the example of the previous subsection, and we introduce back into the governing equations the terms that account for the dispersive mixing. Therefore the model equations are now the complete set (5.23)–(5.27), with the same parameters as those in the previous example, and in the example in subsection 5.2.3, i.e., $C_1 = 0.75$, $M = 0.1$ and $f_{cw} = 0.006$.

We documented in subsection 5.2.3 that the inclusion of the dispersive mixing reduced significantly the onset of shear instabilities of the main flow. For the present simulation our results converged to a steady state solution, whereas previously both the rip-currents and the longshore currents became unstable. Thus, Fig. 5.51 shows the steady, depth-averaged, velocity vectors for the present simulation. The maximum cross-shore velocity at the rip is $\tilde{U} = 0.2\, c_c$ (0.7 m/s), which is equal to that observed for the previous case. The maximum longshore velocity is also equivalent to that seen previously, and thus cross-shore profiles of $\tilde{V}$ are not shown. However, comparing Fig. 5.51 with Fig. 5.40, the rip-current is considerably narrower and

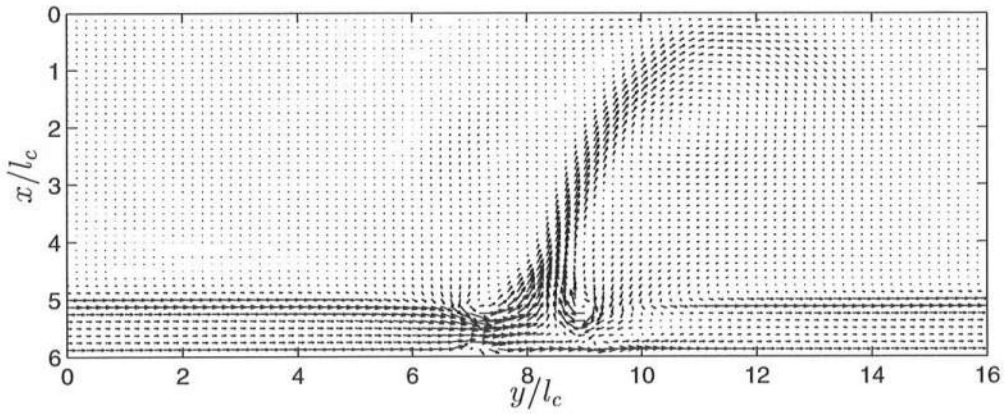

Figure 5.51: Total depth-averaged velocity vectors, $\vec{V}$ for the simulation with depth-varying currents. (See Fig. 5.38 for the wave field properties).

more directed downstream than in the previous situation. It is suspected that the results close to the offshore boundary can be affected by the presence of it, as the absorbing-generating boundary condition used here only absorbs propagating plane waves, and not an unknown steady current. Fig. 5.51 shows also the presence of converging longshore currents towards the rip-channel in the bar-trough region, and a shoreward mass flux at each side of the rip. The current at the beach face is always directed downstream.

The vertical variation of the cross-shore and longshore currents along the rip-channel axis, and at $y = 0$ is shown in Fig. 5.52 and 5.53. For both figures we note that the longshore velocities are nearly depth-uniform, whereas the cross-shore velocities vary significantly with the depth, mainly in the region over the bar-crest. More interesting is it that along the rip-channel the cross-shore velocity is sheared vertically seawards, whereas away from the rip, at $y = 0$, the cross-shore velocity shows the "classical" undertow profile. The vertical shear of U/c_c at $y = 8\,l_c$ is caused by the large bottom shear stress that acts to retard the rip-current. To the

author's knowledge, very few observations of the vertical structure of the velocities along a rip-current have been reported. One of such (Shepard and Inman, 1950) indicates a similar trend to the one predicted in our computations. Conversely, the descriptive accounts given by Shepard *et al.* (1941) indicate that the cross-shore velocity in a rip-current can be the strongest both at the surface and below it. Hence, further verification of vertical variation of the velocities along a rip is needed.

Finally, we show in Fig. 5.54 the magnitude of the terms in the cross-shore and longshore momentum equations along the rip-channel axis ($y = 8\,l_c$). From this plot we extract that the dispersive mixing (–•–), both in the x and y–momentum balance, is only significant in the breaking region. Over the bar-crest, it appears to be a small term even though this region is where the vertical variations of the currents are more pronounced. At other cross-sections though, we observe that the dispersive mixing can be locally large, such as that observed in Fig. 5.36 in the example in section 5.2.4. For example, slightly downstream of the rip-channel the dispersive mixing is a very significant term. Once again (see Fig. 5.44 for comparison), the inertial accelerations are the dominant terms in the y–momentum equation, together with the longshore pressure gradient. Nevertheless, the presence of the seemingly small dispersive mixing term has the effect of stabilizing the previous unstable meandering rip-currents. Note that some care must be taken in the interpretation of the results with the dispersive terms, as the underlying assumption that $V_{1\alpha}$ and $\frac{\partial V_{1\beta}}{\partial x_\alpha}$ are small compared to $\tilde{V}_\alpha$ or $\frac{\partial \tilde{V}_\beta}{\partial x_\alpha}$ may not hold in the region around the rip-current, where rapid variations in the flow field can be present.

In conclusion, the results for the present simulation suggest that a fine balance can exist between the various phenomena that can be present in nearshore flows. Several mechanisms are present at all times, such as turbulent dissipation,

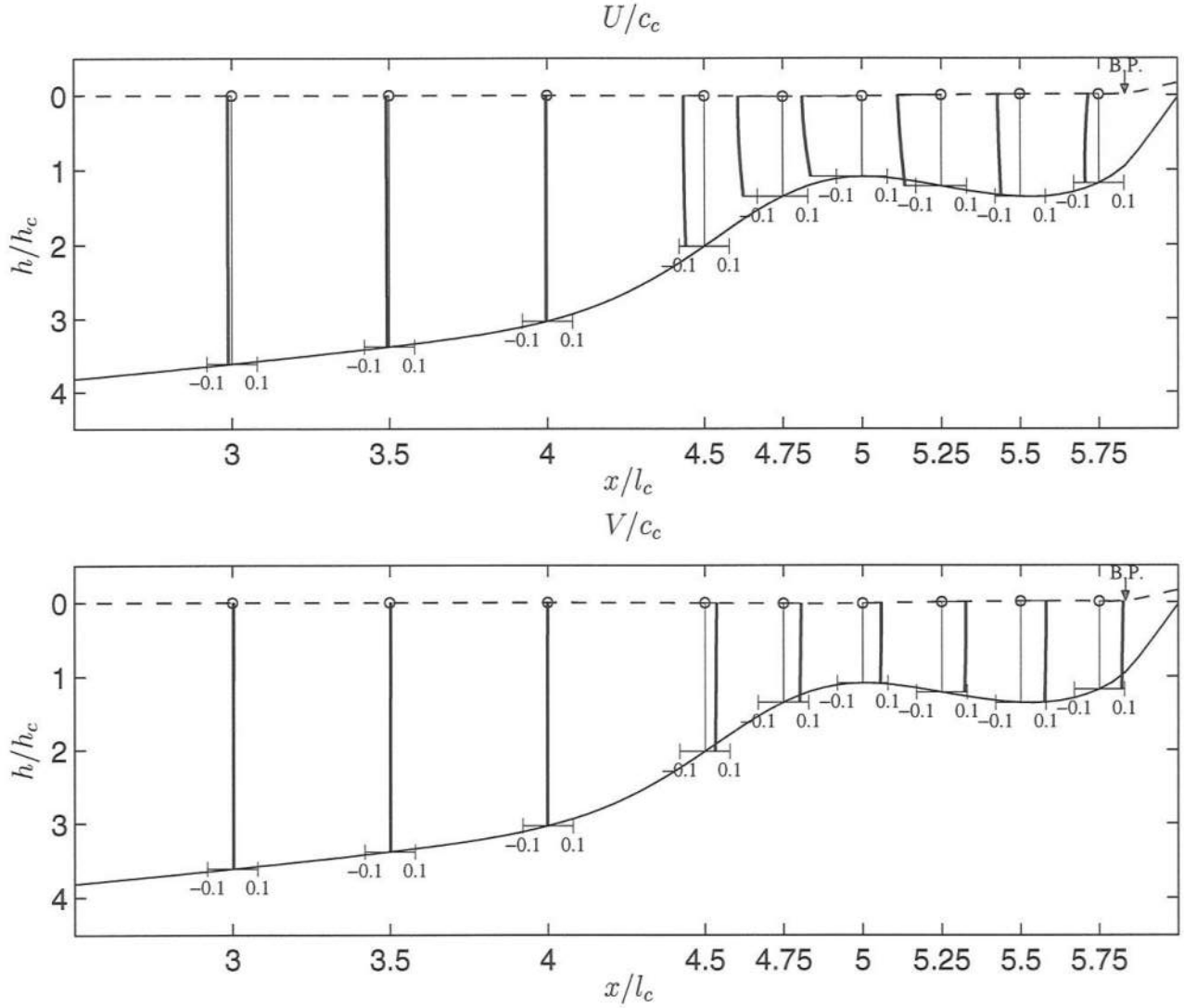

Figure 5.52: Cross-shore variation of the vertical profiles of U/c_c and V/c_c at $y = 8\,l_c$.

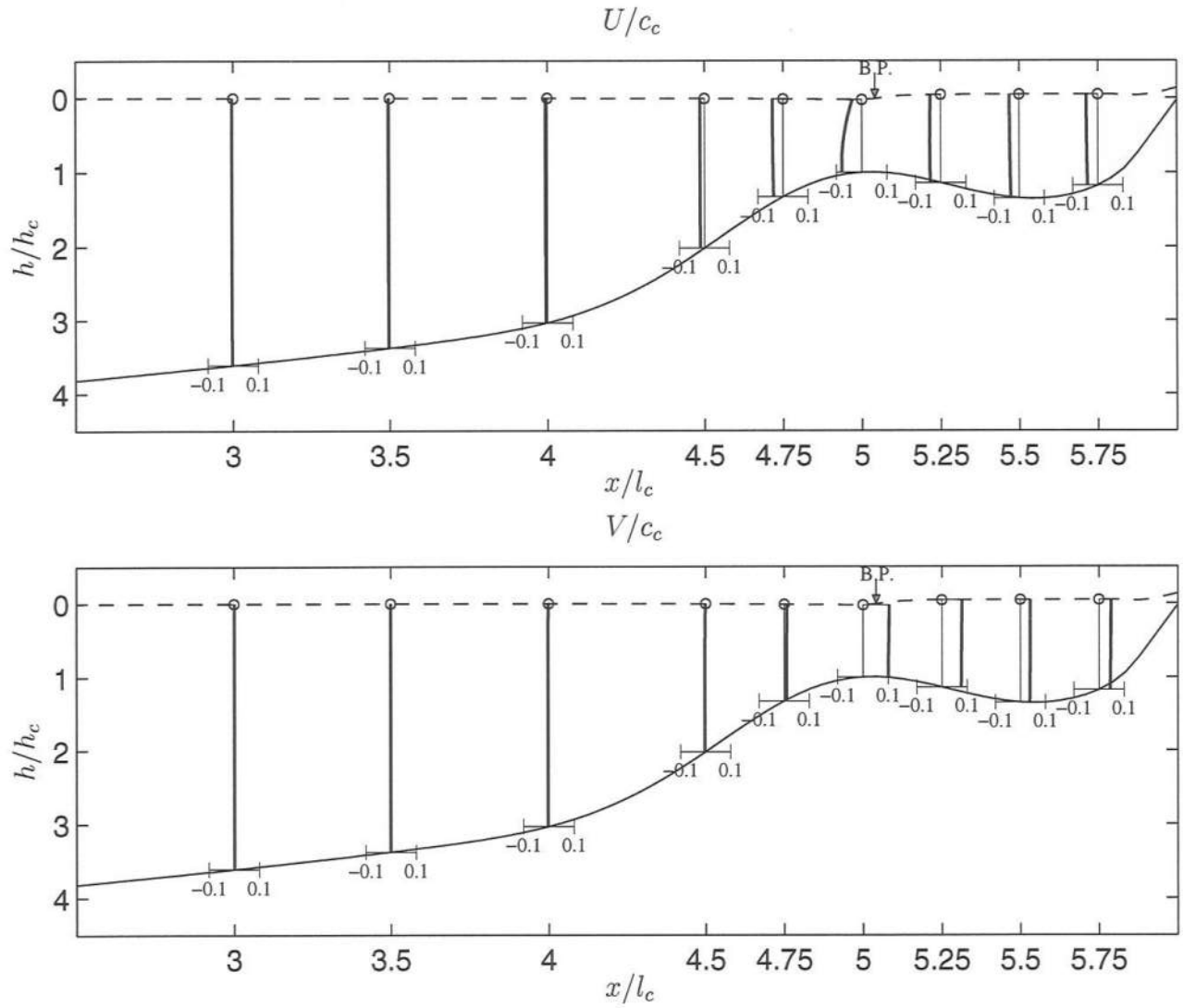

Figure 5.53: Cross-shore variation of the vertical profiles of U/c_c and V/c_c at $y = 0$.

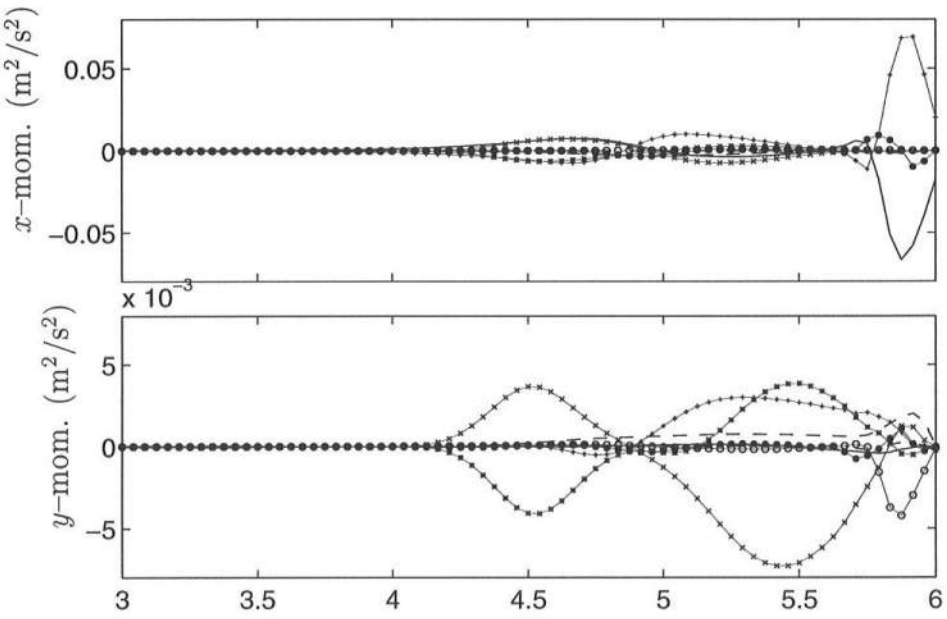

Figure 5.54: Cross shore distribution at (a) $y = 0$, and (b) $y = 8\,l_c$ of the (time-averaged) terms in the momentum equations. Terms in the x–momentum balance: $gh\frac{\partial \bar{\zeta}}{\partial x}$ (+), $\frac{1}{\rho}\frac{\partial S_{xx}}{\partial x}$ (——), $\frac{1}{\rho}\frac{\partial S_{yx}}{\partial y}$ (○), $\frac{\partial}{\partial x}\left(\frac{Q_x^2}{h}\right)$ (×), $\frac{\partial}{\partial y}\left(\frac{Q_x Q_y}{h}\right)$ (∗), – turb. mixing (– ·), $\frac{\tau_x^B}{\rho}$ (– –), – dispersive mixing (–•–). Terms in the y–momentum balance: $gh\frac{\partial \bar{\zeta}}{\partial y}$ (+), $\frac{1}{\rho}\frac{\partial S_{yy}}{\partial y}$ (——), $\frac{1}{\rho}\frac{\partial S_{xy}}{\partial x}$ (○), $\frac{\partial}{\partial y}\left(\frac{Q_y^2}{h}\right)$ (×), $\frac{\partial}{\partial x}\left(\frac{Q_x Q_y}{h}\right)$ (∗), – turb. mixing (– ·), $\frac{\tau_y^B}{\rho}$ (– –), – dispersive mixing (–•–).

momentum dispersion and bottom friction, which are all interrelated. The conservative (pressure gradient) and inertial forces respond to the bottom configuration and the driving forces (radiation stress gradients). Flow instabilities can occur for sufficiently low values of the dissipative and dispersive mechanisms.

5.4 The effect of the bottom friction

It Chapter 2 we discussed the formulation and characterization of the bottom shear stress. Throughout our studies we have kept the nonlinear formulation given by equations (2.98) (repeated in (5.27)). For the simulations in sections 5.2 and 5.3 the bottom friction coefficient was chosen as $f_{cw} = 0.006$, which is within the range of values typically used in prototype situations.

Several studies related to steady and unsteady phenomena in the nearshore region have made use of a linear friction formulation. Linear relations can be recovered from the nonlinear relation used here for the limiting cases of weak or strong currents relative to the magnitude of the wave orbital velocity ($\frac{V_b}{u_0} \ll 1$ and $\frac{V_b}{u_0} \gg 1$). From the results of several simulations with SHORECIRC with both the linear and nonlinear formulations we confirm that it is only required to use the nonlinear formulation when the assumption the linear formula is no longer valid. Though this result is obvious, what it is not so apparent is that in order to find out whether those assumptions are valid or not, we would need to simulate the same physical situation with the nonlinear expression, and thus there would be no need to use the linear formulation. Also, in complex geometries, such as a longshore non-uniform barred beach, the validity of the limits $\frac{V_b}{u_0} \ll 1$ or $\frac{V_b}{u_0} \gg 1$ can be local, i.e., it will be valid in certain regions but not all over the domain. Therefore, we conclude from our studies that it is important to use the nonlinear formulation in cases where the assumptions to use the linear model are not valid everywhere.

More important than the use of the linear or the nonlinear formulations is the proper estimation of the bottom friction coefficient. An increase of the bottom friction will slow the current velocities, but it will also affect the onset and development of flow instabilities as seen in the following example. Thus, in this section, we recover the physical situation and model equations used in subsection 5.3.1 for depth-uniform currents (no dispersive mixing).

Fig. 5.55 shows the depth-averaged velocity vectors at three instants of time (the same as in Fig. 5.50) for a simulation identical to that in subsection 5.3.1, but with a larger bottom friction coefficient, i.e., $f_{cw} = 0.008$ instead of $f_{cw} = 0.006$. The intercomparison between Fig. 5.55 and 5.50 demonstrates that an increase in the bottom friction coefficient altered the development of both longshore currents and rip-currents instabilities. For the case of larger friction, at $t = 1950$ s the instabilities have barely started to develop, whereas at the same time for the smaller friction coefficient the motion is noticeably unstable. At the latter stages we notice that the vortex shedding along the rip-currents is also significantly larger for the smaller friction simulation (Fig. 5.50), and also that the shear waves do not undergo a subharmonic transition for the present case (Fig. 5.55). For the present situation the shear waves are characterized by $T \simeq 500$ s, $L \simeq 1.1\, l_c$, and $c_s \simeq 0.075\, c_c$ ($c_S \simeq 0.25$ m/s). The rip-currents happen to oscillate at the same frequency, but it does not seem appropriate to define a wavelength as the flow is not periodic in space. Both the shear waves and unstable rips are less dynamic and more regular for the higher friction coefficient, which is a property observed by, e.g., Özkan-Haller and Kirby (1997) for the case of shear waves alone over a barred beach. For larger friction coefficients we find that the motion eventually becomes steady, which is similar to the trend observed due to the inclusion of dispersive mixing (see section 5.3.2).

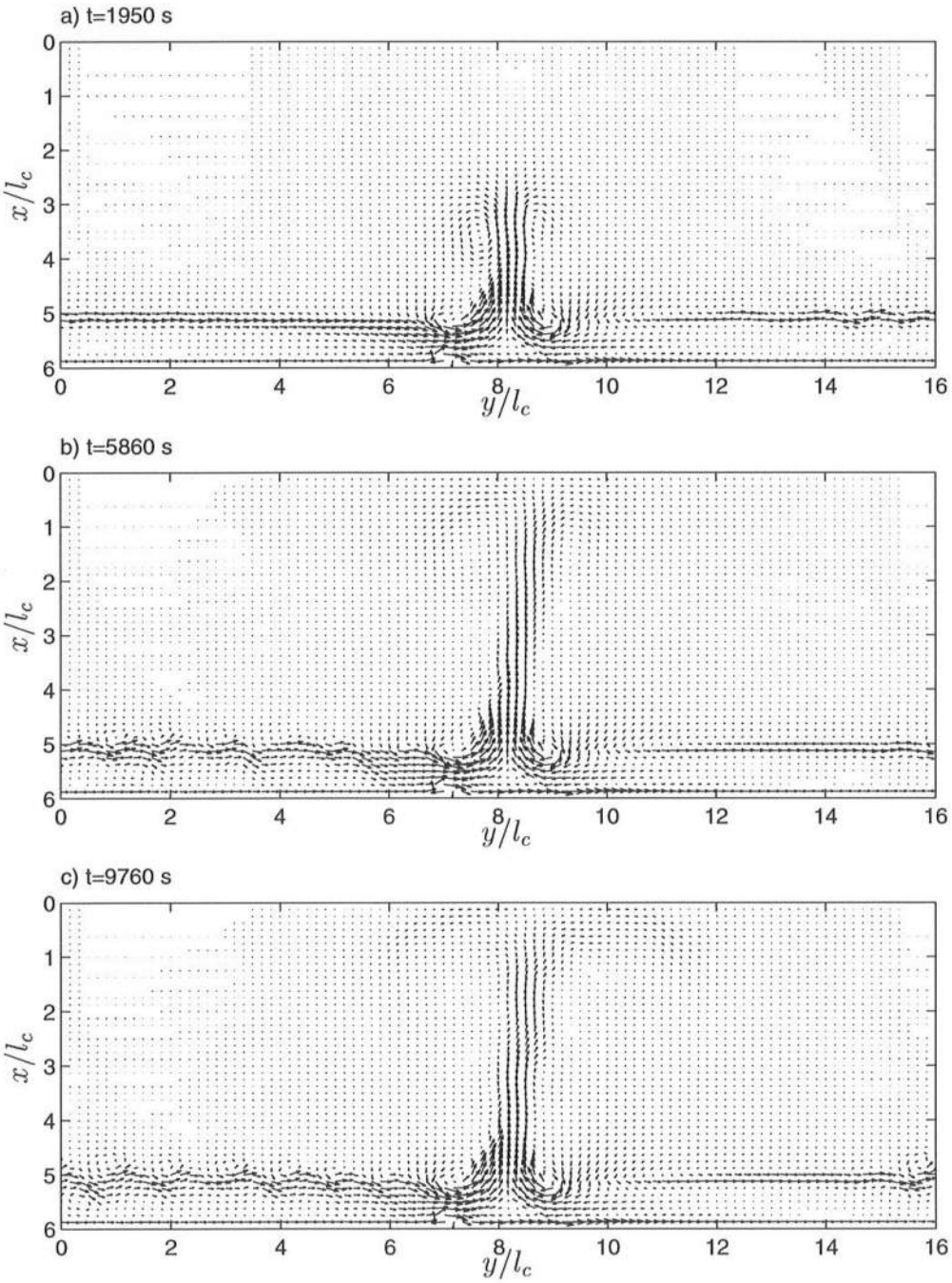

Figure 5.55: Depth-averaged current vectors at three instants of the simulation for the case with higher friction ($f_{cw} = 0.008$). (See Fig. 5.38 for the wave field properties).

The overall time-averaged current velocities are also slightly smaller as expected, with the largest differences near the shoreline peak (see Fig. 5.43 for similar results). Over the bar-crest we find that the velocity profiles are essentially unmodified from the ones shown in Fig. 5.43.

In summary, this one simple example confirmed that a small variation of the bottom friction coefficient, which is a parameter we know with great uncertainty, can significantly modify the dynamics of the flow properties. We have dealt here with a constant friction coefficient over the whole domain, but in field applications it is likely that the friction coefficient can change by 30-50% of the mean value, but this variation is also not known accurately. Hence, the overall uncertainty around the values of the bottom friction coefficient, and the sensitivity of the model predictions to the value of it, suggests that further research should be conducted in this direction.

Chapter 6

MODEL SIMULATION AND COMPARISON WITH THE 1990 DELILAH FIELD DATA

In the present chapter we apply the model SHORECIRC to simulate the conditions observed at certain times during the 1990 DELILAH nearshore field experiment, at Duck, NC (see Fig. 6.1 for location). We focus our modeling efforts on the simulation of three different hydrodynamical conditions, two of them on 10th of October of 1990 at different tidal stages, and one other on the 19th of October for incoming waves from a different sector. Several previous modeling efforts (e.g., Smith *et al.*, 1993; Church and Thornton, 1993; Reniers *et al.*, 1995; Karjadi and Kobayashi, 1996) have failed to predict the maximum of the longshore current velocity in the trough behind the bar. As an example Fig 6.2 shows the results of the application of the longshore current model of Church and Thornton (1993), where longshore uniformity of the topography and wave conditions were assumed. The comparison between the lines and the solid circles clearly indicates that the model predicts a bi-modal current profile, with the maximum over the bar-crest, whereas the data suggests a maximum of the longshore current over the trough. This fact motivated us to apply the more complete model SHORECIRC (relative to the previous models) to study those conditions.

The results from Sancho *et al.* (1995) show that the longshore pressure gradient can be a dominating force in the trough behind a bar, which can induce

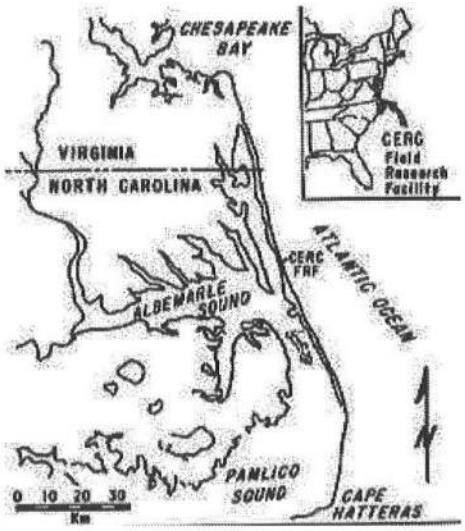

Figure 6.1: Location of the Field Research Facility. (Adapted from Birkemeier *et al.*, 1997).

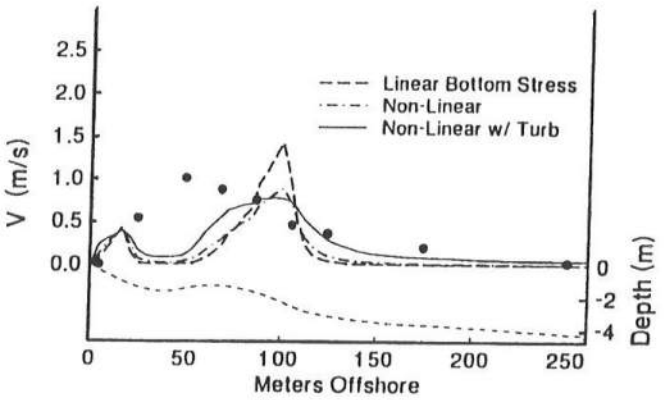

Figure 6.2: Model predictions and observations of longshore currents for DELILAH, 10th Oct. (Results from Church and Thornton, 1993).

a longshore current with the maximum in that region. In Fig. 6.3 we reproduce partially the results from those authors, where it is seen that in a region far away from a rip-channel ($y = 0$ m) the longshore current is bi-modal (i.e., it has two maxima), but as the distance from the rip-channel is reduced (see lower plots) the current profile exhibits a single-peak, located over the trough. Hence, in this chapter we are interested to find out if a significant longshore pressure gradient can be present for the conditions observed during DELILAH, and if so, whether that longshore pressure gradient is the primary force for the observed single-peaked longshore current profile.

Several other studies (e.g., Allender *et al.*, 1978; Greenwood and Sherman, 1986) also indicate the presence of a single-peak of the longshore currents over the trough. However, recently, Feddersen *et al.* (1996) compiled several longshore current measurements during the experiment DUCK94, and found that the maximum of the longshore current is located mostly slightly shoreward of the bar crest, and at times near the shoreline. They also found that frequently the current profile is bi-modal. These authors confirmed the findings of Thornton and Kim (1993) that the longshore currents are strongly tidally correlated: at high-tide the current maxima is mostly located shoreward of the bar-crest ($x' \simeq 0.8\, l_c$), and at low-tide V_{max} is near the bar-crest. Hence, the observations of these studies suggest that the conditions observed at DELILAH can be sporadic.

More than just a comparison effort, this chapter combines several of the ideas exposed in the previous chapters. The simulated beach corresponds to the surveyed topography and exhibits a longshore nonuniform bar. Observations and field data analysis (Church *et al.*, 1992) suggest that shear waves were present on the 10th of October. The model results of SHORECIRC are compared with the field data, and a discussion is provided on the importance and effect of the mechanisms that affect the

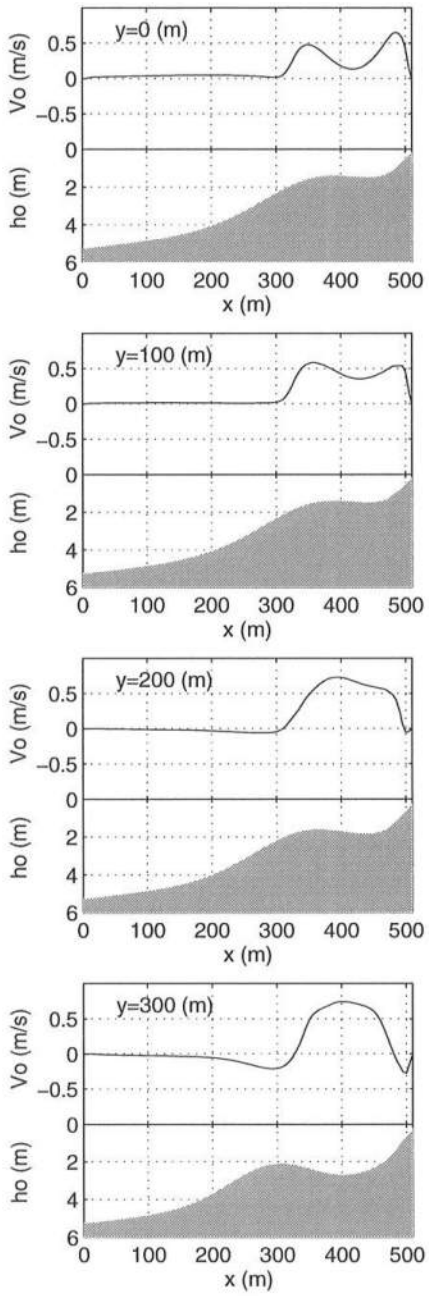

Figure 6.3: Longshore current velocities and depth profiles over a longshore nonuniform barred beach, at four cross-sections, for an obliquely incident wave. (Adapted from Sancho *et al.*, 1995).

results. A discussion is given on the effect of several variables and parameters that affect our predictions, such as the wave climate, the possible existence of external incoming lateral currents, and the friction and eddy viscosity coefficients.

6.1 Experiment overview and test conditions

The DELILAH (Duck Experiment on Low-frequency and Incident-band Longshore and Across-shore Hydrodynamics) experiment was conducted during the fall of 1990 at the US Army Engineer Waterways Experiment Station, Coastal and Hydralics Laboratory, Field Research Facility (FRF) located in Duck, NC (Fig 6.1). This experiment was a cooperative effort of several institutes, and the aim was to measure the wind and wave-forced three-dimensional nearshore hydrodynamics. An extensive overview of the project is given by Birkemeier *et al.* (1997), and briefer descriptions have been presented in several of the works mentioned above. In the following we will compile the most relevant information for this work.

Nineteen electromagnetic current meters were deployed at the beginning of the experiment and data was collected at 8 Hz sampling frequency. Nine gauges form the "primary cross-shore array", which are designated by CM10-CM90 (see Fig 6.4), and the other ten gauges form the secondary arrays. Of those, four current meters were located slightly seaward of the bar-crest position (CM71-CM74) and thus form the "crest sub-array", five were positioned over the trough (CM31-CM35) and form the "trough sub-array", and the last one (CM54) was located such that it formed the "secondary cross-shore array" in combination with two other sensors. (Please note that the coordinate axis in Fig. 6.4 is rotated $-3°$ from the FRF coordinate axis). Along the primary cross-shore array (monitored by the Naval PostGraduate School) at each location there was a Marsh-McBirney current meter, a Paroscientific pressure

gauge[1], and a Setra strain-gauge pressure sensor. The pressure sensors for wave height measurements were only positioned along the primary cross-shore array, and data was also sampled at 8 Hz. At the other locations there were 5 Marsh-McBirney, and 5 Scripps Open Frame electromagnetic sensors (from the Scripps Institution of Oceanography). At the positions designated by CM71-CM74 and CM54 were the 5 Open Frame sensors, which proved to be significantly affected by the growth of biofouling. According to Birkemeier *et al.* (1997), "data collected using Open Frame sensors should be used with caution", as the the response function of these sensors was significantly attenuated throughout the duration of the experiment. The results of the pre- and post-calibration (before and after the data collection) of the instruments is given by Birkemeier *et al.*. The data set was found to be of highest quality between the 6th and the 16th of October.

Throughout the experiment the current meters CM10 and CM20 were, at times, moved vertically to account for changes in water depth. Nevertheless, these current meters were exposed at certain times which is identified by foul readings. Unfortunately, we were not able to find out the true vertical positions of the sensors at all times, and thus the positions at the beginning of the experiment are used for the data comparisons here[2]. Some of the current meters were lost or stopped working along the experiment, namely, CM60 after the 10th, and CM30 around the 14th.

The gauge locations and vertical positions are identified in Table 6.1. The positions are relative to the FRF coordinate system that, as mentioned above, is rotated 3° relative to the coordinate axis in Fig. 6.4. This figure also shows the

[1] These sensors were designed to measure mean surface elevation, but it was later found that they did not provide accurate readings.

[2] Note that this can give misleading errors in the model to data comparison, as we will calculate velocities at the presumed vertical position of the sensors.

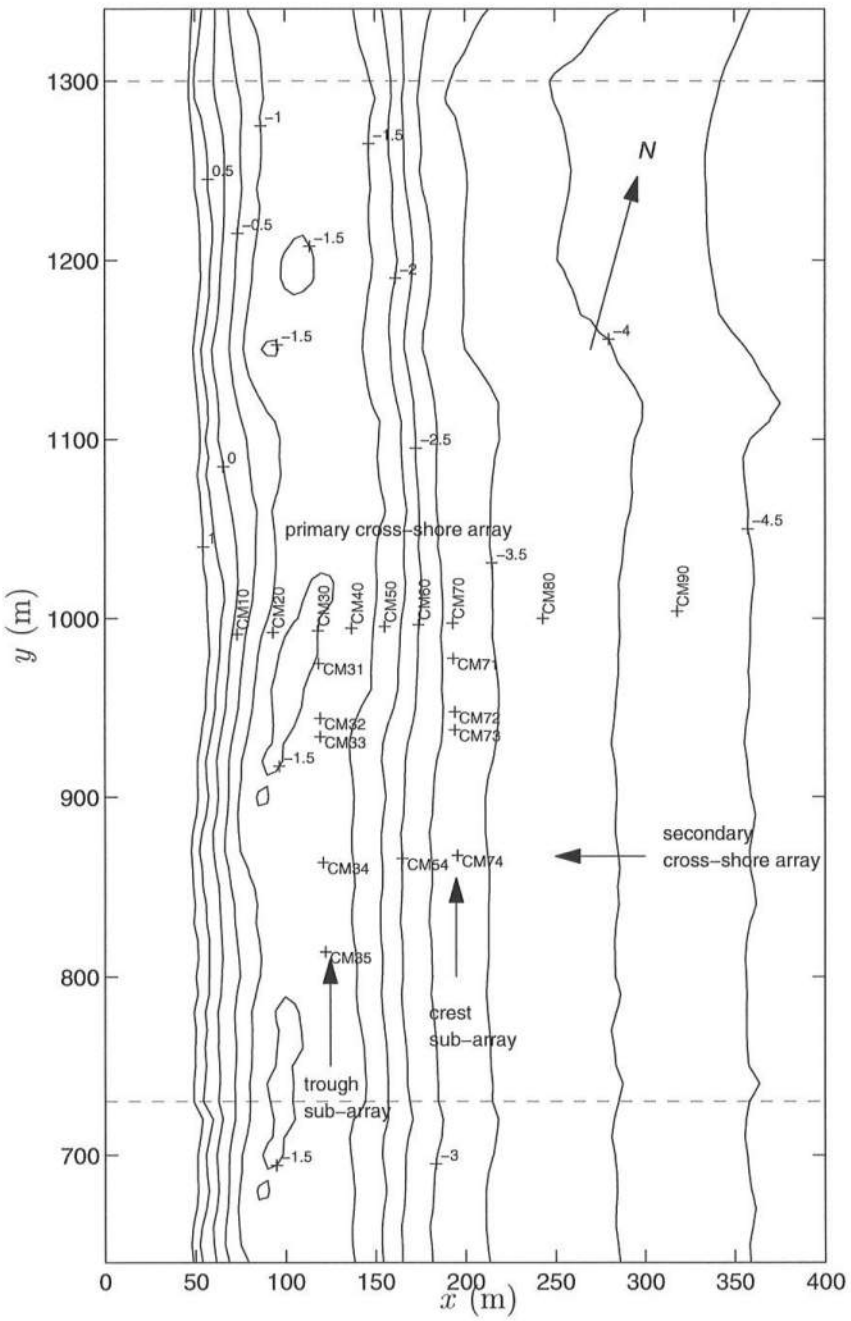

Figure 6.4: Location and numbering of the DELILAH array and depth contours for the 10th Oct. (Adapted from Birkemeier *et al.*, 1997).

bathymetric contours for the 10th Oct. (referenced to the National Geodetic Vertical Datum, NGVD). The cross-shore dashed lines at $y = 730$ m and $y = 1300$ m delimit the region where daily surveys were collected, which is designated as the "mini-grid" region. The surveyed data is then interpolated and mapped onto the desired grid, where we chose $\Delta x = 5$ m and $\Delta y = 10$ m for our calculations (these spacings were found to be a good compromise between the length scales of the problem and the desired computational speed). The areas northward and southward of the mini-grid were artificially extended in order to use periodicity at the lateral boundaries. The depths at $y = 640$ m and $y = 1340$ m match each other, and thus the longshore domain length used for the computations (of the 10th Oct) is $l_y = 700$ m. (A similar transformation from the surveyed data points to a computational grid was performed for the 19th of October).

During the experiment the beach morphology varied significantly within days. The topography exhibited initially a rhythmic bar, which slowly migrated seawards and became more linear. At the 10th of October the bar was mostly linear, but rhythmic longshore nonuniformities of crescentic type were still present as it can be seen in Fig. 6.4 and 6.5. (Note the sensors marked by solid circles in the perspective plot). The latter figure shows that a longitudinal bar is present with the crest located at $x \approx 150$ m, and a trough at $x \approx 100$ m. The most seaward-northward location of the grid in Fig. 6.4 ($x = 400$, $y = 1340$ m) is identified at the (0,0) coordinate for our calculations, with the new x–axis directed shoreward and the new y–axis directed southward. All data and model results are from now on referenced to the new coordinate axis.

We decided to study the conditions observed during the 10th and 19th October in order to compare our model results with those of Reniers *et al.* (1997).

Table 6.1: DELILAH array current meter locations and gauge numbering (adapted from Birkemeier *et al.*, 1997)

Gauge Name	Longshore m	Cross-shore m	Depth* m	Gauge Depth* m
CM10	985.95	125.06	-0.28	0.07
CM20	985.94	144.99	-1.39	-0.77
CM30	985.61	169.97	-0.87	-0.66
CM40	985.95	188.94	-1.32	-0.82
CM50	985.88	207.41	-1.88	-0.98
CM60	986.08	226.25	-2.33	-1.02
CM70	985.91	245.00	-3.03	-1.05
CM80	985.97	295.21	-3.68	-1.66
CM90	986.11	370.12	-4.25	-1.68
CM31	967.22	169.57	-0.94	-0.82
CM32	936.44	168.68	-1.86	-0.78
CM33	926.17	168.21	-1.88	-1.67
CM34	856.09	166.06	-1.60	-0.82
CM35	806.37	164.87	-1.58	-0.92
CM54	855.87	210.37	-2.09	-1.02
CM71	966.04	244.36	-3.02	-0.93
CM72	936.08	243.65	-3.07	-1.01
CM73	926.06	243.16	-3.11	-1.04
CM74	856.05	240.88	-3.21	-1.27

* Depths relative to NVGD at start of DELILAH

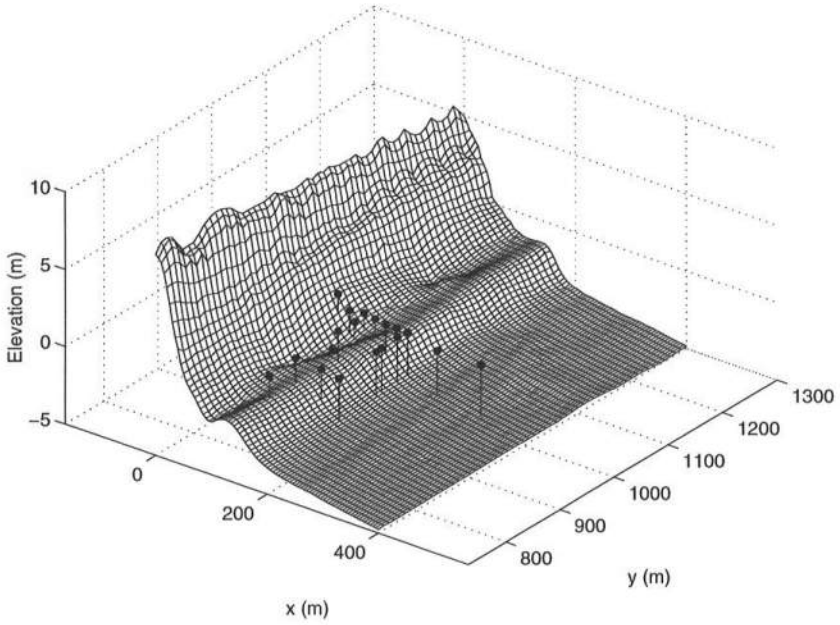

Figure 6.5: DELILAH: Beach bathymetry for the 10th of October.

Offshore directional wave spectra were estimated from an array of 16 pressure sensors mounted at the 8 m depth contour, and centered around the 800 m longshore line. Spectra were measured every 3 hours and provide the wave conditions for the forcing of SHORECIRC. Wind speed and direction were measured at the end of the FRF pier, and were then transformed to the standard 10 m height in order to calculate the wind shear stress by equation (2.114). The wind stress computed in this way is then applied uniformly all over the model domain, and is assumed constant over the simulated time.

For the comparison with field data, following Wu *et al.* (1985), random waves are approximated by a single representative monochromatic wave, with period equal to the peak period of the wave spectrum, and height equal to that of the "root mean square" wave height (H_{rms}). The wave direction is given by the peak angle of the directional spectrum, determined at the 8 m depth array. This direction is then

transformed from the 8 m depth contour to the depth at the seaward gridline of our domain using Snell's law. This procedure is equivalent to assuming that the bottom contours are parallel between the 8 m depth contour and the contour at the offshore location of the model domain. It should be noted that we have no information about the predominant wave angle further inshore than the 8 m depth array, and thus this assumption can introduce errors in the wave angle and the radiation stresses estimates. Hence, in one test, we will analyze the sensitivity of our predictions to the incident wave angle.

The wave height is calculated using the model REF/DIF1 and the results are used to compute the radiation stresses. This model is a monochromatic wave height model, and we found it necessary to modify the breaking criterion and the energy dissipation coefficient γ (see Kirby and Dalrymple, 1994 for details of the model) in order to use the model for the "root-mean-square" wave height. This is so because the breaking index for a random sea is in average much lower than that for a single wave. Hence, those model parameters were tuned to give a good agreement between the measured and predicted wave heights.

Table 6.2 shows the properties of the wave and wind climates that characterize the conditions observed at the given times. Each time for a certain date corresponds to the initial time of a period of three hours, for which the given values are the mean values. The incoming wave conditions were nearly stationary over the three hour periods, as we can see in Fig. 6.6 for one of the simulated periods. The waves were mostly narrow banded for the 10/10/90:0351 and the 10/10/90:1022 periods, though by the end of the three hour record for this last period the local wind had increased significantly. For the 19/10/90:1221 period the offshore spectrum indicates that the wind-sea component is quite significant, which is confirmed by the large wind speed W.

Table 6.2: Observed wind and wave conditions for the given periods during the DELILAH experiment.

Date		10 Oct	10 Oct	19 Oct
Time		0351	1022	1221
H_{rms} (m)$^{\triangle}$	[8 m array]	0.80	0.84	0.88
$\alpha_w(^\circ)$ †	[8 m array]	-35	-37	41
T_p (s)		10.7	9.7	7.6
W (m/s)		2.5	6.5	8.0
$\phi_{wind}(^\circ)$ †		-65	-60	135
H_{rms} (m)‡	[CM90]	0.70	0.68	0.66
H_{rms} (m)	[REF/DIF1]	0.74	0.74	0.64
$\alpha_w(^\circ)$ †	[REF/DIF1]	-26.5	-29	31
Tidal level* (m)		-0.26	0.51	-0.35
H_b/h_b	[REF/DIF1]	0.50	0.45	0.50
γ	[REF/DIF1]	0.30	0.30	0.30

$^{\triangle}$ $H_{rms} = H_{m0}/\sqrt{2}$, where H_{m0} is determined from the energy spectrum.
† Angles relative to the cross-shore direction in our rotated coordinate system with origin at the seaward-northward location.
‡ $H_{rms} = \sqrt{8\,\sigma^2}$, where σ^2 is the variance of the surface elevation record.
* Levels relative to NVGD.

We note (see Table 6.2) that there is a difference between the measured wave height at the 8 m depth array and the wave height at the most seaward sensor in the primary cross-shore array (CM90). This difference can not be explained by linear wave shoaling and refraction (see also Smith *et al.*, 1993). The wave heights and angles used for the REF/DIF1 model input are also given in Table 6.2, as well as the breaking criterion and dissipation parameter γ that give the best agreement for the wave heights along the primary cross-shore array. Thus, an uniform plane wave with $H = H_{rms}$ is specified at the offshore row of the domain for REF/DIF1 calculations.

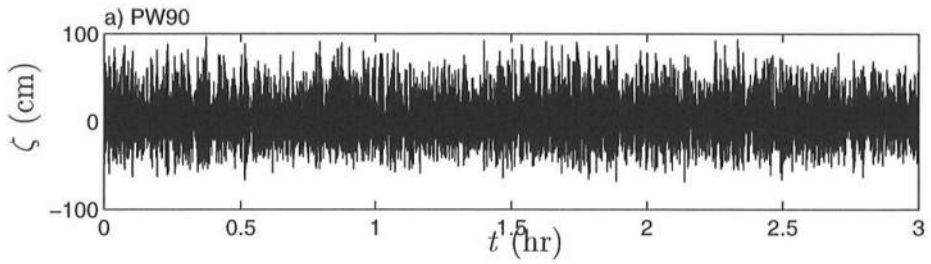

Figure 6.6: Time series of the surface elevation from the pressure sensor PW90 for the 10/10/90:0351 record. (Data given by J. Oltman-Shay).

The mean tidal levels during the 3 hr records are also given in Table 6.2. The records for the chosen periods are close to the high and low tides, and thus the influence of the tidal variation on the pressure and current measurements is minimal. At high and low tide the tidal currents are close to zero, which also minimizes the influence of these in our model to data comparison. Note that at other tidal stages there is not only a stronger tidal current, but moreover, a significant variation in the wave height and wave-induced currents during the 3 hr record due to the local variation in water depth (Thornton and Kim, 1993).

Church *et al.* (1992) reported the presence of significant energy in the far-infragravity frequency range that can be attributed to shear instabilities. Fig. 6.7 shows the time series of the (band-passed) cross-shore and longshore current velocities over the 3 hr record 10/10/90:0351 at the location CM30. Each data point corresponds to a 64 s average of the original data sampled at 8 Hz. This figure shows that there is a considerable variation of both the cross-shore and longshore current velocities on a time scale much longer than that of the short waves. It appears that most energy is in the $500 < T < 1000$ s range, but there is also energy at lower and higher frequencies. In general, Church *et al.* show that the oscillations for periods larger than 200 s are due to shear waves.

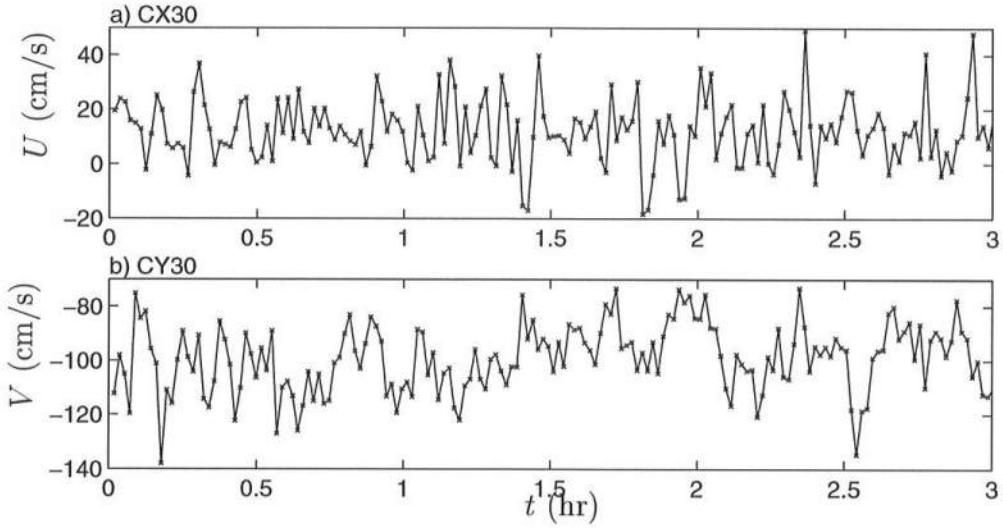

Figure 6.7: Time series of the low-frequency pass cross-shore and longshore velocities at CM30 for the 10/10/90:0351 record. (Data given by J. Oltman-Shay).

Next we will present the results of the model simulations for the conditions at the different dates. We will focus primarily on the time-averaged values of the simulations and compare with the time-averaged values (over 3 hr) of the data. Time series of the velocities and wave heights at the primary cross-shore array for the period between the 6th and 16th of October, and averaged over 5 min, were ceded to us by E. B. Thornton. Raw time series of the data sampled at 8 Hz for each of the three hour records at all gauges were provided by J. Oltman-Shay.

6.2 Simulations for the 10/10/90:0351 period

6.2.1 Standard model results

The topography for this period of simulation has already been shown in Fig. 6.4 and 6.5. The total still water depth is given by the depth referenced to the

NVGD subtracted by the tidal level of -0.26 m. Other input conditions are given in Table 6.2.

For the present simulations we found minimal differences between computations with the moving shoreline, and computations without. Therefore, all the results given here are for the case of a fixed shoreline placed close to the still water level, such that the minimum still water depth is $h_o = 0.05$ m. At this fixed shoreline a zero flux boundary condition is used. The grid points that extended further inshore from this boundary are excluded from the model domain, which then has dimensions $l_x = 340$ m and $l_y = 700$ m. For the model simulations the northward-seaward point in Fig. 6.4 is the (0,0) coordinate, the cross-shore x–axis is directed shoreward, and the longshore y–axis is pointed southward. The grid spacings are $\Delta x = 5$ m and $\Delta x = 10$ m, which reflect the fact that the cross-shore variations of the flow are typically much larger than the longshore variations. Computations with smaller grid spacings did not show appreciable variations from the simulations presented herein. The Courant number is $C_r = 0.7$. At the lateral boundaries we use the periodicity condition, and at the seaward boundary the absorbing-generating condition with zero incoming flow.

The bottom friction is calculated from Swart's formula (2.91), and we chose to compute the Nikuradse roughness as $k_N = 10\, d_{50}$, instead of equation (2.97), to account for a larger bottom roughness due to the combined presence of waves and currents[3]. The cross-shore variation of the sand mean grain diameter, at the 15th of October, is given by Thornton *et al.* (1996). Hence, we assume here d_{50} to be equal to the mean grain, and then estimate a continuous cross-shore distribution of the sand diameter and k_N. These values are used to compute f_{cw}. The eddy viscosity

[3] This increased bottom roughness can also be justified by the presence of sand mega-ripples observed during the experiment (see Birkemeier *et al.*, 1997).

is calculated from equation (2.86), with the values of $C_1 = 0.25$ and $M = 0.1$, which was seen in section 5.2.4 to yield reasonable vertical variations of the current velocities. Fig. 6.8 shows the cross-shore distributions of d_{50}, k_N, f_{cw} and $\nu_t/h\sqrt{g\,h_o}$ for the longshore position closer to the primary cross-shore array ($y = 340$ m). Note that in the region $320 < x < 340$ m the values of f_{cw} are out of the plotting range, and the maximum value is $f_{cw} = 0.033$ at the shoreline. The large values of f_{cw} in this region is caused by the increase of the bottom roughness and by the decrease of the wave orbital amplitude in the very shallow depths. Nevertheless, it is probable that the friction factor is much larger closer to the shoreline than at the other locations. The distribution of the eddy viscosity $\nu_t/h\sqrt{g\,h_o}$ has a relative maximum of 0.016 over the bar associated with wave breaking in that region, and a larger peak next to the shoreline due to the secondary breaking. (Note that this second peak of $\nu_t/h\sqrt{g\,h_o}$ is caused by the nondimensionalization).

The results for the wave height H_{rms} and angle α_w distributions over the model domain are shown in Fig. 6.9. Waves refract almost uniformly towards the beach, except behind the bar where the wave angles change considerably. The depth contours in Fig. 6.9c correspond to the actual still water depth taking into account the tidal level. The crosses indicate the location of the gauges, and the bar-crest is located at $x \simeq 260$ m. Fig. 6.9b shows that the wave height is mostly longshore uniform, but small deviations can be found in the trough behind the bar. It also shows that there is a first breaking line at $x \simeq 230$ m, and a secondary breaking much closer to the shore (at $x \simeq 310$ m). In the trough region between the two breaking zones the wave height is nearly uniform, which means that wave reformation is predicted.

The existence of two distinct breaking regions is confirmed by video time exposures, averaged over 10 min, of the wave conditions taken during the experiment

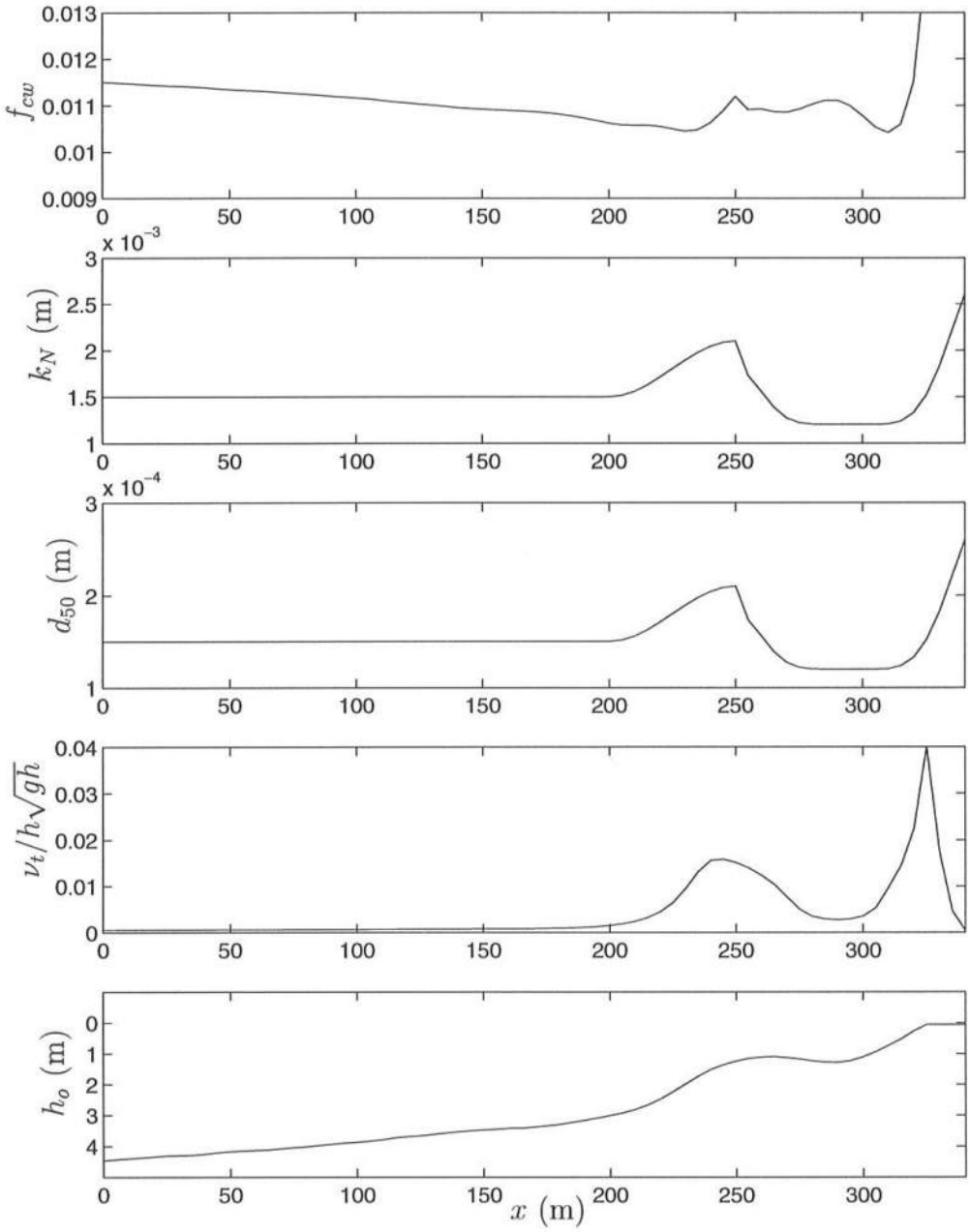

Figure 6.8: Cross-shore profiles of f_{cw}, k_N, d_{50}, $\nu_t/h\sqrt{g\,h_o}$ and h_o at the primary cross-shore array, for the 10/10/90:0351 simulation.

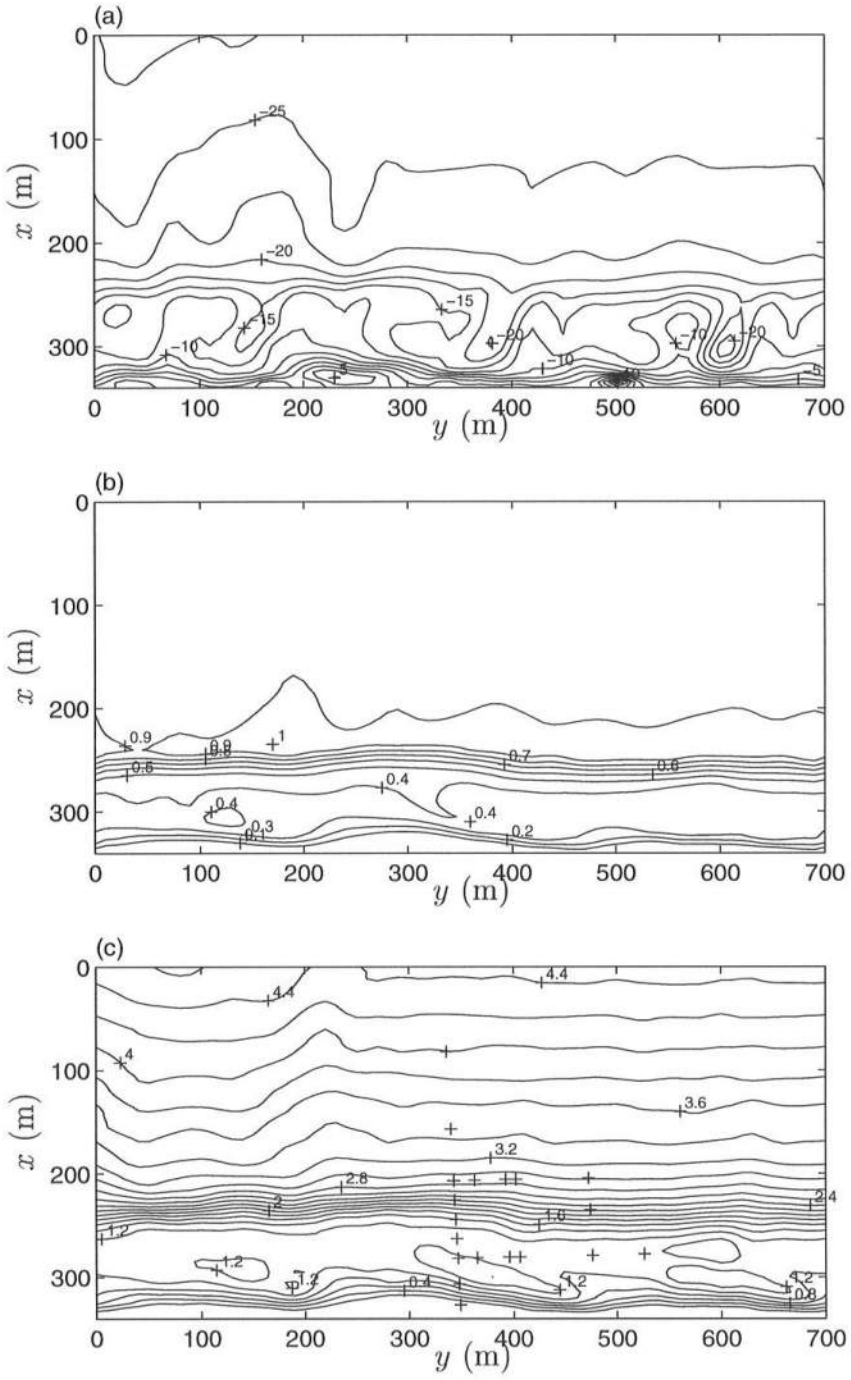

Figure 6.9: Contour plots for the 10/10/90:0351 simulation of: a) wave angle $\alpha_w(^\circ)$; b) wave height H_{rms} (m); and c) still water depth h_o (m).

Figure 6.10: Video time exposure (averaged over 10 min) of the wave conditions at DELILAH during the 10th October at mid-tide level. (Adapted from Birkemeier *et al.*, 1997). The primary cross-shore array is located 1/4 of the picture size down from the top.

(Fig. 6.10). The depicted conditions correspond to the 10th of October at a mid-tide water level. This video technique helps to identify the breaking locations and the position of the bar (Lippmann and Holman, 1989). The video camera is pointed towards the mini-grid area that we are simulating and the regions in white indicate wave breaking. It is observed that the breaking line is sinuous at the foreshore slope, and mostly uniform over the bar, which is also predicted by REF/DIF 1. Note that the primary cross-shore array is located approximately along a horizontal line 1/4 down from the top of the picture. Though wave breaking occurs in two regions, we notice in particular the existence of a wide white region over the bar, next to the cross-shore array, which suggests that the breaking region extends further shoreward than the model predicts. If breaking does occur in that region than it will provide a local forcing for the longshore currents in the region past the bar crest.

The depth and time-averaged (over a simulation period of 2 hr) current velocity vectors predicted by SHORECIRC for the conditions at the 10/10/90:0351 are shown in Fig. 6.11. It appears that the predicted currents are uniform in the longshore direction, though slight deviations from this state can be noticed. We also note that the depicted currents correspond to the total volume flux (including the short-wave induced flux). As it can be seen the depth-averaged cross-shore currents are small, which means that at any cross-section the short-wave induced mass flux is almost in balance with the below-trough return current. The maximum longshore and cross-shore velocities are $\tilde{V}_M = 1.07$ m/s and $\tilde{U}_M = 0.12$ m/s, respectively. The current velocity magnitudes can be distinguished better, though, in the two lower panels of Fig. 6.12. Although not appreciable, there are longshore variations in both $\tilde{U}$ and $\tilde{V}$ which are associated with the longshore topographic variations. The contour plot of the (time-averaged) mean surface elevation $\bar{\zeta}$ (see subplot (a)) clearly defines the line of wave breaking, which coincides with the line where the setup initiates. This figure indicates that the setup is longshore nonuniform, and thus it is likely that the longshore pressure gradient can be an important force for the longshore currents. The cross-shore and longshore profiles along the alignments of the current meters are presented next.

Fig. 6.13 shows the predicted and measured values of the main variables along the primary cross-shore array for the 10/10/90:0351 simulation. The top panel shows that H_{rms} computed by REF/DIF1 with the parameters given in Table 6.2 matches the data very well, especially if we consider that the random wave field is approximated by a single monochromatic wave[4].

The second to fourth subplots in Fig. 6.13 show the mean surface elevation

[4] We recall that the measured values for the velocities are averaged over a 3 hr record, and the H_{rms} is computed from records of the same duration.

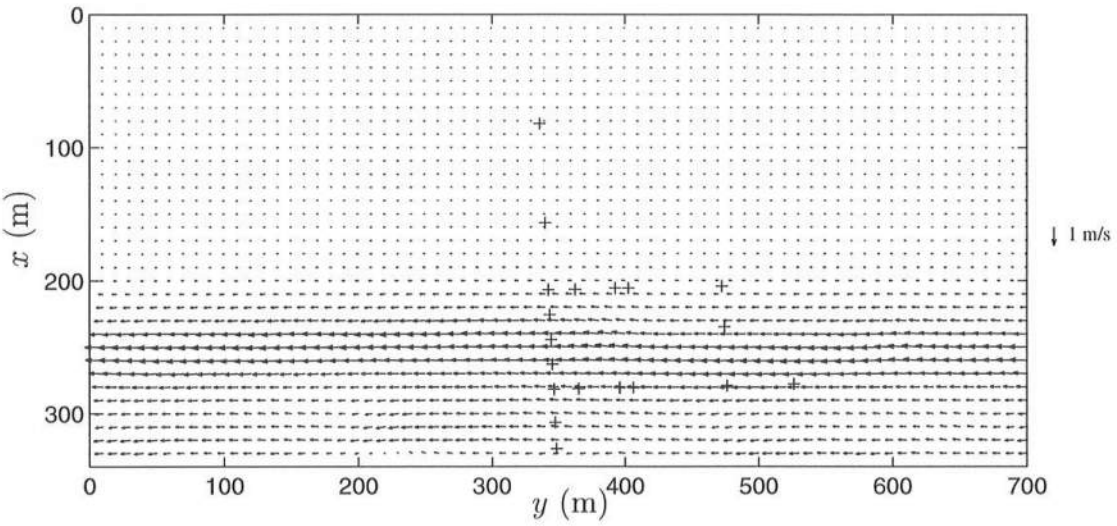

Figure 6.11: Depth and time-averaged current velocity vectors for the 10/10/90:0351 simulation.

and the cross-shore and longshore velocities, respectively. Note that the current meter CM10 was emerged, and thus the measured currents are zero at that location. The variation of the mean surface elevation is in accordance with the wave height (and radiation stress gradient, $\frac{\partial S_{xx}}{\partial x}$) variation. For the cross-shore currents, we have plotted the data measured at a certain depth ($*$), against the computed values at the same depth U_{zdata} ($\circ$), the computed depth-averaged $\tilde{U}$ (– –) and the below-trough averaged U_m (——) velocities. The below-trough averaged velocity corresponds to the total minus the short-wave induced volume flux Q_w divided by the mean water depth. Thus the difference between the solid and dashed lines corresponds to the local depth-averaged wave-induced velocity. The existence of a non-zero $\tilde{U}$ is the result of the longshore nonuniformity of the flow. It is seen that U_m is much larger than $\tilde{U}$, which leads to the conclusion that the below-trough cross-shore velocity is largely dominated by the short-wave induced mass flux, and thus an error in the estimate of this quantity will reflect in an error in the prediction of U_m.

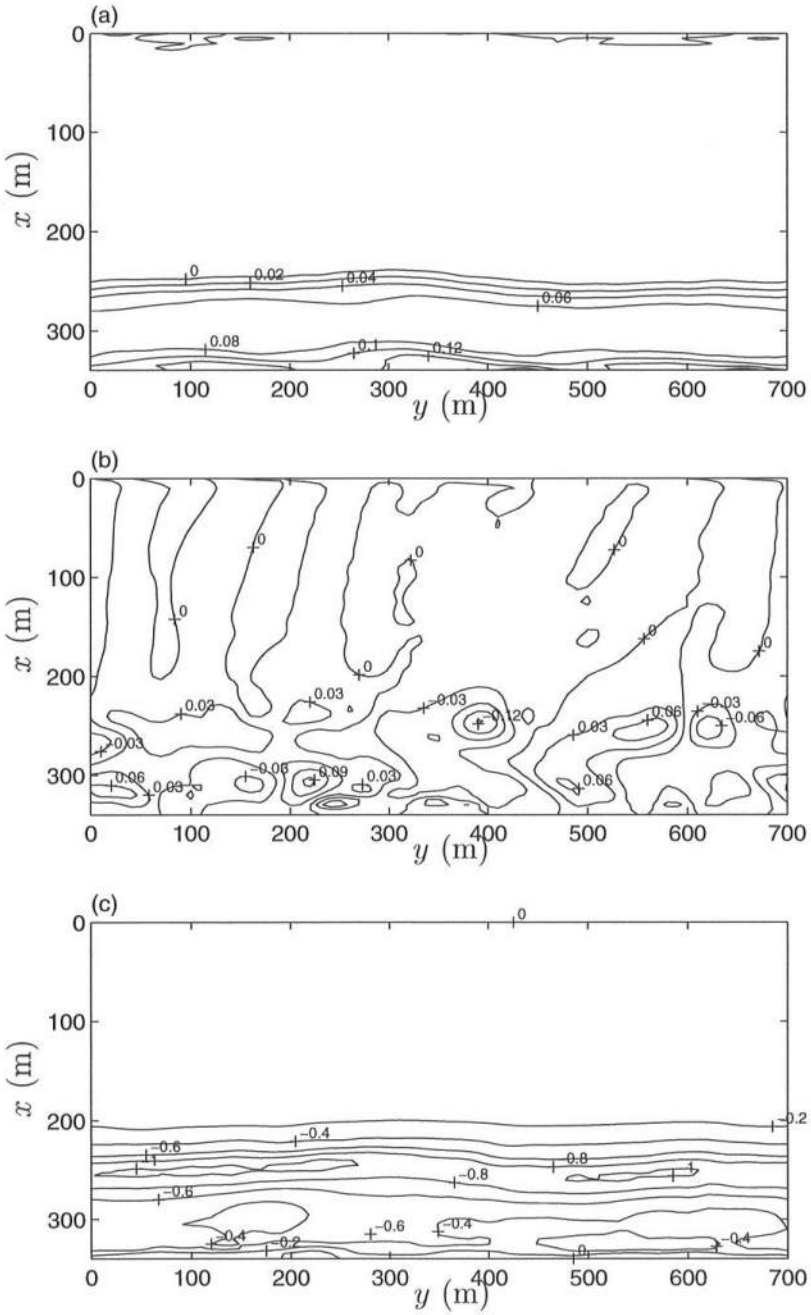

Figure 6.12: Time-averaged flow field for the 10/10/90:0351 simulation. Contour plots of: a) mean free-surface elevation $\bar{\zeta}$; b) cross-shore velocity $\tilde{U}$; c) longshore velocity $\tilde{V}$.

The comparison between the model and data results indicates that we underestimate the cross-shore currents over the bar-crest and overestimate it over the trough. This suggests that the wave-induced mass flux Q_w, which is calculated according to equation (2.110), is too small in the first breaking region and too strong over the bar. This result is somewhat contradictory to the fact that the use of linear wave theory generally overestimates Q_w prior to breaking, and the interpretation of the present results implies that we are underestimating Q_w using linear wave theory. Hence, the existence of large cross-shore velocities in the data might be associated with mechanisms other than the short-wave induced return flow. The data records of U over the duration of the experiment at the positions CM70 and CM90 indicate the existence of an offset error (Birkemeier *et al.*, 1997), which could also contribute to explaining the deviations observed at those locations between the predicted and modeled currents.

Focusing on the longshore currents, we first notice that there are minimal differences between V_m, $\tilde{V}$ and V_{zdata}, where "zdata" refers to the model prediction at the same depth as the measured currents. The predicted longshore current profile is seen to deviate considerably from the measured one at CM30. The maximum of the predicted longshore currents is at the top of the bar, whereas the measured maximum is over the trough, around the position CM30. The measured currents also suggests that there is a strong mixing that causes the longshore currents to be appreciable seaward of the breaking point at the locations CM70 and CM80. The predicted currents in this region are smaller than the measured, which indicates that either the model can not yield such a large mixing, or that other mechanisms are responsible for the large measured currents. One possible reason for the larger velocities of the measured longshore currents seaward of the bar is the mixing due to the existence of random waves, which is not accounted for in our model, though the agreement for the H_{rms} is quite good. Random waves break at different locations

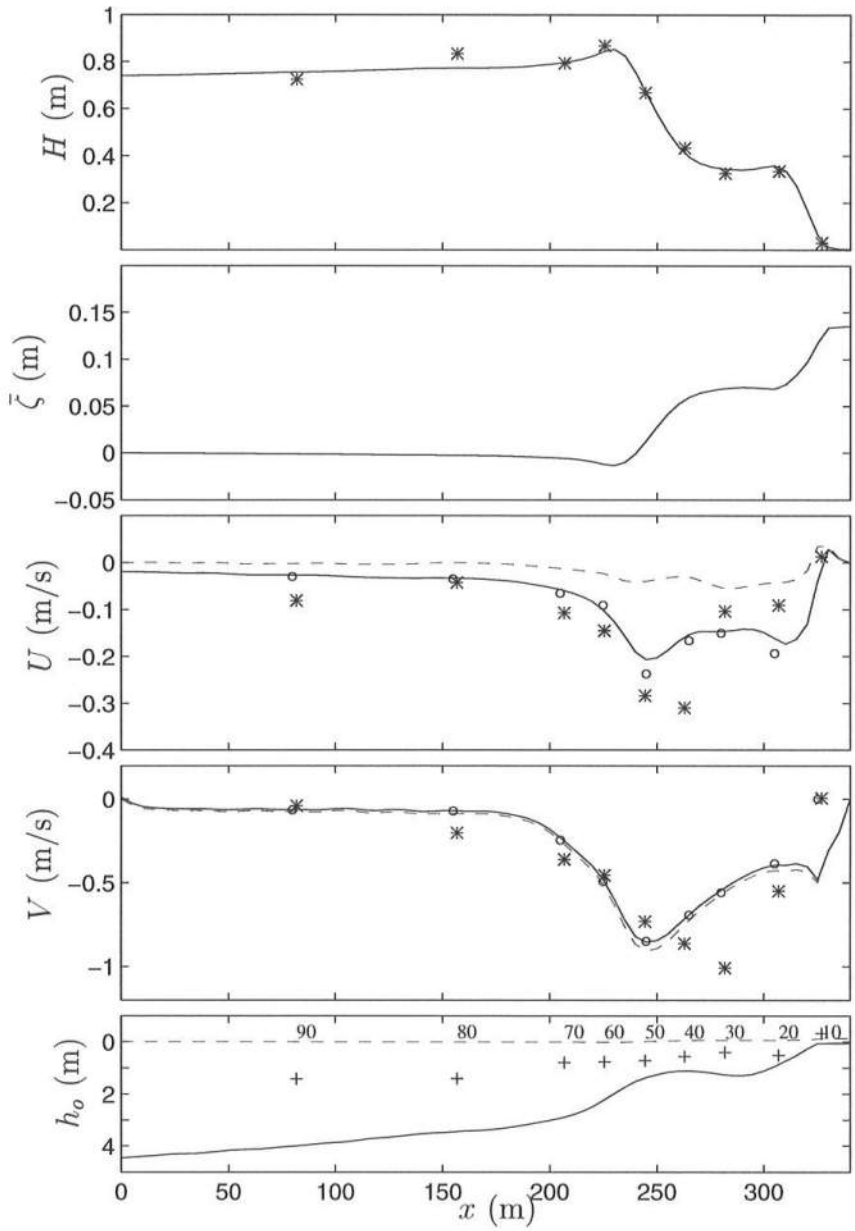

Figure 6.13: Cross-shore distribution at the primary cross-shore array for the 10/10/90:0351 simulation of: (a) H_{rms} model (——), data (∗); (b) $\bar{\zeta}$ model; (c) U_m model (——), $\tilde{U}$ model (– –), U_{zdata} model (○), data (∗); (d) V_m model (——), $\tilde{V}$ model (– –), V_{zdata} model (○), data (∗); (e) h_o (——), $\bar{\zeta}$ (– –), and gauges position (+).

in time and space, and thus a moving breakpoint would introduce a time-varying forcing. We recall that this mechanism is likely to had been present during the measurements, as the existence of a widespread breaking region in Fig. 6.10 may indicate.

Qualitatively, our model predictions for the longshore currents compare well with those of Reniers *et al.* (1997) without the forcing caused by the local longshore pressure gradient. The main difference between the two models (for longshore uniform beaches) is the inclusion in the model of Reniers *et al.* of a forcing mechanism due to the wave-roller in the computation of the radiation stresses, such that their wave-induced forcing in the trough is larger than ours. The model of Reniers *et al.* can account for the effect of a longshore pressure gradient in a similar fashion to that of the model of Putrevu *et al.* (1995). However, based on the discussion in Chapter 4 regarding the accuracy of the Putrevu *et al.* model, the results of Reniers *et al.* including $gh\frac{\partial \bar{\zeta}}{\partial y}$ determined from that model gives results that should be interpreted with caution.

Conversely, if we compare with the results of Church and Thornton (1993) (see Fig. 6.2), who calculate the short-wave forcing from linear wave theory as well, our model results clearly demonstrate that the inclusion of the three-dimensionality of the problem can induce significant currents in the trough behind the bar. Note that the bottom friction coefficient for the nonlinear shear stress used by Church and Thornton is $C_f = 0.006$, which is related to f_{cw} by $f_{cw} = 2\,C_f = 0.012$, and it is seen to be very similar to the friction factor used for the present calculations (see Fig. 6.8).

The comparison between the model and field results along the secondary cross-shore array is shown in Fig. 6.14. We note that the current meters CM54 and CM74 are Scripps Open Frame sensors and the CM34 is a Marsh-McBirney,

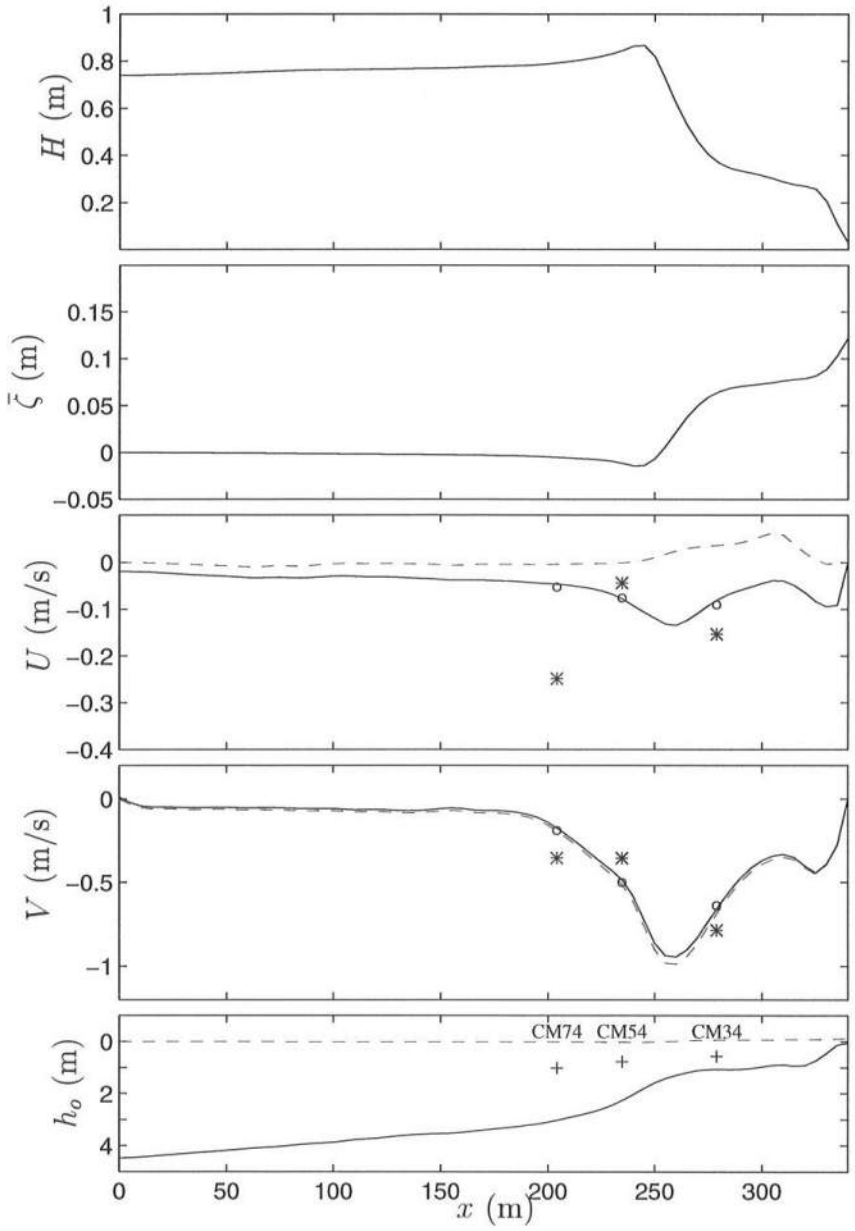

Figure 6.14: Cross-shore distribution at the secondary cross-shore array for the 10/10/90:0351 simulation of: (a) H_{rms} model; (b) $\bar{\zeta}$ model; (c) U_m model (——), $\tilde{U}$ model (– –), U_{zdata} model (○), data (∗); (d) V_m model (——), $\tilde{V}$ model (– –), V_{zdata} model (○), data (∗); (e) h_o (——), $\bar{\zeta}$ (– –), and gauges position (+).

and that there were no pressure gauges mounted at these locations to estimate the wave height. The beach profile exhibits a terrace feature and we first notice that, according to the model, wave breaking is slightly more continuous than at the primary cross-shore array line. Consequently, the setup is also more gradual. The cross-shore depth-averaged velocity $\tilde{U}$ is now positive, meaning onshore flow, though the below-trough averaged velocity U_m is still in the offshore direction. It is also seen that U_{zdata} computed at the sensor depth is equal to the mean U_m below-trough. We suspect a deficiency in the U measured at CM74 because it is unlikely such a large current can exist at that location for the observed topography and wave conditions[5]. For the longshore currents, we notice a reasonable agreement at the trough gauge CM34, but a poorer match at the more seaward sensors. The similarity between the field data of V at the two seaward locations is also suspicious. Comparing the cross-shore variations at the primary and secondary arrays (Fig. 6.13 and 6.14) we notice a larger maximum of the current at the secondary array line, and also that that maximum is shifted nearly 20 m further shorewards. This is mostly due to the fact that the breaking point at the secondary array is also approximately 20 m shoreward than that at the primary array. This is qualitatively confirmed by the video image in Fig. 6.10.

The longshore variation of the predicted and measured quantities along the trough and crest sub-arrays are shown in the left and right panels of Fig. 6.15, respectively. The comparison between the predicted and measured longshore and cross-shore currents indicates an overall fairly poor agreement. The longshore current $\tilde{V}$ along the crest sub-array is satisfactorily predicted, though the data shows a larger variability than the model results (all these current meters are the Open Frame type). The field data of U at both sub-arrays is quite irregular, whereas the

[5] In fact the data records over the duration of the experiment indicate there is an offset error (Birkemeier *et al.*, 1997) for that sensor.

model predictions are fairly regular. However, we notice once again the detection of offset errors in the measured cross-shore velocities for the CM70, CM71, CM73 and CM74 gauges, which have not been corrected. Hence, at the crest sub-array the only current meter that has been indicated to give reliable readings in the cross-shore direction is CM72, which turns out to be accurately predicted. The currents at the vertical position of the gauges (U_{zdata} and V_{zdata}) were not calculated for the present comparison, and the vertical location of the sensor CM33 can not be accurate because it appears that this sensor would then be covered by sand. Last, we notice that the measured readings of V along the trough sub-array seem to be very consistent (these are Marsh-McBirney sensors) and are invariably larger than the predicted values. Hence, we conclude from the time-averaged results that our model fails to predict the large velocities observed over the trough, and consistently predicts the maximum of the longshore currents over the bar-crest.

It is interesting to determine the vertical variation of the horizontal currents. Thus, Fig. 6.15 shows the vertical variation of the time-averaged values of U and V calculated by the model (—), versus the measured values at the gauge depth (←—). The estimated vertical profiles of the cross-shore velocities exhibit the same trends as the profiles of data measured at some other days (Smith *et al.*, 1992). The largest differences between those trends are over the trough, where the measured cross-shore velocities are consistently very small, and the results of our predictions for the 10/10/90:0351 show velocities of the order of 20 cm/s at the positions CM20 and CM30. Note that vertical profiles of the currents in the field were not obtained for the 10th of October. For the longshore velocities, our results show an almost vertically uniform profile, though data at other days and experiments (e.g., Garcez Faria *et al.*, 1996b) displays a slightly larger variability over the water column.

Fig. 6.17 shows the cross-shore distribution of the magnitude of terms of the

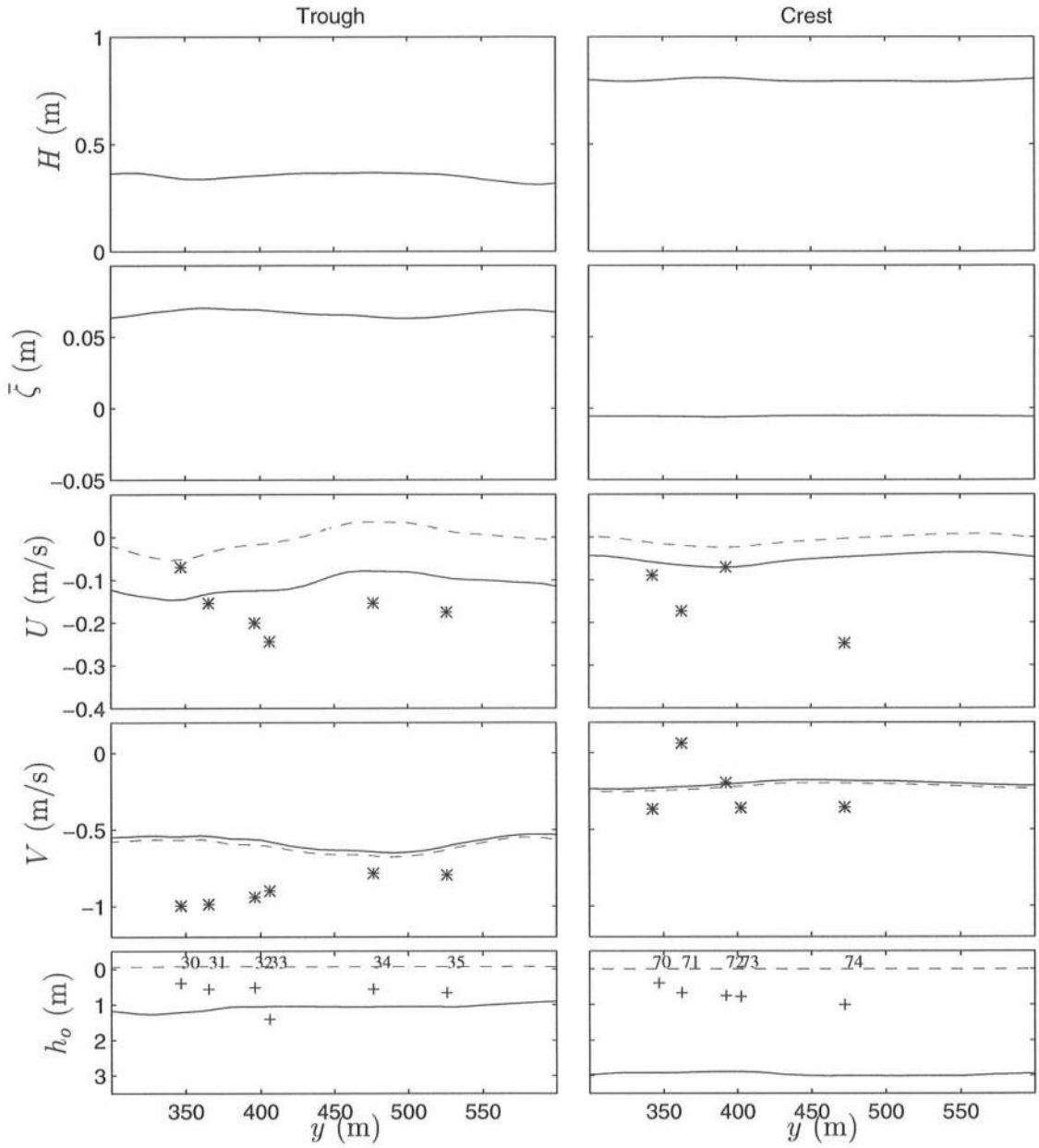

Figure 6.15: Cross-shore distribution at the trough (left) and crest (right) sub-arrays for the 10/10/90:0351 simulation of: (a) H_{rms} model; (b) $\bar{\zeta}$ model; (c) U_m model (——), $\tilde{U}$ model (– –), data (∗); (d) V_m model (——), $\tilde{V}$ model (– –), data (∗); (e) h_o (——), $\bar{\zeta}$ (– –), and gauges position (+).

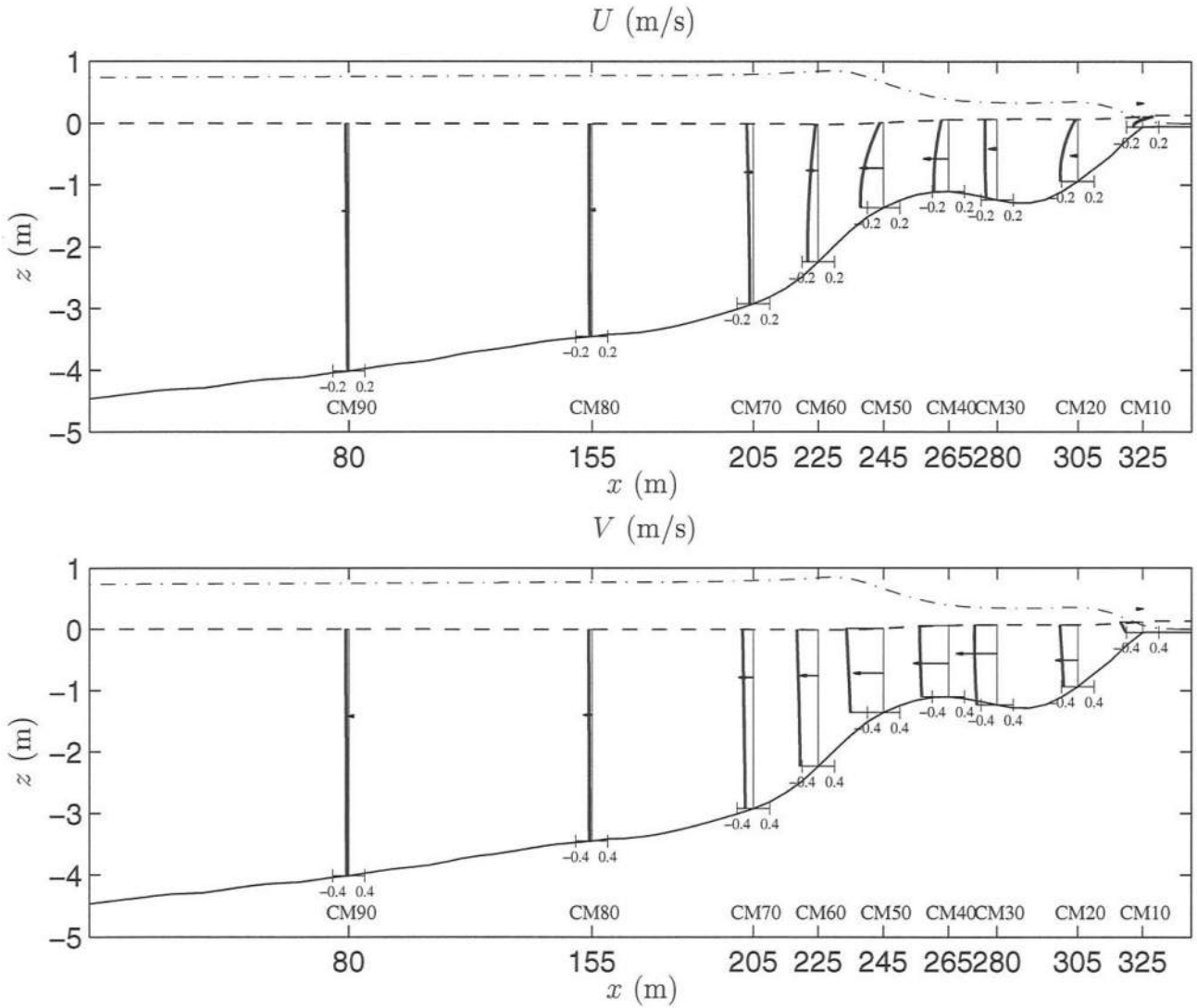

Figure 6.16: Cross-shore variation of the predicted vertical profiles (——) of U and V, versus measured values (⟵), at primary cross-shore array for the 10/10/90:0351 simulation; H_{rms} model (– ·), $\bar{\zeta}$ model (– –).

(time-averaged) momentum equations along the primary cross-shore array alignment. Hence, it indicates what mechanisms are responsible for the generation of longshore (and cross-shore) current profile seen in Fig. 6.13. In the cross-shore momentum equation, we notice the main balance between $\frac{1}{\rho}\frac{\partial S_{xx}}{\partial x}$ and $gh\frac{\partial \zeta}{\partial x}$, with all other terms being much smaller everywhere. The dispersive mixing term is locally important in the regions where $\frac{1}{\rho}\frac{\partial S_{xx}}{\partial x}$ and $gh\frac{\partial \zeta}{\partial x}$ are zero. In the longshore momentum, we first notice that the largest terms are nearly one order of magnitude smaller than the largest terms in the x–momentum balance (which is consistent with the arguments given in Chapter 4). Second, it is seen that the largest term in the y–momentum balance is the short-wave forcing $\frac{1}{\rho}\frac{\partial S_{xy}}{\partial x}$, and then all terms are significant, except for the turbulent mixing and the surface (wind) shear stress. Seaward and over the bar-crest, the inertial accelerations are quite significant, as well as the second wave forcing component $\frac{1}{\rho}\frac{\partial S_{yy}}{\partial y}$ and the pressure gradient. In the trough region $gh\frac{\partial \zeta}{\partial y}$ is the dominant force, seconded by $\frac{\tau_y^B}{\rho}$, which is inevitably important where there is any forcing mechanism. For the present case it turns out that the dispersive mixing is small, though not negligible. Overall, this analysis allows us to conclude that most of the terms in the complete momentum equations can be locally important, especially in the longshore momentum balance, and hence the use of simplified longshore current models, such as those that assume longshore uniformity, is prone to misinterpretations.

The computational results for the present simulation also show the presence of shear instabilities. Thus, we find that the convective acceleration terms depicted in Fig. 6.17 are the sum of the contribution of the mixing due to the unsteady motion (the shear waves), and the contribution of the steady part associated with the local (time-averaged) spatial acceleration of the flow. Note that in the following the term "time-averaging", which is represented by the second overbar, means over the period of the simulation, not just the short-wave motion. Fig. 6.18 shows the

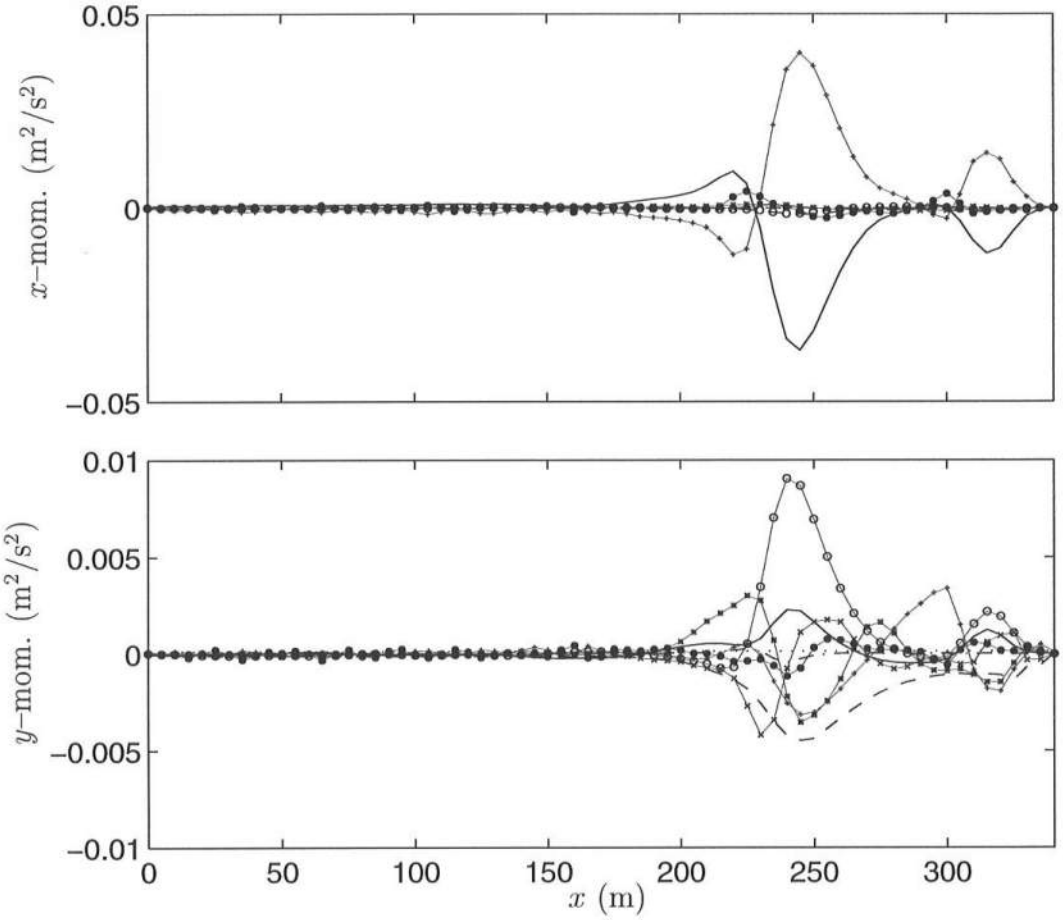

Figure 6.17: Cross-shore distribution at the primary cross-shore array of the terms in the time-averaged momentum equations for the 10/10/90:0351 simulation. Terms in the x–momentum balance: $gh\frac{\partial \bar{\zeta}}{\partial x}$ (+), $\frac{1}{\rho}\frac{\partial S_{xx}}{\partial x}$ (——), $\frac{1}{\rho}\frac{\partial S_{yx}}{\partial y}$ (○), $\overline{\frac{\partial}{\partial x}\left(\frac{\bar{Q}_x^2}{h}\right)}$ (×), $\overline{\frac{\partial}{\partial y}\left(\frac{\bar{Q}_x\bar{Q}_y}{h}\right)}$ (∗), – turb. mixing (– ·), $\frac{\tau_x^B}{\rho}$ (– –), – dispersive mixing (–•–), $\frac{\tau_x^S}{\rho}$ (. . .). Terms in the y–momentum balance: $gh\frac{\partial \bar{\zeta}}{\partial y}$ (+), $\frac{1}{\rho}\frac{\partial S_{yy}}{\partial y}$ (——), $\frac{1}{\rho}\frac{\partial S_{xy}}{\partial x}$ (○), $\overline{\frac{\partial}{\partial y}\left(\frac{\bar{Q}_y^2}{h}\right)}$ (×), $\overline{\frac{\partial}{\partial x}\left(\frac{\bar{Q}_x\bar{Q}_y}{h}\right)}$ (∗), – turb. mixing (– ·), $\frac{\tau_y^B}{\rho}$ (– –), – dispersive mixing (–•–), $\frac{\tau_y^S}{\rho}$ (. . .).

difference between the total time-averaged convective accelerations and the convective accelerations determined from the time-averaged variables, which represents a mixing due to shear waves that can be written as the shear stresses (see equivalent equation (5.30))

$$\begin{aligned}
\sigma_x &= \overline{\frac{\partial}{\partial x}\left(\frac{\bar{Q}_x^2}{h}\right)} - \frac{\partial}{\partial x}\left(\frac{\overline{\bar{Q}}_x^2}{\bar{h}}\right), \\
&+ \overline{\frac{\partial}{\partial y}\left(\frac{\bar{Q}_x\bar{Q}_y}{h}\right)} - \frac{\partial}{\partial y}\left(\frac{\overline{\bar{Q}}_x\overline{\bar{Q}}_y}{\bar{h}}\right) \qquad (6.1) \\
\sigma_y &= \overline{\frac{\partial}{\partial y}\left(\frac{\bar{Q}_y^2}{h}\right)} - \frac{\partial}{\partial y}\left(\frac{\overline{\bar{Q}}_y^2}{\bar{h}}\right) \\
&+ \overline{\frac{\partial}{\partial y}\left(\frac{\bar{Q}_x\bar{Q}_y}{h}\right)} - \frac{\partial}{\partial y}\left(\frac{\overline{\bar{Q}}_x\overline{\bar{Q}}_y}{\bar{h}}\right), \qquad (6.2)
\end{aligned}$$

for the x and y–momentum, respectively. We notice in Fig. 6.18 that the stresses due to the unsteady motion are of the same order in both the x and y–momentum equations and also that the cross-derivative terms are the smallest. The magnitude of the $\frac{\partial}{\partial y}\left(\frac{Q_x Q_y}{h}\right)$ difference-terms in the longshore momentum equation is also seen to be comparable to that of the other terms in the total momentum equation shown in Fig. 6.17 (bottom panel), which means that shear waves dispersion is an effective mechanism in the momentum balance.

To illustrate the dynamics of the shear waves, the time series of $\tilde{U}$ and $\tilde{V}$ at several of the gauge locations along the primary cross-shore array are shown in Fig. 6.19 and 6.20, respectively. We notice first that the amplitude of the perturbations are similar for both $\tilde{U}$ and $\tilde{V}$. Second, that amplitude is seen to be larger at the locations over and shoreward of the bar-crest (CM20-CM50), where the longshore currents are the largest, than at the other seaward locations, where the amplitudes diminish gradually offshore with the distance from the surf zone. At the two surf zone locations CM20 and CM30 the shear instabilities are somewhat regular with a

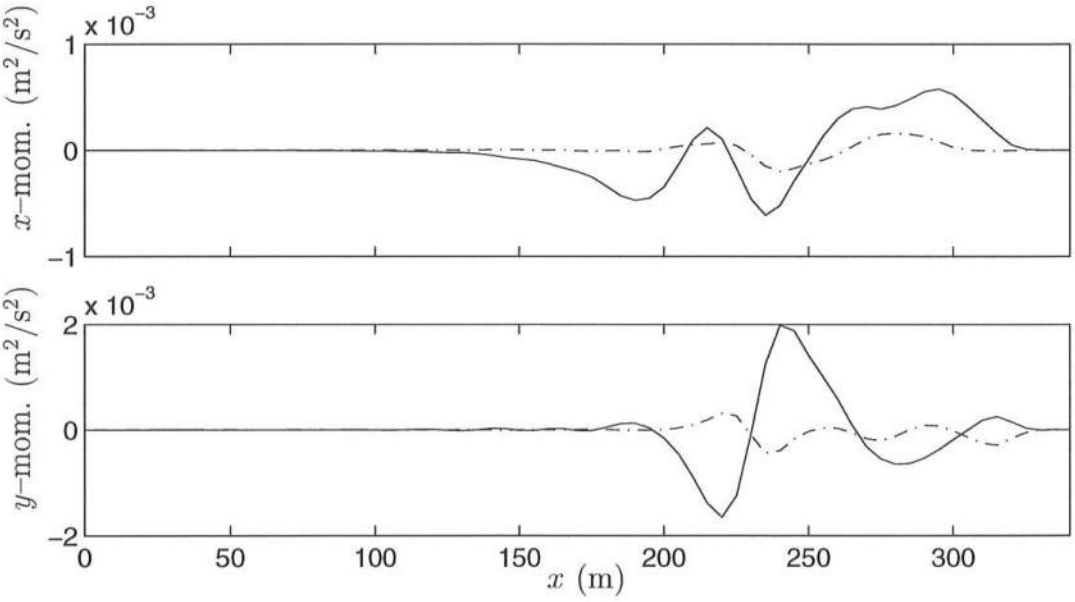

Figure 6.18: Cross-shore distribution at the primary cross-shore array of the stresses associated with the unsteady motion: a) $\overline{\frac{\partial}{\partial x}\left(\frac{\bar{Q}_x^2}{h}\right)} - \frac{\partial}{\partial x}\left(\frac{\overline{\bar{Q}}_x^2}{\bar{h}}\right)$ (——), $\overline{\frac{\partial}{\partial y}\left(\frac{\bar{Q}_x\bar{Q}_y}{h}\right)} - \frac{\partial}{\partial y}\left(\frac{\overline{\bar{Q}}_x\overline{\bar{Q}}_y}{\bar{h}}\right)$ (– ·); b) $\overline{\frac{\partial}{\partial y}\left(\frac{\bar{Q}_y^2}{h}\right)} - \frac{\partial}{\partial y}\left(\frac{\overline{\bar{Q}}_y^2}{\bar{h}}\right)$ (——), $\overline{\frac{\partial}{\partial x}\left(\frac{\bar{Q}_x\bar{Q}_y}{h}\right)} - \frac{\partial}{\partial x}\left(\frac{\overline{\bar{Q}}_x\overline{\bar{Q}}_y}{\bar{h}}\right)$ (– ·);

period of $T \simeq 480$ s. At the next two locations (CM40 and CM50) the time series start to exhibit instabilities at shorter and longer periods especially in the longshore direction (Fig. 6.20), and at the position CM70 the time series of $\tilde{V}$ has a peak period of $T \simeq 1000$ s. These oscillations are within the range $500 < T < 1000$ s where the most energetic shear instabilities were observed (Church *et al.*, 1992). However, a more detailed analysis of the frequency and wavenumber range analogous to that performed by Özkan-Haller and Kirby (1997) would be necessary to compare the observed shear wave motions with the predicted ones. Nevertheless, we point out that the time series of the low-frequency pass cross-shore and longshore velocities at CM30, depicted in Fig. 6.7, show a velocity variation with an amplitude approximately equal to 0.2 m/s. Though clearly more regular, the predicted shear waves at CM30 exhibit also oscillatory velocities with amplitudes of the order of 0.2 m/s (Fig. 6.19b and 6.20b), which is in agreement with the data results.

The most energetic predicted shear wave length is found to be $L \simeq 230$ m, and thus the speed at which the shear waves propagate is $c_S \simeq 0.46$ m/s, or equivalently $c_S \simeq 0.48\,\tilde{V}_M$, where $\tilde{V}_M = 0.96$ m/s is the predicted maximum time-averaged longshore velocity at the primary array. Last, it turns out that the cross-shore velocity fluctuations are all in phase at the different locations of the primary array, whereas the longshore fluctuations change of phase (relative to each other) with the cross-shore location.

6.2.2 Discussion

We shall in this section examine some of the forces and mechanisms that could be responsible for the observed maximum peak of the longshore current over the bar-trough. We will mainly focus on the discrepancy between the predicted and measured longshore current profiles at the primary cross-shore array shown in

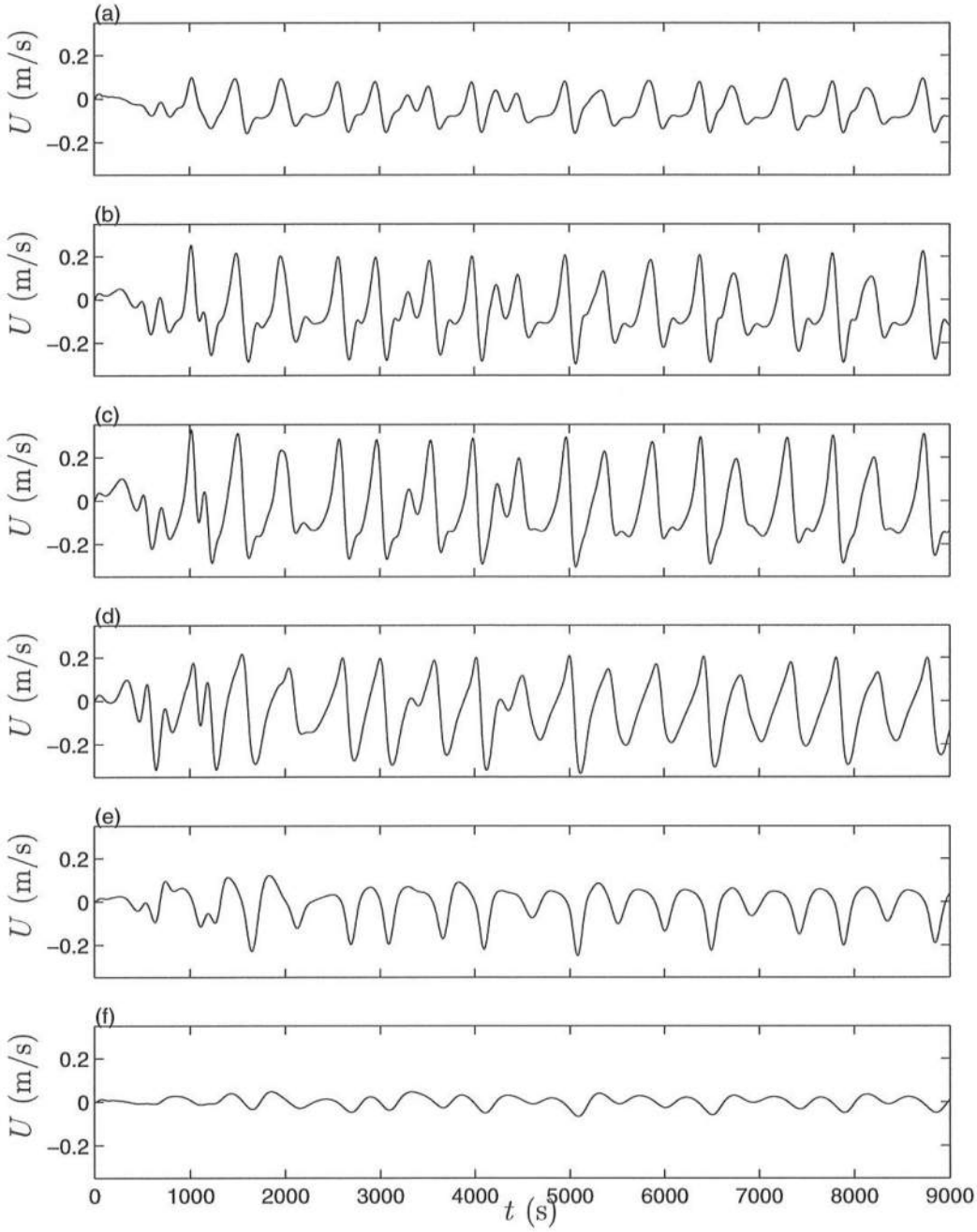

Figure 6.19: Time series of the predicted $\tilde{U}$ for the 10/10/90:0351 simulation at several gauge locations along the primary cross-shore array: (a) CM20, $x = 305$ m; (b) CM30, $x = 280$ m; (c) CM40, $x = 265$ m; (d) CM50, $x = 245$ m; (e) CM70, $x = 205$ m; (f) CM80, $x = 155$ m.

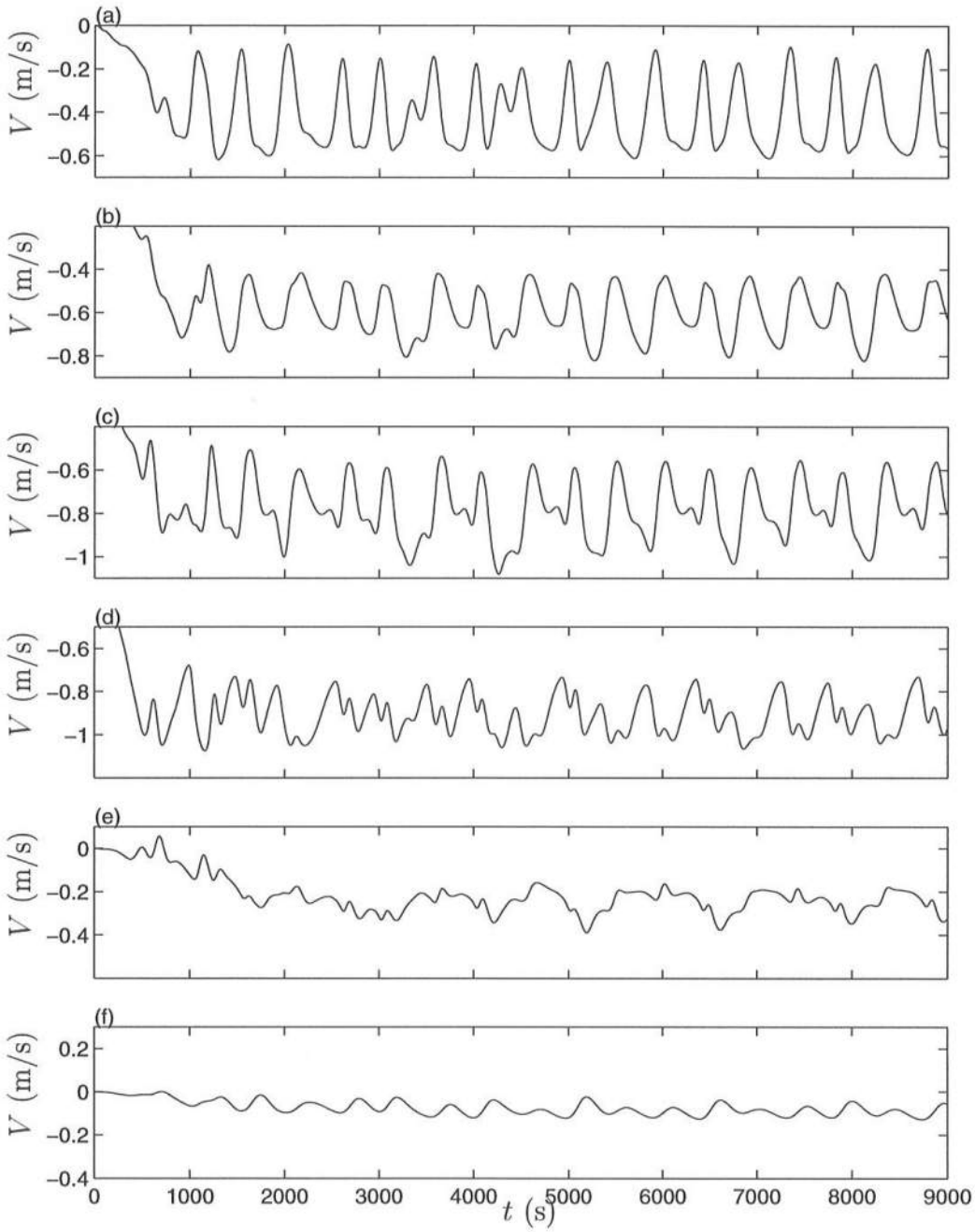

Figure 6.20: Time series of the predicted $\tilde{V}$ for the 10/10/90:0351 simulation at several gauge locations along the primary cross-shore array: (a) CM20, $x = 305$ m; (b) CM30, $x = 280$ m; (c) CM40, $x = 265$ m; (d) CM50, $x = 245$ m; (e) CM70, $x = 205$ m; (f) CM80, $x = 155$ m.

Fig. 6.18, which can not be explained by malfunctions of the sensors. This discussion also includes some other results for the simulation of the 10/10/90:0351 period, with different model parameters.

Large-scale forces

First, due to the completeness of the physical mechanisms already included in the model SHORECIRC, it is tempting to attribute the discrepancies between the measured and predicted longshore current profiles to external flows. This category includes motions that are not accounted for in our simulations due to the limiting size of the model domain, such as tidal currents, wind-driven currents on an area much larger than our model domain (which could include the influence of the Chesapeake Bay north of the FRF location), and other shelf-zone processes.

We performed several model simulations over the same limited region where (to enhance the effect of the wind shear stress) we assumed short waves to be absent. Hence, the only forcing mechanism in that hypothetical situation is the wind shear stress, which is then balanced by the bottom shear stress in the longshore direction and the setup gradient in the cross-shore direction. Assuming constant the wind direction given in Table 6.2 ($\phi_{wind} = -65°$), we found that under these conditions it would require a wind velocity of $W = 10$ m/s (instead of the measured 2.5 m/s) to induce a locally generated longshore current of approximately 10 cm/s. In the presence of waves, however, the effective bottom friction is increased significantly and thus the same wind velocity would only induce a current of 3–4 cm/s.

These results are all for a constant wind forcing over the model region only, and thus do not account for the possible extra currents that could be induced by differential mean surface elevations at different locations of a larger region. The

possible approach of a dynamic wind field can generate a storm surge that is also dynamic, and has different water elevations at different locations. The resulting longshore pressure gradient of this new scenario could potentially generate a longshore flow that could add (or subtract) to the short-wave induced currents. This mechanism will only have an effect if there is such a longshore pressure gradient, which we have no measurements for. Though a possible mechanism, we would then expect an overall increase (or decrease) of the longshore current profile (though not necessarily uniformly across the shore), and not a shift of the location of the maximum of the longshore currents. Hence, such effect could explain the discrepancy between the model results and data at the offshore arrays, but it appears unlikely that it would cause the peak of the measured longshore current profile to be over the trough.

The possible existence of other external mechanisms is not ruled out, but for the same reason as a wind-induced differential setup could force an almost cross-shore uniform longshore current for the present bottom profile, it is not very plausible that other motions of larger scale (such as tides) would shift the location of the maximum of the longshore current. For a deeper bar-trough the same reasoning would not apply as a "river-type" flow could be formed behind the bar. However, since the present topography has a mild bar, a longshore current forced by other mechanism would not necessarily be "trapped" behind the bar.

In order to check the effect of the existence of a possible stronger "feeder" longshore current in the bar-trough, a test was performed with forced current profile at the lateral boundaries, similar to the profile measured at the main array. This test can also help to answer the question: what happens in a situation when a current profile not in balance with the local wave forcing is specified at the model boundaries? Thus, indirectly it enables us to examine the influence or the necessity

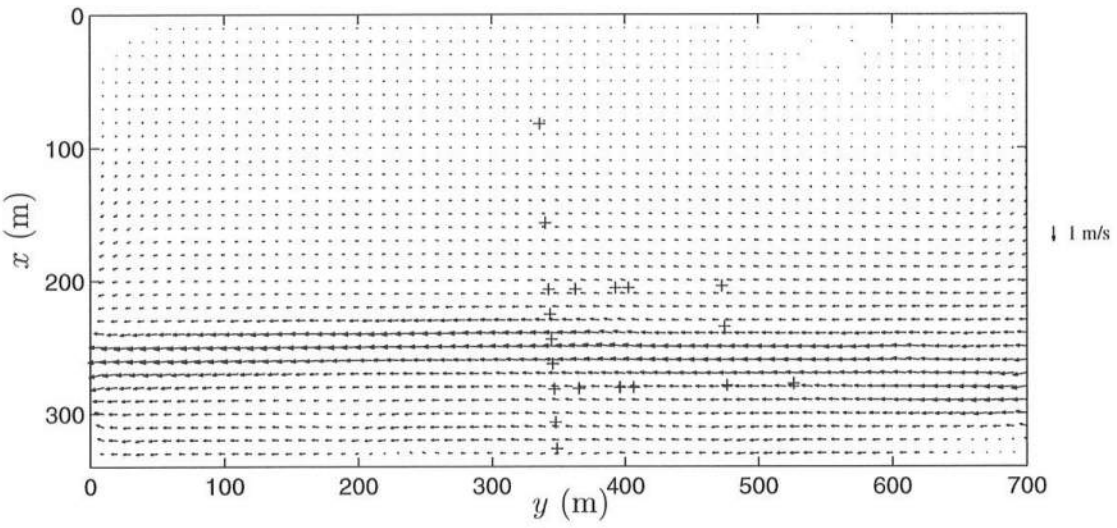

Figure 6.21: Depth and time-averaged current velocity vectors for the 10/10/90:0351 simulation with forced longshore currents at the lateral boundaries.

of knowing the incoming currents to the model domain, and how far we need to place the model lateral boundaries to avoid "contamination" of the boundary conditions in the results in the region of interest. We assumed the existence of an incoming and outgoing longshore current at the upstream and downstream model boundaries, respectively, with a profile equal to that of the measured currents at the primary cross-shore array.

The depth and time-averaged current velocity vectors predicted under those conditions are shown in Fig. 6.21. It can be seen that the strong longshore current over the trough at the upstream boundary is slowly shifted towards the bar-crest. This is more explicitly illustrated in Fig. 6.22, which shows the variation in the longshore current profile at seven longshore locations from the upstream boundary to the downstream boundary. The solid lines represent the results for the present computation, and the dashed lines show the results for the previous simulation in

section 6.2.1 with periodicity at the lateral boundaries. Moving in the downstream direction (from top to bottom of Fig. 6.22) we notice that the largest differences between the current profiles are between $y = 700$ m and $y = 500$ m, and then again at the downwave boundary $y = 0$ m. Between $y = 400$ m and $y = 100$ m the current profiles differ mainly in the magnitude of the maxima over the bar-crest, and at the offshore region. It turns out that for the present simulation with specified up and downstream boundary conditions there is much less shear instabilities than in the previous case. In here, the limited length of the model domain hampers the growth of the shear waves that would otherwise develop on the infinitely long beach (when lateral periodicity is used). Shear waves are locally generated, but because they are a hydrodynamical instability phenomenon a reasonable length in space (and time) is required for the instabilities to grow. Since the present boundary conditions are constant in time, and the domain size is limited, then shear waves can only develop to a certain extent. The comparison shown in Fig. 6.22 indicates that approximately 200–300 m downstream of the section with longshore forced currents ($y = 700$) the currents have nearly adjusted back to the distribution found with the periodicity condition. Further downstream, between $y = 100$ m and $y = 0$ m the currents are seen to adjust to the profile of the forced lateral current. Thus, as expected, the distance over which the boundary conditions affect the local currents is larger at the upstream boundary than at downstream.

The cross-shore variation of the flow properties for this simulation at the primary array location is shown in Fig. 6.23, where we have also plotted for comparison the data-interpolated longshore current profile that is forced at the lateral boundaries. Comparing the present results with the previous ones, where lateral periodicity was used (see Fig. 6.13), we notice that the maximum of $\tilde{V}$ is at the same location, but the current profile is narrower for the present simulation due to the limited development of the shear waves pointed above. In fact, we find that the

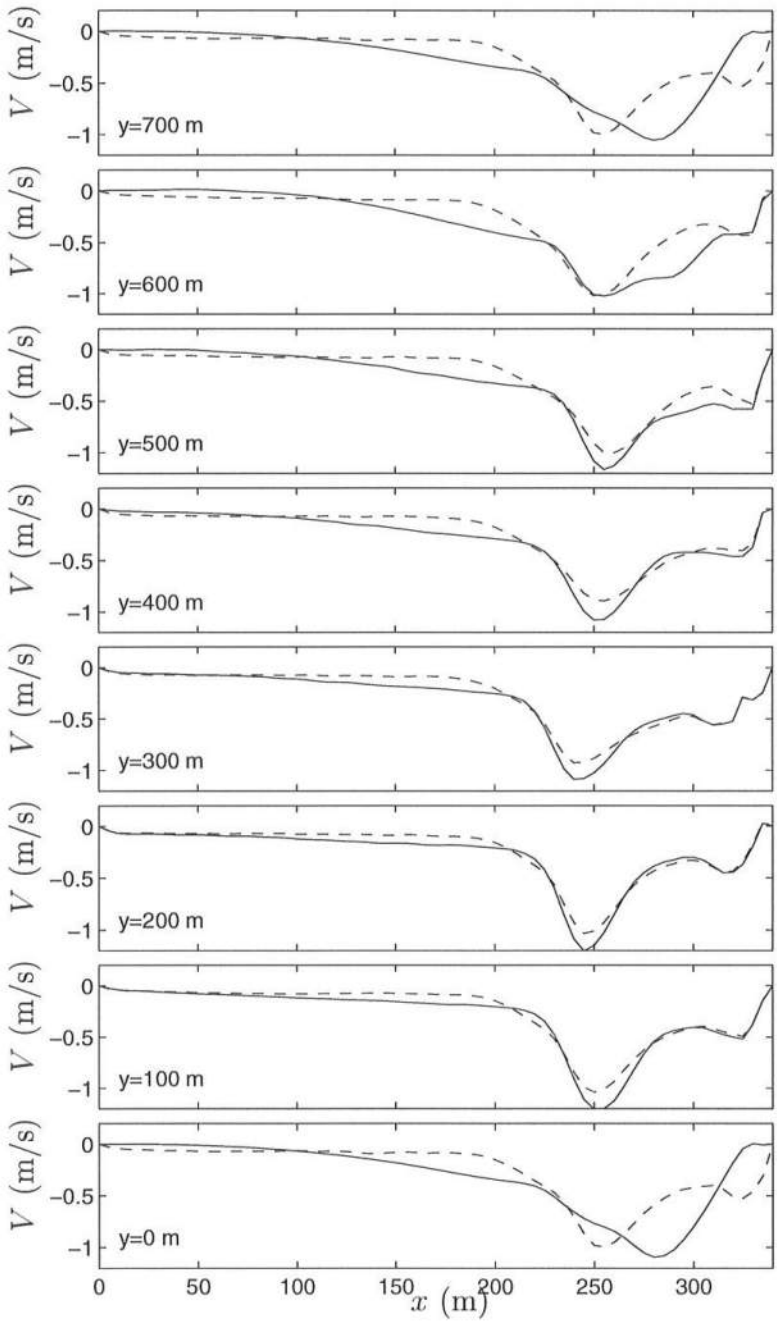

Figure 6.22: Cross-shore distribution of $\tilde{V}$ at several locations from the upstream (top) to the downstream (bottom) boundaries. Simulations for the 10/10/90:0351 with: periodic lateral boundaries (– –), and fixed lateral boundaries (——).

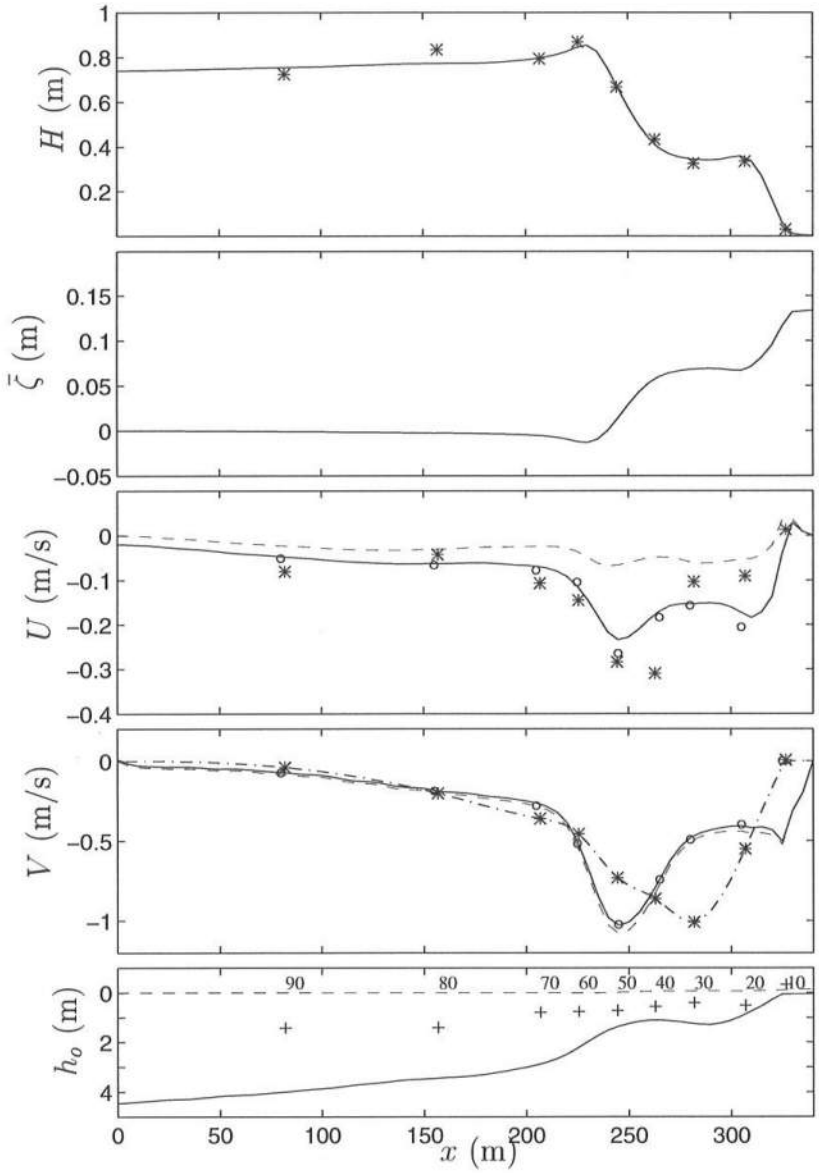

Figure 6.23: Cross-shore distribution at the primary cross-shore array for the 10/10/90:0351 simulation, with forced longshore currents at the lateral boundaries of: (a) H_{rms} model (——), data (∗); (b) $\bar{\zeta}$ model; (c) U_m model (——), $\tilde{U}$ model (– –), U_{zdata} model (○), data (∗); (d) V_m model (——), $\tilde{V}$ model (– –), V_{zdata} model (○), data (∗), data-interpolation (–·); (e) h_o (——), $\bar{\zeta}$ (– –), and gauges position (+).

computed maximum amplitude of the shear waves is just 0.07 m/s at the location of CM40, which should be compared with the previous amplitude of nearly 0.35 m/s predicted at the same location for the previous simulation (see Fig. 6.19 and 6.20). The period of the shear waves in the present simulation is $T \simeq 280$ s, which should be compared to the previous value $T \simeq 480$ s. This variation of the period of the shear waves from one situation to the other confirms that the period and wavelength of simulated shear instabilities are fairly dependent of the domain size (Özkan-Haller and Kirby, 1997).

In summary, we have found that the modifications imposed to the up- and downstream boundaries do not penetrate to the main cross-shore array, which indicates that the predicted currents in that region are dominated by local forcing mechanisms. The boundary effects are significant in the regions adjacent to the boundaries but appear to be minimal in the middle of the model domain. Though we forced a flow with the "correct" longshore current profile, that flow is not sustained unless a forcing mechanism can exist to support it. Therefore, we can conclude that the measured longshore current profile must be generated by forces that have a local contribution, though that local contribution could be generated by large external (to the model region) mechanisms.

Local forces

SHORT-WAVE FIELD

In general, the most important forcing mechanism in the nearshore region is the short-wave action. Although the predicted and measured wave heights H_{rms} compare well, it was mentioned in section 6.1 that there are some uncertainties about the estimates of the wave direction. In particular, we not only assumed a

single principal wave direction, but we have also assumed Snell's law to be valid in the region between the 8 m depth array and the offshore gridline of our model domain. The effect of some of these uncertainties in the SHORECIRC predictions was then assessed as follows.

In one situation, we used the linear spectral model REF/DIF S to calculate the "root-mean-square" wave height and representative direction based on the energy and radiation stresses spectral estimates (Chawla *et al.*, 1997). The input directional spectrum had the same directional spreading as that estimated from the pressure sensors at the 8 m depth array, and the mean direction given in Table 6.2. It turned out from this computation that the wave height and mean angle distributions did not differ significantly from the previous results with REF/DIF1, and thus the predicted nearshore currents were also similar to those already presented.

A second situation is examined here in greater detail in order to check the effect of an error in the incoming mean wave angle. Fig. 6.24 shows the results of the mean flow quantities from SHORECIRC for a simulation where the incident wave angle at the offshore gridline is $\alpha_w = -18°$, which corresponds to a reduction of 30% in the incoming wave angle relative to the previous value ($\alpha_w = -26.5°$). The model results in Fig. 6.24 indicate that the decrease in the mean wave angle caused a proportional reduction of the short-wave forcing in the longshore direction, and thus the longshore currents are correspondingly smaller than those calculated before (Fig. 6.13). It is seen that the location of the maximum of the longshore current remained over the bar-crest, which means that, though the short-wave forcing is smaller in the present simulation, it is still the predominant mechanism for the longshore currents in the surf zone.

We have mentioned previously that the model results given by Reniers *et al.* (1997) for the case of longshore uniformity happened to be similar to ours. The

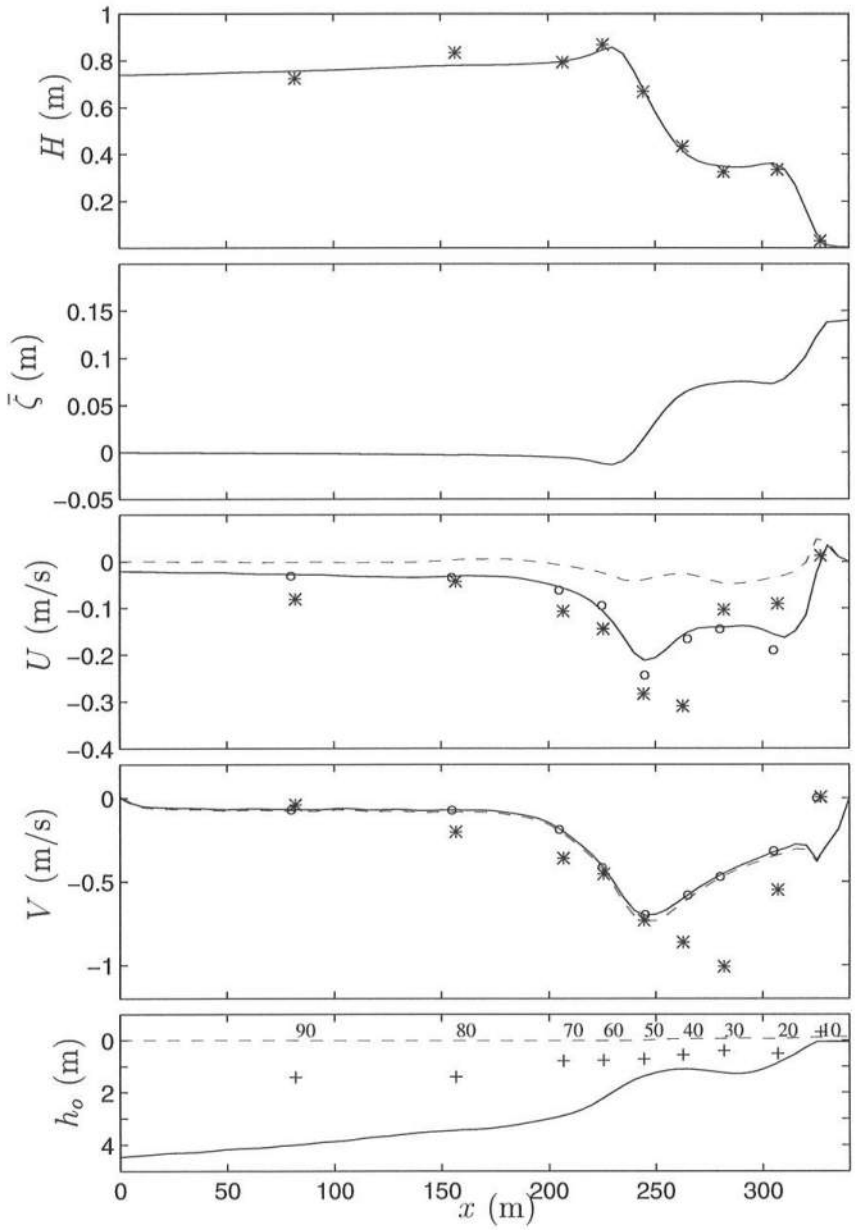

Figure 6.24: Cross-shore distribution at the primary cross-shore array for the 10/10/90:0351 simulation, with $\alpha_w - 18°$, of: (a) H_{rms} model (——), data (∗); (b) $\bar{\zeta}$ model; (c) U_m model (——), $\tilde{U}$ model (– –), U_{zdata} model (○), data (∗); (d) V_m model (——), $\tilde{V}$ model (– –), V_{zdata} model (○), data (∗); (e) h_o (——), $\bar{\zeta}$ (– –), and gauges position (+).

radiation stress term $\frac{\partial S_{xy}}{\partial x}$ in the model equations of those authors include also a forcing from the wave-roller, which was not accounted for here. Several authors (e.g., Svendsen, 1984b; Okayasu, 1989; Nairn *et al.*, 1990; Osiecki and Dally, 1996) have discussed that the presence of the surface roller in a breaking wave is able to increase the radiation stresses in the surf zone. In particular, the inclusion of the momentum transported by the roller in the governing equations seems to be able to shift shorewards the maximum of the total (short-wave plus roller) radiation stress forcing. We note that the analysis of field data by Feddersen *et al.* (1996) confirms that there is a spatial lag in the maximum of $\frac{\partial S_{xy}}{\partial x}$ and the maximum of $\tilde{V}$. Therefore it is likely that this mechanism alone could create a stronger forcing for the longshore currents in the trough region, and a better short-wave driver is needed to account for it.

In addition to the absence of a roller contribution in the present radiation stresses formulation, we pointed out previously from the video image of the breaking region (see Fig. 6.10) that breaking appears to exist even past the bar-crest. This is likely to be caused by a moving breakpoint which is not represented by the use of the wave model REF/DIF 1. The existence of breaking in the trough is therefore an indication of an additional force for the large longshore currents observed in that region.

BOTTOM SHEAR STRESS

We have discussed in this work the uncertainties associated with the specification or calculation of the bottom friction coefficient. For the results in section 6.2.1 we estimated the friction factor f_{cw} from Swart's formula with the Nikuradse roughness $k_N = 10\, d_{50}$. Fig. 6.8 shows that the resulting friction factor is ~ 0.011 at all cross-shore locations, except close to the shoreline. Since it is known that the magnitude of f_{cw} can affect the model predictions significantly we did further

numerical tests with different distributions of f_{cw}.

First, we realize that the use of a constant ratio between the bottom roughness and sediment size over the whole domain will not distinguish regions with different bottom forms. In fact, sand mega-ripples were present in the trough behind the bar, which would in face of the present knowledge contribute to an increase of the roughness and hence the bottom friction. Since the current velocity is inversely proportional to the friction factor, then an increase of f_{cw} in the trough would cause a corresponding decrease of V over the same region, which would enhance the discrepancy already observed between the model predictions and the measurements. Therefore, we did not try to correct the friction factor to account for the possible existence of different bottom forms along the beach.

Second, instead of using a varying f_{cw} such as that shown in Fig. 6.8, simulations were performed with a constant friction factor over the whole domain. The results of a computation with a constant $f_{cw} = 0.011$ were only minimally different from the ones given previously, with the largest variations in the region adjacent to the shoreward boundary ($x > 320$ m). At the other cross-shore positions the differences were imperceptible, which indicates that local variations of the friction coefficient within 5–10% do not change the shape of the longshore current profile.

Having examined the cross-shore distribution of f_{cw}, it is relevant to analyze and discuss a variation in magnitude of f_{cw}, where we chose to decrease f_{cw} in an attempt to improve the longshore current prediction over the trough. Fig. 6.25 shows the computed and measured mean water level and current velocities for a simulation where the Nikuradse roughness is computed by the traditional formula $k_N = 2\,d_{50}$, which implies that $f_{cw} \simeq 0.008$ everywhere except near the shoreline. Hence, the results presented in Fig. 6.25 correspond to depth-averaged velocities determined with a friction factor approximately 70% of the friction factor for the results in Fig. 6.13.

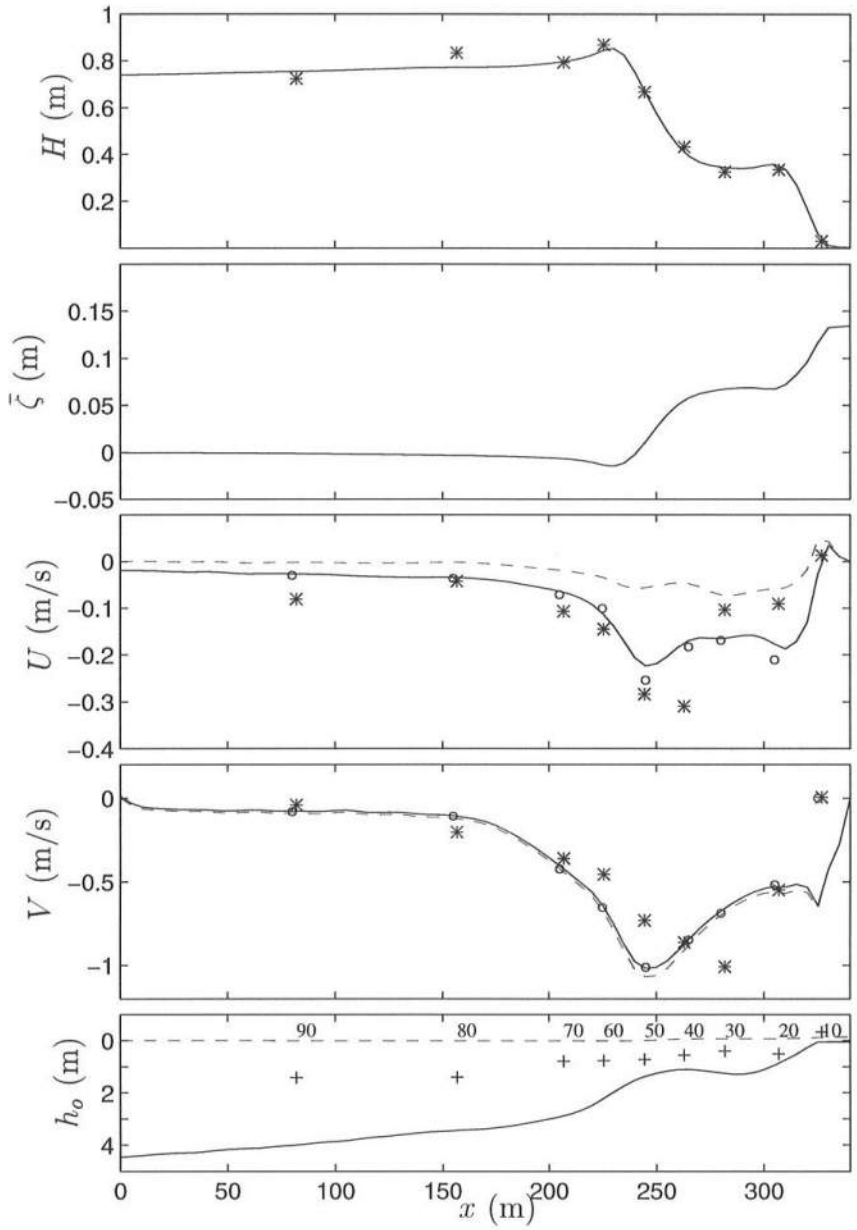

Figure 6.25: Cross-shore distribution at the primary cross-shore array for the 10/10/90:0351 simulation, with $f_{cw} \simeq 0.008$, of: (a) H_{rms} model (——), data (∗); (b) $\bar{\zeta}$ model; (c) U_m model (——), $\tilde{U}$ model (– –), U_{zdata} model (○), data (∗); (d) V_m model (——), $\tilde{V}$ model (– –), V_{zdata} model (○), data (∗); (e) h_o (——), $\bar{\zeta}$ (– –), and gauges position (+).

It is seen that the agreement between the predicted and measured longshore currents for the present computations is fair. In fact, the conformance is good in the trough region at sensors CM20 and CM40, but less accurate in the surf zone over the bar-crest. We further notice through the inter-comparison of the model predictions between the two simulations (Fig. 6.13 and 6.25) that the shape of the longshore current profile remained unaltered. Hence, the reduction in the magnitude of the bottom friction induced an almost spatially constant increase in $\tilde{V}$ over the active surf zone. For the lower friction case, the shear instabilities are more energetic, and thus the mixing induced by the shear waves is responsible for the larger currents computed seaward of the position CM60 (relative to the case with larger friction). It turns out that at CM40 the maximum variation of the velocity perturbations is now 0.5 m/s, which should be compared with the previous value of 0.35 m/s. The energy frequency band of the shear instabilities is also wider for the present simulation with a smaller friction factor, which is in agreement with the findings of other studies on shear waves (e.g., Özkan-Haller and Kirby, 1997). However, assuming that we can trust all the gauges in the main array, we still find that the predicted cross-shore variation of V differs from the measured profile.

Last, we find that the vertical profiles of the longshore and cross-shore velocities show the same trends as those seen in Fig. 6.16 (and thus are not presented). In summary, we have examined the influence of a reduction of the friction factor and found out that the shape of the longshore current profile is largely unaffected. An increase in the friction factor similarly conserves the predicted shape. We conclude that it would require a large uneven decrease in f_{cw} at the trough, which can not be justified on the present information, in order to change the computed longshore current profile to a profile with a peak over the trough by changing the friction factor.

DISPERSION

A third mechanism that can influence the distribution of the depth-averaged nearshore currents is the dispersion of momentum due to the vertical variation of the currents. Though the vertical profiles of the time-averaged currents shown in Fig. 6.16 appear to have the correct trends, it is convenient to evaluate the sensitivity of the results with respect to a variation of the eddy viscosity, which is a free parameter of the model. The dispersion is the largest in the regions where the vertical variation is also the largest, which happens to be in the regions where breaking is more intense, i.e., over and slightly seaward of the bar-crest, and near the shoreline. Therefore, the dispersion is already acting to spread the large short-wave forcing existent in those regions. Nevertheless, the dispersive mixing was seen (Fig. 6.17) to have a relatively small magnitude in the total y–momentum balance, and hence in the following test we study a situation where the dispersive mixing is larger than previously.

The cross-shore distribution of the eddy viscosity coefficient for the new test is given in Fig. 6.26. This coefficient is computed with $C_1 = 0.25$ and $M = 0.075$ in equation (2.86) instead of the previous $C_1 = 0.25$ and $M = 0.1$. Essentially, this means that the mixing coefficient due to breaking waves is reduced by 25%. This change is fully within the range of uncertainty associated with the estimation of the eddy viscosity. The time and depth-averaged current velocities along the primary array for a simulation with the above distribution of the eddy viscosity is given in Fig. 6.27. Comparing this figure with Fig. 6.13, the shape of the modeled $\tilde{V}$ has similar characteristics in both computations. The maximum of $\tilde{V}$ is slightly larger and shifted shorewards for the present situation, which means that the agreement with the data improved behind the bar, but only minimally, and deteriorated offshore of the bar. In general, the maximum of $\tilde{V}$ in Fig. 6.27 is slightly narrower than for the

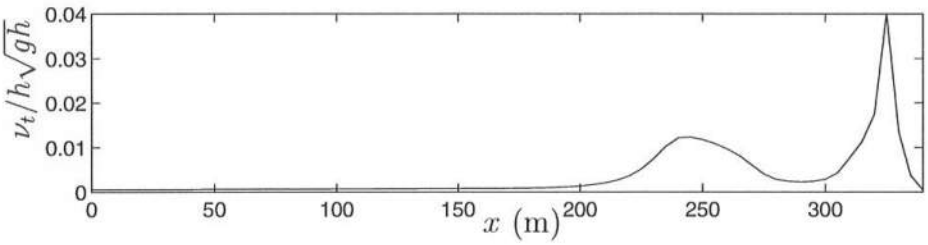

Figure 6.26: Cross-shore profile of $\nu_t/h\sqrt{g\,h_o}$ at the primary cross-shore array, for the 10/10/90:0351 simulation with $C_1 = 0.25$ and $M = 0.075$.

previous case shown in Fig. 6.13, which means that the total mixing is smaller here. It turns out that, similarly to the examples examined in sections 5.2.2–5.2.4, the difference between the mixing in the two simulations is not only due to the dispersive mixing, but also due to different amplitudes of the shear wave motion. For the present simulation the dispersive mixing is stronger, but is somewhat compensated by a weaker shear wave mixing.

This simulation allows us to conclude that, though we increased the dispersive mixing in the breaking region so that it could enhance the magnitude of the longshore current over the trough, the shear wave mixing became proportionally smaller, and thus the overall profile of the longshore velocity remained essentially unmodified. Hence, it emerges from this analysis that an alteration of the eddy viscosity can affect the current profile to some extent, but it does not seem to be a plausible mechanism to affect the location of the maximum of $\tilde{V}$.

In conclusion for all the model simulations for the 10/10/90:0351 wave conditions, we failed to predict the observed maximum of the longshore currents over the trough. The pressure gradient is seen to be an important force in that region, but other mechanisms must be present as well. It appears that the existence of a nonsteady, random, wave field with a varying breakpoint is an effect likely to be

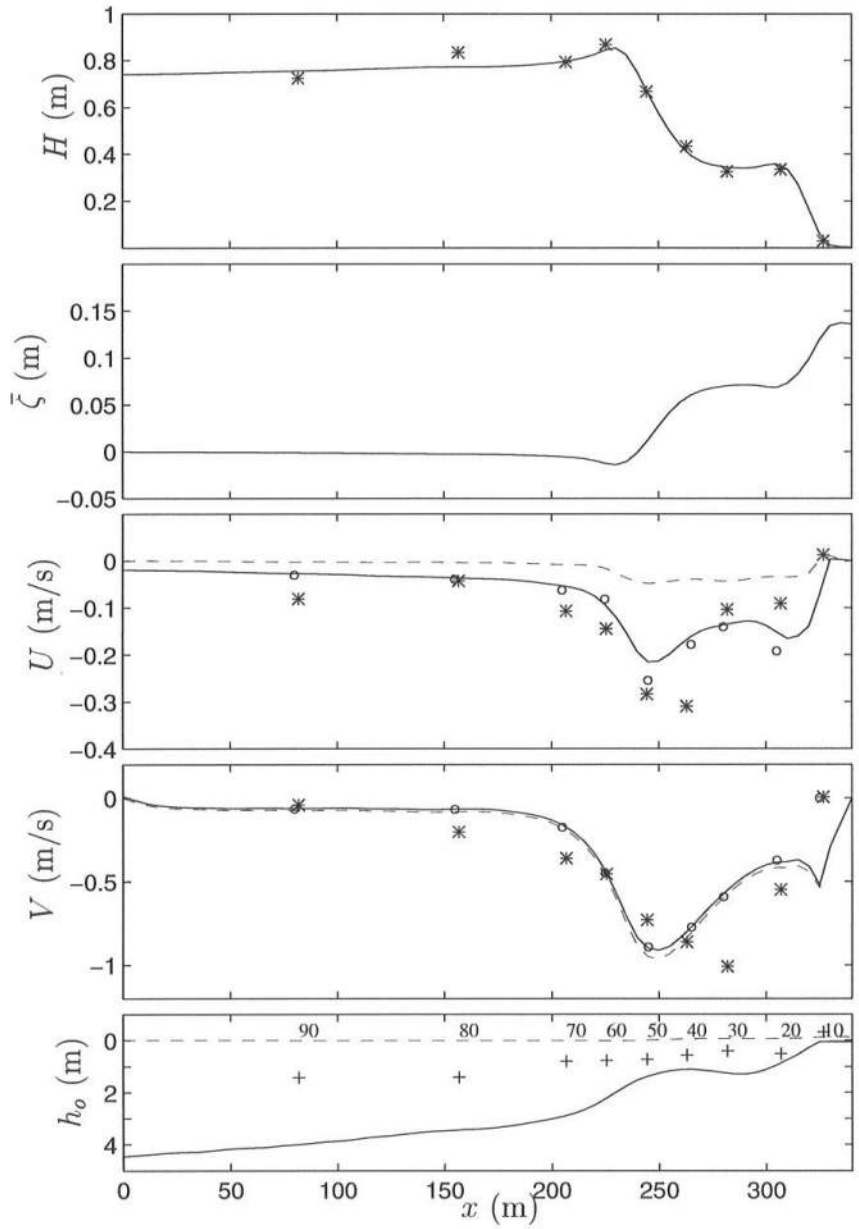

Figure 6.27: Cross-shore distribution at the primary cross-shore array for the 10/10/90:0351 simulation, with $M = 0.075$, of: (a) H_{rms} model (——), data ($*$); (b) $\bar{\zeta}$ model; (c) U_m model (——), $\tilde{U}$ model (– –), U_{zdata} model ($\circ$), data ($*$); (d) V_m model (——), $\tilde{V}$ model (– –), V_{zdata} model ($\circ$), data ($*$); (e) h_o (——), $\bar{\zeta}$ (– –), and gauges position (+).

responsible for the measured strong currents over the trough. In addition to the varying breakpoint, the proper representation of the forcing to the mean currents induced by the roller could have an effect of reducing the discrepancy between the measured and predicted currents over the trough region.

6.3 Simulations for the 10/10/90:1022 period

In this section we apply the model SHORECIRC to simulate the conditions at the 10th of October at a high-tide level, for the 3 hr period starting at 10:22am. The input wave conditions for this simulation are very similar to those for the previous case (see Table 6.2), as the wave field was nearly stationary until the end of this period.

The beach topography for the present simulation is given in Fig. 6.4 and 6.5. The model region is, once again, limited by the most seaward location in Fig. 6.4 and a no-flux boundary condition at a fixed location at the shoreline with still water depth $h_o = 0.05$ m. For the present simulation, the dimensions of the model domain are $l_x = 350$ m and $l_y = 700$ m, which is just 10 m larger in the cross-shore direction than the domain for the previous simulations to account for the beach inundation due to the increase in tidal level. The boundary conditions at the other boundaries, and the grid spacings are the same as before. Likewise, the eddy viscosity parameters are the "default" values used often throughout this study ($C_1 = 0.25$, $M = 0.1$), and the bottom friction coefficient is calculated from Swart's formula with $k_N = 10\,d_{50}$, which yields the distribution of f_{cw} shown in Fig. 6.28. This figure shows that the computed f_{cw} for the present case ($f_{cw} \simeq 0.0125$) is larger than that for the simulation of the 10/10/90:0351 period (see Fig. 6.8), due to a decrease in the wave orbital motion near the bed (which is caused by a raise in water depth). The cross-shore distribution of $\nu_t/h\sqrt{g\,h_o}$ along the primary cross-shore array is also shown in Fig. 6.28. Minor differences can be found between this variation and that for the 10/10/90:0351 period.

Though the incident wave conditions are similar for the two periods at the 10th of October, the local variations in water depth due to the tide can affect substantially the nearshore wave field. This can be seen through the comparison of

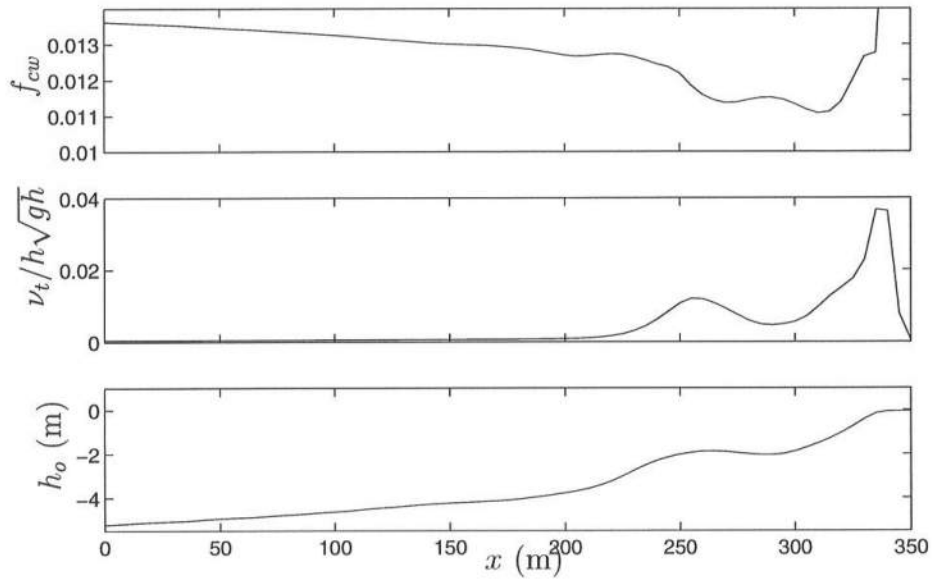

Figure 6.28: Cross-shore profiles of f_{cw}, $\nu_t/h\sqrt{g\,h_o}$ and h_o at the primary cross-shore array, for the 10/10/90:1022 simulation.

Fig. 6.29 for the present case with Fig. 6.9 for the low tide situation. The most interesting differences are in the wave height field (center panels). Whereas previously $H_{rms} \simeq 0.4$ m over the trough, we now observe that for the high-tide situation $H_{rms} \simeq 0.6$ m in the same region. Breaking is now a lot more intense over the beach face and barely evident over the bar-crest (see also the cross-shore distribution in Fig. 6.31). In the top panel of the two figures we also notice that there are no appreciable differences in the computed wave angle for both cases.

The depth- and time-averaged (over a period of 2 hr) predicted current velocities for the present case are given in Fig. 6.30. The depicted currents are essentially longshore uniform, which is confirmed by the fact that the maximum depth-averaged cross-shore velocity is smaller than 0.10 m/s (it would be zero for a longshore uniform beach). The longshore currents appear to be fairly uniformly distributed over the region between the bar crest and the beach face. A perspective plot of the mean

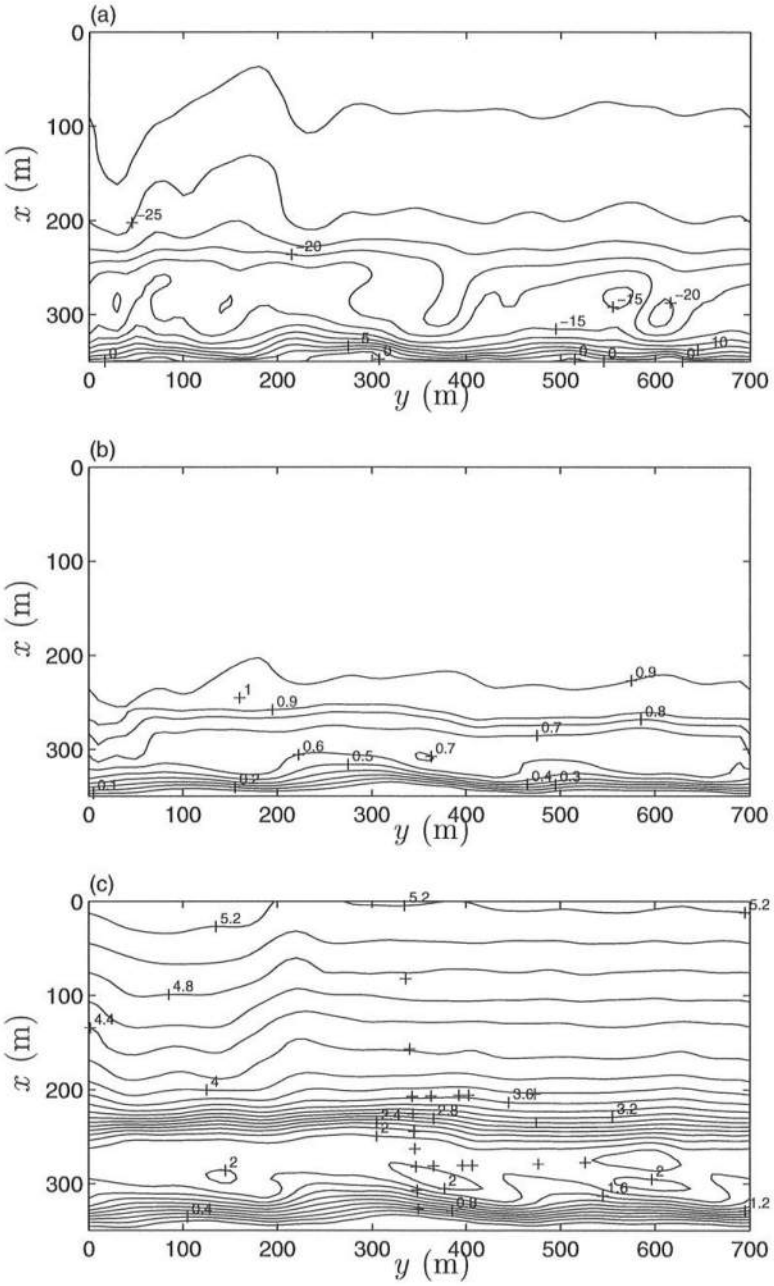

Figure 6.29: Contour plots for the 10/10/90:1022 simulation of: a) wave angle $\alpha_w(^\circ)$; b) wave height H_{rms} (m); and c) still water depth h_o (m).

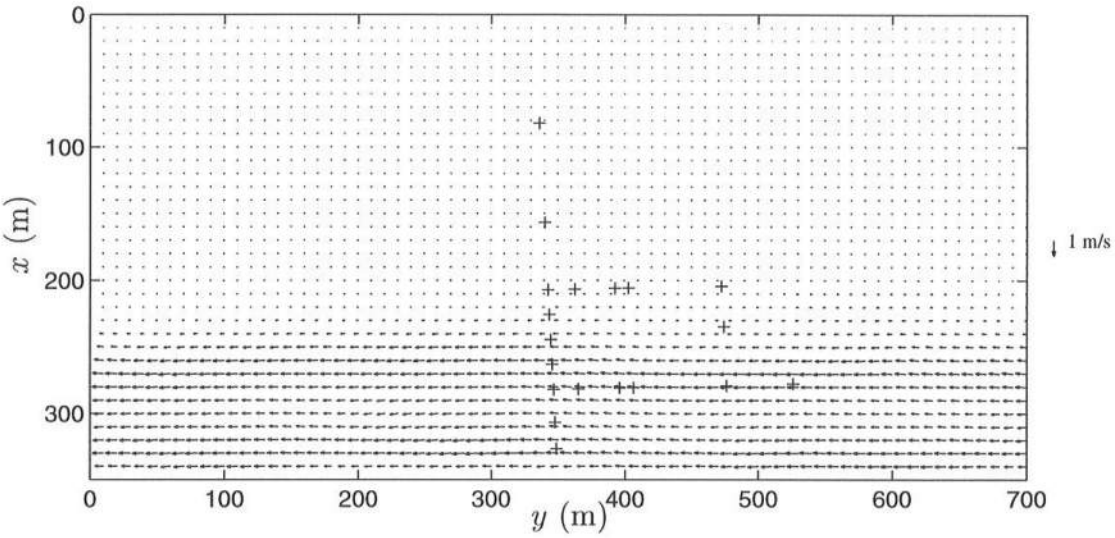

Figure 6.30: Depth and time-averaged current velocity vectors for the 10/10/90:1022 simulation.

surface elevation (not shown) indicates the existence of longshore variations of that quantity, which it will be seen later to drive the currents in the trough region.

Fig 6.31 shows the cross-shore variation of the time-averaged flow variables along the primary cross-shore array. First, we notice that the predicted H_{rms} does not compare so well with the data as for the 10/10/90:0351 period (Fig 6.13), despite several attempts with various combinations of the breaking-related parameters in REF/DIF 1 to produce a better agreement. Nevertheless, the agreement between the predicted and measured H_{rms} is considered satisfactory. Second, it is seen that the breaking over the bar is much weaker for the present high-tide case, which means that only part of the wave energy (and momentum flux) is released in that region. Therefore we expect a greater concentration of the currents closer to the shore, which is seen in both the data and model results for $\tilde{V}$.

The measured cross-shore currents at the primary cross-shore array are seen

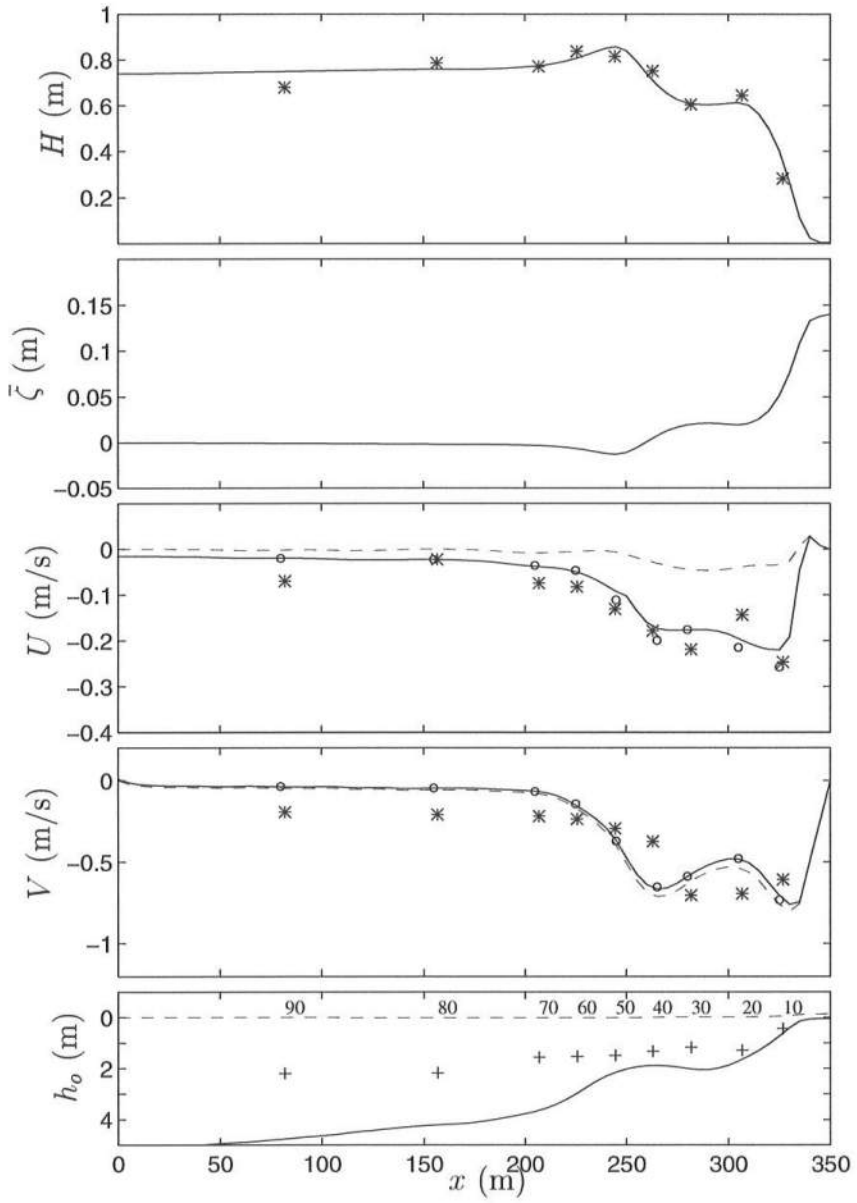

Figure 6.31: Cross-shore distribution at the primary cross-shore array for the 10/10/90:1022 simulation of: (a) H_{rms} model (——), data (∗); (b) $\bar{\zeta}$ model; (c) U_m model (——), $\tilde{U}$ model (– –), U_{zdata} model (○), data (∗); (d) V_m model (——), $\tilde{V}$ model (– –), V_{zdata} model (○), data (∗); (e) h_o (——), $\bar{\zeta}$ (– –), and gauges position (+).

to be fairly well predicted by the model at most locations except at CM20 and CM90[6]. It is also seen that the predicted below-trough averaged current U_m is similar to the current at the gauge vertical location (U_{zdata}), and thus is a good representative value of the magnitude of the cross-shore currents. The good agreement between U_m (or U_{zdata}) and the data also indicates that the estimate of Q_w by equation (2.110) with $B_0 = 0.125$ (linear wave theory) happens to be good. Again, this fact contradicts the expectancy that the use of linear wave theory overestimates the values Q_w in the breaking region.

Focusing in the longshore current velocities at the primary cross-shore array (Fig. 6.31) the model still predicts a bi-modal current profile, whereas the data suggests the existence of a maximum over the trough. The discrepancy between modeled and measured V is the largest at CM20 and CM40, and also at the offshore gauges. In particular, the measured currents seaward of CM50 are fairly constant and relatively large ($V \simeq 0.2$ m/s), which contrasts with the model predictions that decay to nearly zero seawards of the CM60 location. This large velocities at the offshore locations can not be simply explained by the wind shear stress which induces a longshore current of only 5 cm/s. Overall, we fail to predict the shape of the longshore current profile, but not the magnitude of the maximum velocities.

The vertical variation of the simulated time-averaged current velocities at the primary array is given in Fig. 6.32. As before, the vertical profiles for the cross-shore velocities are a lot more pronounced than for the longshore velocities. In fact the profiles of both U and V exhibit the same trends as the profiles often measured in field conditions (Rodriguez *et al.*, 1994). Recall also that we are not solving for the bottom boundary layer, and thus we expect the given profiles to change considerably close to the bottom if we had included a solution for the governing equations in that

[6] Recall the existence of an offset error of U at CM90.

region.

As before, the magnitude of the terms in the momentum equations (time-averaged over a 2 hr period) along the primary array alignment for the period of 10/10/90:1022 is given in Fig. 6.33. In the x–momentum equation the same main balance between $gh\frac{\partial \bar{\zeta}}{\partial x}$ and $\frac{1}{\rho}\frac{\partial S_{xx}}{\partial x}$ is visible. In the y–momentum equation the wave forcing is bi-modal despite the weak breaking over the bar, and more important, is that most of the forcing in the trough is caused by the longshore pressure gradient. In fact, this term is also large at the beach face and over the crest, but with opposite sign to that of the wave forcing, which means that the longshore pressure gradient in those regions is contributing to a reduction of the longshore currents. The convective accelerations are again not small, though most of this contribution turns out to be due to the time-averaged currents, and only a small component is caused by shear wave motion. As in the 10/10/90:0351 simulation, we find that the dispersive mixing is small but not negligible for the present results. Comparing these results with those in section 5.2.4 (see fig. 5.36) for a nearly longshore uniform barred beach with a rip-channel, it appears that the dispersive mixing is smaller here, in the presence of larger topographical variations in both the longshore and cross-shore directions.

Time series of the depth-averaged current velocities ($\tilde{U}$, $\tilde{V}$) from SHORECIRC at the positions CM20, CM40 and CM60 are given in Fig. 6.34. These locations are representative of the conditions over the trough, over the bar-crest and on the seaward slope of the bar, respectively. These time series show the prediction of velocity fluctuations on a time scale identified with the presence of shear instabilities. Note that the velocity fluctuations are not so intense as those for the previous case (Fig. 6.19 and 6.20). The peak period of the velocity fluctuations is $T \simeq 750$ s and the wavelength is approximately $L \simeq 230$ m, which implies a propagation speed

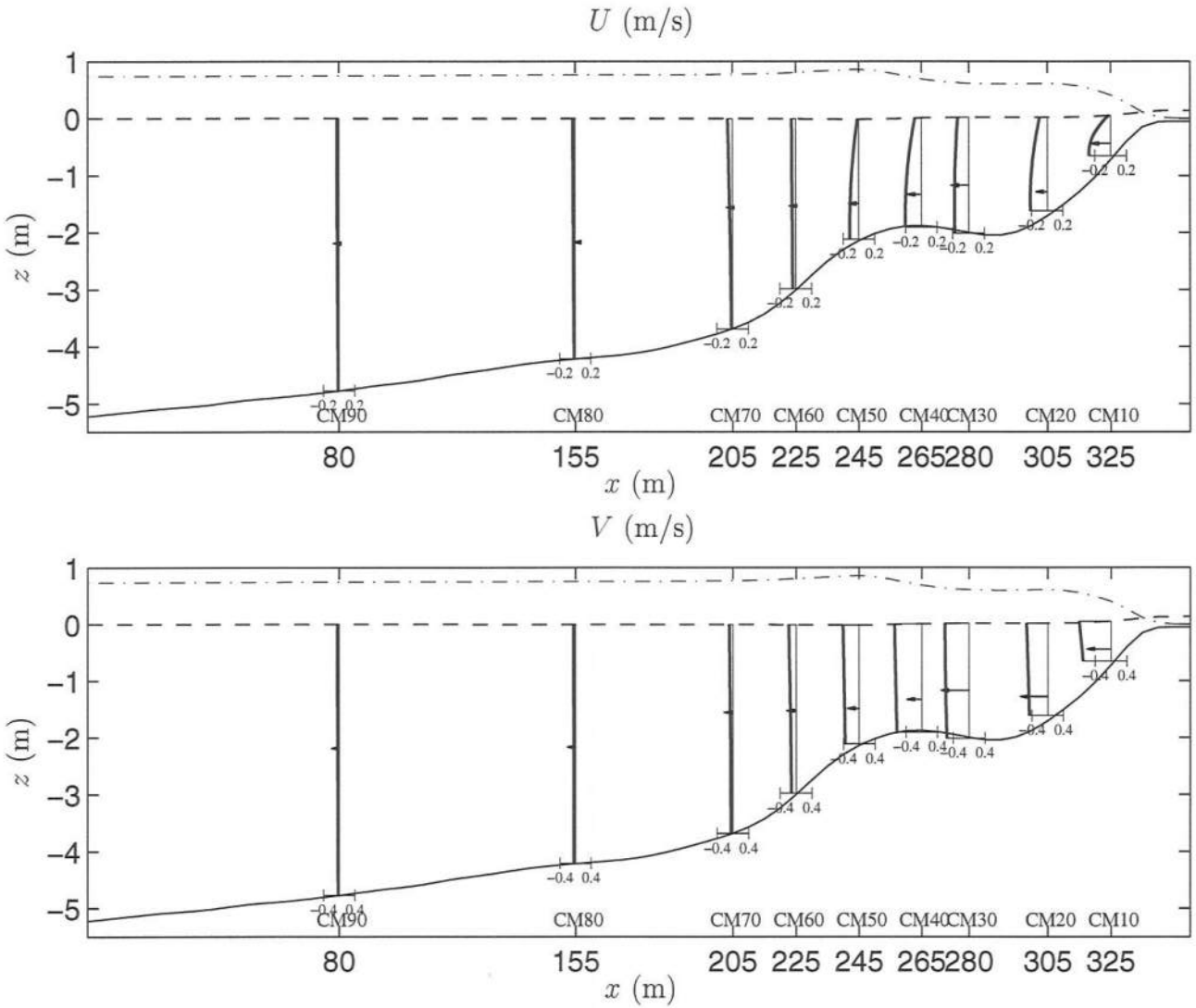

Figure 6.32: Cross-shore variation of the predicted vertical profiles (——) of U and V, versus measured values (←—), at primary cross-shore array for the 10/10/90:1022 simulation; H_{rms} model (– ·), $\bar{\zeta}$ model (– –).

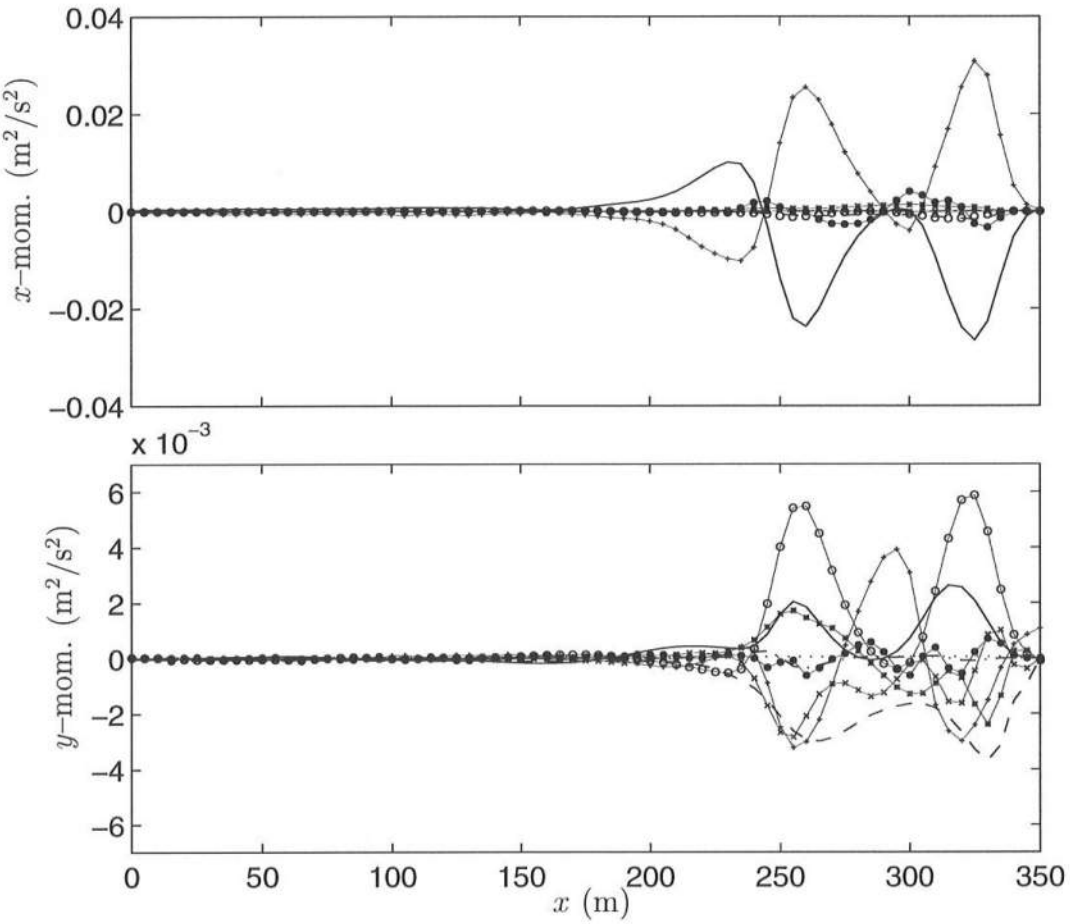

Figure 6.33: Cross-shore distribution at the primary cross-shore array of the terms in the time-averaged momentum equations for the 10/10/90:1022 simulation. Terms in the x–momentum balance: $gh\frac{\partial\bar{\zeta}}{\partial x}$ (+), $\frac{1}{\rho}\frac{\partial S_{xx}}{\partial x}$ (——), $\frac{1}{\rho}\frac{\partial S_{yx}}{\partial y}$ (○), $\overline{\frac{\partial}{\partial x}\left(\frac{\bar{Q}_x^2}{h}\right)}$ (×), $\overline{\frac{\partial}{\partial y}\left(\frac{\bar{Q}_x\bar{Q}_y}{h}\right)}$ (∗), – turb. mixing (– ·), $\frac{\tau_x^B}{\rho}$ (– –), – dispersive mixing (—•—), $\frac{\tau_x^S}{\rho}$ (. . .). Terms in the y–momentum balance: $gh\frac{\partial\bar{\zeta}}{\partial y}$ (+), $\frac{1}{\rho}\frac{\partial S_{yy}}{\partial y}$ (——), $\frac{1}{\rho}\frac{\partial S_{xy}}{\partial x}$ (○), $\overline{\frac{\partial}{\partial y}\left(\frac{\bar{Q}_y^2}{h}\right)}$ (×), $\overline{\frac{\partial}{\partial x}\left(\frac{\bar{Q}_x\bar{Q}_y}{h}\right)}$ (∗), – turb. mixing (– ·), $\frac{\tau_y^B}{\rho}$ (– –), – dispersive mixing (—•—), $\frac{\tau_y^S}{\rho}$ (. . .).

of $c_S \simeq 0.31$ m/s, or $c_S \simeq 0.39\,\tilde{V}_M$, where $\tilde{V}_M = 0.80$ m/s is the maximum longshore velocity at the primary cross-shore array alignment. Hence, the shear waves for the 10/10/90:1022 period are predicted to propagate slower than those for the 10/10/90:0351 period ($c_S \simeq 0.46$ m/s). Also, for the 10/10/90:1022 period, the estimated frequency-wavenumber spectrum from the secondary crest sub-array given by Church *et al.* (1992) indicates the existence of shear waves traveling at a speed within the range $0.40 < c_S < 0.50$ m/s, which is slightly faster than the speed predicted in our computations for the same case. One possible reason for this discrepancy is the limited domain dimensions in our computations, which affects the wavelength and the propagation speed of the shear waves.

For completeness, the comparison between model and data results at the secondary array and the trough and crest sub-arrays is indicated in Fig. 6.35 and 6.36. Recall that it is known from the data analysis that the cross-shore velocity records at CM70, CM71, CM73 and CM74 have an offset error. Focusing first on the cross-shore profiles we note large differences between the variations of all the quantities, except for the longshore velocities ($\tilde{V}$ and V_m), at this alignment and at the primary cross-shore array (Fig. 6.31). This indicates that there is a strong longshore variability in the flow properties, which was not apparent in Fig. 6.30. The comparison with the data is not very informative for the lack of more current meters.

At the trough sub-array (left panel in Fig. 6.36) we find a fairly good agreement between the model below-trough averaged U_m and the data. In the longshore direction, the measured velocities are also seen to be reasonably well predicted by the model results. In fact, there are locations in the trough where the model predictions are even larger (in absolute value) than the measured currents, which seems

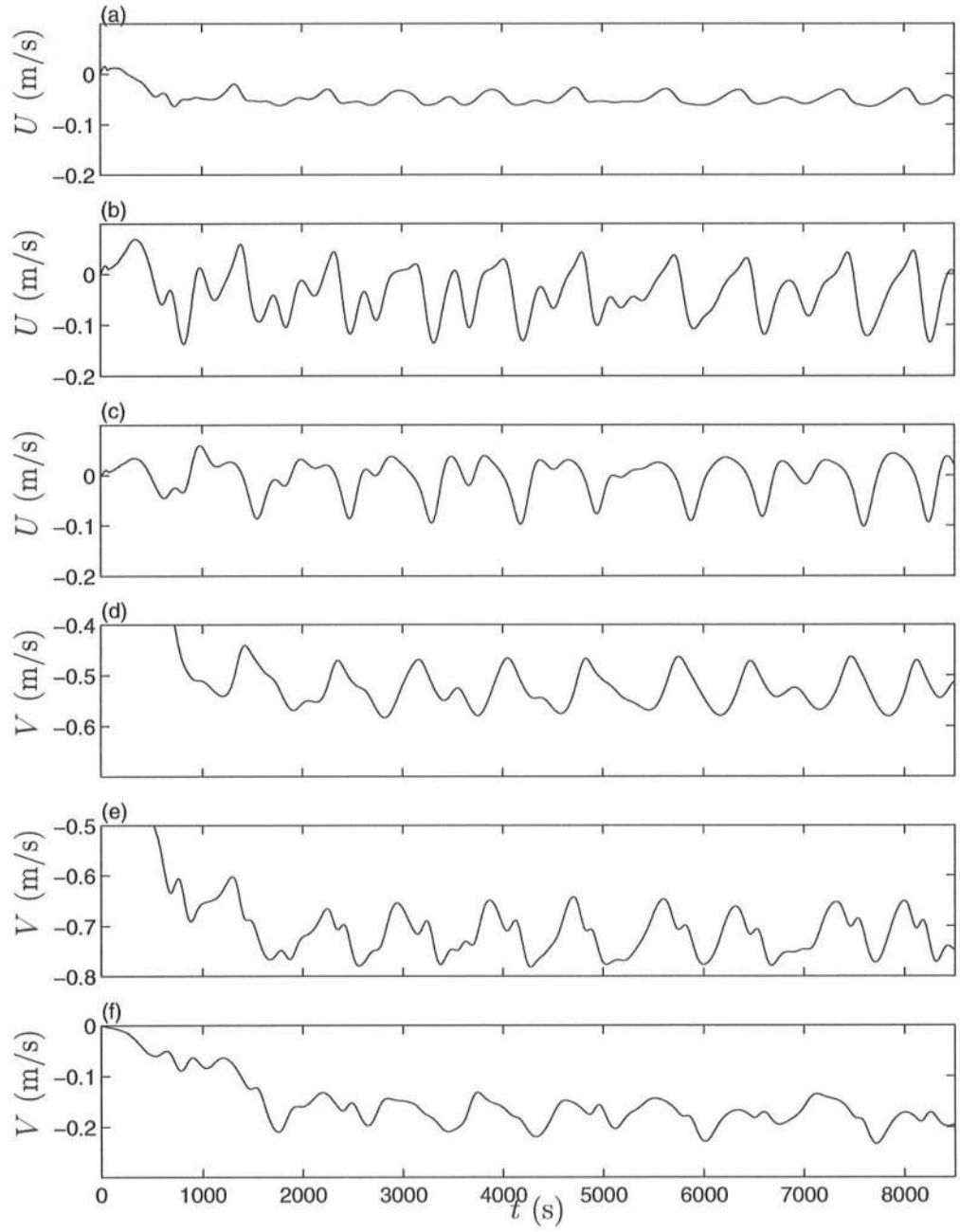

Figure 6.34: Time series of the predicted $\tilde{U}$ (3 upper plots) and $\tilde{V}$ (3 lower plots) for the 10/10/90:1022 simulation at three locations along the primary cross-shore array: (a,d) CM20, $x = 305$ m; (b,e) CM40, $x = 265$ m; (c,f) CM60, $x = 225$ m.

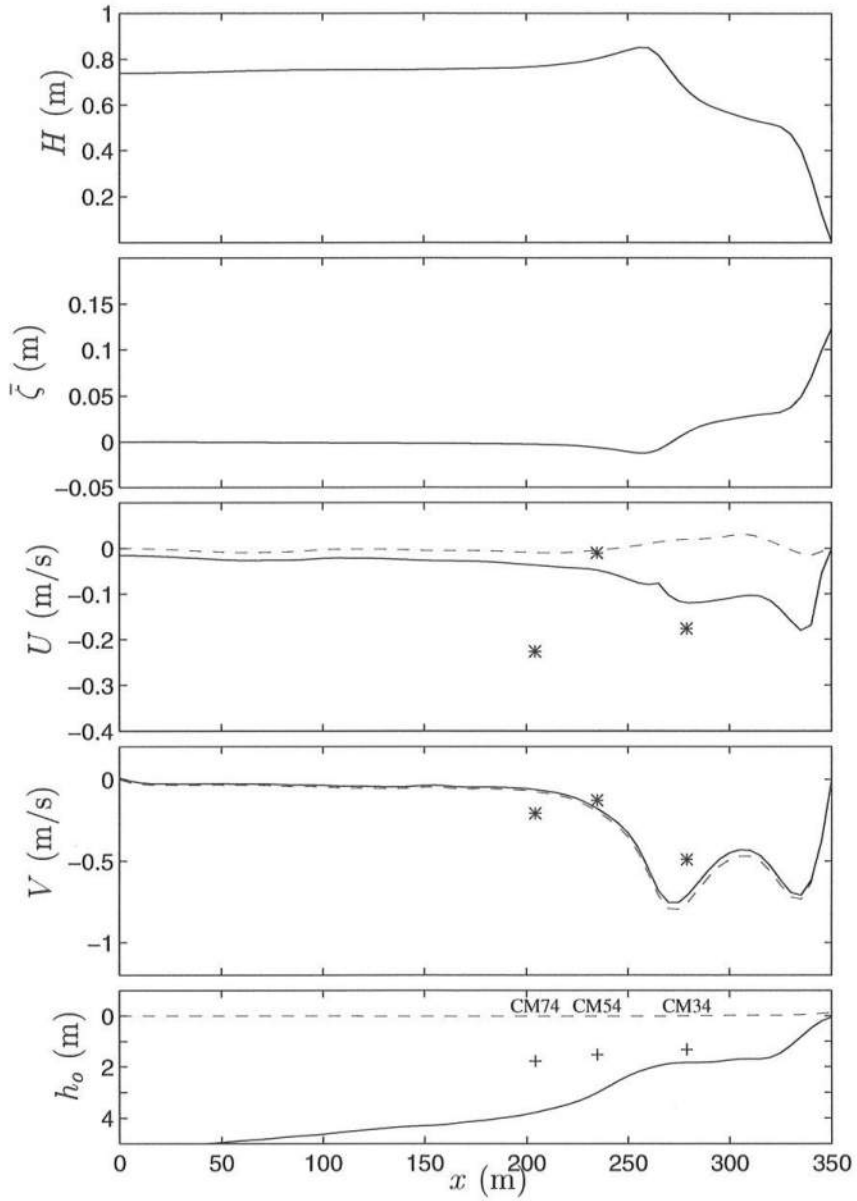

Figure 6.35: Cross-shore distribution at the secondary cross-shore array for the 10/10/90:1022 simulation of: (a) H_{rms} model; (b) $\bar{\zeta}$ model; (c) U_m model (——), $\tilde{U}$ model (– –), data (∗); (d) V_m model (——), $\tilde{V}$ model (– –), data (∗); (e) h_o (——), $\bar{\zeta}$ (– –), and gauges position (+).

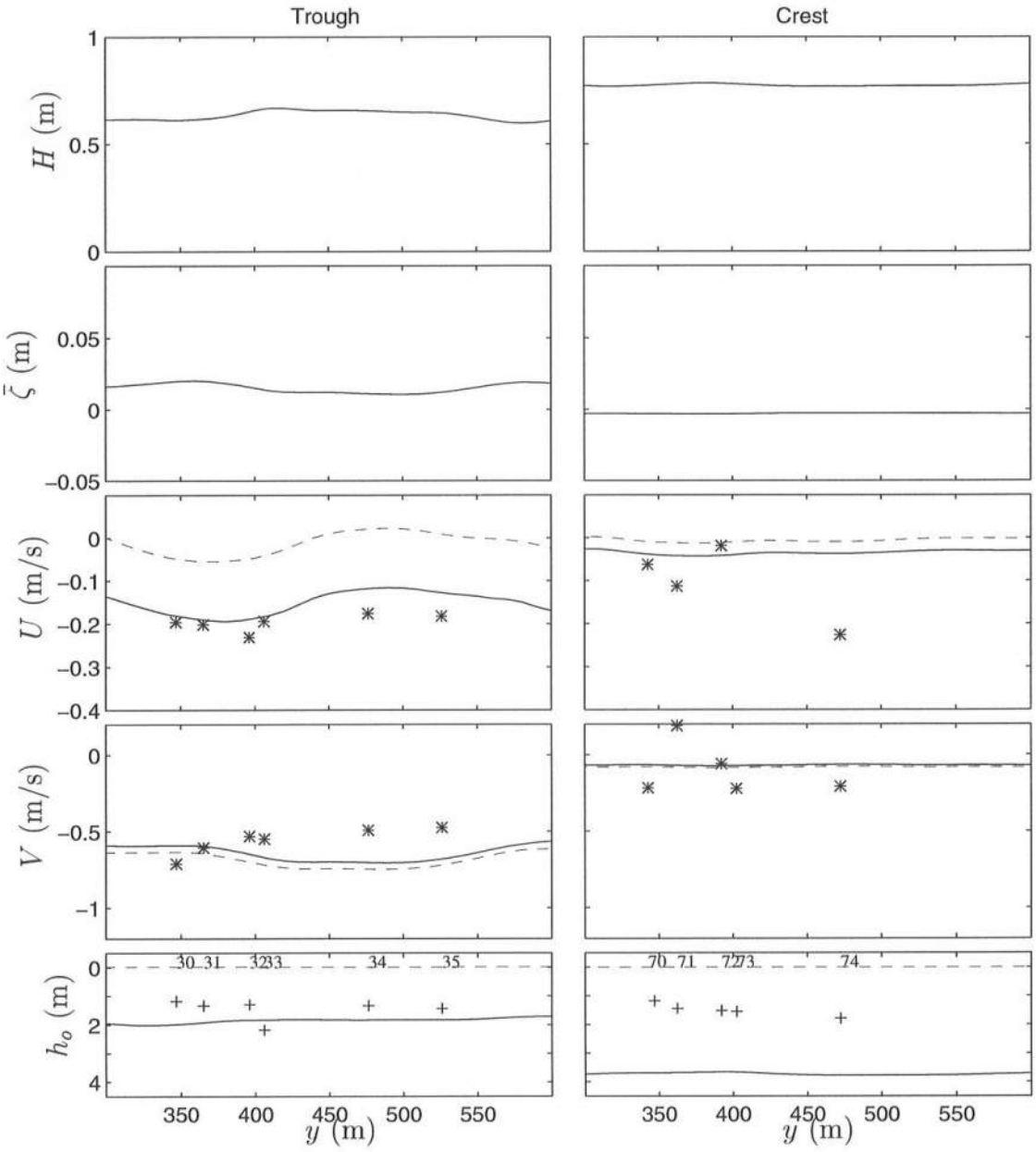

Figure 6.36: Cross-shore distribution at the trough (left) and crest (right) sub-arrays for the 10/10/90:1022 simulation of: (a) H_{rms} model; (b) $\bar{\zeta}$ model; (c) U_m model (——), $\tilde{U}$ model (– –), data (∗); (d) V_m model (——), $\tilde{V}$ model (– –), data (∗); (e) h_o (——), $\bar{\zeta}$ (– –), and gauges position (+).

to indicate that for the present simulation the model is able to predict the relatively large currents observed over the trough. The comparison of U at the crest array (right panel in Fig. 6.36) is deceptive, because as mentioned previously all the gauges gave false readings except the CM72, which is matched by the model results. For the longshore velocities, the predicted currents at most locations are lower than the measured currents. No explanation is found for this discrepancy. It appears though that a mixing mechanism of larger magnitude than the ones included in the model (such as that due to random waves) is responsible for those (relatively) large longshore currents measured seaward of the bar crest.

In summary, through the comparison of the results in this section (for high-tide) with those of the previous section (for low-tide) we have confirmed the findings of other authors that the nearshore currents are strongly tidal modulated. The change in water level modifies primarily the wave field, which consequently modifies the distribution of the wave force and the longshore currents. At the primary cross-shore array location, we find that at low-tide the predicted longshore current profile is strongly double-peaked (Fig. 6.31), whereas at high-tide the current profile is nearly uniform in the region between the bar and the beach face. In both cases the longshore pressure gradient is an important driving force, though.

6.4 Simulations for the 19/10/90:1221 period

We chose to analyze a third situation at DELILAH observed during the 19th of October, between 12:21 and 15:21. The beach topography changed considerably from that seen in the 10th of October, due to the passage of a "southeaster" storm on the 11th and the proximity of the Hurricane Lili on the 13th. Around the 12th of October, a prominent topographical feature, similar to a secondary bar, appeared at the southern end of the mini-grid surveying area, which remained permanent until

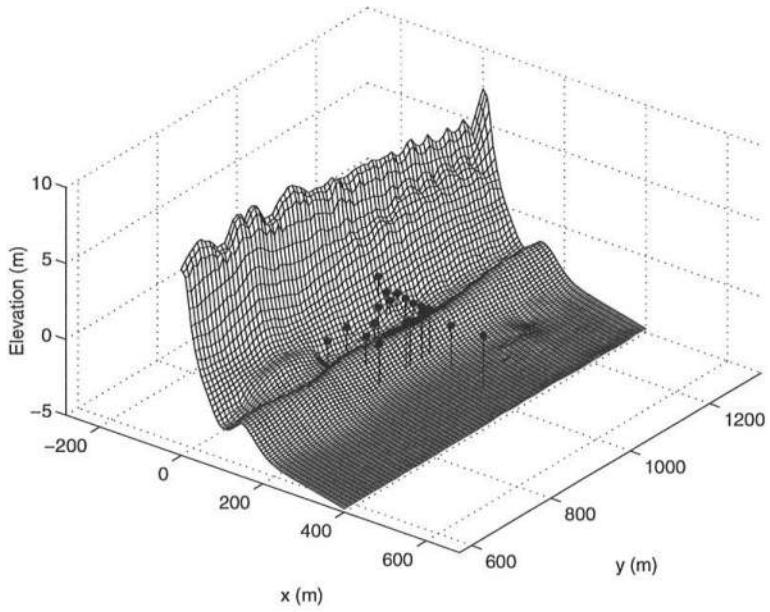

Figure 6.37: DELILAH: Beach bathymetry for the 19th of October.

the 19th, though with slight changes in form. This can be seen in Fig. 6.37 around the 700 and 800 m longitudinal mark (in a coordinate system rotated -3° from the FRF coordinate system). It should be noted that in order to use periodicity at the lateral boundaries we had to artificially match the surveyed cross-shore profile at the south end of the mini-grid with that at the north end of the mini-grid. Therefore, the original mini-grid area of length $l_y = 570$ m is extended in the longshore direction for 190 m in order to provide that match, yielding the total domain length for the calculations of $l_y = 760$ m. Though this procedure is likely to introduce errors in the simulation, we find it acceptable in view of the findings in section 6.2.2 about the small effect of the lateral boundary conditions on the simulated currents at the primary cross-shore array location.

The topographical feature we pointed out in Fig. 6.37 is likely to be poorly represented due to the lack of information outside the mini-grid area. Nevertheless,

it is also unlike to affect our results significantly because that feature is downstream of the array locations for the wave direction observed on the 10/10/90:1022 period (see Table 6.2).

Fig. 6.38 shows the contour plots of the computed wave angle α_w and "root-mean-square" wave height H_{rms} for the incident wave conditions given in Table 6.2. The bottom panel shows the depth contours (for the present low-tide case), where the largest topographical variations are observed over the trough at the right (downstream) of the sensor locations. (Note that these plots are given in the computational grid coordinate system, with origin at the northern-seaward point of the domain). The wave angles are positive, which means that waves are coming from the north-east sector, instead from the south-east sector as it was seen for the simulations in the 10th of October.

The simulations with SHORECIRC for the present conditions predict again the presence of shear waves. The friction factor is calculated as before from Swart's formula with $k_N = 10\,d_{50}$ and it turns out to give $f_{cw} \simeq 0.0125$, which is similar to that found for the 10/10/90:1022 simulation. The eddy viscosity parameters are also the "default" values $C_1 = 0.25$ and $M = 0.1$. We are more interested in analyzing the time-averaged (over the period of the simulation) flow properties. However, it is also interesting to provide an instantaneous "picture" of the flow field to better understand the type of phenomena simulated herein. Fig. 6.39 shows the instantaneous (subplot (a)) and the time-averaged (subplot (b)) depth-averaged velocity vectors for the present conditions. The instantaneous flow field (after 1 hr of simulation) has several vortices at different locations, which are associated with flow instabilities that propagate with the longshore current. The vortices are created by the shear instability mechanism, but also by the convergence and divergence of the streamlines around prominent topographical features. Rapid accelerations of

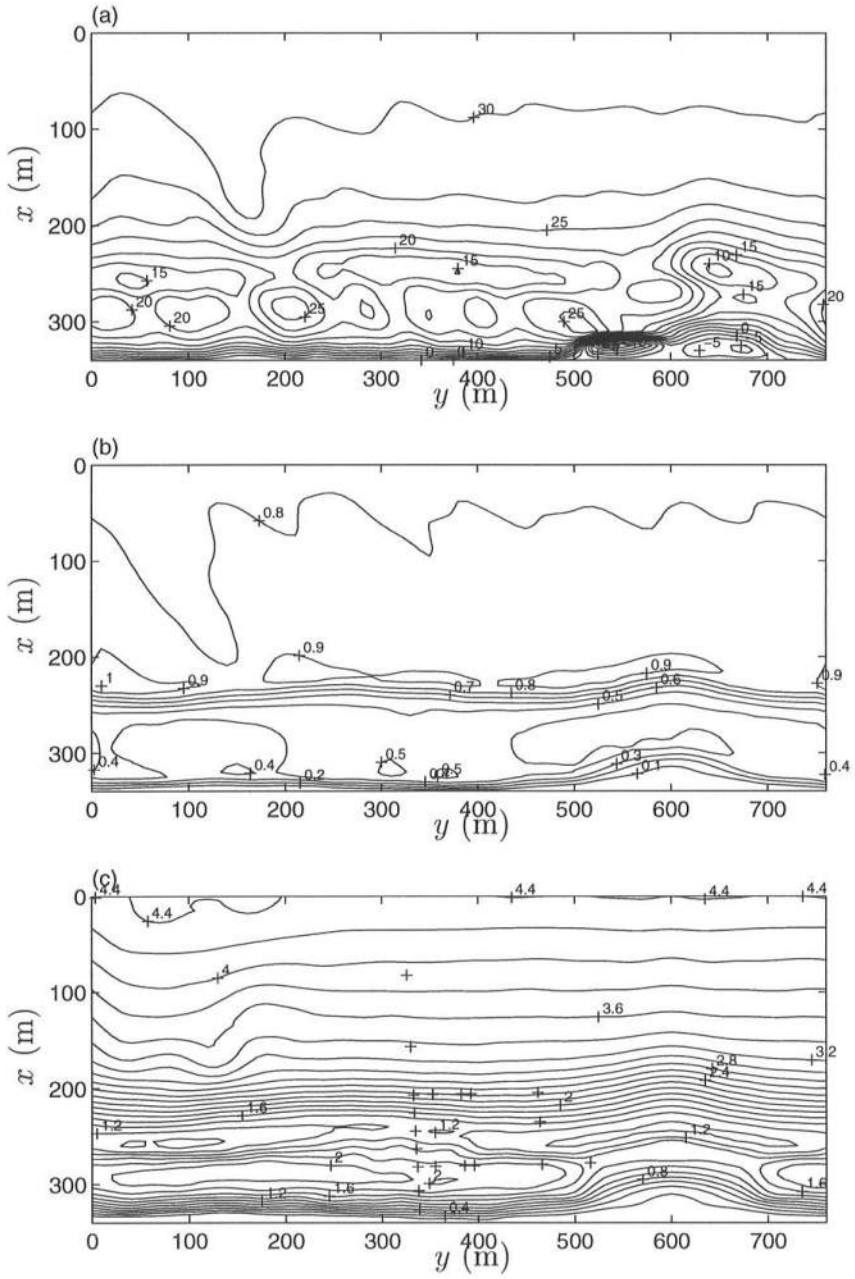

Figure 6.38: Contour plots for the 19/10/90:1221 simulation of: a) wave angle $\alpha_w(^\circ)$; b) wave height H_{rms} (m); and c) still water depth h_o (m).

the flow can even be seen in the time-averaged velocity vectors (see bottom panel of Fig. 6.39 at $y \simeq 600$ m).

The cross-shore variation of H_{rms}, $\bar{\zeta}$, U and V along the the primary cross-shore array and at the trough and crest sub-arrays are given in Fig. 6.40 and 6.41, respectively. Notice that at the primary array, the sensors CM30 and CM60 were out of order, and the sensors CM70 and CM90 have offset errors in the measurements of U. The measured cross-shore velocities in Fig. 6.40 are fairly well predicted by the model results, with exception of the position CM80. For the longshore velocities, we find again a bi-modal current structure predicted by the model. The data shows velocities much larger than the predicted seaward of the bar, and slightly larger in the shoreward slope of the bar crest (positions CM40 and CM50). The latter indicates that the forcing predicted by the model in that region is lower than the existent, which can probably be due to an improper modeling of the radiation stresses in the breaking region.

At the trough array (left in Fig. 6.41) we find a fairly good agreement between the predicted and measured below-trough cross-shore and longshore velocities (solid lines). (CM30 is out of order). This is somewhat consistent with the results for the 10/10/90:1022 period (section 6.3), where we also found a relatively good agreement at the trough array. For the crest array, the predictions seem poor, but we recall that CM72 is the only reliable sensor for the cross-shore velocities. For the longshore velocities we have no confirmation whether the sensors are faulty or not, but it is likely that some of them can be malfunctioning due to the large variability of readings for a series of sensors no more than 50 m apart (CM70–CM74).

During the experiment, vertical profiles of both U and V were measured with an instrumented sled (Smith *et al.*, 1992; Birkemeier *et al.*, 1997). The sled was towed offshore of the breaker line once a day, starting on the 16th of October, and

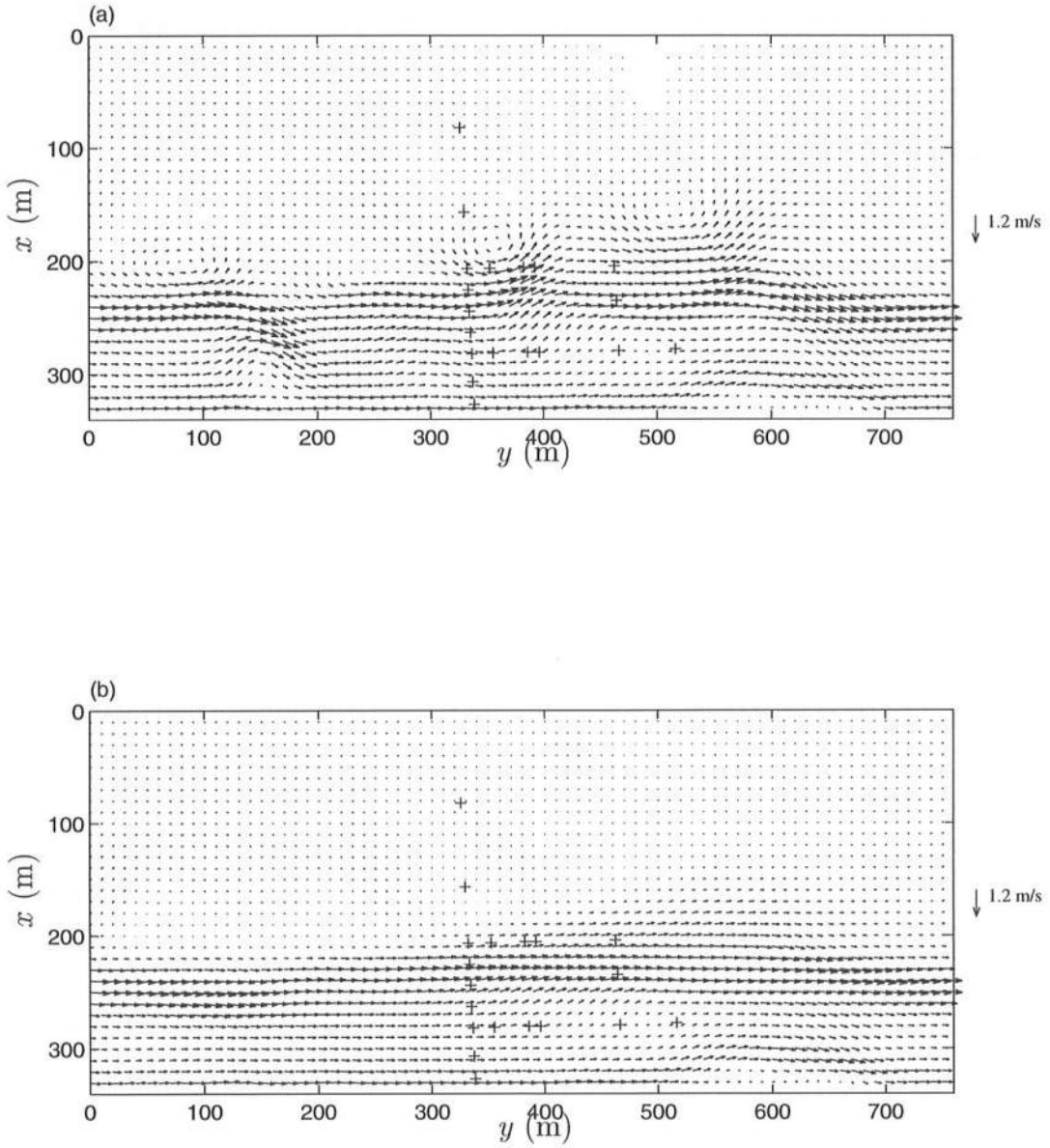

Figure 6.39: Depth-averaged current velocity vectors for the 19/10/90:1221 simulation: (a) instantaneous flow field at $t = 3790$ s; (b) time-averaged flow field over a period of 2 hr.

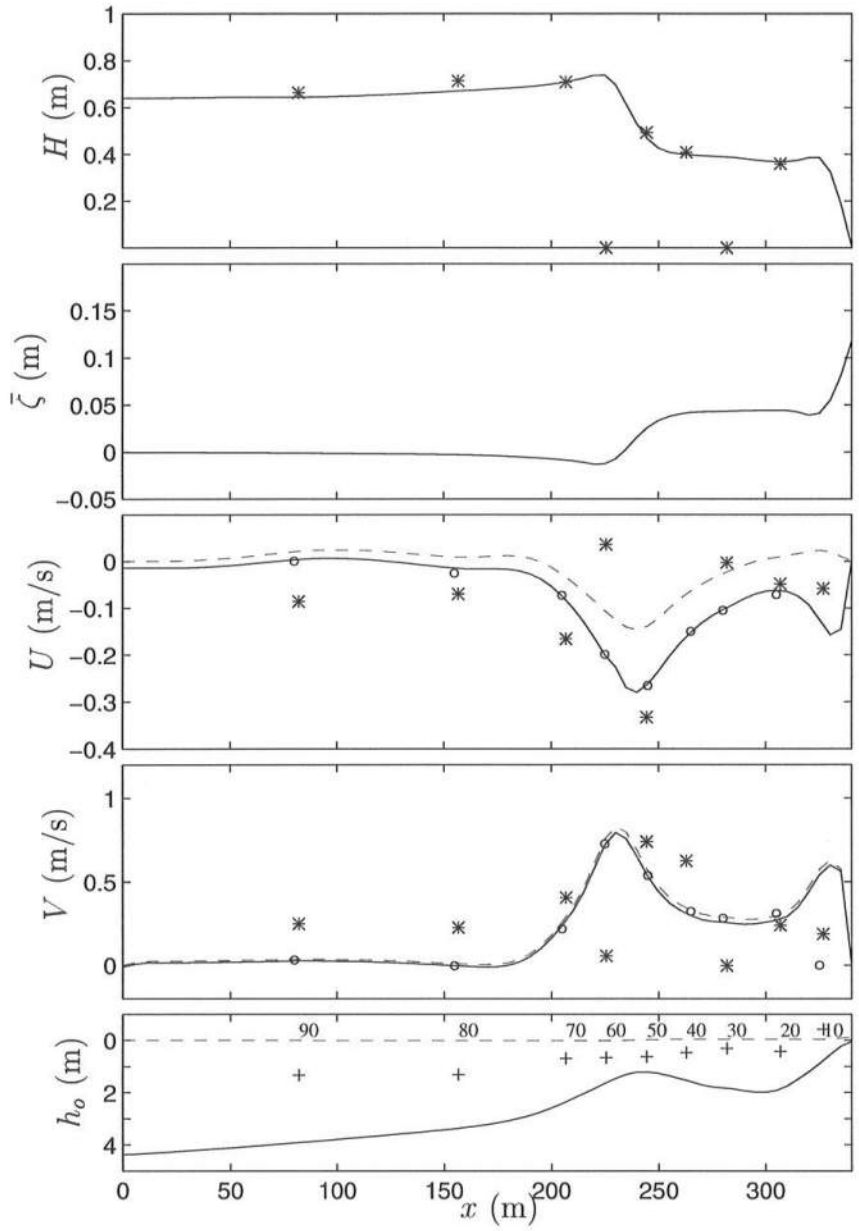

Figure 6.40: Cross-shore distribution at the primary cross-shore array for the 10/10/90:1221 simulation of: (a) H_{rms} model (——), data (∗); (b) $\bar{\zeta}$ model; (c) U_m model (——), $\tilde{U}$ model (– –), U_{zdata} model (○), data (∗); (d) V_m model (——), $\tilde{V}$ model (– –), V_{zdata} model (○), data (∗); (e) h_o (——), $\bar{\zeta}$ (– –), and gauges position (+).

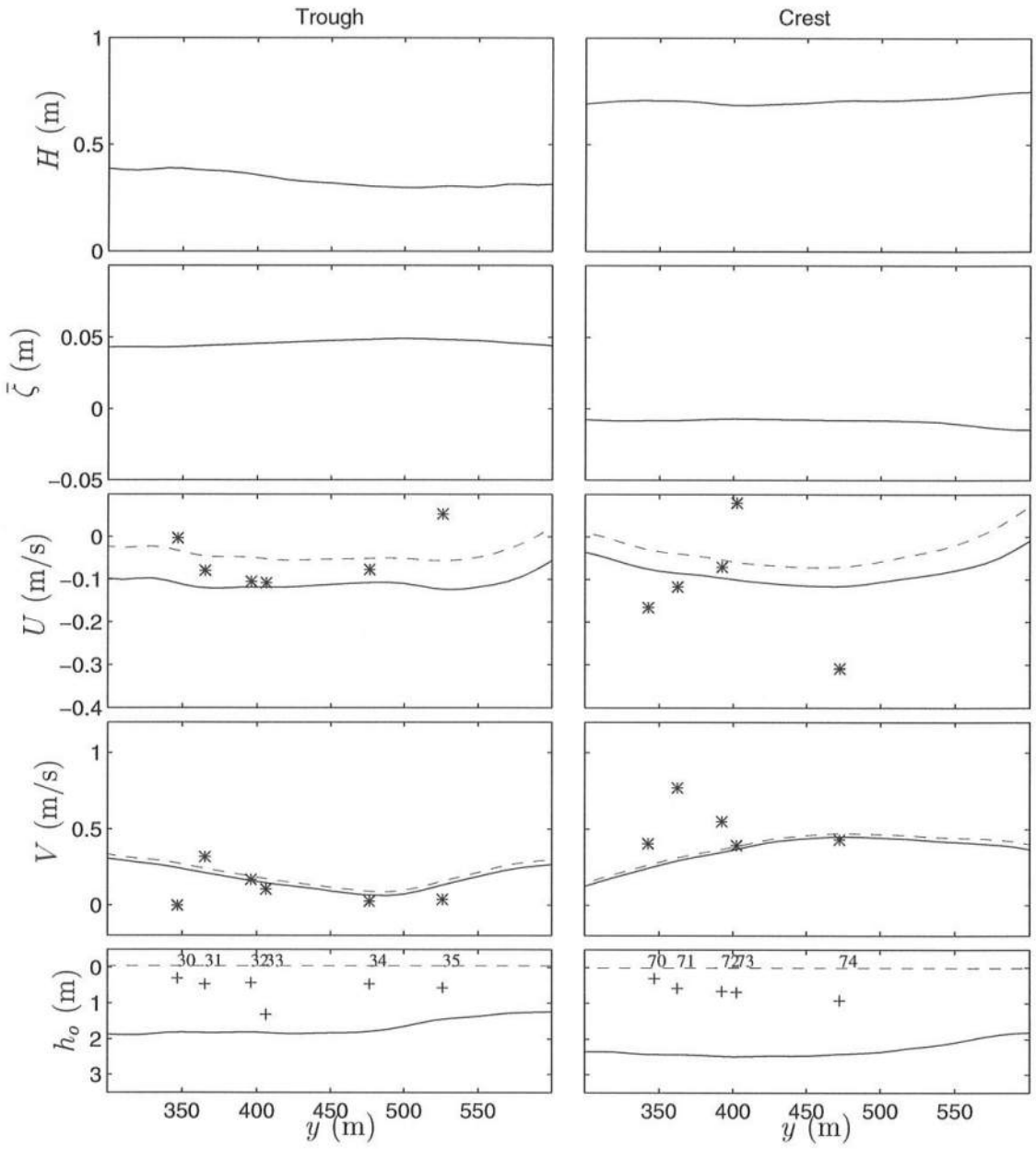

Figure 6.41: Cross-shore distribution at the trough (left) and crest (right) sub-arrays for the 19/10/90:1221 simulation of: (a) H_{rms} model; (b) $\bar{\zeta}$ model; (c) U_m model (——), $\tilde{U}$ model (– –), data (∗); (d) V_m model (——), $\tilde{V}$ model (– –), data (∗); (e) h_o (——), $\bar{\zeta}$ (– –), and gauges position (+).

then it was pulled back to shore in steps of 20 m. At each stopping position (which were close to the primary cross-shore array gauge locations), data were collected for 34 min. The interval between the starting acquisition time at consecutive locations was approximately 40 min. The data were obtained with five electromagnetic current meters mounted at 0.35, 0.60, 1.00, 1.35 and 1.75 m above the bed. During the 19th of October six vertical profiles were collected between 12:30 and 16:30. Here, we will assume for model to data comparison that these profiles are representative of the time-averaged currents over the 3 hr period starting at 12:21. Essentially, the period between 12:30 and 16:30 starts (and finishes) slightly before (and after) low-tide. Therefore, the variation of the cross-shore and longshore currents due to differences in water depth (and thus wave conditions) is assumed to be minimal over this period.

Fig. 6.42 shows the comparison of the measured currents at each sled position (averaged over 34 min) with the predicted currents at the same location (averaged over 2 hr of the model simulation). Note that the longshore alignment of these measurements is just 20 m North of the primary cross-shore array alignment. It can be seen that the cross-shore currents are relatively well represented, though large variations can be observed at the location $x = 245$ m. This is likely to be due to a low value of the estimated wave mass flux Q_w in that region, even though that value is determined using linear wave theory ($B_0 = 0.125$) and a contribution from the wave roller. For the longshore currents, we find that the maximum of the measured currents is clearly over the bar and not over the trough. Second, the comparison between the data and the model estimates is fairly good everywhere except at the location $x = 225$ m, just before the bar-crest. Moreover, the sled-measured longshore currents at the locations parallel to those of the gauges CM40 and CM50 ($x = 260$ and $x = 245$ m, respectively) indicate a depth-averaged value lower than that measured by those gauges (see Fig. 6.40)[7]. We also notice that the

[7] This can be an indicative of some error in the readings of those gauges too.

predicted vertical profiles compare well with the measured profiles, and both are nearly uniform along the vertical. The data shows a slightly larger variation of V along the vertical than the model, and we further notice that the currents at the second and third sensors from the bottom are systematically lower than at other positions. No explanation is found for this observation.

Last, the cross-shore variation of the magnitude of the terms in the time-averaged momentum equations along the primary cross-shore array is given in Fig. 6.43. Several important features are worth noticing. First, the convective accelerations in the longshore momentum equation are the largest terms in most regions. A more detailed analysis of the flow reveals that a partial contribution (nearly 40%) to these large values of the convective accelerations comes from the mixing induced by shear waves. However, the contribution of the steady convective acceleration is the largest (60%) of the two, which means that a seemingly small change of direction of the flow (see Fig. 6.39b) is associated with large convective accelerations. Second, we find that for this example the time-averaged longshore pressure gradient is a small term at all cross-shore locations. Finally, the dispersive mixing is also small in the y–momentum balance, but locally important in the x–momentum balance.

In conclusion, for the simulation of the 19/10/90:1221 data set the model results are consistent with the results for other periods. Due to several failures of the fixed current meters during the experiment, fewer data are available for comparison for this date. The comparison between the estimated depth-profiles of the (time-averaged) current velocities with the measured profiles from sled-mounted instruments indicates good agreement.

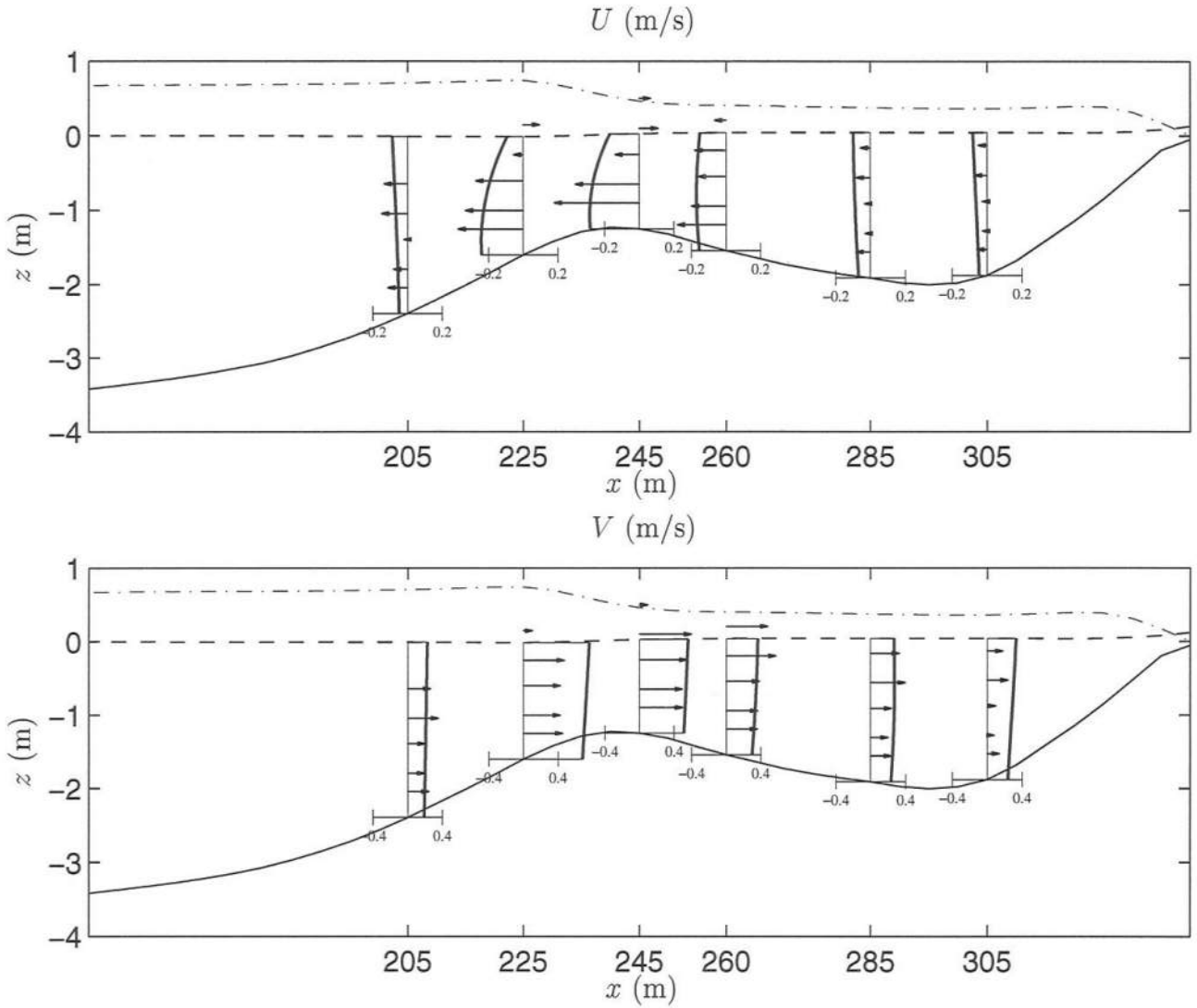

Figure 6.42: Cross-shore variation of the predicted vertical profiles (——) of U and V, versus sled-measured profiles (←—), parallel to the primary cross-shore array for the 19/10/90:1221 simulation; H_{rms} model (– ·), $\bar{\zeta}$ model (– –).

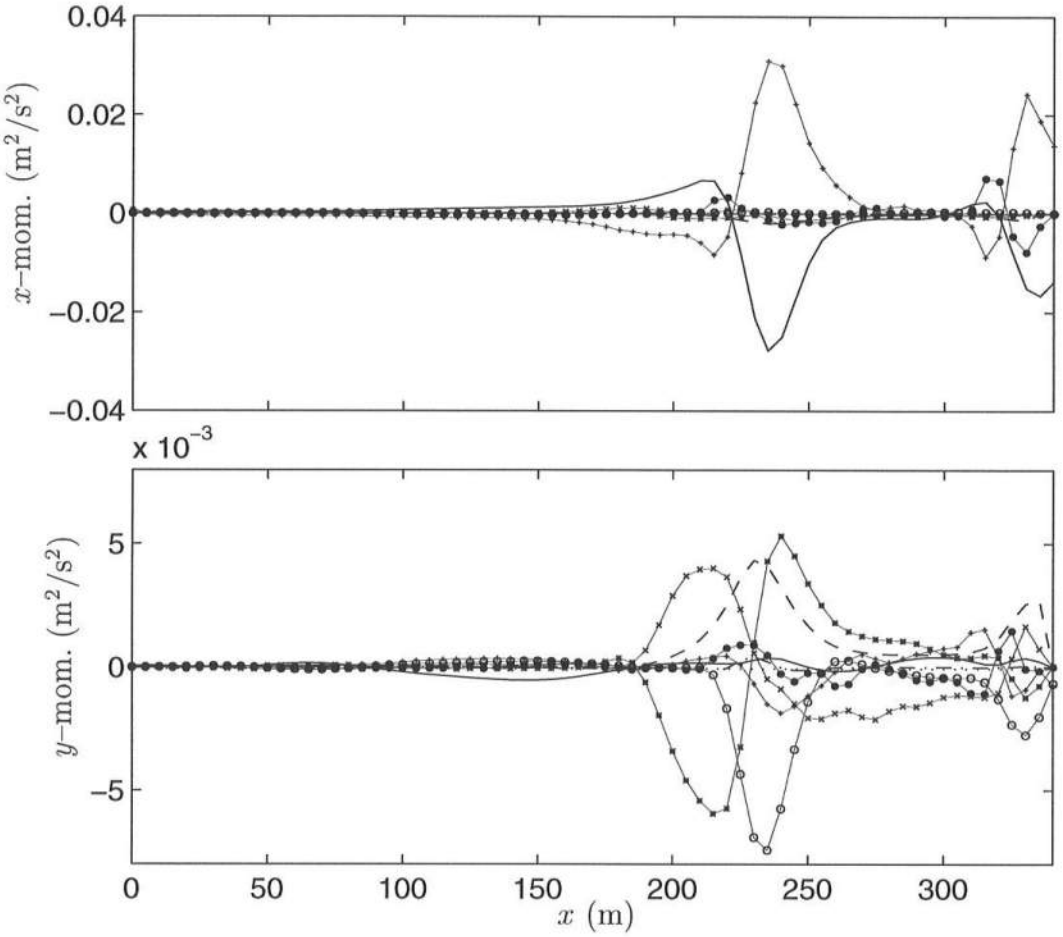

Figure 6.43: Cross-shore distribution at the primary cross-shore array of the terms in the time-averaged momentum equations for the 19/10/90:1221 simulation. Terms in the x–momentum balance: $gh\frac{\partial\bar{\zeta}}{\partial x}$ (+), $\frac{1}{\rho}\frac{\partial S_{xx}}{\partial x}$ (——), $\frac{1}{\rho}\frac{\partial S_{yx}}{\partial y}$ (○), $\overline{\frac{\partial}{\partial x}\left(\frac{\bar{Q}_x^2}{h}\right)}$ (×), $\overline{\frac{\partial}{\partial y}\left(\frac{\bar{Q}_x\bar{Q}_y}{h}\right)}$ (∗), – turb. mixing (– ·), $\frac{\tau_x^B}{\rho}$ (– –), – dispersive mixing (—●—), $\frac{\tau_x^S}{\rho}$ (. . .). Terms in the y–momentum balance: $gh\frac{\partial\bar{\zeta}}{\partial y}$ (+), $\frac{1}{\rho}\frac{\partial S_{yy}}{\partial y}$ (——), $\frac{1}{\rho}\frac{\partial S_{xy}}{\partial x}$ (○), $\overline{\frac{\partial}{\partial y}\left(\frac{\bar{Q}_y^2}{h}\right)}$ (×), $\overline{\frac{\partial}{\partial x}\left(\frac{\bar{Q}_x\bar{Q}_y}{h}\right)}$ (∗), – turb. mixing (– ·), $\frac{\tau_y^B}{\rho}$ (– –), – dispersive mixing (—●—), $\frac{\tau_y^S}{\rho}$ (. . .).

Chapter 7

CONCLUSIONS AND RECOMMENDATIONS

This thesis covers the simulation of multiple nearshore phenomena with engineering interest to the coastal community. The governing equations are derived from the conservation of mass and momentum principles, integrated over the depth and over the short-wave and turbulent motions. The turbulent Reynolds stresses are modeled using the eddy viscosity concept, which is further assumed to be constant in time and in the vertical direction. The eddy viscosity model provides a simple closure to determine analytical profiles for the vertical variation of the horizontal currents. A second closure in the model equations is provided by a nonlinear formulation for the wave-current bottom shear stress. The model equations are solved numerically using a high-order finite difference scheme, which is proven to give accurate results compared with the model of Özkan-Haller and Kirby (1997). The numerical scheme given here is implemented in a new version of the model SHORECIRC.

Svendsen and Putrevu (1994) identified a mechanism of momentum dispersion induced by the depth integration of the nonlinear terms in the horizontal momentum equations. Here we follow the procedure of Van Dongeren and Svendsen (1997b) to calculate the dispersion terms induced by the depth-varying currents. The analytical evaluation of the local vertical profiles hinges on the calculated value

for the eddy viscosity coefficient. In this work we introduced an eddy viscosity formulation which includes a contribution to the turbulent stresses from the bottom boundary layer, and one from the turbulence generated by surface breaking waves (following e.g. De Vriend and Stive, 1987). The eddy viscosity formulation is thus characterized by two free parameters C_1 and M, which are both of $\mathcal{O}(0.1)$.

We find in several applications that the vertical profiles of the horizontal currents are reasonably estimated with the chosen eddy viscosity parameterization. It appears, though, that the vertical variation of the longshore currents is slightly underestimated in several cases, which can be corrected through changes in the local eddy viscosity. The results also suggest there is a need to perform detailed physical (or field) experiments on the turbulence levels over barred beaches, both inside and outside the breaking region, in order to validate the turbulence closure in the SHORECIRC model. Nevertheless, the comparison of the modeled with the measured (during DELILAH) vertical profiles of the cross-shore and longshore currents indicates good agreement, which leads to the conclusion that the present eddy viscosity formulation seems to capture the correct variations of the turbulence in the nearshore zone.

The accuracy of the simplified longshore current model given by Putrevu *et al.* (1995) is examined against the more complete SHORECIRC model equations. It is found that the model of Putrevu *et al.* overestimates the contribution of the longshore pressure gradient for the forcing of the longshore currents over a barred beach with a small longshore bottom variation similar to a rip-channel. The mechanisms responsible for the innacuracies are analyzed and found to be due to several factors. One important factor contributing to the observed discrepancy is that the largest forces (i.e., terms) in the longshore direction are an order of magnitude smaller than the largest cross-shore forces. It is also found that including

consistently all terms up to the same order in the x- and y-momentum equations greatly improves the simplified model predictions. We conclude that the Putrevu *et al.* model is limited to extremely smoothly-varying bottom contours, and it should not be used under conditions where the basic assumptions are not strictly satisfied.

The model SHORECIRC is also applied here to examine the development and propagation of shear instabilities over a longshore uniform plane beach. Our results compare well with those of previous authors (Özkan-Haller and Kirby, 1995; Allen *et al.*, 1996), and we confirme the conclusions of the first authors that shear waves provide a mixing mechanism for the longshore currents in the surf zone. We further conclude that, contrary to the suggestion of Bowen and Holman (1989), there is not a simple relationship for the phase difference between the cross-shore and longshore velocity fluctuations (associated with the shear wave motion) calculated at the same location. This seems to limit the possibility of extracting information of the shear wave motion from phase spectra analysis of field data.

Shear waves over a barred beach are predicted for several different incident wave conditions. In a study of the currents over a longshore nonuniform barred beach with quasi longshore-uniform incident waves, it is found that shear waves can be initiated by a topographical variation in the form of a small rip-channel. In the absence of dispersive mixing the shear instabilities are very energetic and present different signatures at different cross-shore locations. The mixing provided by the shear wave motion is reduced, though, with the inclusion of the dispersive mixing (depth-varying currents) in the model equations. In the latter case we find that the shear instabilities became less energetic, exhibiting more regular wave-like variations than in the former case. In general, we conclude that the final time-averaged longshore current (cross-shore) profile is the same in the presence or absence of the dispersive mixing, due to the respective decrease or increase of the mixing provided

by the shear waves such that the total mixing is identical in both situations. It appears that a critical balance exists between the dispersive and the shear wave mixing, which is dictated by the parameters C_1 and M chosen for the eddy viscosity formulation.

For a barred beach under wave conditions such that there is a strongly longshore variability of the wave field in the neighborhood of the rip-channel the model results indicate the formation of rip-currents. Longshore currents converge to the rip-channel and "feed" the rip-currents. It is found that the largest driving force for the longshore currents in that region is the longshore gradient of the mean surface elevation. For sufficiently low values of the bottom friction coefficient and the dispersive mixing mechanism, both shear waves and meandering rip-currents are formed, suggesting that these two phenomena are "two faces" of a similar hydrodynamic instability phenomena. The meandering rip-currents oscillate at a frequency of the same order of magnitude to that of the shear waves, and release vortices that detach at times from the rip-current. We conclude that the largest terms of the (time-averaged) momentum equations along the rip-channel axis are the convective accelerations, which gives support to the mechanism for the occurrence of rip-currents discussed by Arthur (1962).

Finally, we apply the model SHORECIRC to simulate the conditions observed at certain times during the DELILAH 1990 field experiment. The comparisons between the model predictions and the data suggests that we fail to predict the large longshore current measured over the trough region for the 10th of October. The local longshore pressure gradient included in the model equations is found to be a significant term to drive the currents in that region, though it is not strong enough to justify the large measured currents. It is also found that all the terms in the longshore momentum equation are important, and thus the use of simplified

models even for nearly longshore uniform conditions may not capture some of the important mechanisms responsible for the longshore current distribution.

The possible existence of a larger scale longshore pressure gradient (such as tidally-induced or a gradient caused by differential wind-induced setup) during DELILAH is discussed, and found to be a possible driving mechanism. A second mechanism that could explain the discrepancy between the data and the model predictions is the too simplistic representation of the wave forcing provided by the wave-driver used herein (REF/DIF 1), that does not predict wave breaking in the region behind the bar crest. Real waves are random and thus the breaking location is variable, which is not modeled by the present wave-driver. The use of a nonlinear wave-driver with a proper account of the wave breaking mechanism is likely to provide a better estimate of the radiation stresses gradients and thus the wave forcing in SHORECIRC. A second, more simplistic approach, is to account for a delay in the transfer of momentum from the short waves to the mean flow in a similar fashion to that of Nairn *et al.* (1990), Smith *et al.* (1993), and others.

Despite the deficiencies mentioned above, we find that the use of the nonlinear formulation of the bottom shear stress, with a variable friction coefficient determined by the formula proposed by Swart (1974), gives the correct order of magnitude of the currents in the surf zone. We also find that the use of linear wave theory, plus a contribution of the wave-roller in the breaking region, for the estimate of the short-wave induced volume flux Q_w gives a reasonable prediction of the return current. This conclusion contradicts the accepted knowledge that the use of linear theory overestimates Q_w in the breaking region.

For all three dates simulated here of the conditions during DELILAH we predict the existence of shear wave motions. The restricted dimensions of the model domain does, however, limit the growth of shear wave energy at the lowest spatial

and time frequencies. A more extensive comparison of the shear wave regime should be possible for a larger domain. We find that the predicted shear waves contribute to the mixing for the longshore currents, and that the dispersive mixing contributes less significantly. It can also be concluded that dispersive mixing over strongly longshore-varying topographies is generally smaller than that for similar conditions over a longshore uniform beach.

Based on the conclusions of this thesis, suggestions for future work are outlined as follows:

- Improvement of the short-wave predictions in the surf zone. We recommend the use of Boussinesq-type models with a sufficiently accurate description of the wave breaking to calculate the short-wave induced mass and momentum flux. Such a wave-driver would also enable the simulation of non-stationary random waves with a variable breakpoint, which can be important for the study of field conditions.

- An alternative approach to the above method is the development of an appropriate parameterization of the wave-induced volume flux Q_w, and nondimensional radiation stress tensor $P_{\alpha\beta}$, valid in the surf zone. Such a parameterization would intrinsically include the effect of the wave roller in the breaking region.

- In this study we intentionally neglected the effect of the currents on the short-wave field. In situations where rip-currents are formed, this approximation is definitely erroneous (e.g. Birkemeier and Dalrymple, 1975). Therefore, the use of Boussinesq-type models, or the complete wave-current energy equation, to accurately predict the wave field is desired.

- We found little information on the turbulence field outside the breaking region and over barred beaches. Hence, we point out the need to perform detailed measurements of the turbulent properties of the flow for both monochromatic and random waves in order to calibrate or improve the turbulence closure used here.

- Similar suggestions apply to measure the bed shear stress in combined wave and current flows, over various regimes and bottom profiles, in order to properly estimate the bottom friction coefficient. A detailed characterization of the bed friction coefficient in the surf zone for several bottom forms is desired as well. For example, a relation for the ratio k_N/d_{50} at different cross-shore locations could be useful in estimating f_{cw}.

- Finally, it has been observed in several occasions that the beach morphology can change in a time scale of a few hours, which is equivalent to that of some of the simulations performed herein. Therefore, it can be desirable to include an equation for the conservation of sediment in the model equations, where the sediment transport rate would be related with the flow velocities.

Appendix A

FINITE DIFFERENCE CONTINUITY EQUATION

In this Appendix we put together the finite difference equations (3.13) and (3.14), which corresponds to get the finite difference form for the combined predictor and corrector steps. We show only the procedure for the continuity equation, and we suffice to mention that the same procedure is applied to get the finite difference equations for the x and y-momentum balance.

For convenience, we repeat the difference equations (3.12)–(3.13) for the predictor step

$$\bar{\zeta}^{\star}_{i,j} = \bar{\zeta}^{n}_{i,j} - \Delta t\,\alpha_0 \left(\alpha_1 \left.\frac{\partial \bar{Q}_\alpha}{\partial x_\alpha}\right|^{n}_{i,j} + \alpha_2 \left.\frac{\partial \bar{Q}_\alpha}{\partial x_\alpha}\right|^{n-1}_{i,j} + \alpha_3 \left.\frac{\partial \bar{Q}_\alpha}{\partial x_\alpha}\right|^{n-2}_{i,j} \right) , \quad \text{(A.1)}$$

$$\left.\bar{Q}_\alpha\right|^{\star}_{i,j} = \left.\bar{Q}_\alpha\right|^{n}_{i,j} - \Delta t\,\alpha_0\, g\, h_0 \left(\alpha_1 \left.\frac{\partial \bar{\zeta}}{\partial x_\alpha}\right|^{n}_{i,j} + \alpha_2 \left.\frac{\partial \bar{\zeta}}{\partial x_\alpha}\right|^{n-1}_{i,j} + \alpha_3 \left.\frac{\partial \bar{\zeta}}{\partial x_\alpha}\right|^{n-2}_{i,j} \right) , \quad \text{(A.2)}$$

and (3.14)–(3.15) for the corrector step

$$\bar{\zeta}^{n+1}_{i,j} = \bar{\zeta}^{n}_{i,j} - \Delta t\,\beta_0 \left(\beta_1 \left.\frac{\partial \bar{Q}_\alpha}{\partial x_\alpha}\right|^{\star}_{i,j} + \beta_2 \left.\frac{\partial \bar{Q}_\alpha}{\partial x_\alpha}\right|^{n}_{i,j} + \beta_3 \left.\frac{\partial \bar{Q}_\alpha}{\partial x_\alpha}\right|^{n-1}_{i,j} \right) , \quad \text{(A.3)}$$

$$\left.\bar{Q}_\alpha\right|^{n+1}_{i,j} = \left.\bar{Q}_\alpha\right|^{n}_{i,j} - \Delta t\,\beta_0\, g\, h_0 \left(\beta_1 \left.\frac{\partial \bar{\zeta}}{\partial x_\alpha}\right|^{\star}_{i,j} + \beta_2 \left.\frac{\partial \bar{\zeta}}{\partial x_\alpha}\right|^{n}_{i,j} + \beta_3 \left.\frac{\partial \bar{\zeta}}{\partial x_\alpha}\right|^{n-1}_{i,j} \right) . \quad \text{(A.4)}$$

For simplicity we will designate Q_x by Q and Q_y by P. The partial derivatives in equation (A.2) can be substituted by the difference formula (3.8). Hence, we obtain for Q

$$\begin{aligned}
\bar{Q}^{\star}_{i,j} \;=\; & \bar{Q}^{n}_{i,j} \;-\; g\, h_o\, \alpha_0\, \delta\, \frac{\Delta t}{\Delta x} \\
& \Big[\; \alpha_1 \left(\gamma_{-2}\, \bar{\zeta}^{n}_{i-2,j} \;+\; \gamma_{-1}\, \bar{\zeta}^{n}_{i-1,j} \;+\; \gamma_1\, \bar{\zeta}^{n}_{i+1,j} \;+\; \gamma_2\, \bar{\zeta}^{n}_{i+2,j}\right) \\
& + \alpha_2 \left(\gamma_{-2}\, \bar{\zeta}^{n-1}_{i-2,j} \;+\; \gamma_{-1}\, \bar{\zeta}^{n-1}_{i-1,j} \;+\; \gamma_1\, \bar{\zeta}^{n-1}_{i+1,j} \;+\; \gamma_2\, \bar{\zeta}^{n-1}_{i+2,j}\right) \\
& + \alpha_3 \left(\gamma_{-2}\, \bar{\zeta}^{n-2}_{i-2,j} \;+\; \gamma_{-1}\, \bar{\zeta}^{n-2}_{i-1,j} \;+\; \gamma_1\, \bar{\zeta}^{n-2}_{i+1,j} \;+\; \gamma_2\, \bar{\zeta}^{n-2}_{i+2,j}\right) \Big] \;, \qquad \text{(A.5)}
\end{aligned}$$

and for P

$$\begin{aligned}
\bar{P}^{\star}_{i,j} \;=\; & \bar{P}^{n}_{i,j} \;-\; g\, h_o\, \alpha_0\, \delta\, \frac{\Delta t}{\Delta y} \\
& \Big[\; \alpha_1 \left(\gamma_{-2}\, \bar{\zeta}^{n}_{i,j-2} \;+\; \gamma_{-1}\, \bar{\zeta}^{n}_{i,j-1} \;+\; \gamma_1\, \bar{\zeta}^{n}_{i,j+1} \;+\; \gamma_2\, \bar{\zeta}^{n}_{i,j+2}\right) \\
& + \alpha_2 \left(\gamma_{-2}\, \bar{\zeta}^{n-1}_{i,j-2} \;+\; \gamma_{-1}\, \bar{\zeta}^{n-1}_{i,j-1} \;+\; \gamma_1\, \bar{\zeta}^{n-1}_{i,j+1} \;+\; \gamma_2\, \bar{\zeta}^{n-1}_{i,j+2}\right) \\
& + \alpha_3 \left(\gamma_{-2}\, \bar{\zeta}^{n-2}_{i,j-2} \;+\; \gamma_{-1}\, \bar{\zeta}^{n-2}_{i,j-1} \;+\; \gamma_1\, \bar{\zeta}^{n-2}_{i,j+1} \;+\; \gamma_2\, \bar{\zeta}^{n-2}_{i,j+2}\right) \Big] \;. \qquad \text{(A.6)}
\end{aligned}$$

Equations (A.3) and (3.8) are then used to get a finite difference equation for $\bar{\zeta}^{n+1}_{i,j}$ in the corrector step, which reads:

$$\begin{aligned}
\bar{\zeta}^{n+1}_{i,j} \;=\; & \bar{\zeta}^{n}_{i,j} \;-\; \beta_0\, \delta\, \frac{\Delta t}{\Delta x} \\
& \Big[\; \beta_1 \left(\gamma_{-2}\, \bar{Q}^{\star}_{i-2,j} \;+\; \gamma_{-1}\, \bar{Q}^{\star}_{i-1,j} \;+\; \gamma_1\, \bar{Q}^{\star}_{i+1,j} \;+\; \gamma_2\, \bar{Q}^{\star}_{i+2,j}\right) \\
& + \beta_2 \left(\gamma_{-2}\, \bar{Q}^{n}_{i-2,j} \;+\; \gamma_{-1}\, \bar{Q}^{n}_{i-1,j} \;+\; \gamma_1\, \bar{Q}^{n}_{i+1,j} \;+\; \gamma_2\, \bar{Q}^{n}_{i+2,j}\right) \\
& + \beta_3 \left(\gamma_{-2}\, \bar{Q}^{n-1}_{i-2,j} \;+\; \gamma_{-1}\, \bar{Q}^{n-1}_{i-1,j} \;+\; \gamma_1\, \bar{Q}^{n-1}_{i+1,j} \;+\; \gamma_2\, \bar{Q}^{n-1}_{i+2,j}\right) \Big] \\
& - \beta_0\, \delta\, \frac{\Delta t}{\Delta y} \\
& \Big[\; \beta_1 \left(\gamma_{-2}\, \bar{P}^{\star}_{i,j-2} \;+\; \gamma_{-1}\, \bar{P}^{\star}_{i,j-1} \;+\; \gamma_1\, \bar{P}^{\star}_{i,j+1} \;+\; \gamma_2\, \bar{P}^{\star}_{i,j+2}\right) \\
& + \beta_2 \left(\gamma_{-2}\, \bar{P}^{n}_{i,j-2} \;+\; \gamma_{-1}\, \bar{P}^{n}_{i,j-1} \;+\; \gamma_1\, \bar{P}^{n}_{i,j+1} \;+\; \gamma_2\, \bar{P}^{n}_{i,j+2}\right) \\
& + \beta_3 \left(\gamma_{-2}\, \bar{P}^{n-1}_{i,j-2} \;+\; \gamma_{-1}\, \bar{P}^{n-1}_{i,j-1} \;+\; \gamma_1\, \bar{P}^{n-1}_{i,j+1} \;+\; \gamma_2\, \bar{P}^{n-1}_{i,j+2}\right) \Big] \;. \qquad \text{(A.7)}
\end{aligned}$$

We can now insert the values of $\bar{Q}^{\star}$ and $\bar{P}^{\star}$ determined by equations (A.5) and (A.6) at the various grid positions (i,j) into equation (A.7) for $\bar{\zeta}_{i,j}^{n+1}$. This step gives the combined predictor-corrector continuity equation, which contains the unknown $\bar{\zeta}_{i,j}^{n+1}$ on the LHS and all known quantities on the RHS:

$$
\begin{aligned}
\bar{\zeta}_{i,j}^{n+1} \;=\;& \bar{\zeta}_{i,j}^{n} \;-\; \beta_0\,\delta\,\frac{\Delta t}{\Delta x} \\
& \Big\{ \;\beta_1\,\gamma_{-2}\,\big[\;\bar{Q}_{i-2,j}^{n} \;-\; g\,h_o\,\alpha_0\,\delta\,\frac{\Delta t}{\Delta x} \\
& \quad \{\;\alpha_1\,\big(\gamma_{-2}\,\bar{\zeta}_{i-4,j}^{n} \;+\; \gamma_{-1}\,\bar{\zeta}_{i-3,j}^{n} \;+\; \gamma_1\,\bar{\zeta}_{i-1,j}^{n} \;+\; \gamma_2\,\bar{\zeta}_{i,j}^{n}\big) \\
& \quad +\alpha_2\,\big(\gamma_{-2}\,\bar{\zeta}_{i-4,j}^{n-1} \;+\; \gamma_{-1}\,\bar{\zeta}_{i-3,j}^{n-1} \;+\; \gamma_1\,\bar{\zeta}_{i-1,j}^{n-1} \;+\; \gamma_2\,\bar{\zeta}_{i,j}^{n-1}\big) \\
& \quad +\alpha_3\,\big(\gamma_{-2}\,\bar{\zeta}_{i-4,j}^{n-2} \;+\; \gamma_{-1}\,\bar{\zeta}_{i-3,j}^{n-2} \;+\; \gamma_1\,\bar{\zeta}_{i-1,j}^{n-2} \;+\; \gamma_2\,\bar{\zeta}_{i,j}^{n-2}\big)\;\}\;\big] \\
+\;& \beta_1\,\gamma_{-1}\,\big[\;\bar{Q}_{i-1,j}^{n} \;-\; g\,h_o\,\alpha_0\,\delta\,\frac{\Delta t}{\Delta x} \\
& \quad \{\;\alpha_1\,\big(\gamma_{-2}\,\bar{\zeta}_{i-3,j}^{n} \;+\; \gamma_{-1}\,\bar{\zeta}_{i-2,j}^{n} \;+\; \gamma_1\,\bar{\zeta}_{i,j}^{n} \;+\; \gamma_2\,\bar{\zeta}_{i+1,j}^{n}\big) \\
& \quad +\alpha_2\,\big(\gamma_{-2}\,\bar{\zeta}_{i-3,j}^{n-1} \;+\; \gamma_{-1}\,\bar{\zeta}_{i-2,j}^{n-1} \;+\; \gamma_1\,\bar{\zeta}_{i,j}^{n-1} \;+\; \gamma_2\,\bar{\zeta}_{i+1,j}^{n-1}\big) \\
& \quad +\alpha_3\,\big(\gamma_{-2}\,\bar{\zeta}_{i-3,j}^{n-2} \;+\; \gamma_{-1}\,\bar{\zeta}_{i-2,j}^{n-2} \;+\; \gamma_1\,\bar{\zeta}_{i,j}^{n-2} \;+\; \gamma_2\,\bar{\zeta}_{i+1,j}^{n-2}\big)\;\}\;\big] \\
+\;& \beta_1\,\gamma_{1}\,\big[\;\bar{Q}_{i+1,j}^{n} \;-\; g\,h_o\,\alpha_0\,\delta\,\frac{\Delta t}{\Delta x} \\
& \quad \{\;\alpha_1\,\big(\gamma_{-2}\,\bar{\zeta}_{i-1,j}^{n} \;+\; \gamma_{-1}\,\bar{\zeta}_{i,j}^{n} \;+\; \gamma_1\,\bar{\zeta}_{i+2,j}^{n} \;+\; \gamma_2\,\bar{\zeta}_{i+3,j}^{n}\big) \\
& \quad +\alpha_2\,\big(\gamma_{-2}\,\bar{\zeta}_{i-1,j}^{n-1} \;+\; \gamma_{-1}\,\bar{\zeta}_{i,j}^{n-1} \;+\; \gamma_1\,\bar{\zeta}_{i+2,j}^{n-1} \;+\; \gamma_2\,\bar{\zeta}_{i+3,j}^{n-1}\big) \\
& \quad +\alpha_3\,\big(\gamma_{-2}\,\bar{\zeta}_{i-1,j}^{n-2} \;+\; \gamma_{-1}\,\bar{\zeta}_{i,j}^{n-2} \;+\; \gamma_1\,\bar{\zeta}_{i+2,j}^{n-2} \;+\; \gamma_2\,\bar{\zeta}_{i+3,j}^{n-2}\big)\;\}\;\big] \\
+\;& \beta_1\,\gamma_{2}\,\big[\;\bar{Q}_{i+2,j}^{n} \;-\; g\,h_o\,\alpha_0\,\delta\,\frac{\Delta t}{\Delta x} \\
& \quad \{\;\alpha_1\,\big(\gamma_{-2}\,\bar{\zeta}_{i,j}^{n} \;+\; \gamma_{-1}\,\bar{\zeta}_{i+1,j}^{n} \;+\; \gamma_1\,\bar{\zeta}_{i+3,j}^{n} \;+\; \gamma_2\,\bar{\zeta}_{i+4,j}^{n}\big) \\
& \quad +\alpha_2\,\big(\gamma_{-2}\,\bar{\zeta}_{i,j}^{n-1} \;+\; \gamma_{-1}\,\bar{\zeta}_{i+1,j}^{n-1} \;+\; \gamma_1\,\bar{\zeta}_{i+3,j}^{n-1} \;+\; \gamma_2\,\bar{\zeta}_{i+4,j}^{n-1}\big) \\
& \quad +\alpha_3\,\big(\gamma_{-2}\,\bar{\zeta}_{i,j}^{n-2} \;+\; \gamma_{-1}\,\bar{\zeta}_{i+1,j}^{n-2} \;+\; \gamma_1\,\bar{\zeta}_{i+3,j}^{n-2} \;+\; \gamma_2\,\bar{\zeta}_{i+4,j}^{n-2}\big)\;\}\;\big] \\
+\;& \beta_2\,\big(\gamma_{-2}\,\bar{Q}_{i-2,j}^{n} \;+\; \gamma_{-1}\,\bar{Q}_{i-1,j}^{n} \;+\; \gamma_1\,\bar{Q}_{i+1,j}^{n} \;+\; \gamma_2\,\bar{Q}_{i+2,j}^{n}\big) \\
+\;& \beta_3\,\big(\gamma_{-2}\,\bar{Q}_{i-2,j}^{n-1} \;+\; \gamma_{-1}\,\bar{Q}_{i-1,j}^{n-1} \;+\; \gamma_1\,\bar{Q}_{i+1,j}^{n-1} \;+\; \gamma_2\,\bar{Q}_{i+2,j}^{n-1}\big)\;\Big\} \\
-\;& \beta_0\,\delta\,\frac{\Delta t}{\Delta y}
\end{aligned}
$$

$$
\begin{aligned}
\Big\{ \quad & \beta_1\,\gamma_{-2}\,\Big[\;\bar{P}^{n}_{i,j-2} \;-\; g\,h_o\,\alpha_0\,\delta\,\frac{\Delta t}{\Delta y} \\
& \{\;\alpha_1\left(\gamma_{-2}\,\bar{\zeta}^{n}_{i,j-4} + \gamma_{-1}\,\bar{\zeta}^{n}_{i,j-3} + \gamma_1\,\bar{\zeta}^{n}_{i,j-1} + \gamma_2\,\bar{\zeta}^{n}_{i,j}\right) \\
& +\alpha_2\left(\gamma_{-2}\,\bar{\zeta}^{n-1}_{i,j-4} + \gamma_{-1}\,\bar{\zeta}^{n-1}_{i,j-3} + \gamma_1\,\bar{\zeta}^{n-1}_{i,j-1} + \gamma_2\,\bar{\zeta}^{n-1}_{i,j}\right) \\
& +\alpha_3\left(\gamma_{-2}\,\bar{\zeta}^{n-2}_{i,j-4} + \gamma_{-1}\,\bar{\zeta}^{n-2}_{i,j-3} + \gamma_1\,\bar{\zeta}^{n-2}_{i,j-1} + \gamma_2\,\bar{\zeta}^{n-2}_{i,j}\right)\;\}\;\Big] \\
+ \quad & \beta_1\,\gamma_{-1}\,\Big[\;\bar{P}^{n}_{i,j-1} \;-\; g\,h_o\,\alpha_0\,\delta\,\frac{\Delta t}{\Delta y} \\
& \{\;\alpha_1\left(\gamma_{-2}\,\bar{\zeta}^{n}_{i,j-3} + \gamma_{-1}\,\bar{\zeta}^{n}_{i,j-2} + \gamma_1\,\bar{\zeta}^{n}_{i,j} + \gamma_2\,\bar{\zeta}^{n}_{i,j+1}\right) \\
& +\alpha_2\left(\gamma_{-2}\,\bar{\zeta}^{n-1}_{i,j-3} + \gamma_{-1}\,\bar{\zeta}^{n-1}_{i,j-2} + \gamma_1\,\bar{\zeta}^{n-1}_{i,j} + \gamma_2\,\bar{\zeta}^{n-1}_{i,j+1}\right) \\
& +\alpha_3\left(\gamma_{-2}\,\bar{\zeta}^{n-2}_{i,j-3} + \gamma_{-1}\,\bar{\zeta}^{n-2}_{i,j-2} + \gamma_1\,\bar{\zeta}^{n-2}_{i,j} + \gamma_2\,\bar{\zeta}^{n-2}_{i,j+1}\right)\;\}\;\Big] \\
+ \quad & \beta_1\,\gamma_{1}\,\Big[\;\bar{P}^{n}_{i,j+1} \;-\; g\,h_o\,\alpha_0\,\delta\,\frac{\Delta t}{\Delta y} \\
& \{\;\alpha_1\left(\gamma_{-2}\,\bar{\zeta}^{n}_{i,j-1} + \gamma_{-1}\,\bar{\zeta}^{n}_{i,j} + \gamma_1\,\bar{\zeta}^{n}_{i,j+2} + \gamma_2\,\bar{\zeta}^{n}_{i,j+3}\right) \\
& +\alpha_2\left(\gamma_{-2}\,\bar{\zeta}^{n-1}_{i,j-1} + \gamma_{-1}\,\bar{\zeta}^{n-1}_{i,j} + \gamma_1\,\bar{\zeta}^{n-1}_{i,j+2} + \gamma_2\,\bar{\zeta}^{n-1}_{i,j+3}\right) \\
& +\alpha_3\left(\gamma_{-2}\,\bar{\zeta}^{n-2}_{i,j-1} + \gamma_{-1}\,\bar{\zeta}^{n-2}_{i,j} + \gamma_1\,\bar{\zeta}^{n-2}_{i,j+2} + \gamma_2\,\bar{\zeta}^{n-2}_{i,j+3}\right)\;\}\;\Big] \\
+ \quad & \beta_1\,\gamma_{2}\,\Big[\;\bar{P}^{n}_{i,j+2} \;-\; g\,h_o\,\alpha_0\,\delta\,\frac{\Delta t}{\Delta y} \\
& \{\;\alpha_1\left(\gamma_{-2}\,\bar{\zeta}^{n}_{i,j} + \gamma_{-1}\,\bar{\zeta}^{n}_{i,j+1} + \gamma_1\,\bar{\zeta}^{n}_{i,j+3} + \gamma_2\,\bar{\zeta}^{n}_{i,j+4}\right) \\
& +\alpha_2\left(\gamma_{-2}\,\bar{\zeta}^{n-1}_{i,j} + \gamma_{-1}\,\bar{\zeta}^{n-1}_{i,j+1} + \gamma_1\,\bar{\zeta}^{n-1}_{i,j+3} + \gamma_2\,\bar{\zeta}^{n-1}_{i,j+4}\right) \\
& +\alpha_3\left(\gamma_{-2}\,\bar{\zeta}^{n-2}_{i,j} + \gamma_{-1}\,\bar{\zeta}^{n-2}_{i,j+1} + \gamma_1\,\bar{\zeta}^{n-2}_{i,j+3} + \gamma_2\,\bar{\zeta}^{n-2}_{i,j+4}\right)\;\}\;\Big] \\
+ \quad & \beta_2\left(\gamma_{-2}\,\bar{P}^{n}_{i,j-2} + \gamma_{-1}\,\bar{P}^{n}_{i,j-1} + \gamma_1\,\bar{P}^{n}_{i,j+1} + \gamma_2\,\bar{P}^{n}_{i,j+2}\right) \\
+ \quad & \beta_3\left(\gamma_{-2}\,\bar{P}^{n-1}_{i,j-2} + \gamma_{-1}\,\bar{P}^{n-1}_{i,j-1} + \gamma_1\,\bar{P}^{n-1}_{i,j+1} + \gamma_2\,\bar{P}^{n-1}_{i,j+2}\right)\Big\}\,. \qquad \text{(A.8)}
\end{aligned}
$$

This equation is utilized in Chapter 3 to obtain the amplification matrix to find the stability limits of the numerical scheme.

Appendix B

AMPLIFICATION MATRIX FOR THE STABILITY ANALYSIS OF THE FINITE DIFFERENCE SCHEME

In this Appendix we present the coefficients of the amplification matrix $\mathbf{G}$ given by equation (3.25) in Section 3.2. This matrix is repeated here for convenience:

$$\mathbf{G} = \begin{pmatrix} g_{11} & g_{12} & g_{13} & g_{14} & g_{15} & g_{16} & g_{17} & 0 & 0 \\ g_{21} & g_{22} & g_{23} & g_{24} & g_{25} & g_{26} & 0 & g_{28} & g_{29} \\ g_{31} & g_{32} & g_{33} & g_{34} & g_{35} & g_{36} & 0 & g_{38} & g_{39} \\ 1 & 0 & 0 & 0 & 0 & 0 & 0 & 0 & 0 \\ 0 & 1 & 0 & 0 & 0 & 0 & 0 & 0 & 0 \\ 0 & 0 & 1 & 0 & 0 & 0 & 0 & 0 & 0 \\ 0 & 0 & 0 & 1 & 0 & 0 & 0 & 0 & 0 \\ 0 & 0 & 0 & 0 & 1 & 0 & 0 & 0 & 0 \\ 0 & 0 & 0 & 0 & 0 & 1 & 0 & 0 & 0 \end{pmatrix} . \tag{B.1}$$

In order to write the matrix coefficients it is convenient to define

$$\begin{aligned} s_1 &= \gamma_{-2}\, e^{-4\,\theta_1} + \gamma_{-1}\, e^{-3\,\theta_1} + \gamma_1\, e^{-\,\theta_1} + \gamma_2\,, \\ s_2 &= \gamma_{-2}\, e^{-3\,\theta_1} + \gamma_{-1}\, e^{-2\,\theta_1} + \gamma_1 + \gamma_2\, e^{\theta_1}\,, \\ s_3 &= \gamma_{-2}\, e^{-\,\theta_1} + \gamma_{-1} + \gamma_1\, e^{2\,\theta_1} + \gamma_2\, e^{3\,\theta_1}\,, \\ s_4 &= \gamma_{-2} + \gamma_{-1}\, e^{\theta_1} + \gamma_1\, e^{3\,\theta_1} + \gamma_2\, e^{4\,\theta_1}\,, \end{aligned}$$

and

$$
\begin{aligned}
r_1 &= \gamma_{-2}\, e^{-4\,\theta_2} + \gamma_{-1}\, e^{-3\,\theta_2} + \gamma_1\, e^{-\theta_2} + \gamma_2\,, \\
r_2 &= \gamma_{-2}\, e^{-3\,\theta_2} + \gamma_{-1}\, e^{-2\,\theta_2} + \gamma_1 + \gamma_2\, e^{\theta_2}\,, \\
r_3 &= \gamma_{-2}\, e^{-\theta_2} + \gamma_{-1} + \gamma_1\, e^{2\,\theta_2} + \gamma_2\, e^{3\,\theta_2}\,, \\
r_4 &= \gamma_{-2} + \gamma_{-1}\, e^{\theta_2} + \gamma_1\, e^{3\,\theta_2} + \gamma_2\, e^{4\,\theta_2}\,,
\end{aligned}
$$

where $\gamma_{-2}, \gamma_{-1}, \gamma_1, \gamma_2$ are given by equation (3.9), and θ_1 and θ_2 are defined by (3.20).

Using the coefficients $\alpha_k, \beta_k, \delta$ defined by the equalities (3.3), (3.5) and (3.9), the coefficients of the amplification matrix are then given by

$$
\begin{aligned}
g_{11} &= 1 + \beta_0\,\alpha_0\,\delta^2\,\beta_1\,\alpha_1\,\nu_1^2\,(\gamma_{-2}\,s_1 + \gamma_{-1}\,s_2 + \gamma_1\,s_3 + \gamma_2\,s_4) \\
&+ \beta_0\,\alpha_0\,\delta^2\,\beta_1\,\alpha_1\,\nu_2^2\,(\gamma_{-2}\,r_1 + \gamma_{-1}\,r_2 + \gamma_1\,r_3 + \gamma_2\,r_4)
\end{aligned}
$$

$$
g_{12} = -\,\beta_0\,\delta\,\frac{\nu_1}{c_0}\,(\beta_1 + \beta_2)\left(\gamma_{-2}\,e^{-2\,\theta_1} + \gamma_{-1}\,e^{-\theta_1} + \gamma_1\,e^{\theta_1} + \gamma_2\,e^{2\,\theta_1}\right)
$$

$$
g_{13} = -\,\beta_0\,\delta\,\frac{\nu_2}{c_0}\,(\beta_1 + \beta_2)\left(\gamma_{-2}\,e^{-2\,\theta_2} + \gamma_{-1}\,e^{-\theta_2} + \gamma_1\,e^{\theta_2} + \gamma_2\,e^{2\,\theta_2}\right)
$$

$$
\begin{aligned}
g_{14} &= \beta_0\,\alpha_0\,\delta^2\,\beta_1\,\alpha_2\,\nu_1^2\,(\gamma_{-2}\,s_1 + \gamma_{-1}\,s_2 + \gamma_1\,s_3 + \gamma_2\,s_4) \\
&+ \beta_0\,\alpha_0\,\delta^2\,\beta_1\,\alpha_2\,\nu_2^2\,(\gamma_{-2}\,r_1 + \gamma_{-1}\,r_2 + \gamma_1\,r_3 + \gamma_2\,r_4)
\end{aligned}
$$

$$
g_{15} = -\,\beta_0\,\delta\,\frac{\nu_1}{c_0}\,\beta_3\left(\gamma_{-2}\,e^{-2\,\theta_1} + \gamma_{-1}\,e^{-\theta_1} + \gamma_1\,e^{\theta_1} + \gamma_2\,e^{2\,\theta_1}\right)
$$

$$
g_{16} = -\,\beta_0\,\delta\,\frac{\nu_2}{c_0}\,\beta_3\left(\gamma_{-2}\,e^{-2\,\theta_2} + \gamma_{-1}\,e^{-\theta_2} + \gamma_1\,e^{\theta_2} + \gamma_2\,e^{2\,\theta_2}\right)
$$

$$
g_{17} = \beta_0\,\alpha_0\,\delta^2\,\beta_1\,\alpha_3\,\nu_1^2\,(\gamma_{-2}\,s_1 + \gamma_{-1}\,s_2 + \gamma_1\,s_3 + \gamma_2\,s_4)
$$

$$+ \quad \beta_0\,\alpha_0\,\delta^2\,\beta_1\,\alpha_3\,\nu_2^2\,(\gamma_{-2}\,r_1 \,+\, \gamma_{-1}\,r_2 \,+\, \gamma_1\,r_3 \,+\, \gamma_2\,r_4)$$

$$g_{21} \;=\; g\,h_o\,g_{12}$$

$$g_{22} \;=\; g_{11}$$

$$g_{23} \;=\; \beta_0\,\alpha_0\,\delta^2\,\beta_1\,\alpha_1\,\nu_1\,\nu_2\,(\gamma_{-2}\,r_1 \,+\, \gamma_{-1}\,r_2 \,+\, \gamma_1\,r_3 \,+\, \gamma_2\,r_4)$$

$$g_{24} \;=\; g\,h_o\,g_{15}$$

$$g_{25} \;=\; \beta_0\,\alpha_0\,\delta^2\,\beta_1\,\alpha_2\,\nu_1^2\,(\gamma_{-2}\,s_1 \,+\, \gamma_{-1}\,s_2 \,+\, \gamma_1\,s_3 \,+\, \gamma_2\,s_4)$$

$$g_{26} \;=\; \beta_0\,\alpha_0\,\delta^2\,\beta_1\,\alpha_2\,\nu_1\,\nu_2\,(\gamma_{-2}\,r_1 \,+\, \gamma_{-1}\,r_2 \,+\, \gamma_1\,r_3 \,+\, \gamma_2\,r_4)$$

$$g_{28} \;=\; \beta_0\,\alpha_0\,\delta^2\,\beta_1\,\alpha_3\,\nu_1^2\,(\gamma_{-2}\,s_1 \,+\, \gamma_{-1}\,s_2 \,+\, \gamma_1\,s_3 \,+\, \gamma_2\,s_4)$$

$$g_{29} \;=\; \beta_0\,\alpha_0\,\delta^2\,\beta_1\,\alpha_3\,\nu_1\,\nu_2\,(\gamma_{-2}\,r_1 \,+\, \gamma_{-1}\,r_2 \,+\, \gamma_1\,r_3 \,+\, \gamma_2\,r_4)$$

$$g_{31} \;=\; g\,h_o\,g_{13}$$

$$g_{32} \;=\; \beta_0\,\alpha_0\,\delta^2\,\beta_1\,\alpha_1\,\nu_1\,\nu_2\,(\gamma_{-2}\,s_1 \,+\, \gamma_{-1}\,s_2 \,+\, \gamma_1\,s_3 \,+\, \gamma_2\,s_4)$$

$$g_{33} \;=\; g_{11}$$

$$g_{34} = g\, h_o\, g_{16}$$

$$g_{35} = \beta_0\, \alpha_0\, \delta^2\, \beta_1\, \alpha_2\, \nu_1\, \nu_2\, (\gamma_{-2}\, s_1 + \gamma_{-1}\, s_2 + \gamma_1\, s_3 + \gamma_2\, s_4)$$

$$g_{36} = \beta_0\, \alpha_0\, \delta^2\, \beta_1\, \alpha_2\, \nu_1^2\, (\gamma_{-2}\, r_1 + \gamma_{-1}\, r_2 + \gamma_1\, r_3 + \gamma_2\, r_4)$$

$$g_{38} = \beta_0\, \alpha_0\, \delta^2\, \beta_1\, \alpha_3\, \nu_1\, \nu_2\, (\gamma_{-2}\, s_1 + \gamma_{-1}\, s_2 + \gamma_1\, s_3 + \gamma_2\, s_4)$$

$$g_{39} = \beta_0\, \alpha_0\, \delta^2\, \beta_1\, \alpha_3\, \nu_1^2\, (\gamma_{-2}\, r_1 + \gamma_{-1}\, r_2 + \gamma_1\, r_3 + \gamma_2\, r_4)$$

BIBLIOGRAPHY

Allen, J., P. A. Newberber, and R. A. Holman (1996). Nonlinear shear instabilities of alongshore currents on plane beaches. *J. Fluid Mech.* (310), 181–213.

Allender, J. H., J. D. Ditmars, W. Harrison, and R. A. Paddock (1978). Comparison of model and observed nearshore circulation. In *Proc. 16th Int. Conf. Coastal Engng.*, Vol. 1, Hamburg, 810–827. ASCE.

Arthur, R. S. (1962). A note on the dynamics of rip-currents. *J. Geophys. Res. 67*(7), 2777–2779.

Banner, M. L. and O. M. Phillips (1974). On the incipient breaking of small scale waves. *J. Fluid Mech.* (65), 647–656.

Battjes, J. A. (1975). Modeling of turbulence in the surf zone. In *Proc. Symp. on Modelling Techniques*, San Francisco, 1050–1061.

Battjes, J. A. (1983). Surfzone turbulence. In *Proc. Symp. on Hydrodynamics of Waves in Coastal Areas*, Moscow, 137–140. IAHR.

Battjes, J. A. (1988). Surf-zone dynamics. *Ann. Rev. Fluid Mech.* (20), 257–293.

Bijker, E. W. (1967). Some considerations about scales for coastal models with movable bed. Publication No. 50, Delft Hydraulics Lab.

Birkemeier, W. A. and R. A. Dalrymple (1975). Nearshore water circulation induced by wind and waves. In *Proc. Symp. on Modelling Techniques*, San Francisco, 1062–1081.

Birkemeier, W. A., C. Donoghue, C. E. Long, K. K. Hathaway, and C. Baron (1997). 1990 DELILAH nearshore experiment: summary report. Technical Report CHL-97-24, U.S. Army Corps of Engineers, Waterways Experiment Station.

Bowen, A. J. (1969a). The generation of longshore currents on a plane beach. *J. Marine Res.* (27), 206–215.

Bowen, A. J. (1969b). Rip currents. 1-theoretical investigations. *J. Geophys. Res. 74*(23), 5467–5478.

Bowen, A. J. and R. A. Holman (1989). Shear instabilities in the mean longshore current: 1-theory. *J. Geophys. Res. 94*(C12), 18023–18030.

Bowen, A. J., D. L. Inman, and V. P. Simmons (1968). Wave set-down and set-up. *J. Geophys. Res. 73*(8), 2569–2577.

Brocchini, M. (1996). Flows with freely moving boundaries: the swash zone and turbulence at a free surface. Ph. d. dissertation, School of Mathematics, University of Bristol.

Brocchini, M. and D. H. Peregrine (1996). Integral flow properties of the swash zone and averaging. *J. Fluid Mech.* (317), 241–273.

Chawla, A., H. T. Özkan Haller, and J. T. Kirby (1997). Spectral model for wave transformation and breaking over irregular bathymetry. Submitted to *J. of Waterway, Port, Coastal and Ocean Engng.*.

Christensen, E. D., R. Deigaard, and J. Fredsœ(1994). Sea bed stability on a long straight coast. In *Proc. 24th Int. Conf. Coastal Engng.*, Vol. 2, Kobe, 1865–1879. ASCE.

Christoffersen, J. B. and I. G. Jonsson (1985). Bed friction and dissipation in a combined current and wave motion. *Ocean Engng. 12*(5), 387–423.

Church, J. C. and E. B. Thornton (1993). Effects of breaking wave induced turbulence within a longshore current model. *Coastal Engng. 20*, 1–28.

Church, J. C., E. B. Thornton, and J. Oltman-Shay (1992). Mixing by shear instabilities of the longshore current. In *Proc. 23rd Int. Conf. Coastal Engng.*, Vol. 3, Venice, 2999–3011. ASCE.

Clarke, A. J. and D. S. Battisti (1981). The effect of continental shelves on tides. *Deep-Sea Res. 28A*(7), 665–682.

Coffey, F. C. and P. Nielsen (1984). Aspects of wave current boundary layer flows. In *Proc. 19th Int. Conf. Coastal Engng.*, Vol. 3, Houston, 2232–2245. ASCE.

Cox, D. T., N. Kobayashi, and A. Okayasu (1995). Experimental and numerical modeling of surf zone hydrodynamics. (Ph. D. Dissertation) Res. Report CACR-95-07, Center for Applied Coastal Research, Univ. of Delaware.

Dally, W. R. and R. G. Dean (1986). Mass flux and undertow in a surf zone, by I. A. Svendsen – Discussion. *Coastal Engng. 10*, 289–299.

Dalrymple, R. A. (1978). Rip currents and their causes. In *Proc. 16th Int. Conf. Coastal Engng.*, Vol. 2, Hamburg, 1414–1427. ASCE.

Davies, A. M. (1987). On extracting current profiles from vertically integrated numerical models. *Coastal Engng. 11*, 445–477.

De Vriend, H. J. and M. J. F. Stive (1987). Quasi-3d modelling of nearshore currents. *Coastal Engng. 11*, 565–601.

Deigaard, R., E. D. Christensen, J. S. Damgaard, and J. Fredsœ(1994). Numerical simulation of finite amplitude shear waves and sediment transport. In *Proc. 24th Int. Conf. Coastal Engng.*, Vol. 2, Kobe, 1919–1933. ASCE.

Dingemans, M. W., A. C. Radder, and H. J. De Vriend (1987). Computation of the driving forces of wave-induced currents. *Coastal Engng. 11*, 539–563.

Dodd, N., J. Oltman-Shay, and E. B. Thornton (1992). Shear instabilities in the longshore current: A comparison of observation and theory. *J. Phys. Oceanogr. 22*(1), 62–82.

Drazin, P. G. and W. H. Reid (1982). *Hydrodynamic stability.* Cambridge: Cambridge University Press. pp. 527.

Elder, J. W. (1959). The dispersion of marked fluid in turbulent shear flow. *J. Fluid Mech. 5*, 544–560.

Falqués, A., A. Montoto, and V. Iranzo (1996). Coastal morphodynamic instabilities. In *Proc. 25th Int. Conf. Coastal Engng.*, Vol. 3, Orlando, 3560–3573. ASCE.

Feddersen, F., R. T. Guza, S. Elgar, and T. H. C. Herbers (1996). Cross-shore structure of longshore currents during duck94. In *Proc. 25th Int. Conf. Coastal Engng.*, Vol. 3, Orlando, 3666–3679. ASCE.

Galvin, C. J. and P. S. Eagleson (1965). Experimental study of longshore currents on a plane beach. Technical Memo 10, U.S. Army Coastal Engng. Research Center.

Garcez Faria, A. F., E. B. Thornton, and T. P. Stanton (1995). A quasi-3D model of longshore currents. In *Coastal Dynamics'95*, Gdansk, 389–400. ASCE.

Garcez Faria, A. F., E. B. Thornton, and T. P. Stanton (1996a). A review of the undertow problem using field data. In *Proc. Amer. Geophys. Union, Fall Meeting*, S. Francisco, F421. AGU.

Garcez Faria, A. F., E. B. Thornton, and T. P. Stanton (1996b). Small-scale morphology related to wave and current parameters over a barred beach. In *Proc. 25th Int. Conf. Coastal Engng.*, Vol. 3, Orlando, 3391–3404. ASCE.

George, R., R. E. Flick, and R. T. Guza (1994). Observations of turbulence in the surf zone. *J. Geophys. Res. 99*(C1), 801–810.

Greenwood, B. and D. J. Sherman (1986). Longshore current profiles and lateral mixing across the surfzone on a barred nearshore. *Coastal Engng. 10*, 149–168.

Haller, M. C., R. A. Dalrymple, and I. A. Svendsen (1997). Rip channels and nearshore circulation. In *Coastal Dynamics'97*, Plymouth, in press. ASCE.

Hansen, J. B. (1990). Periodic waves in the surf zone: analysis of experimental data. *Coastal Engng. 14*, 19–41.

Hattori, M. and T. Aono (1985). Experimental study on turbulence under spilling breakers. In Y. Toba and H. Mitsuyasu (Eds.), *The Ocean Surface*, Hingham, Mass., 419–424. D. Reidel Publishing Company.

Hino, M. (1974). Theory on formation of rip-current and cuspidal coast. In *Proc. 14th Int. Conf. Coastal Engng.*, Vol. 1, Copenhagen, 901–919. ASCE.

Hoffman, J. D. (1992). *Numerical methods for engineers and scientists.* New York: McGraw-Hill, Inc. pp. 825.

Jin, X., N. Booij, and C. Kranenburg (1991). A coupled Quasi-3D numerical model of circulations in shallow waters. In *Proc. 24th IAHR Conf.*, Vol. B, Madrid, 271–280. IAHR.

Jonsson, I. G. (1966). Wave boundary layers and friction factors. In *Proc. 10th Int. Conf. Coastal Engng.*, Vol. 1, Tokyo, 127–148. ASCE.

Jonsson, I. G., O. Skovgaard, and T. S. Jacobsen (1974). Computation of longshore currents. In *Proc. 14th Int. Conf. Coastal Engng.*, Vol. 2, Copenhagen, 699–714. ASCE.

Kamphuis, J. W. (1975). Friction factors under oscillatory waves. *J. of Waterways, Harbors, and Coastal Engng. WW2*(10), 135–144.

Karjadi, E. A. and N. Kobayashi (1996). Time-dependent Quasi-3d modeling of breaking waves on beaches. In *Proc. 25th Int. Conf. Coastal Engng.*, Vol. 1, Orlando, 233–246. ASCE.

Kirby, J. T. and R. A. Dalrymple (1983). A parabolic equation for the combined refraction-diffraction of stokes waves by mildly varying topography. *J. Fluid Mech. 136*, 543–566.

Kirby, J. T. and R. A. Dalrymple (1994). Combined refraction/diffraction model REF/DIF1, Version 2.5. Res. Report CACR-94-22, Center for Applied Coastal Research, Univ. of Delaware.

Kobayashi, N., E. A. Karjadi, and B. D. Johnson (1997). Dispersion effects on longshore currents in surf zones. *J. of Waterway, Port, Coastal and Ocean Engng. 123*(5), 240–248.

Lapidus, L. and G. F. Pinder (1982). *Numerical solution of partial differencial equations in science and engineering.* New York: John Wiley & Sons, Inc. pp. 677.

Larson, M. and N. C. Kraus (1991). Numerical model of longshore current for bar and trough beaches. *J. Waterway Port Coastal and Ocean Eng. 117*(4), 326–347.

Lippmann, T. C. and R. A. Holman (1989). Quantification of sand bar morphology: A video technique based on wave dissipation. *J. Geophys. Res. 94*, 995–1011.

Liu, P. L.-F. and R. A. Dalrymple (1978). Bottom frictional stress and longshore currents due to waves with large angles of incidence. *J. Marine Res.* (36), 357–375.

Longuet-Higgins, M. S. (1956). The mechanics of the boundary-layer near the bottom in a progressive wave. In *Proc. 6th Int. Conf. Coastal Engng.*, Vol. 1, Miami, 184–193. ASCE.

Longuet-Higgins, M. S. (1970b). Longshore currents generated by obliquely incident sea waves, 1. *J. Geophys. Res. 75*(33), 6778–6789.

Longuet-Higgins, M. S. (1970a). Longshore currents generated by obliquely incident sea waves, 2. *J. Geophys. Res. 75*(33), 6790–6801.

Longuet-Higgins, M. S. (1972). Recent progress in the study of longshore currents. In R. E. Meyer (Ed.), *Waves on beaches and resulting sediment transport*, 203–248. Academic Press.

Longuet-Higgins, M. S. and R. W. Stewart (1963). A note on wave set-up. *J. Marine Res.* (21), 4–10.

Longuet-Higgins, M. S. and R. W. Stewart (1964). Radiation stresses in water waves; a physical discussion with applications. *Deep Sea Res.* (11), 529–562.

Mayerle, R., A. Schröter, and W. Zielke (1994). Simulation of nearshore wave current ineraction by coupling a Boussinesq wave model with a 3D hydrodynamic model. In *Proc. 24th Int. Conf. Coastal Engng.*, Vol. 3, Kobe, 2340–2349. ASCE.

Mei, C. C. (1989). *The Applied Dynamics of Ocean Surface Waves.* Singapore: World Scientific. pp. 740.

Mei, C. C. and P. L.-F. Liu (1977). Effects of topography on the circulation in and near the surf zone - linear theory. *Estuarine and Coastal Marine Science 5*, 25–37.

Myrhaug, D. and O. H. Slaattelid (1990). A rational approach to wave-current friction coefficients for rough, smooth and transitional turbulent flow. *Coastal Engng. 14*, 265–293.

Nadaoka, K. and T. Kondoh (1982). Laboratory measurements of velocity field structure in the surf zone by ldv. *Coastal Engng. in Japan 25*, 125–145.

Nairn, R. B., J. A. Roelvink, and H. N. Southgate (1990). Transition zone width and implications for modelling surfzone hydrodynamics. In *Proc. 22nd Int. Conf. Coastal Engng.*, Vol. 1, Delft, 68–81. ASCE.

Newland, D. E. (1993). *An introduction to random vibrations, spectral & wavelet analysis.* New York: John Wiley & Sons, Inc. pp. 477.

Nielsen, P. and Z.-J. You (1996). Eulerian mean velocities under non-breaking waves on horizontal bottoms. In *Proc. 25th Int. Conf. Coastal Engng.*, Vol. 4, Orlando, 4066–4078. ASCE.

Okayasu, A. (1989). *Characteristics of turbulence structure and undertow in the surf zone.* Ph. D. thesis, University of Tokyo.

Okayasu, A., T. Shibayama, and N. Mimura (1986). Velocity field under plunging waves. In *Proc. 20th Int. Conf. Coastal Engng.*, Vol. 1, Taipei, 660–674. ASCE.

Oltman-Shay, J., P. A. Howd, and W. A. Birkemeier (1989). Shear instabilities in the mean longshore current: 2-field observations. *J. Geophys. Res. 94*(C12), 18031–18042.

Osiecki, D. A. and W. R. Dally (1996). The influence of rollers on longshore currents. In *Proc. 25th Int. Conf. Coastal Engng.*, Vol. 3, Orlando, 3419–3430. ASCE.

Özkan-Haller, H. T. and J. T. Kirby (1995). Finite amplitude shear wave instabilities. In *Coastal Dynamics'95*, Gdansk, 465–476. ASCE.

Özkan-Haller, H. T. and J. T. Kirby (1996). Numerical study of low frequency surf zone motions. In *Proc. 25th Int. Conf. Coastal Engng.*, Vol. 2, Orlando, 1361–1374. ASCE.

Özkan-Haller, H. T. and J. T. Kirby (1997). Nonlinear evolution of shear instabilities of the longshore current. (Ph. D. Dissertation), Res. Report CACR-97-08, Center for Applied Coastal Research, Univ. of Delaware.

Pechon, P. and C. Teisson (1994). Numerical modelling of three-dimensional wave-driven currents in the surf-zone. In *Proc. 24th Int. Conf. Coastal Engng.*, Vol. 3, Kobe, 2503–2512. ASCE.

Peregrine, D. H. (1983). Breaking waves on beaches. *Ann. Rev. Fluid Mech.* (15), 149–178.

Peregrine, D. H. and I. A. Svendsen (1978). Spilling breakers, bore and hydraulic jumps. In *Proc. 16th Int. Conf. Coastal Engng.*, Vol. 1, Hamburg, 540–550. ASCE.

Phillips, O. M. (1977). *The Dynamics of the Upper Ocean.* New York: Cambridge University Press. pp. 336.

Putnam, J. A., W. H. Munk, and M. A. Traylor (1949). The prediction of longshore currents. In *Trans. AGU*, Vol. 30, 337–345. AGU.

Putrevu, U., J. Oltman-Shay, and I. A. Svendsen (1995). Effect of alongshore nonuniformities on longshore current predctions. *J. Geophys. Res. 100*(C8), 16119–16130.

Putrevu, U. and I. A. Svendsen (1991). Wave induced nearshore currents: a study of the forcing, mixing and stability characteristics. (Ph. D. Dissertation), Res. Report CACR-91-11, Center for Applied Coastal Research, Univ. of Delaware.

Putrevu, U. and I. A. Svendsen (1992a). A mixing mechanism in the nearshore region. In *Proc. 23rd Int. Conf. Coastal Engng.*, Vol. 3, Venice, 2758–2771. ASCE.

Putrevu, U. and I. A. Svendsen (1992b). Shear instability of longshore currents: A numerical study. *J. Geophys. Res. 97*(C5), 7283–7303.

Putrevu, U. and I. A. Svendsen (1993). Vertical structure of the undertow outside the surf zone. *J. Geophys. Res. 98*(C12), 22707–22716.

Putrevu, U. and I. A. Svendsen (1997). Shear dispersion of momentum in the nearshore. *Submitted to: J. Fluid Mech. ???*(?), ??

Rakha, K. A. and J. W. Kamphuis (1997). Wave-induced currents in the vicinity of a seawall. *Coastal Engng. 30*, 23–52.

Reniers, A. J. H. M., J. A. Battjes, A. Falqués, and D. A. Huntley (1997). A laboratory study on the shear instability of longshore currents. *J. Geophys. Res. 102*(C4), 8597–8609.

Reniers, A. J. H. M., E. B. Thornton, and T. C. Lippman (1995). Longshore currents over barred beaches. In *Coastal Dynamics'95*, Gdansk, 413–424. ASCE.

Reniers, A. J. H. M., E. B. Thornton, and T. C. Lippman (1997). Effects of alongshore non-uniformities on longshore currents measured in the field. *J. Geophys. Res.* (Submitteed for publication).

Rodi, W. (1984). *Turbulence models and their application in hydraulics.* Int. Assoc. Hydraulic Res. pp. 104.

Rodriguez, A., A. Sanchez-Arcilla, F. R. C. V. Gracia, and M. G. Courissat (1994). Waves and currents at the ebro delta surf zone: measurements and modelling. In *Proc. 23rd Int. Conf. Coastal Engng.*, Vol. 3, Kobe, 2542–2556. ASCE.

Sanchez-Arcilla, A., F. Collado, C. Lemos, and F. Rivero (1990). Another quasi-3d model for surf-zone flows. In *Proc. 22nd Int. Conf. Coastal Engng.*, Vol. 1, Delft, 316–329. ASCE.

Sanchez-Arcilla, A., F. Collado, and A. Rodriguez (1992). Vertically varying velocity field in q-3d nearshore circulation. In *Proc. 23rd Int. Conf. Coastal Engng.*, Vol. 3, Venice, 2811–2824. ASCE.

Sancho, F. E., I. A. Svendsen, A. R. Van Dongeren, and E. B. Thornton (1996). Numerical modeling of longshore currents: Comparison with field data. In *Proc. Amer. Geophys. Union, Fall Meeting*, S. Francisco, F395. AGU.

Sancho, F. E. P., I. A. Svendsen, A. R. Van Dongeren, and U. Putrevu (1995). Longshore nonuniformities of nearshore currents. In *Coastal Dynamics'95*, Gdansk, 425–436. ASCE.

Shapiro, R. (1970). Smoothing, filtering, and boundary effects. *Reviews of Geophysics and Space Physics 8*(2), 359–387.

Shepard, F. P., K. O. Emery, and E. C. La Fond (1941). Rip currents: A process of geological importance. *J. Geology XLIX*(4), 337–369.

Shepard, F. P. and D. L. Inman (1950). Nearshore water circulation related to bottom topography and wave refraction. *Transactions American Geophys. Union 31*(2), 196–212.

Simons, R. R., T. J. Grass, and M. Mansour-Teharani (1992). Bottom shear stresses in the boundary layers under waves and currents crossing at right angles. In *Proc. 23rd Int. Conf. Coastal Engng.*, Vol. 1, Venice, 604–617. ASCE.

Simons, R. R., R. D. MacIver, and W. M. Saleh (1996). Kinematics and shear stresses from combined waves and longshore currents in the uk coastal research facility. In *Proc. 25th Int. Conf. Coastal Engng.*, Vol. 3, Orlando, 3481–3494. ASCE.

Sleath, J. F. A. (1987). Turbulent oscillatory flow over rough beds. *J. Fluid Mech. 182*, 369–409.

Smith, J. M., M. Larson, and N. C. Kraus (1993). Longshore current on a barred beach: Field measurements and calculation. *J. Geophys. Res. 98*(C12), 22717–22731.

Smith, J. M., I. A. Svendsen, and U. Putrevu (1992). Vertical structure of the nearshore current at delilah: measured and modeled. In *Proc. 23rd Int. Conf. Coastal Engng.*, Vol. 3, Venice, 2825–2838. ASCE.

Sonu, C. J. (1972). Field observation of nearshore circulation and meandering currents. *J. Geophys. Res. 77*(18), 3232–3246.

Soulsby, R. L. (1983). The bottom boundary layer of shelf seas. In B. Johns (Ed.), *Physical Oceanography of Coastal and Shelf Seas*, Amsterdam, 189–266. Elsevier.

Stive, M. J. F. (1980). Velocity and pressure field of spilling breakers. In *Proc. 17th Int. Conf. Coastal Engng.*, Vol. 1, Sydney, 547–566. ASCE.

Stive, M. J. F. and H. G. Wind (1982). A study of radiation stress and set-up in the nearshore region. *Coastal Engng. 6*, 1–25.

Stive, M. J. F. and H. G. Wind (1986). Cross-shore mean flow in the surf zone. *Coastal Engng. 10*, 325–340.

Supharatid, S., H. Tanaka, and N. Shuto (1992). Interactions of waves and current (part i: Experimental investigation). *Coastal Engng. in Japan 35*(2), 167–186.

Svendsen, I. A. (1984a). Mass flux and undertow in a surf zone. *Coastal Engng. 8*, 347–365.

Svendsen, I. A. (1984b). Wave heights and set-up in a surf zone. *Coastal Engng. 8*, 303–329.

Svendsen, I. A. (1987). Analysis of surf zone turbulence. *J. Geophys. Res. 92*(C5), 5115–5124.

Svendsen, I. A. and J. Buhr Hansen (1988). Cross-shore currents in surf-zone modelling. *Coastal Engng. 12*, 23–42.

Svendsen, I. A. and R. S. Lorenz (1989). Velocities in combined undertow and longshore currents. *Coastal Engng. 13*, 55–79.

Svendsen, I. A. and U. Putrevu (1990). Nearshore circulation with 3-d profiles. In *Proc. 22nd Int. Conf. Coastal Engng.*, Vol. 1, Delft, 241–254. ASCE.

Svendsen, I. A. and U. Putrevu (1993). Surf-zone wave parameters from experimental data. *Coastal Engng. 19*, 283–310.

Svendsen, I. A. and U. Putrevu (1994). Nearshore mixing and dispersion. *Proc. R. Soc. Lond. A*(445), 561–576.

Svendsen, I. A. and U. Putrevu (1996). Surf zone hydrodynamics. In P. L.-F. Liu (Ed.), *Advances in Coastal and Ocean Engineering*, Vol. 2, 1–78. World Scientific.

Svendsen, I. A., H. A. Schaffer, and J. Buhr Hansen (1987). The interaction between the undertow and the boundary layer flow on a beach. *J. Geophys. Res. 92*(C11), 11845–11856.

Swart, D. H. (1974). Offshore sediment transport and equilibrium beach profiles. Publication No. 131, Delft Hydraulics Lab.

Taylor, G. I. (1954). The dispersion of matter in turbulent flow through a pipe. *Proc. R. Soc. Lond. A*(223), 446–468.

Thornton, E. B. (1970). Variation of longshore current across the surf zone. In *Proc. 12th Int. Conf. Coastal Engng.*, Vol. 1, Washington, 306–316. ASCE.

Thornton, E. B. and R. T. Guza (1986). Surf zone longshore currents and random waves: Field data and models. *J. of Physical Oceanography 16*(7), 1165–1178.

Thornton, E. B., R. T. Humiston, and W. Birkemeier (1996). Bar/trough generation on a natural beach. *J. Geophys. Res. 101*(C5), 12097–12110.

Thornton, E. B. and C. S. Kim (1993). Longshore current and wave height modulation at tidal frequency inside the surf zone. *J. Geophys. Res. 98*(C9), 16509–16519.

Thornton, E. B., C. M. C. V. Soares, and T. P. Stanton (1995). Vertical profiles of longshore currents and bed shear stress. In *Coastal Dynamics'95*, Gdansk, 449–459. ASCE.

Van Dongeren, A. R., F. E. P. Sancho, I. A. Svendsen, and U. Putrevu (1994). Shorecirc: A quasi-3d nearshore model. In *Proc. 24th Int. Conf. Coastal Engng.*, Vol. 3, Kobe, 2741–2754. ASCE.

Van Dongeren, A. R. and I. A. Svendsen (1997a). An absorbing-generating boundary condition for shallow water models. *J. of Waterway, Port, Coastal and Ocean Engng. 123*(6), 303–313.

Van Dongeren, A. R. and I. A. Svendsen (1997b). Quasi-3D modeling of nearshore hydrodynamics. (Ph. D. Dissertation), Res. Report CACR-97-04, Center for Applied Coastal Research, Univ. of Delaware.

Van Dongeren, A. R., I. A. Svendsen, and F. E. P. Sancho (1996). Generation of infragravity waves. In *Proc. 25th Int. Conf. Coastal Engng.*, Vol. 2, Orlando, 1335–1348. ASCE.

Visser, P. J. (1986). Wave basin experiments on bottom friction due to current and waves. In *Proc. 20th Int. Conf. Coastal Engng.*, Vol. 1, Taipei, 807–821. ASCE.

Visser, P. J. (1991). Laboratory measurements of uniform longshore currents. *Coastal Engng. 15*, 563–593.

WAMDI Group (1988). The WAM model: A third generation ocean wave prediction model. *J. of Physical Oceanography 18*, 1775–1810.

Whitford, D. J. and E. B. Thornton (1996). Bed shear stress coefficient for longshore currents over a barred profile. *Coastal Engng. 27*, 243–262.

Wu, C.-H. and P. L.-F. Liu (1984). Effects of nonlinear inertial forces on nearshore currents. *Coastal Engng. 8*, 15–32.

Wu, C.-H., E. B. Thornton, and R. T. Guza (1985). Waves and longshore currents: Comparison of a numerical model with field data. *J. Geophys. Res. 90*(C3), 4951–4958.

You, Z.-J. (1994). A simple model for current velocity profiles in combined wave-current flows. *Coastal Engng. 23*, 289–304.

You, Z.-J. and P. Nielsen (1996). Movable bed roughness in the flow of irregular waves and currents over movable beds. In *Proc. 25th Int. Conf. Coastal Engng.*, Vol. 3, Orlando, 3495–3506. ASCE.